Polarisation Controlled Quasi-Phase Matching of High Harmonic Generation

Lewis Z. Liu

Department of Physics

Merton College, University of Oxford

Supervised by

Professor Simon Hooker

A thesis submitted for the degree of

Doctor of Philosophy

Trinity Term 2014

dedicated to Mom, Dad, and Sam

Acknowledgements

I would first like to thank Simon for all your mentorship, insights and guidance. Working with you these last four years has been a privilege and an inspiration. You have my deepest gratitude for considering even my silliest ideas – at least we managed to squeeze out a few papers from them! My doctorate would not have been possible without you.

Kevin and David, it has been a pleasure working alongside you, and you have my sincere thanks for helping me my way around the lab. Special thanks to everyone else in the Hooker Group and the Simon Room: Wolf, James, Nicolas, Chris, Gavin, and Jena.

I would also like to thank Mom and Dad for your unwavering support through my entire life. I cannot imagine more loving, dedicated, and thoughtful parents, and I feel extremely blessed to have you. I would also like to thank my little brother Samuel, especially for being a such a source of joy and wonder. I feel extremely lucky to be able to share my passion for physics with you, and hope you may have infinite success at my old alma mater and beyond. Sincere thanks to Auntie (DaYi) for your love and support all these years.

I also wish to acknowledge Julian, Tom, Emily, Boris, Josh, Nic, Buck, Momin, Daniel and Gillian who helped me through these four years. Special thanks to Momin for reminding me of my dreams and principles; and to Julian for your advice and wisdom.

Finally I'd like to thank my beloved Andrea for being there, always.

Abstract

This thesis focuses on the development of high harmonic generation (HHG) by using polarisation controlled quasi-phase matching QPM as well as related topics.

A new class of QPM techniques called polarisation-controlled QPM is introduced where linear or circlar birefringence enables the modulation of the driving field's polarisation state called polarisation-beating QPM (PBQPM) for linear birefringence and optical rotation QPM (ORQPM) for circular birefringence respectively. PBQPM uses a linear birefringence to modulate periodically the driving pulse between linear and circular/elliptical polarisation states. Because elliptical or circular polarisation of the driving pulse suppresses harmonic generation, by appropriately matching the beat length of the driving field's polarisation state to the coherence length of the harmonic generation, QPM can be achieved. In the second technique, ORQPM, propagation of the driving radiation in a system exhibiting circular birefringence causes its plane of polarisation to rotate; by appropriately matching the period of rotation to the coherence length, it is possible to avoid destructive interference of the generated radiation. Not only does ORQPM have similar enhancements as true-phase matching, it is also the first proposed QPM source for circularly polarised high harmonics.

The importance of phase modulation in QPM, especially relating to mode-beating in hollow-core waveguides where harmonics is being generated are also

explored theoretically. Based on this, a novel technique for analyzing random phase matching using a continuous phase-diffusion treatment has been developed; theoretical analytical models are shown to produce excellent agreement with simulations. It is further shown that random phase matching may be responsible for additional broadening of the high harmonic spectrum, especially at higher harmonic orders.

Because mode and polarisation control is central to polarisation-controlled QPM, four waveguide mode decomposition techniques from single shot CCD data have been developed. The extraction of phase and coupling coefficients are demonstrated experimentally. A novel analytical general solution for the phase introduced by a phase-only spatial light modulator to generate a given far-field phase and amplitude was developed. The solution was demonstrated experimentally and shown to enable excellent control of the far-field amplitude and phase.

Finally, circular and linear birefringent waveguides were explored. Analytic solutions to rectangular birefringent hollow-core waveguides were developed and some initial demonstration experiments were performed.

Publications, Patents, and Conferences

Publications

1. **L.Z.Liu**, K.O'Keeffe, D. T. Lloyd and S.M.Hooker. "A general analytic solution for far-field phase and amplitude control with a phase-only spatial light modulator," *Optics Letters*, 39(7):2137, (2014)

2. **L.Z.Liu**, K.O'Keeffe, and S.M.Hooker. "Multi-mode polarization beating quasi-phase matching for high harmonic generation," *Physical Review A*, 87(2): 023810 (2013)

3. **L.Z.Liu**, K.O'Keeffe, and S.M.Hooker. "Optical rotation quasi-phase-matching for circularly polarized high harmonic generation," *Optics Letters*, 37(12): 2415–2417 (2012)

4. **L.Z.Liu**, K.O'Keeffe, and S.M.Hooker. "Quasi-phase-matching of high harmonic generation using polarization beating in optical waveguides," *Physical Review A*, 85(5): 053823 (2012)

Patents

1. **L.Z.Liu**, K.O'Keeffe, and S.M.Hooker. "High Harmonic Optical Generator [Optical Rotation]," Isis Innovation, *UK Patent Application* GB1208753.2 (18/5/2012)

2. **L.Z.Liu**, K.O'Keeffe, and S.M.Hooker. "High Harmonic Optical Generator [Polarization Beating 2/2]," Isis Innovation, *UK Patent Application* GB1207963.8 (8/5/2012)

3. **L.Z.Liu**, K.O'Keeffe, and S.M.Hooker. "High Harmonic Optical Generator [Polarization Beating 1/2]," Isis Innovation, *UK Patent Application* GB1117355.6 (7/10/2011)

Conferences & Talks

1. **L.Z.Liu**, K.O'Keeffe, and S.M.Hooker. "Polarisation control for high harmonic generation," Conference Talk. Munich, Germany. *The European Conference on Lasers and Electro-Optics (CLEO)* (2013)

2. **L.Z.Liu** "Technique for circularly polarized coherent soft X-Rays with high harmonic generation," Invited Talk, Department Seminar. London, UK. *London Centre for Nanotechnology, University College London* (2012)

3. **L.Z.Liu**, K.O'Keeffe, and S.M.Hooker. "Polarization-controlled quasi-phase matching for high harmonic generation," Conference Talk. Durham, UK. *Institute of Physics Photon12* (2012)

4. **L.Z.Liu**, K.O'Keeffe, and S.M.Hooker. "Polarization-controlled quasi-phase matching for high harmonic generation," Poster Presentation. Lausanne, Switzerland. *XVIII International Conference of Ultrafast Phenomena* (2012)

5. **L.Z.Liu**, K.O'Keeffe, and S.M.Hooker. "Polarization beating quasi-phase matching for high harmonic generation," Conference Talk, Abingdon, UK, *High Power Laser Science Community Meeting* (2011)

Contents

Chapter 1

Introduction

1.1 Motivation

The invention of the laser is one of the the most significant achievements in physics of the twentieth century. The application of coherent light has found applications across all fields from medicine to manufacturing to computer technology. In addition to advancements in technology, the laser has become a fundamental scientific research tool in the areas of spectroscopy, laser cooling, or even gene manipulation. Different applications require different wavelengths, but most of the research focus in the first few decades of laser development has been on the visible through to longer wavelength regimes due to the ease in which population inversion can be obtained and with the available materials.

However, shorter wavelengths in the extreme ultraviolet (XUV - 10-120nm), soft x-ray (0.1-10nm), or hard x-ray (< 0.1nm) regimes have been much more difficult to achieve. This is because in a traditional laser, the pump energy required scales as $\sim 1/\lambda_0^4$, where λ_0 is the laser wavelength [50]. Hence, to achieve usable brightness in the x-ray or XUV regime requires billions or trillion times more pump energy than say in the visible regime for a given gain coefficient.

The generation of coherent short wavelength sources has been a tremendous area of research in recent years. Different methods for achieving XUV or soft X-rays include synchrotron, laser-plasma sources, free electron lasers (FELs), or high harmonic generation. Although synchrotrons and FELs achieve high spectral brightness and high photon energies, they are massive installations – some over a few kilometers long – and cost up to billions of dollars to build. Hence, there is a real need for affordable and compact coherent XUV or x-ray sources. This thesis focuses on one in particular, which is high harmonic generation.

1.2 Coherent extreme ultraviolet or x-ray sources

This section gives a brief introduction to each of the various sources. Figure 1.1 gives an overall map of the research area for XUV or soft X-rays sources. We note that peak spectral brightness, B, is defined by,

$$B = \frac{N}{\tau \Omega A \sigma} \tag{1.1}$$

where N is the number of photons per pulse, Ω is the solid angle of emission, A is the cross sectional area, τ is the pulse duration, and σ is the spectral bandwidth. The spectral brightness B is usually given in units of s^{-1} mrad $^{-2}$ mm $^{-2}$ per 0.1% of bandwidth. We note that in recent years, the photon energy of phase-matched harmonics has been extended using longer wavelength drivers, which should also extend the theoretical maximum of photon energy for quasi-phase matching as well [92]. Moreover, although high harmonic generation cannot attain the type of peak brightness as an FEL, as mentioned above, they are significantly cheaper and more compact. In the next few subsections, we will discuss the various types of sources.

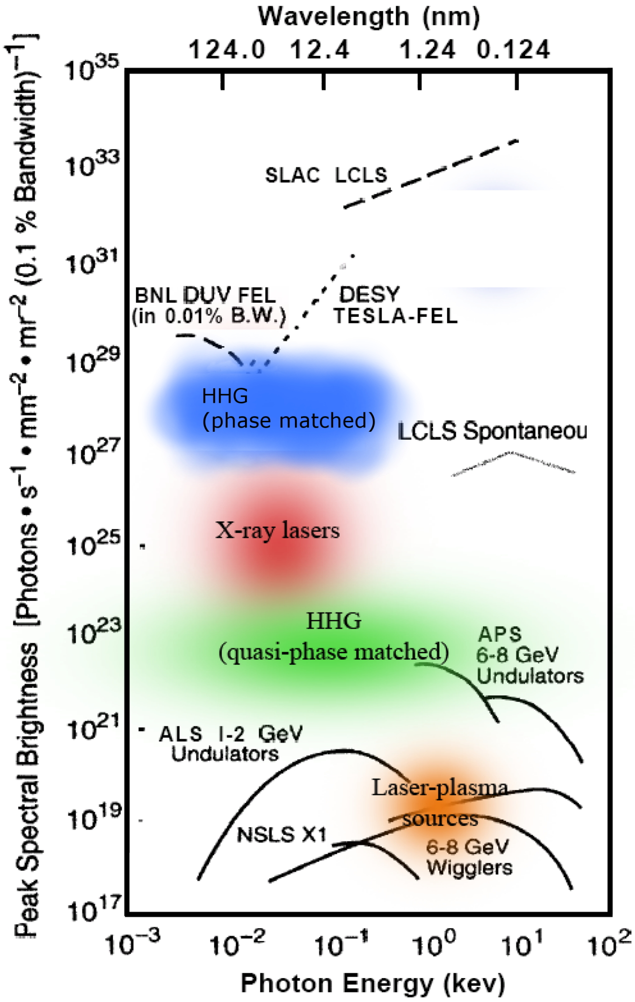

Figure 1.1: Landscape of various coherent XUV or x-ray sources by peak spectral brightness and photon energy. Figure adapted from [11; 97].

1.2.1 Synchrotrons

Synchrotrons are particle accelerators adapted to exploit the photon radiation generated from accelerated particles. In the earlier days of particle physics, synchrotron radiation was viewed as an undesirable consequence of electric and magnetic field driven circular particle accelerators because they limited the particle energy which could be achieved in a circular machine. Hence, the LHC at CERN in Geneva had to be built over 27 km in circumference in order to achieve proton energies up to 4TeV required for its experiments.

In the context of coherent XUV or X-ray generation however, sychrotrons can be built specifically for photon generation and can have very high brightness on the order of $> 10^{19}$ s^{-1} mrad $^{-2}$ mm $^{-2}$ per 0.1% of bandwidth. Later generation synchrotrons can inject maximally accelerated electrons into larger circular storage rings in high vacuum that can hold particle bunches for hours to be used on demand. In the straight sections of the storage rings, static magnetic fields in periodic opposite polarities can then be employed to 'wiggle' the electrons bunches as they pass through. Given the high velocity of the electrons, the magnetic field imparts very sharp acceleration onto them due to the Lorentz Force Law, generating bright coherent high energy photons. Thus as a result, these devices are called 'wigglers' or 'undulators'.

In conclusion, synchrotron facilities can achieve high brightness and photon energies, but due to the size and sophisticated engineering required, powerful synchrotrons are on the order of several tens to hundreds of millions of dollars to build and very expensive to maintain. Hence, there are limited number of them around the world with strictly rationed beam-time.

1.2.2 X-Ray Free Electron Lasers

Free Electron Lasers (FELs) also utilize synchrotrons but are significantly brighter – upward of a billion times more – since it utilizes complete coherent buildup of photons. In a synchrotron, photons are generated uniformly and randomly which causes partial destructive interference of the light. An FEL, however, utilizes microbunches of electrons which are periodic to the same wavelength of the generated XUV or X-rays. The microbunches are spaced with the period of one optical wavelength, enabling in-phase radiation. Hence, the light is able to coherently add in-phase giving the type of coherence only available in conventional lasers. As of today, there are no effective X-ray mirrors given the lack of materials required for high reflectivity in this wavelength regime so FELs use a single pass geometry with around 1000 undulator periods, but this prevents the construction of an FEL oscillator. However, even if such mirrors were available, the electron bunches are very short. Hence, each round trip of x-ray photons would need to interact with a fresh electron bunch.

Another major drawback of FELs is that they have a 'noisy' start-up and hence do not allow for temporal coherence. Techniques to 'seed' the FEL with another X-ray source have been used to address this issue. In fact, seeding FELs is one of the major potential applications for HHG [38].

FELs can be used for ultrafast physics given the fact that the microbunches are in the order of femtoseconds [18], and the wavelength can be tuned by adjusting the magnetic field or electron beam energy.

Like synchrotrons, FELs are prohibitively expensive (over one billion US dollars) and there are only a few of them around the world. The first one was DESY at Hamburg where it utilized a 30 m long undulator that was able to produce pulses of coherent light at around 6.5nm in the soft X-ray regime. The first true x-ray FEL, the Linac Coherent Light Source at Stanford has been able to produce x-rays in the hard x-ray regime, and most recently the European x-ray free electron laser (European XFEL) is under construction and expected to be in operation by 2017 generating coherent photons with wavelengths down to 0.05nm [1]. Other examples of FELs include the SPring-8 in Switzerland and the SACLA in Japan.

1.2.3 X-ray lasers

As mentioned above, the primary problem with generating coherent XUV or X-ray source using a laser is the λ^{-4} wavelength scaling factor. Moreover, the medium typically has to be highly ionized in order for the gap between the energy levels to be the x-ray regime. Two other major problems are that it is difficult to find materials that have the right transitions required for an X-ray laser and that there are limited materials that have high reflectivity in the XUV or X-ray regime so that the laser must be built with a single pass geometry.

As of today however, there are no commercially viable X-ray lasers and hence the research community has been exploring other alternatives. However, perhaps one of closest X-ray laser designs to being commercially available is that pioneered by Rocca's group in Colorado State by using discharge excited x-ray lasers [99]. Most recently, a team in California achieved a 10 Hz repetition rate laser was achieved with a wavelength of 18.9nm. By using a two-stage pumping process, the optimum electron density was achieved to increase the absorption for a specified gain region [60]. Even more recently, the Rocca group achieved lasing down to 7.36nm at 1Hz using transitions of higher-Z nickel-like lanthanide ions using a similar approach [4]. The total optical pump energy of 7.5J was one of the lowest ever reported at the time. However, the low repetition rate and still relatively high pump energy implies that further development in this area is required to make x-ray lasers commercially attractive. Finally, we would like to mention two more detailed review articles on this topic, which can be found in Refs [29; 51].

1.2.4 High Z laser plasma sources

By focusing an intense laser pulse on order of $10^{15} - 10^{16}$ W/cm^2 onto a high-Z metal, *incoherent* high energy photons can be generated. The heated plasma as a result of the ablative reaction caused by the laser emits characteristic X-ray fluorescent lines and has a short pulse comparable to the short pulse width of the driving laser pulse. Hence, this source is useful for table-top, affordable but incoherent, uncollimated short pulses of X-rays.

1.2.5 High harmonic generation

This thesis focuses on high harmonic generation (HHG), which is a compact and affordable technique that enables the generation of bright, coherent, collimated, ultrafast XUV or x-ray pulses. We note that the next chapter provides a more detailed discussion on the physical process of HHG. The basic experimental setup of HHG is simple. By focusing a laser to very high intensities on order of 10^{14} W/cm^2 into a gaseous (or other) medium, extremely high order of harmonics (>100) of the driving laser pulse can be generated.

The basic physics of this technique can be explained in the following semi-classical way: the electric field of the driving laser pulse distorts the Coulomb potential of the gaseous medium and enables an electron to quantum tunnel out. The electron is then accelerated through the laser field and may recombine with the parent ion emitting a high harmonic photon. The harmonic field that is generated exhibits similar coherence properties of the driver.

However, one of the key limiting factors of HHG is that the driving field and the harmonic field have different phase velocities causing cancellation of the harmonics. Various techniques have been developed to address this issue, which will be explored in the following chapters. We also note that the medium for HHG can also be solid targets as well, but that is beyond the scope of this thesis.

1.3 Applications for HHG

The three key characteristics of high harmonic light is that it has short wavelengths, is coherent, and is ultrafast (femtosecond or attosecond time scales). This, combined with the fact that the source is both compact and relatively affordable gives a wide breadth of applications for HHG.

Imaging resolution scales linearly with wavelength. Hence, similar to above, HHG can also be used for nano-scale coherent diffractive imaging (CDI) [101]. CDI is lensless and uses a coherent beam scattering off an object. In the far-field, an image captured by the detector proportional to the Fourier transform of the amplitude in the object plane can be captured. Various phase retrieval algorithms can then be employed to reconstruct the object. Moreover, the carbon K-absorption edge is around 284 eV (4.4nm) and the oxygen K-absorption edge is around 539 eV (2.3nm), which can be used to probe biological systems. In this wavelength range, the light is also transparent to water, enabling observation of biological processes *in vivo*.

Given the ultrafast nature of HHG, another application includes time-resolved measurements of molecular or electronic dynamics [22; 103; 117; 120]. Paul et al. [89] in 2001 first demonstrated trains of HHG pulses, each of order of 250as, using phase locking from five consecutive harmonics in Argon, based on theory from Farkas and Toth [39] who proposed that a broad spectrum of harmonics can generate pulses in the attosecond range. Even more recently, it has been proposed that zeptosecond pulses may theoretically be generated with high harmonics [49].

1.4 Scope of thesis

This thesis explores theoretical and some experimental aspects of high harmonic generation in hollow-core optical waveguides, in particular, on the use of quasi-phase-matching by control of modes and/or polarisation states of the driving laser pulse.

The thesis is overall divided into three themes:

1. *Introduction* (Chapters 1-3) – These chapters give a brief introduction to HHG as well as to the overall problem this thesis attempts to tackle. The next chapter, Chapter 2, will give a brief introduction of the HHG process on an atomic scale while Chapter 3 will give an overview of the phase mismatch problem and a broad view of the various potential solutions to address it.

2. *Theoretical Framework* (Chapters 4-8) – These chapters develop some theoretical groundwork. Chapter 4 provides a basic theoretical framework for waveguide modes that will be critical for the remaining text of the thesis. Chapter 5 will discuss a novel way of using linear birefringence for quasi-phase matching of HHG based on our paper from [73]. Chapter 6 will discuss another novel method of using circular birefringence to generate circularly polarized high harmonics based on our paper from [72]. Chapter 7 develops a unified theoretical framework for modal and linear birefringent quasi-phase matching based on our work in [74]. Finally, Chapter 8 is a slight detour where we explore random phase matching using a novel theoretical analytical model that follows from the previous chapters.

3. *Tools, methodologies, and future work* (Chapters 9-12) – These chapters cover some of the tools and methods developed to be able to conduct experiments relating to modal or polarization control HHG. Chapter 9 develops a few potentially novel methods for extracting modal information based on a single CCD measurement. Chapter 10 discusses a new and theoretically unified way of generating arbitrary spatial beam profiles in the focal plane using a phase-only spatial light modulator (SLM) based on our paper from [75]. Chapter 11 discusses some possible ideas on building birefringent waveguides and provide some extremely preliminary experimental results. Chapter 12 gives a brief conclusion and discusses possible future work.

1.5 Role of the Author

The ideas for polarization controlled QPM – both polarisation beating QPM (linear birefringence) and optical rotation QPM (circular birefringence) – were initially originated by the Author and worked through in detail with Professor Hooker. The theoretical framework for unifying modal and linear birefringent QPM (called MMPBQPM in later chapters) was developed together by the Author and Professor Hooker. The theoretical model for random phase matching was developed by the Author based on MMPBQPM with some key insights from Professor Hooker.

The four mode analysis methods presented were developed independently by the Author. The new SLM theory and method were originated by the Author with its phase unwrapping analysis supported by David Lloyd. The rectangular waveguide analysis and twisted capillary experiment were conducted by the Author.

All simulations unless otherwise specified were conducted by the Author. Finally, the Author built and conducted all experiments, and they were all advised by both Professor Hooker and Dr. Kevin O'Keeffe.

Chapter 2

High Harmonic Generation

High harmonic generation is a result of a nonlinear response to an intense driving laser field interacting with a gaseous medium. Under the right conditions, high order harmonics of the driving laser can be achieved. Typical experimental parameters for HHG include laser intensities above $10^{14}\mathrm{W/cm^2}$, driver wavelengths between $800 - 2000\mathrm{nm}$, low gas pressures of order of 10s to 100s of mbar (although, the pressure can be as high as a few atmospheres for long wavelength drivers [92]), and noble gas (Argon, Neon) as the species medium. At this intensity, the laser field is much stronger than, or comparable with, the field binding electrons to the atom; hence, the HHG process is non-perturbative, which is why high-order harmonics can be observed. In this chapter, we will describe the origins of these harmonics as well as specific properties in the generation process related to the scope of this thesis.

2.1 Corkum's Three Step Model

The simple theoretical semi-classical model written down by Corkum for high harmonic generation gives a very useful framework for understanding the process [26]. It can be broken down into three key steps, as illustrated schematically in Figure 2.1:

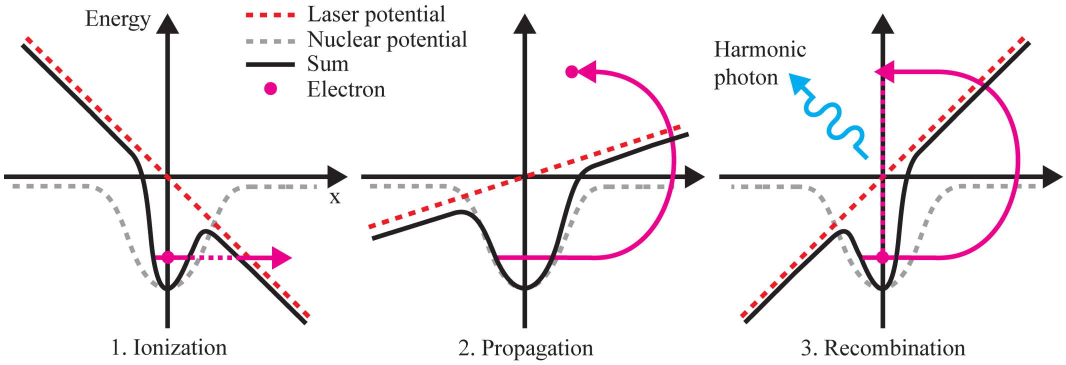

Figure 2.1: 3-step model for HHG, figure from [97]

1. Ionization – The strong laser field perturbs the atomic Coulomb potential, which the electron may become ionized via quantum tunneling and an electron is born into the continuum.

2. Propagation – The electron propagates, assuming a classical trajectory, in the continuum under the electromagnetic force of the oscillating laser field.

3. Recombination – After the field reverses, the electrons are accelerated back to the atom, and they have a chance of recombining with the atom, emitting a harmonic photon with energy that is the sum of its kinetic energy plus the atomic binding energy I_p.

The driving laser field at time t with amplitude e and angular frequency ω can be described as,

$$E = [E_x, E_y] = e[\cos(\omega t), s\sin(\omega t)] \tag{2.1}$$

where $s = 0$ for a linearly polarised driving laser field and $s = \pm 1$ for a circularly polarised driving laser field. Magnetic fields are ignored given that the electric field forces dominate over the magnetic field forces, assuming that the speed of the electron is much less than the speed of light. The ionisation tunneling rate Corkum uses is the Ammosov-Delone-

Krainov (ADK) approximation for hydrogen [5]. After the electron tunnels out, the electron motion in the oscillating electric field are described classically by,

$$x = -x_0 \cos(\omega t) - v_{0x} t + x_{0x} \tag{2.2}$$

$$y = -s x_0 \sin(\omega t) + s v_{0y} t + y_{0y} \tag{2.3}$$

$$v_x = v_0 \sin(\omega t) + v_{0x} \tag{2.4}$$

$$v_y = -s v_0 \cos(\omega t) + v_{0y} \tag{2.5}$$

where $v_0 = ee/(m_e\omega)$, $x_0 = ee/(m_e\omega^2)$, e is the electron charge, m_e is the electron mass, and x_{0x}, y_{0y}, v_{0x}, v_{0y} are initial conditions that can be calculated for time $t = 0$.

It may be shown that if the driving field is circularly polarised with $s = \pm 1$, the electron never returns to the parent ion, suggesting that circular polarisation inhibits the harmonic generation process. This will be explored in a bit more in detail later in the chapter, since this concept is key to polarisation beating quasi-phase matching explored in this thesis.

For a linearly x-axis polarised driving pulse where $s = 0$, the electron trajectory can be confined to the x-dimension, and is given by,

$$x(t,\tau) = \frac{ee}{m_e\omega^2}[\cos(\omega\tau) - \cos(\omega t) - (\omega t - \omega\tau)\sin(\omega\tau)] \tag{2.6}$$

where the trajectory of the electron depends on the initial condition phase $\phi_b = \omega\tau$, where τ is the time of ionisation. Figure 2.2 shows some sample paths of the electrons as a function of intial condition ϕ_b whilst Figure 2.3 shows the kinetic energy of the electron on recollision. We note here that only for initial phases $0 < \phi_b < \pi/2$ does the electron recombine with the parent ion, and hence only half of the ionized electrons return to their parent. Moreover, the recollision energy is dependent on the ϕ_b as well, and in general there are two values of ϕ_b which yield the same recollision energy; for each

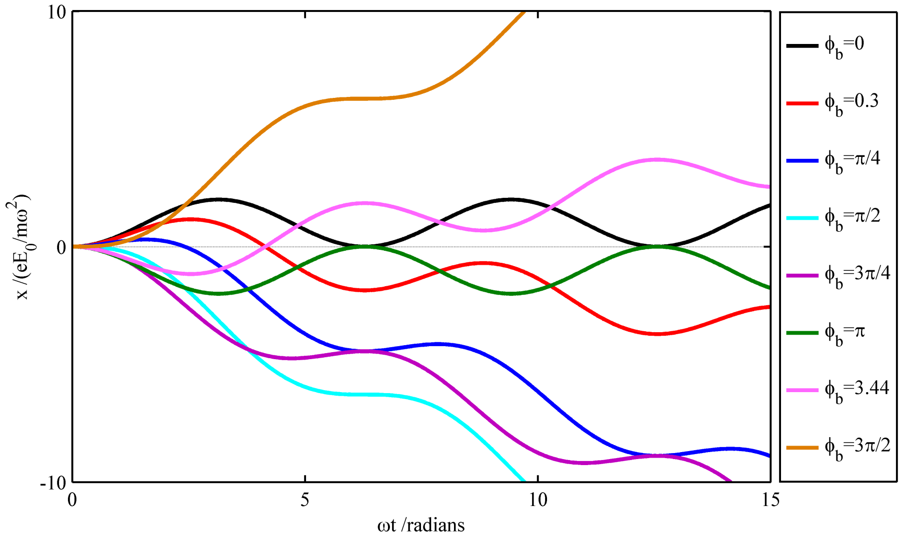

Figure 2.2: Electron trajectories for ionisation at times $\tau = \phi_b/\omega$ in a linearly-polarised electric field $E(t) = e\cos(\omega t)$. Electrons ionized at phases $0 \leq \phi_b \leq \pi/2$ of the driving electric field recombine, whereas those with $\pi/2 \leq \phi_b \leq \pi$ do not return to the parent ion, figure and caption from [97].

recollision energy the electron trajectory with the smaller value of ϕ_b is known as the 'short trajectory', the other being the 'long trajectory' as seen in Figure 2.3.

In general, the harmonic spectrum has a characteristic shape as shown schematically in Figure 2.4. After the first few harmonics, there is a steep drop off in intensity followed by a plateau region where the intensity is relatively independent of the harmonic order. After which, there is a another steep drop off at the cut-off point, which is the highest harmonic with appreciable intensity. This is called the cut-off harmonic; the energy for the cut-off harmonic can be written as,

$$E_c = I_p + 3.17U_p \tag{2.7}$$

where $U_p = e^2e^2/4m\omega^2$ is the pondermotive energy.

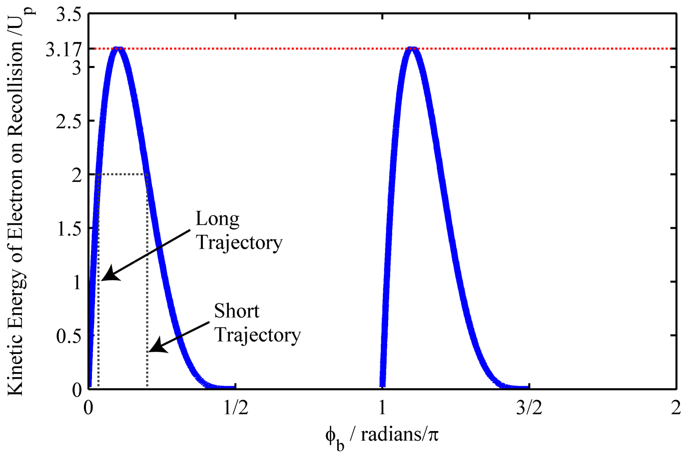

Figure 2.3: Kinetic energy of electrons on recollision, as calculated from Equation (2.6). The maximum energy is seen to be $3.17U_p$. For other recollision energies, it can be seen that there are two possible trajectories every half-cycle of the driving electric field. Figure and caption from [97]

2.2 Lewenstein's Quantum Model

2.2.1 Sketch of the derivation

Corkum's model gives a simple intuitive model on the process of high harmonic generation but it does not contain some of the more nuanced quantum mechanical elements of the phenomena. A semi-classical model by Lewenstein et al. provides a more comprehensive view. In this section, we will sketch out the arguments below based on the full derivation of the theory [68] and some intuitive simplifications made from [97].

For a complete quantum description, the time dependent Schrodinger's equation (TDSE) must be solved. In the length gauge, the full TDSE for an electron moving in an atomic potential $V(r)$ and laser field $\vec{E}(t)$ can be given by,

$$i\frac{\partial}{\partial t}|\Psi(\vec{r},t)\rangle = \left[-\frac{1}{2}\nabla^2 + V(\vec{r}) - \vec{E}(t)\right]|\Psi(\vec{r},t)\rangle \tag{2.8}$$

.

Of course the most direct way to solve the equation above would be to use numerical

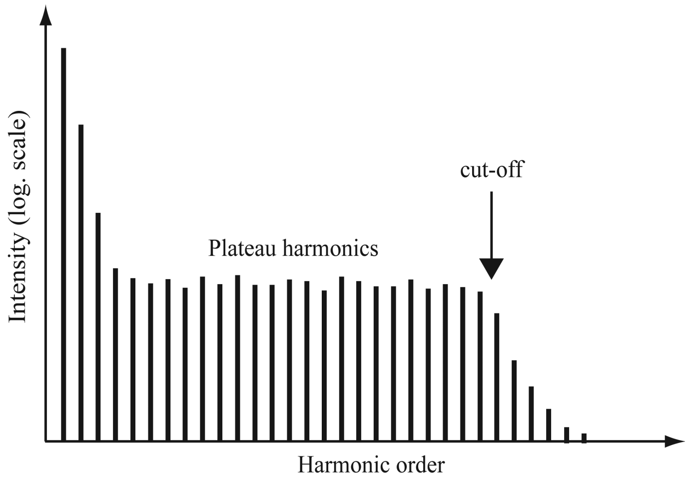

Figure 2.4: Harmonic intensity as a function of harmonic order, figure from [97]

methods. Unfortunately, purely numerical methods give limited physical insight. Hence, with a few key assumptions, namely the strong field approximation, Lewenstein and colleagues were able to afford a more physical interpretation of the quantum model [68]:

1. Only the ground state $|0\rangle$ is considered. The evolution of the system of all other bound states can be neglected.

2. The depletion of the ground state can be ignored ($U_p < U_{sat}$) where U_{sat} is the saturation level.

3. The atomic potential $V(\vec{r})$ is assumed to have no effect on the electron when it is in the continuum and is treated as a free moving particle (strong field approximation).

Lewenstein et al. noted that assumptions (1) and (3) are only valid for short range potentials and when there are no intermediate resonances. Here we assume that we are dealing with tunneling or over-the-barrier ionisation, e.g., when the Keldysh parameter $\gamma = \sqrt{I_p/2U_p} < 1$.

Assuming the polarisation of the laser field $E = e\cos(\omega t)$ is in the x-direction, the dipole moment Lewenstein derives, in atomic units ($\hbar = e = m_e = a_0 = 1$ where a_0 is the

Bohr radius), is,

$$\langle x(t)\rangle = \langle\Psi(t)|x|\Psi(t)\rangle \tag{2.9}$$

$$= i\int_{\tau}^{t} d\tau \int d^3\vec{p}e\cos(\tau)d_x[\vec{p}-\vec{A}(\tau)]e^{-iS(\vec{p},t,\tau)}d_x^*[\vec{p}-\vec{A}(t)] + \text{c.c.} \tag{2.10}$$

where $\vec{p} = \vec{v} + \vec{A}(t)$ is the canonical momentum and

$$S(\vec{p},t,\tau) = \int_{\tau}^{t} d\tau' \left\{ \frac{[\vec{p}-\vec{A}(\tau')]^2}{2} + I_p \right\} \tag{2.11}$$

is the semiclassical action.

Equation (2.10) has an intuitive physical interpretation. The first part of the integral $a_{\text{ion}} \sim e\cos(\tau)d_x[\vec{p}-\vec{A}(\tau)]$ is the probability amplitude of the electron being tunnel ionised at time τ with canonical momentum $\vec{p}$, where $d_x[..]$ is the dipole matrix element for a Hydrogen-like atom. The electron then propagates through the continuum between times τ and t acquiring a phase factor $a_{\text{prop}} \sim e^{iS}$ moving under the laser field with momentum p. Finally, the last part of the integral $a_{\text{recomb}} \sim d_x^*[\vec{p}-\vec{A}(t)]$ describes the probability amplitude of recombination at time t. Hence, Equation (2.10) can be loosely written as,

$$\langle x(t)\rangle \sim \int_0^t a_{\text{ion}} \times a_{\text{prop}} \times a_{\text{recomb}} d\tau. \tag{2.12}$$

2.2.2 High harmonic spectrum

The acceleration of the dipole moment gives rise to electromagnetic radiation. Hence, the intensity spectrum is the square of the Fourier Transform of the acceleration of the dipole moment,

$$I(\omega) \sim \left| \int \frac{\partial^2\langle x(t)\rangle}{\partial t^2} e^{i\omega t} dt \right|^2. \tag{2.13}$$

However, Bandrauk et al. showed that the Fourier transform of both the velocity of $\langle x(t) \rangle$ and just the dipole moment itself $\langle x(t) \rangle$ gives a similar enough results for the spectra unless the driving field intensity is significantly greater than intensity required for over-barrier ionisation [15].

Figure 2.5 shows the simulated HHG spectrum calculated with the following Fourier relation [15; 97],

$$I(\omega) \sim \left| \int \langle x(t) \rangle e^{i\omega t} dt \right|^2 . \tag{2.14}$$

It is evident from the simulations that they match the schematic of the shape of the harmonic spectrum: a sharp fall in harmonic intensity followed by a plateau region and then a cut-off point scaled by $I_p + 3.17U_p$. Moreover, the harmonics are odd, which can be argued from two reasons. First, from a symmetry consideration, a spherically symmetric atom that has an induced polarisation must result from an odd function of the electric field. An even function would not result in an induced polarisation. Alternatively, since electrons can be ionised for positive and negative values of the electric field, electron re-collisions occur – and hence harmonics are generated – twice per optical cycle. Hence, the frequencies of the harmonics are spaced by 2ω, leading to $\omega + 2q\omega$, which are odd harmonics.

2.3 Intensity dependent phase and spectral blueshift

Under the strong field approximation, the phase of the qth order harmonic can be written as,

$$\phi_q = S(p, t, \tau) - q\omega t. \tag{2.15}$$

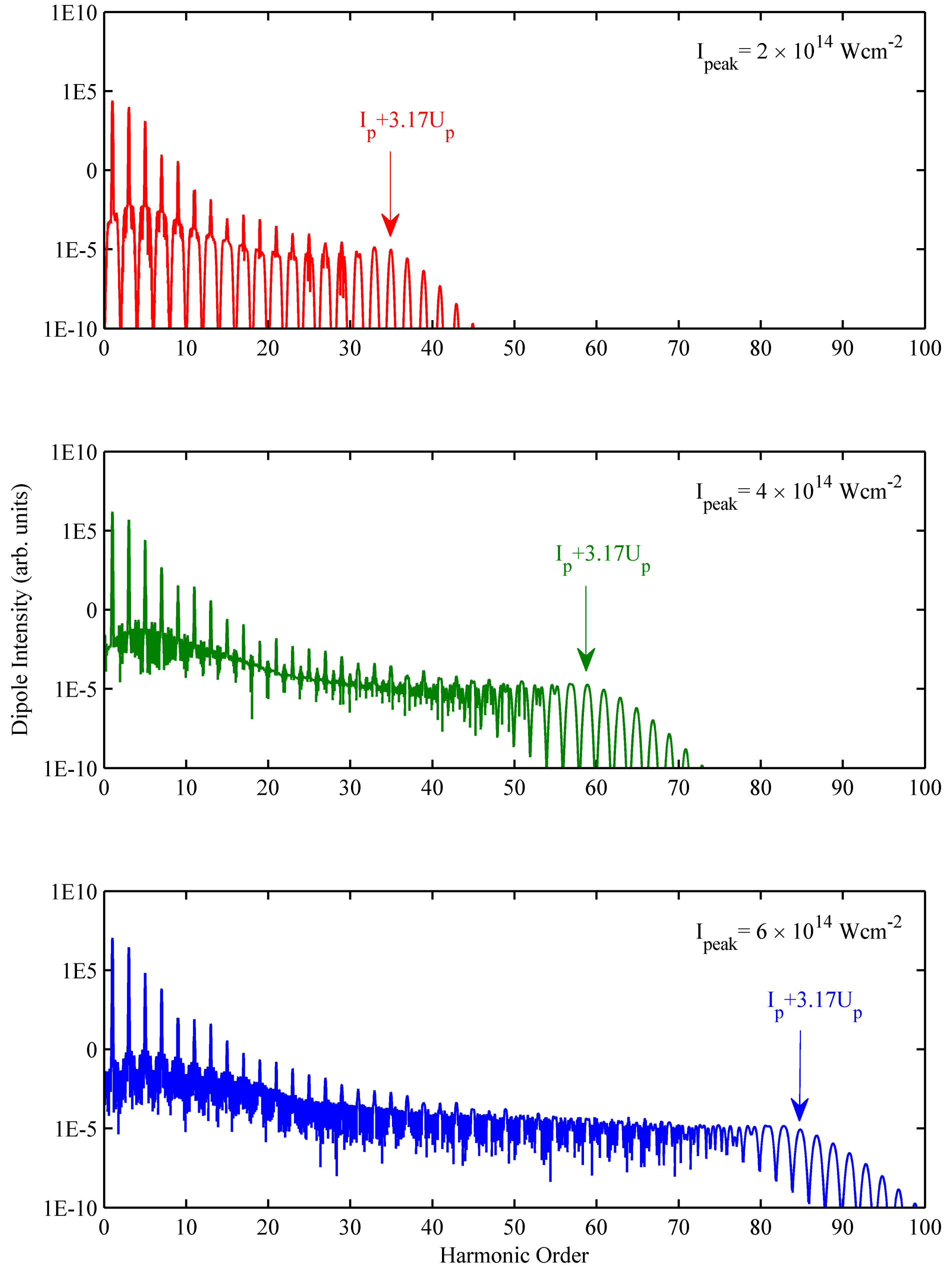

Figure 2.5: HHG intensity spectrum for Argon with a driving laser of $\lambda_0 = 800$nm and pulse width of 50 fs and varying peak intensities, figure from [97]

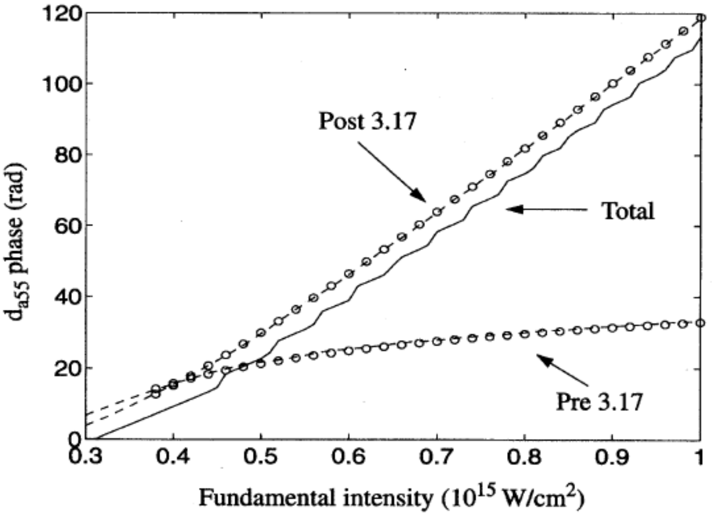

Figure 2.6: Phase of the 55th harmonic (solid line) and the phases of the pre-3.17U_p and post-3.17U_p components (dashed lines) as obtained from dipole acceleration calculations. Phases as calculated from [Lewenstein Model] for the pre-3.17U_p and post-3.17U_p components are shown by circles, figure and caption from from [37]

where S the semiclassical action is as before in Equation (2.11).

It is evident that the phase of the harmonic is dependent on the semi-classical movement of the electron in the continuum, which in itself depends on the intensity of the driver. Hence, the harmonic phase is dependent on driver intensity, as seen in the simulations conducted by Kan et al [37] or Shin et al [107]. In Figure 2.6 [107] the upper curve shows a stronger dependence on intensity and arises from the long trajectory; short trajectories give rise to the lower curve [37].

Another way of looking at this is by examining the fractional frequency shift of the harmonic described as[107],

$$\frac{\Delta\omega_q}{\omega_q} = \frac{1}{q\omega}\frac{\Delta\phi_q}{\Delta t} = \frac{2I_d}{\pi q}\left(\frac{d\phi_q}{dI_d}\right)_{I_d}\frac{\delta E}{E} \tag{2.16}$$

where $\Delta\omega_q$ is the frequency shift of the qth harmonic, $\Delta t = t - \tau$, I_d is driver intensity, and δE is the electric field variation of the laser pulse during a half-optical cycle. The

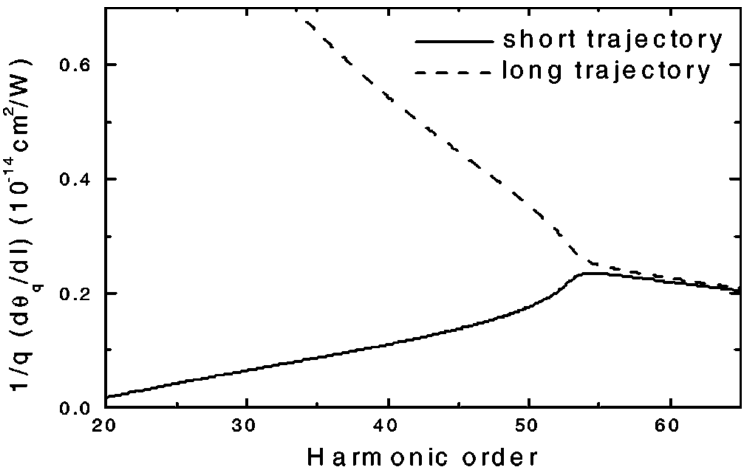

Figure 2.7: Order dependence of the intensity-dependent phase term, $1/q(d\phi_q/dI)$, obtained from Ar at the laser intensity $I_d = 53 \times 10^{14}$ W/cm^2. The solid line indicates the intensity-dependent phase term for the short trajectory and the dashed line indicates that for the long trajectory., figure and caption from from [107]

component $\frac{2I_d}{\pi q}\left(\frac{d\phi_q}{dI_d}\right)_{I_d}$ is the intensity-dependent phase which depends also on harmonic order. Figure 2.7 shows the calculated order dependency of the intensity-dependent phase component as a function of q for driver intensity of 3×10^{14} W/cm^2. For the short trajectories, the slope of the phase dependency $\frac{1}{q}\frac{d\phi_q}{dI_d}$ increases with harmonic order whilst the opposite is true for long trajectories for a specific driver intensity and for harmonics below the cut-off harmonic, e.g., post $3.17U_p$. However, these two branches merge around the 53rd harmonic because that is the cut-off for this driver intensity.

Finally, it is shown that this fractional blue shift is caused by the intensity-dependent phase component and the laser pulse shape. Figure 2.8 shows the dependency of the fractional blueshift on intensity. A more thorough analysis with both theory and experiment of the fractional blueshift can be found in Shin et al [107].

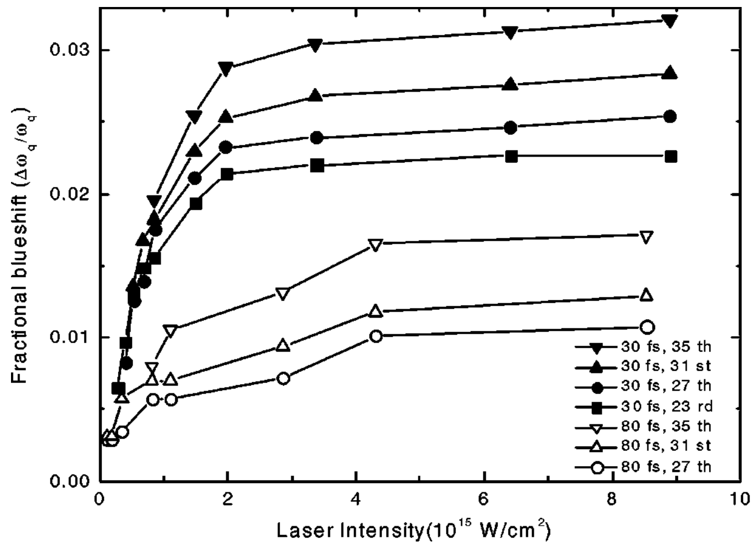

Figure 2.8: Fractional blueshift of harmonics from Ar driven by 30-fs laser pulses with respect to the applied laser intensity. The gas density was 2×10^{17} cm^2, figure and caption from [107]

2.4 Dependence of HHG on polarisation of the driving radiation

As mentioned in Section 2.1, if the polarisation state of the driving laser field is circular, the classical trajectory of the electron does not return to the parent ion and hence circularly polarised driving fields do not generate harmonics. We note that this is the crux of the argument for polarisation beating quasi-phase matching, which is one of the key new ideas described in this thesis and will also be explored in Chapters 5 and 6.

The dependence of HHG on the polarization of the driving laser field was first observed in 1993 by Budil et al. [20]. Figure 2.9 shows the dependence of driver ellipticity for harmonic intensity. Note that for non linearly-polarised drivers, the harmonic intensity drops off very quickly. Budil et al estimated this as,

$$I_q \sim \left(\frac{1 - \varepsilon^2}{1 + \varepsilon^2} \right)^{q-1} \tag{2.17}$$

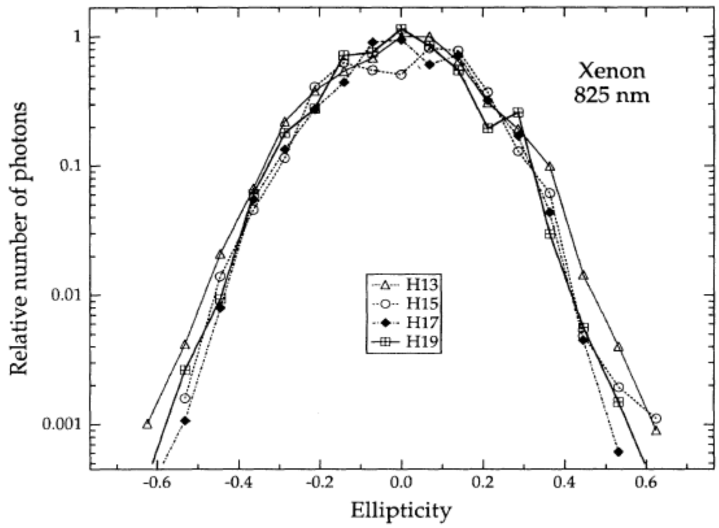

Figure 2.9: Measurements of relative photon count as a function of driver ellipticity, figure from from [107]

where ε is the driver ellipticity defined as the ratio between the minor axis to the major axis of the electric field. This simplification is described further in Chapter 5.

We note here also that there are many different definitions of ellipticity in the literature, and for the sake of clarity, in this thesis we will only use this definition for the term ellipticity and will point out other definitions when relevant.

The approximation in Equation (7.16) suggests that harmonic intensity becomes more sensitive for higher harmonic orders. The theory of this explored in detail in [111] and measured experimentally in [110]. Figure 2.10 shows the simulations and measurements of threshold ellipticity (the ellipticity required to reduce harmonic intensity by a factor of two) versus harmonic order.

Not only is the intensity of the harmonic influenced by the driver ellipticity, but also the angle offset and ellipticity of the harmonic itself are affected by this parameter. A recent description of this process can be found in Strelkov et al [112]. They showed that although the offset harmonic angle ψ, the angle between the harmonic's major axis polarisation angle and that of the driving field's major axis, can be described simply by

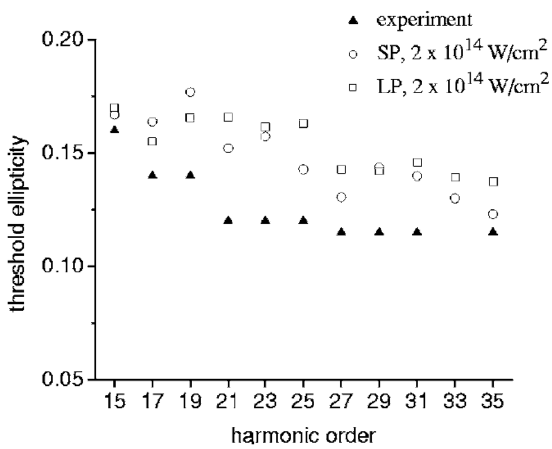

Figure 2.10: Threshold ellipticity (i.e., the driving ellipticity for which the harmonic signal is twice as low as that for the linearly polarized driving field) measured experimentally in Ref. [110] and calculated theoretically, figure and capition from from [111]

Corkum's model, the calculation of the harmonic ellipticity itself requires a full quantum description.

For a driving laser linearly-polarized along the x-axis, Corkum's model predicts that the motion of the electron is restricted to the x-axis. However for an elliptically polarised driver, the electron also moves in the y-direction. Hence, one can define the classical rotation of the angle by the direction of the electron momentum at the time of the recollision with its parent ion:

$$\psi_{\text{class}} = \arctan\left[\frac{p_y - \bar{y}/(t-\tau)}{p_x}\right] \tag{2.18}$$

where p_x and p_y are the classical momentum components of the electron, $\bar{y}$ is the transverse shift caused by the non-linear driving field and $t - \tau$ is the time of the electron in the continuum as before. If we substitute the classical electron parameters into the equation above, we find [112],

$$\psi_{\text{class}} = \varepsilon\left[\frac{1}{\omega(t-\tau)} + \frac{\cos(\omega\tau)}{\sqrt{(q\omega - I_p)/(2U_p)}}\right] \tag{2.19}$$

A more accurate picture would be to take the angle of the quantum mechanical complex amplitudes of the electron wave packet [112],

$$
\begin{aligned}
\psi_{\mathrm{qm}} &= \arctan\left[\Re(f_y/f_x)\right] && (2.20)\\
&= \varepsilon\left[\frac{\cos(\omega\tau)-\omega(t-\tau)\sin(\omega\tau)(1+\frac{4}{(t-\tau)^2\Delta p_T^4})+\frac{\sqrt{(q\omega-I_p)/(2U_p)}}{\omega(t-\tau)}}{\sqrt{(q\omega-I_p)/(2U_p)}(1+\frac{4}{(t-\tau)^2\Delta p_T^4})}\right] && (2.21)
\end{aligned}
$$

where $\Re$ is the real component, f_x and f_y are the respective complex electronic amplitudes, Δp_T is the quantum uncertainty of the transverse electron momentum after ionisation given by $\Delta p_T^2 = 2I_p e\cos(\omega\tau)$ [111].

Although the Corkum model is able to give a classical estimate for the offset angle, it is unable to provide a description for the ellipticity of the harmonic. Hence, to estimate the harmonic ellipticity requires a quantum treatment. Stretlov et al. argue that the harmonic ellipticity originates from quantum uncertainty of the electron motion [112], which is defined as,

$$
\varepsilon_q = \arctan\left\{\Re\left[\frac{if_y}{f_x}\right]\right\} = \frac{\bar{y}}{p_x\left[\frac{(t-\tau)^2\Delta p_T^2}{2}+\frac{2}{\Delta p_T^2}\right]} \approx \frac{\varepsilon}{I_p\omega\sqrt{2(q\omega-I_p)}} \qquad (2.22)
$$

where the last approximation assumes $\omega(t-\tau)2I_p\sqrt{2(q\omega-I_p)} \gg 1$.

Figure 2.11 compares the analytical results from numerical simulations of the TDSE. Except for lower harmonic orders, it seems that the analytical arguments agree. Moreover, it appears that for the offset angle, the Corkum model agrees quite well with the quantum argument.

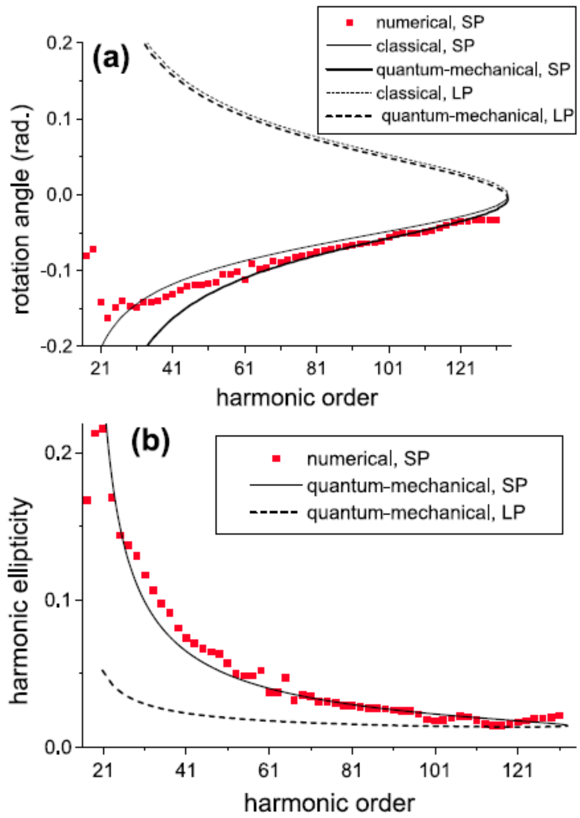

Figure 2.11: Harmonic rotation angle (a) and ellipticity (b) as functions of the harmonic order, the laser parameters given as $\lambda_0 = 1300$nm, peak intensity 2.2×10^{14}W/cm^2, elliptically polarised with $\varepsilon = 0.1$. Numerical results for the short quantum path (squares), analytical quantum-mechanical results given by Eq. (2.21) (graph a) and Eq. (2.22) (graph b) for the short (solid line) and the long (dashed line) quantum path. Graph (a) presents also classical rotation angle given by Eq. (2.21), figure from from [112]

2.5 Conclusion

In this chapter, we explored the origins of high harmonic generation and sketched out the arguments for Corkum's simple three-step model as well as a more full quantum description with the Lewenstein model. The structure of the harmonic spectrum and its relationship with driver intensity was explored. Moreover, we described the process determining the phase of the generated harmonics and how this causes blue-shifting. Finally, the effect of elliptical or circular polarisation states of the driver was explored. Most of the arguments presented in this chapter relate to a single atom response of the laser field. In the next chapter, we will explore how propagation of the driver and harmonic radiation in a microscopic system affect the intensity of the generated harmonics.

Chapter 3

The phase-mismatch problem

3.1 Phase mismatch

In the previous chapter, we looked at a single atom response to a strong laser field for generating high harmonics. Moving now to the macro scale, we explore the phase-mismatch problem, which is the most significant factor in restricting harmonic generation intensity. Because the the harmonic and driving laser radiation propagate at different phase velocities, after a certain propagation distance, the harmonics generated will become out of phase with previously generated harmonics causing destructive interference. In this chapter, we will calculate the origin of the phase mismatch, especially for the case of harmonics being generated in a hollow core waveguide, and explore some existing as well as novel techniques for tackling this problem.

3.1.1 Derivation of the phase mismatch

The amplitude of the driving radiation propagating along the z-axis can be expressed as,

$$E^{(\omega)}(z,t) = \frac{E_0^{(\omega)}}{2} e^{i[k(\omega)z - \omega t]} + \text{c.c.} \tag{3.1}$$

where ω is the angular frequency, $k(\omega)$ is the angular wavenumber, E_0 is the driving amplitude modulus, t is time, and c.c. is the complex conjugate of the previous term. At $z = 0$, the driving radiation is given by,

$$E^{(\omega)}(z,t) = \frac{E_0^{(\omega)}}{2} e^{-i\omega t} + \text{c.c.} \tag{3.2}$$

The harmonic radiation is then characterized by the nonlinear response $\mathcal{P}_{\text{NL}}^{q\omega}$ and oscillates at frequency $q\omega$,

$$\mathcal{P}_{\text{NL}}^{(q\omega)} = \frac{\mathcal{P}_{\text{NL},0}^{(q\omega)}}{2} e^{-iq\omega t} + \text{c.c.} \tag{3.3}$$

where $\mathcal{P}_{\text{NL},0}^{q\omega}$ is the amplitude of the nonlinear response; we also note that $\mathcal{P}_{\text{NL}}^{(q\omega)}$ is a function of $E_0^{(\omega)}$ and of the atomic species. Because the driver field $E^{(\omega)}(z,t)$ is known for all z and t, it is invariant under time translation of $t \to t - k(\omega)z/\omega$; meaning that,

$$E^{(\omega)}(z,t) = E^{(\omega)}\left(0, t - \frac{k(\omega)z}{\omega}\right) = \frac{E^{(\omega)}}{2} e^{i[k(\omega)z - \omega t]} \tag{3.4}$$

The nonlinear polarisation also adheres to the same invariance, giving,

$$\mathcal{P}_{\text{NL}}^{(q\omega)}(z,t) = \mathcal{P}_{\text{NL}}^{(q\omega)}\left(0, t - \frac{k(\omega)z}{\omega}\right) = \frac{\mathcal{P}_{\text{NL},0}^{(q\omega)}}{2} e^{i[qk(\omega)z - q\omega t]} \tag{3.5}$$

The electromagnetic field generated by this nonlinear polarization will oscillate with the same frequency as the nonlinear polarisation. Using Maxwell's equation, the harmonic field is determined by,

$$\nabla^2 E^{(q\omega)} + k(q\omega)^2 E^{(q\omega)} = \mu q^2 \omega^2 \mathcal{P}_{\text{NL}}^{(q\omega)} \tag{3.6}$$

where $k(q\omega)^2 = (q\omega/c)^2\epsilon^{(1)}(q\omega)$ is the linear part of the polarisation, and the second term on the left hand side and the right hand side derives from partial time derivatives. We now write the harmonic field in terms its envelope function $\xi^{(q\omega)}$:

$$E^{(q\omega)}(z,t) = \frac{1}{2}\xi^{(q\omega)}(z)e^{i[k(q\omega)z-q\omega t]} + \text{c.c.} \tag{3.7}$$

Substituting Eq. (3.5) and Eq. (3.7) into Maxwell's equation Eq. (3.6) and making the slowing varying approximation, meaning we neglect second order derivative terms of the envelope, we get

$$\frac{d\xi^{(q\omega)}}{dz}ik(q\omega)e^{i[k(q\omega)z-q\omega t]} + \text{c.c.} = -\frac{1}{2}\mu q^2\omega^2\mathcal{P}^{(q\omega)}_{\text{NL},0}e^{i[qk(\omega)z-q\omega t]} + \text{c.c.} \tag{3.8}$$

Because this is invariant under time translation, we can ignore the complex conjugate parts, leaving,

$$2ik(q\omega)e^{ik(q\omega)z}\frac{d\xi^{(q\omega)}}{dz} = -\mu_0 q^2\omega^2\mathcal{P}^{(q\omega)}_{NL} \tag{3.9}$$

noting that the nonlinear term $\mathcal{P}^{(q\omega)}_{NL,0}$ is oscilating with frequency $qk(\omega)$ where $\mathcal{P}^{(q\omega)}_{NL} = \mathcal{P}^{(q\omega)}_{NL,0}e^{qk(\omega)z}$. Hence, we can rewrite Eqn. (3.9) as:

$$\frac{d\xi^{(q\omega)}}{dz} = A^{(q\omega)}e^{-i\Delta k(q\omega)z} \tag{3.10}$$

where $A^{(q\omega)} = i\mu_0 q^2\omega^2\mathcal{P}^{(q\omega)}_{NL,0}/[2k(q\omega)]$ and

$$\Delta k(q\omega) = k(q\omega) - qk(\omega) \tag{3.11}$$

is defined to be the wave vector mismatch. In the case of phase mismatch, which is when $k(q\omega) \neq qk(\omega)$ or $\Delta k(q\omega) \neq 0$, we can solve the differential equation Equation (3.10) by integrating across z:

$$\xi^{(q\omega)}(z) = \int_0^z A^{(q\omega)} e^{-\Delta k(q\omega) z'} dz' \tag{3.12}$$

$$= \frac{A^{(q\omega)}}{i\Delta k(q\omega)} \left(1 - e^{-i\Delta k(q\omega) z}\right) \tag{3.13}$$

The harmonic intensity is given by $I^{(q\omega)} = \frac{\epsilon_0 c}{2} |E^{(q\omega)}(z,t)|^2$. In the case of the envelope approximiation, we then write,

$$I^{(q\omega)} = |\xi^{(q\omega)}(z)|^2 \tag{3.14}$$

$$= \frac{[2A^{(q\omega)}]^2 \epsilon_0 c}{[\Delta k(q\omega)]^2} \sin^2\left(\frac{\Delta k(q\omega)}{2} z\right). \tag{3.15}$$

It is clear from the equation above that the harmonic intensity oscillates with a period of $\pi/\Delta k$. Hence, it is now convenient to define the coherence length:

$$L_c^{(q\omega)} = \frac{\pi}{\Delta k(q\omega)} \tag{3.16}$$

which is the length it takes for the harmonic pulse and the driver pulse to be π out of phase. In other words, the coherence length is defined by the length it takes for the system to move from constructive inteference to desctructive interference. In the case of phase-mismatch and without absoption, the maximum intensity of harmonic pulse $\{[A^{(q\omega)}]^2 \epsilon_0 c\}/\{[\Delta k(q\omega)]^2\}$ generated over $2L_c^{(q\omega)}$ is shown in Fig. 3.3. Further in this chapter, we will discuss the origins of phase-mismatch, especially for the case of a hollow-core waveguide.

For $\Delta k(q\omega) = 0$, Eqn (3.13) becomes quite straightforward, and the intensity of the

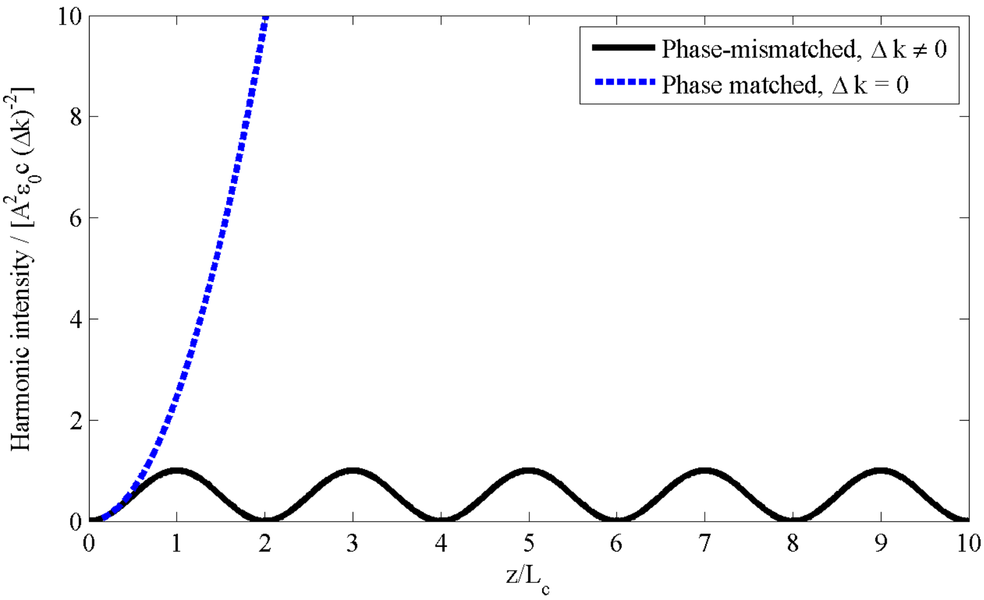

Figure 3.1: Harmonic intensity $I^{(q\omega)}$ as a function of propagation distance z showing both the phase mismatched and the phase matched situations.

harmonics without absoption becomes:

$$I^{(q\omega)}(z) = \frac{[A^{(q\omega)}]^2 \epsilon c}{4} z^2. \tag{3.17}$$

Here, the harmonic intensity experiences quadratic growth as can be seen in Fig. 3.3. In the rest of this chapter, in order to reduce the clutter, we will drop the $(q\omega)$ superscripts if it is clear from the context that we are refering to the harmonic pulse.

An intuitive way of thinking about the phase evolution and its effect on harmonic intensity is to imagine that the amplitude of harmonic radiation generated in each slice of material can be represented by a phasor of the form or angle $\arg(\Delta k z)$ and magnitude A, and hence the integral of Eqn (3.13) corresponds to the vector sum of the phasors. Under phase matching conditions when $\Delta k = 0$, all the phasors point in the same direction and hence the harmonics add up constructively as shown in the dotted blue line in Figure 3.2. If there is a phase mismatch however, the phasors rotate by π after one coherence

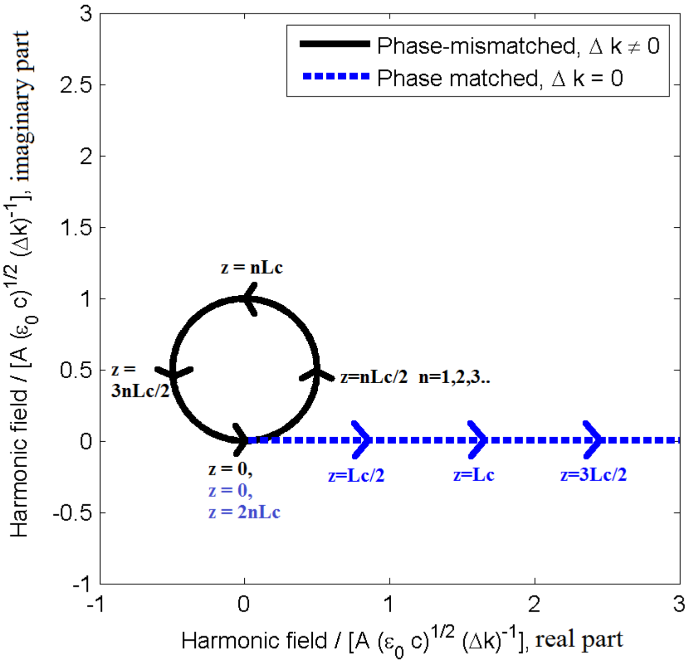

Figure 3.2: Complex harmonic field $\xi^{(q\omega)}$ progressing through the propagation axis. Blue line and text representing perfect phase matching; black line and text representing no phase matching. The x-axis represents the real component of the harmonic field whilst the y-axis represents the imaginary component.

length. Hence, tracing the integral in the phase diagram in the black line in Fig 3.2, we see that the complex harmonic field loops back on itself in a circle with a period of $2L_c$, which is consistent with the intensity osscilation with period of $2L_c$ as evident in Fig 3.3.

3.2 Dispersion in a hollow-core waveguides

In this section, we will discuss the origin of the phase mismatch, especially in the case of HHG in a hollow-core gas-filled waveguide. Although HHG was originally investigated using free-focus geometry, hollow-core waveguides are frequently used to extend the harmonic generation region beyond the Rayleigh length.

Three key dispersion elements for HHG in a hollow-core waveguide are: plasma, neutral gas, and waveguide dispersion. These three dispersion elements can be added up linearly such that [35; 100],

$$\Delta k = \Delta k_{\text{plasma}} + \Delta k_{\text{neutral}} + \Delta k_{\text{waveguide}}. \tag{3.18}$$

It is important to note that one we assume that each dispersion term is independent of each other.

3.2.1 Plasma dispersion

As described in the previous chapter, HHG requires partial ionization of gases. Hence, plasma dispersion contributes to the phase mismatch. In basic plasma physics, the index of refraction of plasma is given by:

$$n_{\text{plasma}} = \sqrt{1 - \left(\frac{\omega_p}{\omega}\right)^2} \tag{3.19}$$

such that

$$\omega_p^2 = \frac{N_e e_0^2}{\epsilon_0 m_e} \tag{3.20}$$

where ω_p is the plasma frequency, ω is the optical frequency, N_e is the free electron density, e_0 is the electron charge, and m_e is the electron mass. For HHG, because ionization is low, we can assume that $\omega_p \ll \omega_0$ and $\omega_p \ll \omega_q$, meaning that harmonic and driver radiation can propagate through the plasma without being reflected. Hence, we can linearly expand Eqn. (3.19) and derive the wavenumber for the qth harmonic as:

$$k_{\text{plasma}} \approx \frac{\omega}{c}\left(1 - \frac{\omega_p^2}{2\omega^2}\right) = \frac{2\pi q}{\lambda_0} - \frac{N_e r_e \lambda_0}{q} \tag{3.21}$$

where $r_e = e_0^2/[4\pi\epsilon_0 m_e c^2]$ is the classical free electron radius and noting that the equation applies also for $q = 1$.

The plasma phase mismatch between the driver and the qth harmonic for plasma dispersion is thus given by [35; 100]:

$$\Delta k_{\text{plasma}} = qk_{\text{plasma}}(\omega_0) - k_{\text{plasma}}(q\omega_0) = -N_e r_e \lambda_0 q + \frac{N_e r_e \lambda_0}{q^2} \tag{3.22}$$

noting that the $2\pi q/\lambda_0$ cancels out and that the q^2 comes from $\lambda_q = \lambda_0/q$.

In the case of high harmonics where $q \gg 1$, we can drop the second term,

$$\Delta k_{\text{plasma}} = -N_e r_e \lambda_0 q. \tag{3.23}$$

3.2.2 Neutral gas dispersion

The index of refraction in neutral gas differs for different wavelengths, contributing to the phase mismatch. Assuming the ideal gas law, the index of refraction for wavelength λ due to neutral gas becomes,

$$k_{\text{neutral}} = \frac{2\pi}{\lambda}[n_{\text{gas}}(\lambda)](1-\eta)\frac{P}{P_{\text{atm}}} \tag{3.24}$$

where P is the pressure of the gas, P_{atm} is gas pressure at STP (1 ATM and 298K), n_{gas} is the index of refraction of the specific gas at STP which can be found at any technical database or relavent Sellmeier equation, and η is the ionisation fraction.

Hence, the phase mismatch caused by neutral gas for harmonic q is calculated to be [35; 100],

$$\Delta k_{\text{neutral}} = \frac{2\pi q}{\lambda_0}[n_{\text{gas}}(\lambda_0) - n_{\text{gas}}(\lambda_0/q)](1-\eta)\frac{P}{P_{\text{atm}}} \tag{3.25}$$

3.2.3 Waveguide dispersion

If we are to generate harmonics in a waveguide, we must consider the waveguide dispersion. In Chapter 4, we will discuss waveguide dispersion and modes in more detail, but we note here that the real part of the waveguide wavenumber for the $EH_{n,m}$ mode for is given by [28]:

$$\Re[k_{n,m}] \approx \frac{2\pi}{\lambda}\left[1 - \frac{1}{2}\left(\frac{u_{n,m}\lambda}{2\pi a}\right)^2\right] \tag{3.26}$$

where $\Re$ denotes the real part, $u_{n,m}$ is the mth root of the equation $J_{n-1}(x) = 0$ with J_{n-1} being the Bessel function of the first kind. Hence, the waveguide wavenumber for the qth harmonic becomes,

$$k_{\text{waveguide}} = \frac{2\pi q}{\lambda_0} - \frac{u_{n,m}^2 \lambda_0}{4\pi a^2} \tag{3.27}$$

where a is the radius of the waveguide. Using the same type of argument in Sec. 3.2.1, we calculate the waveguide plasma mismatch being [35; 100],

$$\Delta k_{\text{waveguide}} = -\frac{u_{n,m}^2 \lambda q}{4\pi a^2} \tag{3.28}$$

For many of the phase matching experiments described, the fundamental EH_{11} mode is generally taken to be the driver mode. However, as we shall see in the following chapters, waveguide dispersion can become an important lever for multi-mode or polarisation control HHG.

3.3 Phase matching, $\Delta k = 0$

As described above, one way of avoiding the destructive interference is phase-matching by setting $\Delta k = 0$. Instead of getting a periodic intensity modulation, one achieves quadratic intensity growth. Phase-matching in a hollow core waveguide can be achieved by balancing all the dispersion elements.

We can see this by putting all these dispersion elements together[35; 100],

$$\Delta k = \Delta k_{\text{plasma}} + \Delta k_{\text{neutral}} + \Delta k_{\text{waveguide}} \tag{3.29}$$

$$= -N_e r_e \lambda_0 q + \frac{2\pi q}{\lambda_0}[n_{\text{gas}}(\lambda_0) - n_{\text{gas}}(\lambda_0/q)](1-\eta)\frac{P}{P_{\text{atm}}} - \frac{u_{n,m}^2 \lambda q}{4\pi a^2} \tag{3.30}$$

Because these terms are different signs, phase-matching can be achieved by adjusting the pressure until $\Delta k = 0$. We note that the equation above is derived from the Taylor expansion of certain equations, and small corrections can be applied if necessary.

Experimentally, this was first achieved by Murane and Kapteyn's group in JILA Colorado [35; 100], phase matched harmonics up to $q = 33$. Pulses from a Ti:sapphire laser (4.5 mJ energy, 20fs pulse width, $\lambda = 800$nm, 1kHz repetition rate) were focused into $a = 75$ μm waveguide filled with xeon, krypton, argon, and hydrogen gases.

However, phase matching is limited to lower-order harmonics due to the fact that in order for higher orders of harmonics to be generated, one requires higher driver energies, which corresponds to higher ionisation fractions. However, there is a point where the ionisation fraction is too high for pressure tuning to balance out the three terms. This limit can be simply calculated by setting $\Delta k_{\text{waveguide}} = \Delta k_{\text{neutral}}$, noting that waveguide dispersion is small compared with waveguide and neutral gas dispersion. The critical ionisation fraction is hence,

$$\eta_{\text{critical}} = \left(1 + \frac{N_{\text{atm}} \lambda_0^2 r_e}{2\pi[n_{\text{gas}}(\lambda_0) - n_{\text{gas}}(\lambda_0/q)]}\right)^{-1} \tag{3.31}$$

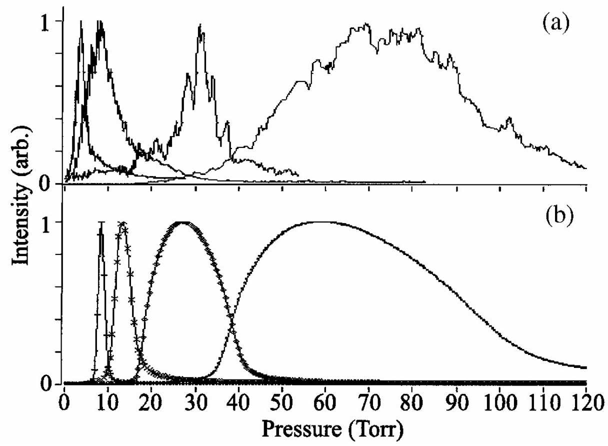

Figure 3.3: Measured (a) and calculated (b) harmonic intensity as a function of pressure tuning showing several peaks exhibiting phase matching conditions. In order of increasing optimum pressure corresponds to the following gases: xenon, krypton, argon, and hydrogen. Figure from [35]

.

In the case of argon it is found that $n_{\text{critical}} \approx 5\%$, and for a 50fs, 800nm driving pulse, Argon's critical ionisation rate corresponds to phase matching being limited to $\lambda > 26$nm or $q < 31$ [97].

One way of circumventing this phase matching limit is to use longer wavelength drivers. As discussed in the previous chapter, the harmonic cut-off scales linearly with the pondermotive energy and thus quadratically with wavelength. Hence, by using longer wavelength drivers, the harmonic cutoff is extended. Hence, higher harmonic orders could be generated with lower resultant ionisation fractions giving a larger range for phase matching. Most recently Murnane and Kapteyn's group acheived phase matched HHG pulses in the KeV range using a 3.9 µm driver (10 mJ, 80 fs, 20 Hz) using a parametric chirped-pulse amplification laser system [92].

3.4 Quasi-phase matching

Because long wavelength drivers are not as readily accessible as Ti:Sapphire lasers and because in theory even with long wavelength drivers one would still want to extend

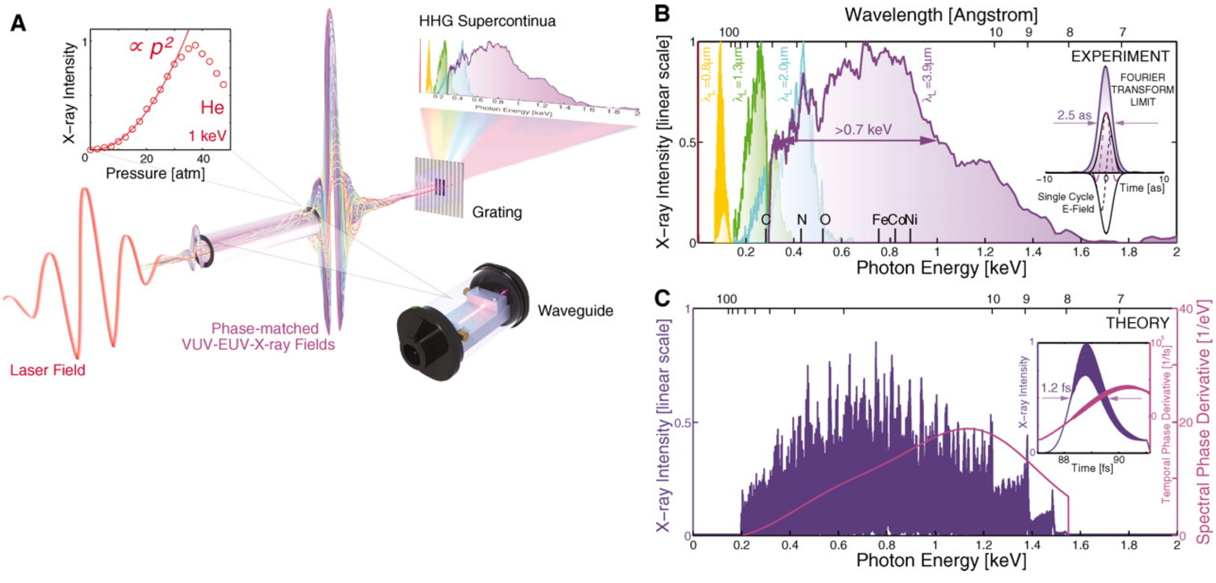

Figure 3.4: Schematic illustration of the coherent kev volt x-ray supercontinua emitted when a mid-IR laser pulse is focused into a high-pressure gas-filled waveguide. The experimental phase-matched harmonic signal grows quadratically with pressure, demonstrating phase-matched coherent buildup with increasing pressure P. (B) Experimental HHG spectra emitted under full phase-matching conditions as a function of driving-laser wavelength (yellow, 0.8 µm green, 1.3 µm; blue, 2 µm; purple, 3.9 µm). (Inset) Fourier transformlimited pulse duration of 2.5 as. (C) Calculated spectrum and temporal structure of one of the phase-matched HHG bursts driven by a six-cycle FWHM 3.9-m pulse at a laser intensity of 3.3 10^{14} W/cm^2. Figure and caption adapted from [92]

.

the harmonics beyond the phase matching limit, it is important to explore alternative approaches to enhancing harmonic intensity. One method is quasi-phase matching (QPM) where corrections to either generation intensity or to the phase are used to ‘disrupt’ or modify the destructive interference process.

QPM was first proposed by Pershan’s group at Harvard for second harmonic generation where the phase mismatch was corrected using periodically poled materials corresponding to the coherence length. In this case, the periodicity of the poled materials equaled twice the coherence length of the interaction [56]. However, because gas is isotropic and has no direction, periodically poled materials cannot be used to correct the phase mismatch in HHG; other techniques must be developed.

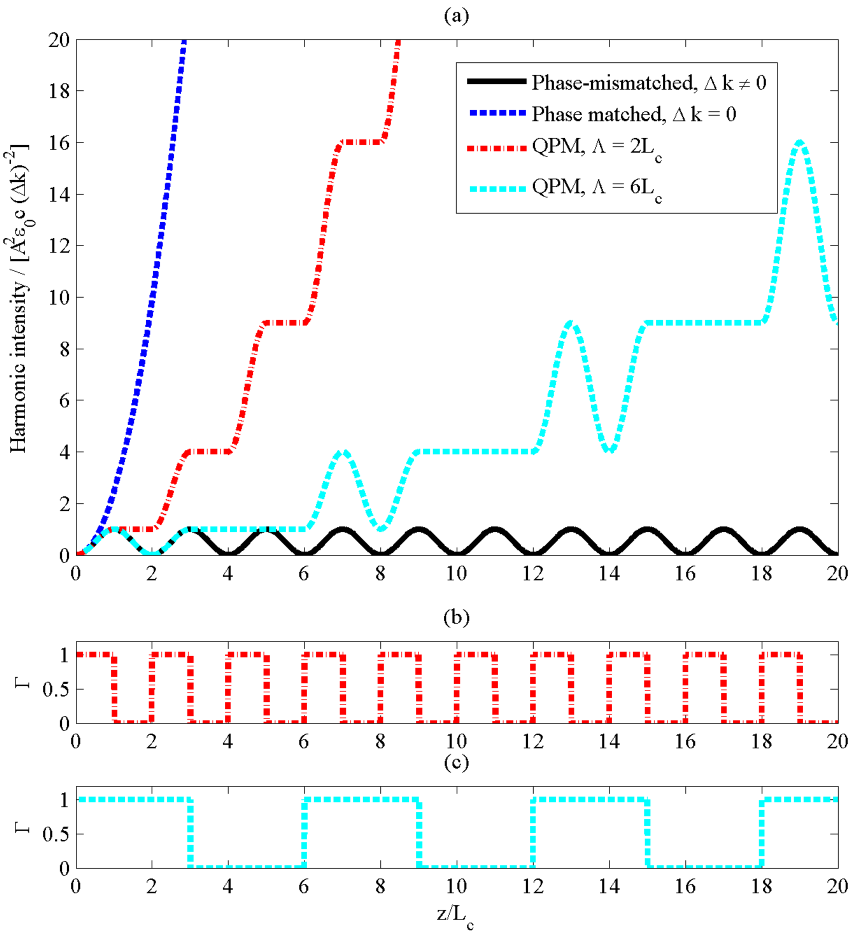

Figure 3.5: Normalised harmonic intensity (a), normalised harmonic generation coefficient for $\Lambda = 2L_c$ (b) and $\Lambda = 6L_c$ (c)

.

A simple example of QPM is to 'turn off' harmonic generation in the destructive zones. This can be acheived in a variety of ways described briefly below and in more detail in the later chapters. If this process is completely efficient, then harmonic generation is 100% 'turned on' in the constructive zones and completely 'turned off' in the destructive zones. Mathematically, this corresponds to the harmonic generation occuring over a square wave

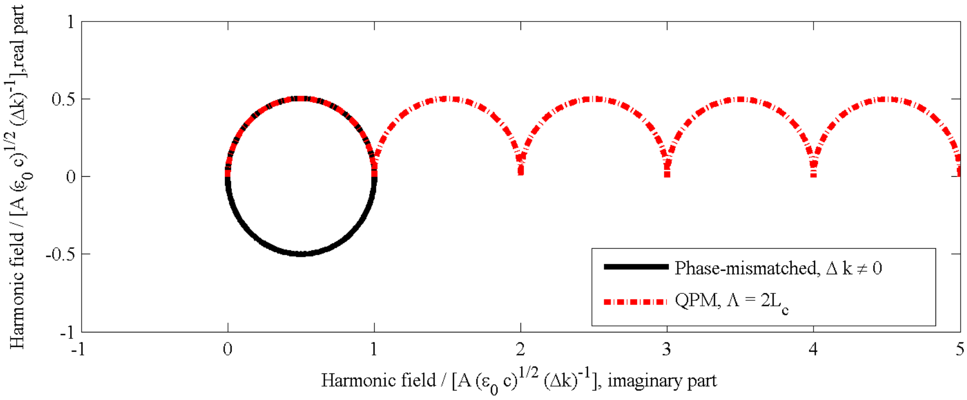

Figure 3.6: Harmonic field phasor diagram for QPM at $\Lambda = 2L_c$. Note that the imaginary and real axes are flipped for ease of formatting for the page.

.

with a period of $\Lambda = 2L_c$, expressed by

$$\Gamma(z) = \begin{cases} 1 & \text{if } 2nL_c < z < (2n+1)L_c \\ 0 & \text{if } (2n+1)L_c < z < 2(n+1)L_c \end{cases} \tag{3.32}$$

where $n = 0, 1, 2, 3...$, and $\Gamma(z)$ is the normalized efficiency coefficient of harmonic generation such that $A \to \Gamma A$. Fig. 3.5 shows the harmonic intensity for phase-mismatched, perfect phase matching, and QPM for $\Lambda = 2L_c$ (dash-dot red line). Fig. 3.6 shows the phase diagram of the progression of ξ after $10L_c$ for $\Lambda = 2L_c$.

In the following chapters, we will explore more general conditions for QPM, but we note here that $\Lambda = 2L_c$ is the lowest order and most efficient QPM in this ideal square-wave scheme; however, higher order QPMs may also exist. Fig. 3.5c shows the normalised coefficient for $\Lambda = 6L_c$, a higher order QPM, corresponding to the intensity growth indicated in Fig. 3.5a. Moreover, other QPM schemes can perform better than ideal square wave modulation such as optical rotation QPM as we will discuss later.

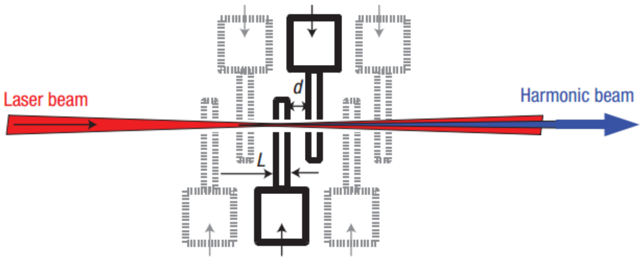

Figure 3.7: Schematic diagram of a sequence of harmonic sources formed by gas-phase generation media enclosed in thin tubes described in the main text. The sources are arranged along the optical axis of a (gently) focused laser beam and pumped by the same laser pulse. In the present proof-of-concept study we have used only two sources (shown in black); further sources can be added for scaling the SXR harmonic yield in future experiments (shown in grey). Caption and figures from [105]

.

3.4.1 Multiple gas jets

One of the most obvious ways of turning on and off harmonic generation is to modulate the density of gas in the axis of propagation. The use of multiple gas jets was first proposed by Shkolnikov in 1994 [108] but was not demonstrated experimentally until 2007 [105]. Figure 3.7 shows a schematic of this demonstration. The experiment was demonstrated using a 15fs, 2mJ, 750nm wavelength laser at 1 Hz with a confocal parameter of 18 mm; the gas jets had a width of 0.4 mm. The separation of the gas jets were varied between 0 and 4 mm, an optimal separation was found at around 1.7 mm which corresponded to an enhancement factor of approximately 10 for photons at 300eV. The authors here define enhancement as the ratio between a single gas jet 0.4mm thick versus two gas jets both at 0.4mm thick. Fig. 3.8 shows the harmonic intensity as a function of optimal separation. Further improvements and coherent control have been achieved in [43; 105; 127].

As discussed above, one of the biggest problems with free-focal geometry is the fact that the interaction region is limited by the Rayleigh length. Hence, one could not achieve a high number of coherence zones. Furthermore, higher harmonics correspond to shorter coherence lengths, resulting in narrower gas jets, which presents a greater engineering

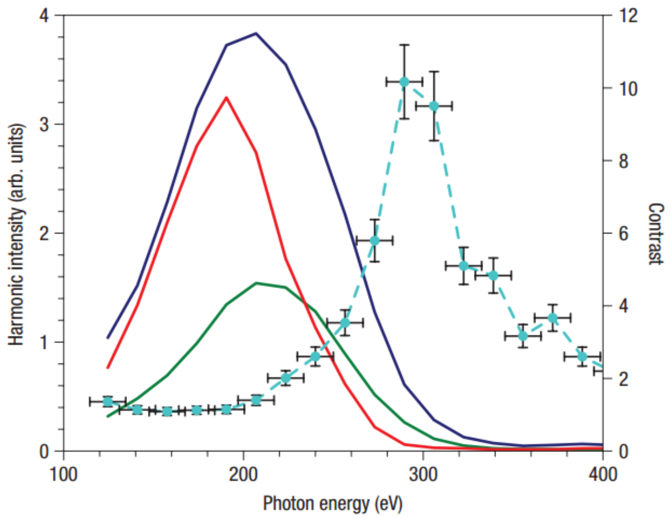

Figure 3.8: Harmonic spectra from a single 0.4-mm-thick source placed approximately 1 mm downstream from the beam waist of the pump laser beam (green curve) and from two identical 0.4-mm-thick successive sources with the second source pushed to close proximity of the first one (red curve) and removed from the first source so that their centres were separated by d $\sim$ 1.7 mm (blue curve). The backing pressure for both sources was 120 mbar. The dashed line shows the ratio of the harmonic yields from the successive sources placed at optimum separation (blue curve) and merged (red curve) on the scale shown on the right vertical axis (the vertical error bars are standard deviations and the horizontal error bars correspond to the channel width of the spectrograph). Caption and figures from [105]

.

challenge.

3.4.2 Modulated waveguides

Harmonic intensity is very sensitive to driver intensity. Hence, one way of modulating harmonic generation along the propagation axis is to modulate the driver intensity by modulating the hollow-core waveguide diameter. This was originally proposed by Christov et al. in 2000 [25] and has been acheived by Murnane and Kapteyn's group in 2003 [46; 88].

In these experiments, precision gas-blowing techniques were used to generate sinusoidal modulations of the waveguide diameter. Fig. 3.9 shows an image of one of the

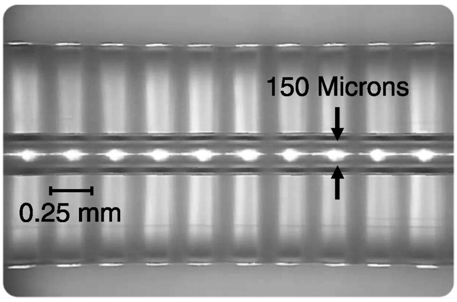

Figure 3.9: Precision glass-blown waveguide with modulated periodic diameter. Figure from [46]

.

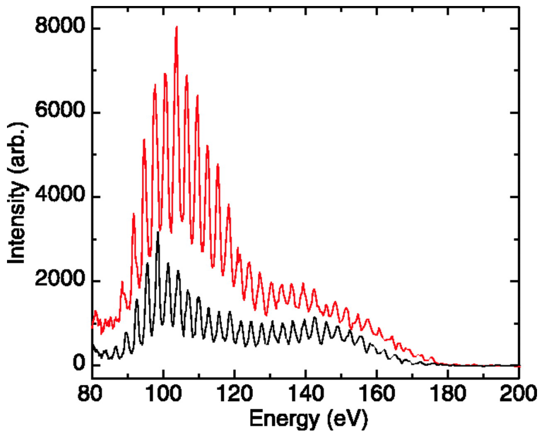

Figure 3.10: Harmonic intensity with standard constant width (black line) and modulated width (red line) waveguides. Figure from [46]

.

capillaries with modulations of 0.25 mm, diameters on order of 50 microns, and length of around 25mm. The authors used a 1 KHz Ti:sapphire laser system with a pulse energy of 1 to 3 mJ. Fig 3.10 shows that enhancements of up to 3 can be achieved with harmonics corresponding to 110eV having the strongest enhancement. The authors calculated that the phase-mismatch was around $\Delta k = 20000m^{-1}$ which roughly corresponded with the waveguide modulation of $2\pi/\Lambda_{mod} = 25400m^{-1}$. We note that in Chapter 8, we discuss an alternative interpretation of these results where the amplification of a broad spectrum may be due to random phase matching. This technique is limited by engineering constraints given the glass-blowing requirements of the inner-diameter of the waveguide.

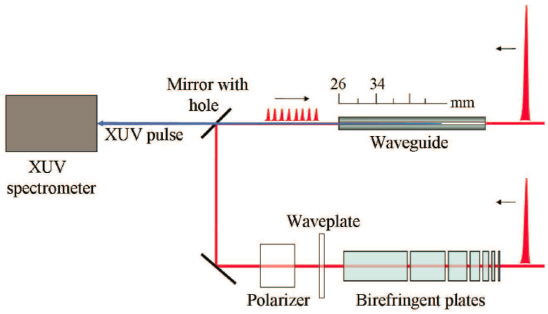

Figure 3.11: Schematic of a counter-propagating pulse experiment. Figure from [85]
.

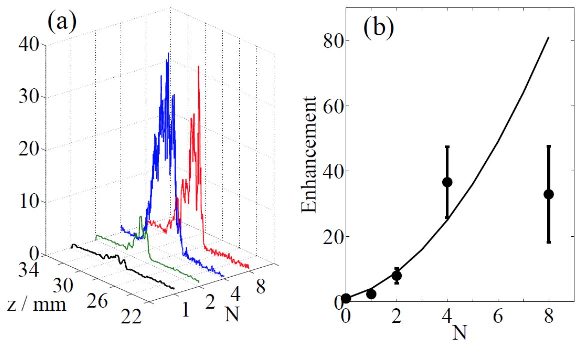

Figure 3.12: (a) Measured enhancement as a function of z for trains of $N = 1$ (black line), 2 (green line), 4 (blue line), and 8 pulses (red line). (b) Measured enhancement of the 27th harmonic as a function of N (circles), as well as the expected scaling of harmonic intensity with pulse number (solid line). Figure and caption from [85]
.

3.4.3 Counter-propagating waves

Another way of disrupting harmonic generation in a periodic way is to use a counter-propagating wave [32; 76; 85; 90; 98; 136]. Even small amounts of energy in the counter-propagating wave will disrupt the phase and hence the destructive zones. The counter-propagating wave can be either parallel or perpendicularly polarized. The present group has shown that the energy required for perpendicular polarized counter-propagating wave to extinguish harmonic generation is twice as much as that for parallel polarization [65]. When the counter-propagating polarization is parallel, the phase of the harmonic generation is scrambled due to direct interference between the driver and the counter-propagating pulse as well as intensity dependent phase. However, when the counter-propagating pulse polarization is perpendicularly polarized, the resultant elliptical driver dampens harmonic generation.

In theory, N counter-propagating pulses contains $N+1$ generating zones. Hence, the harmonic intensity should scale as $(N+1)^2$. Most recently, up to eight counter-propagating pulses have been achieved by the present group. A schematic of the experiment can be seen in Fig. 3.11. However, enhancements of the harmonics flattened out after four pulses suggesting drifts in the coherence length possibly caused by mode interference within the waveguide as seen in Fig 3.12. As a result, the present group developed a method to generate continuously-tunable pulse trains that could theoretically adapt to the drift in coherence length. In theory, this technique should be able to quasi-phase match tens of microns in coherence length, enabling the enhancement of much higher photon energies [84].

3.4.4 Multi-mode (parallel polarisation)

Similar to the modulated waveguides, if two or more modes with parallel polarisations are coupled into the waveguide, the interfering modes may cause intensity modulations. If these modulations are then properly matched with the coherence lengths of the harmonics, then QPM enhancements may occur. The present group presented enhancements of 3 orders of magnitude of 300eV harmonics and showed that mode beating may be the primary reason for these enhancements [135]. The experiment was performed at Rutherford Appleton Laboratories, where ~ 40 fs at ~ 50 mJ pulses were delivered to a waveguide with a bore radius of $\sim 90\,\mu\text{m}$. Figure 3.13 shows enhancement of water-window harmonics at 20 mbar of argon, but at phase mismatched conditions of 42 mbar of argon, enhancement was not observed. For 300 eV photons, the peak brightness was estimated to be $> 10^{21}$ photons/s/mm^2/mrad^2, making it the brightest water-window

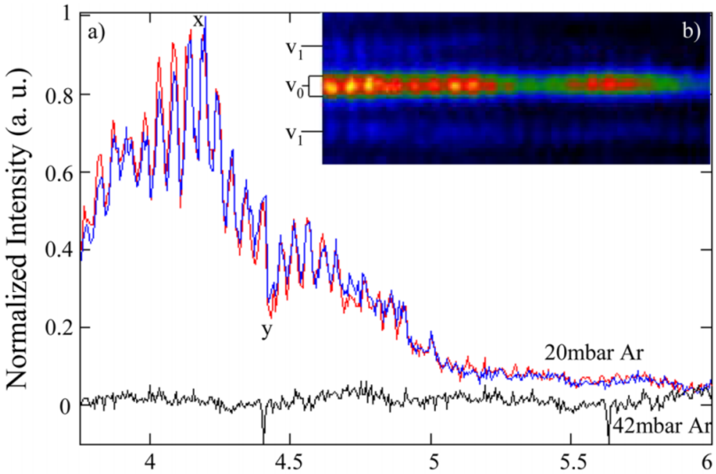

Figure 3.13: Quasi-phase-matched HHG in the water window. The red and blue traces are two separate shots recorded at $p \sim 20$ mbar Ar with the signal corrected for system transmission, while the black trace is obtained for mismatched conditions with $p \sim 42$ mbar Ar. Both harmonic signal traces (red and blue) are normalized to the value of the peak of the blue trace (labeled x) showing the good short term reproducibility of the data (3-minute interval). The dip in harmonic intensity at ~ 4.4 nm (labeled y) is due to uncertainty in the absolute transmission around the CK edge of the 0.2 µm Al/0.3 µm CH filter used to block optical light. The raw data from the CCD are shown in the inset. A lower limit of the conversion efficiency per harmonic order is calculated by vertical integration of the background subtracted signal in the bright region over the interval v_0 only and correcting for system transmission. Significant signal with clear harmonic structure is present for one side lobe (marked v_1 in the inset) either side of the bright central order, v_0. Up to six side lobes were observed experimentally and are likely due to off axis QPM. Figure and caption from [135]

.

x-ray from HHG at time of publication in 2007. One advantage the authors pointed out about MMQPM is that high order modes enabled the quasi-phase matching of very short coherence lengths, corresponding to very high order harmonics. The authors argued that strong intensity beating over short distances enabled QPM to occur for very high order harmonics [135].

Further in this thesis, we will explore mode beating in more detail and will argue that perhaps mode beating enhancements arise not only from intensity modulations but also also from more complicated phase modulations as well.

3.4.5 Polarisation control

In this thesis, we propose a new class of QPM techniques by controlling the polarization in an optical waveguide by either: (i) rotating the polarization of the driving field [71; 72] in a circularly birefringent waveguide; or (ii) modulating the ellipticity of the driver polarization [70; 73; 74] in a linearly birefringent system. The key advantage of this new class of polarization-controlled QPM is its simplicity compared to other QPM techniques since it avoids the need for additional laser pulses such as in counter-propagating waves or longitudinally-structured waveguides. Instead, the only requirement is a waveguide with a suitable value of birefringence. Moreover, as we show in Chapter 6, the circular birefringent scheme affords significantly greater conversion efficiencies than other QPM schemes and also provides the first circularly polarized quasi-phase matched or phase-matched harmonic source. As we will also see, polarization control can also be achieved in coupling in modes with polarization state control as well. Chapters 5-7 will focus on discussing polarization-control in detail.

3.5 Random phase matching

The key to harmonic intensity enhancement is to make sure that the phase does not add up destructively. The phase diagram in Fig 3.2 and Fig. 3.6 suggests that any mechanism that enables the sum of all the phasors to be as far away from the origin as possible can be effective in HHG enhancement. If each of the phasors are random in phase for each step, then the harmonic field undergoes a random walk in the complex amplitude space while it moves along the propagation axis. The total distance from origin is proportional to $\sqrt{N}$ where N is the number of steps. In the Chapter 8, we will explore the exact conditions for random phase matching.

3.6 Conclusion

This this chapter, we derived the origin of the phase mismatch problem and gave a brief introduction of the various solutions – phase matching ($\Delta k = 0$), various quasi-phase matching schemes, and random phase matching. In the following chapters, we will explore in more detail both from a theoretical and from an experimental perspective mode beating, polarisation control and random phase matching.

Chapter 4

Modes in lossy hollow-core waveguides

4.1 Introduction

Last chapter we discussed the phase-mismatch problem and potential solutions involving phase and quasi-phase matching. Most notably, we discussed phase matching and QPM techniques in hollow-core waveguides, which is a main focus of this thesis. HHG in hollow-core waveguides provides a few key advantages. First it extends the generation zone of the harmonics by maintaining driver intensity for a longer length. Second, it enables better control of gas conditions and pressures inside the hollow-core waveguide. Finally, it makes it possible for phase matching or quasi-phase matching as described in the previous chapter. Hence, in this chapter we will discuss the properties of modes and mode propagation in a hollow-core waveguide in this chapter; in particular, we will focus on radially symmetric modes.

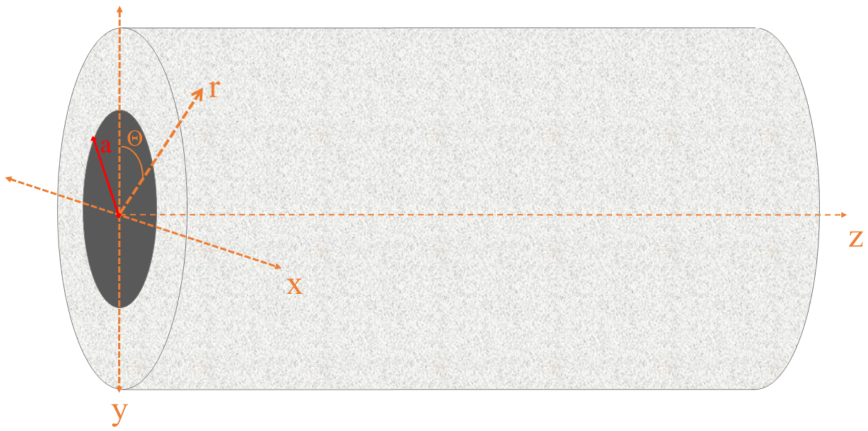

Figure 4.1: Schematic coordinate diagram for a hollow-core waveguide.

4.2 Basic solutions of hybrid modes

For most of the history of waveguide engineering, the focus has been on solid core waveguides where the index of refraction of the core is slightly higher than that of the cladding. As a result the laser field is confined inside the core due to total internal reflection. The modes of this type of guiding have long been well understood and have been straightforward to solve analytically [83].

The interest in hollow-core waveguides, however, has been a more recent development. Applications such as high harmonic generation or terahertz communications [52; 114] has encouraged further study of the modal structures of hollow-core waveguides.

It was not until 2002 that the full equations for circular hollow-core waveguide modes were derived [28]. In general, hollow-core modes can be grouped into transverse TE or TM modes and into hybrid EH modes. However, Gaussian linearly polarised laser beams are not suitable to couple into the transverse modes because the polarisation states are not linear, so we will focus our discussion on hybrid $EH_{1,m}$ modes, which do have linear polarisation. We note that much of the derivation of the mode solutions can be found in Cros et al. [28] and this chapter will focus on the key results relevant for high harmonic

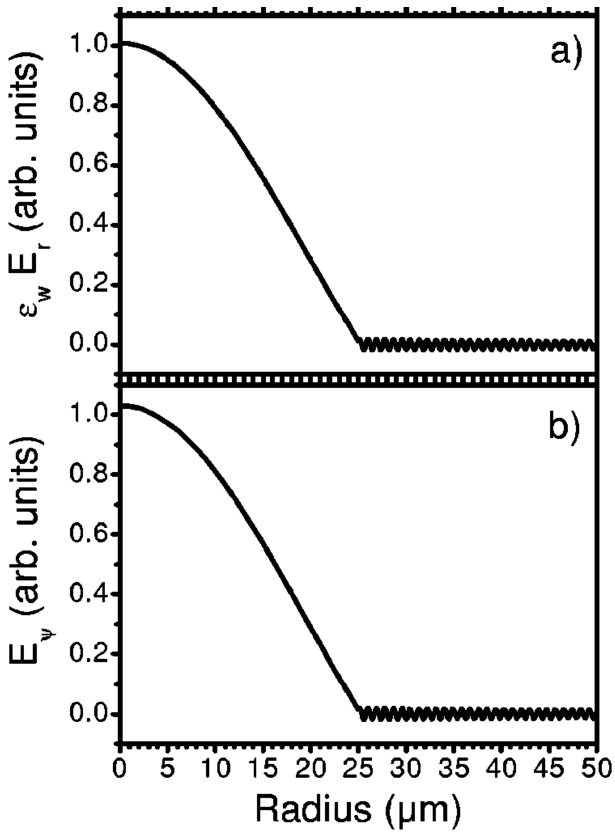

Figure 4.2: a) Radial and b) azimuthal components of the electric field of the EH11 mode as a function of the radial position for $\omega t - \beta_m z = \theta = \pi/4$, in the case of glass walls $\epsilon_w = 2.25$, an incident wavelength of 1 um and a capillary tube radius $a = 25$um, figure and caption from [28].

generation.

Fig. 4.1 shows the general schematic and coordinate labels for a hollow-core waveguide with a being the core radius, r being the radial coordinate, and z being the coordinate in the direction of laser propagation. We also note that $n = n_w$ is the refractive index of the cladding material and we will set $n = 1$ for the refractive index of the hollow-core. We also define the electric permittivity as $\epsilon_w = \sqrt{n_w}$ assuming that the magnetic permeability is 1.

In general, a propagating mode electric field can be written as product of the transverse modal profile $\vec{E}(r,\theta)$ and the propagation term $e^{-i(\omega t - kz)}$,

$$\vec{E}(z,r,\theta,t) = \vec{E}(\theta,r)e^{-i(\omega t - kz)} \tag{4.1}$$

where k_m is the complex propagation constant of the mode,

$$k_m = \beta_m + i\alpha_m. \tag{4.2}$$

The constant β_m is the phase constant that describes the modal dispersion while the constant α_m is the attenuation constant.

The propagating electric field in the z-direction for an EH_{nm} mode for $r \leq a$ can be written in cylindrical coordinates as [28],

$$
\begin{aligned}
E_z &= -\frac{u_m}{\beta_m a} J_n(u_m \frac{r}{a}) \sin(n\theta)\sin(\omega t - \beta_m z) e^{-\alpha_m z} && (4.3)\\
E_r &= \left\{ J_{n-1}(u_m \frac{r}{a}) \sin(n\theta)\cos(\omega t - \beta_m z) + \frac{u_m}{2k_0 a}\left[\left(\eta\frac{r}{a} + \mu\frac{a}{r}\right) J_n(u_m\frac{r}{a}) \right.\right. \\
&\quad \left.\left. + \eta\frac{2-n}{u_m} J_{n-1}(u_m\frac{r}{a}) \right] \sin(n\theta)\sin(\omega t - \beta_m z) \right\} e^{-\alpha_m z} && (4.4)\\
E_\theta &= \left\{ J_{n-1}(u_m \frac{r}{a}) \cos(n\theta)\cos(\omega t - \beta_m z) + \frac{u_m}{2k_0 a}\left[\left(\eta\frac{r}{a} - \mu\frac{a}{r}\right) J_n(u_m\frac{r}{a}) \right.\right. \\
&\quad \left.\left. + \left(\eta\frac{2-n}{u_m} + \mu\frac{u_m}{n}\right) J_{n-1}(u_m\frac{r}{a}) \right] \cos(n\theta)\sin(\omega t - \beta_m z) \right\} e^{-\alpha_m z} && (4.5)
\end{aligned}
$$

where J_ν is the Bessel function of the first kind, $\mu = \sqrt{\epsilon_w - 1}$, $\eta = (1 + \epsilon_w)/\mu$, u_m is solved via the dispersion relation and is the mth zero of $J_0(x) = 0$. For completeness, the magnetic fields are given by for $r \leq a$,

$$
\begin{aligned}
B_z &= \frac{\beta_m}{\omega}\frac{u_m}{\beta_m} J_n(u_m\frac{r}{a})\cos(n\theta)\sin(\omega t - \beta_m z)e^{-\alpha_m z} && (4.6)\\
B_r &= -\frac{\beta_m}{\omega} E_\theta && (4.7)\\
B_\theta &= \frac{\beta_m}{\omega} E_r. && (4.8)
\end{aligned}
$$

For outside the waveguide core (e.g., within the wall material), $r > a$, the electric field of the modes are given by,

$$
\begin{aligned}
E_z &= -\frac{u_m}{\beta_m a} J_n(u_m) \sqrt{\frac{a}{r}} \sin(n\theta) \sin[\omega t - \beta_m z - \beta_m \mu (r-a)] e^{-\alpha_m z} && (4.9) \\
E_r &= \frac{u_m}{\beta_m a \mu} J_n(u_m) \sqrt{\frac{a}{r}} \sin(n\theta) \sin[\omega t - \beta_m z - \beta_m \mu (r-a)] e^{-\alpha_m z} && (4.10) \\
E_\theta &= \frac{u_m}{\beta_m a \mu} J_n(u_m) \sqrt{\frac{a}{r}} \cos(n\theta) \sin[\omega t - \beta_m z - \beta_m \mu (r-a)] e^{-\alpha_m z}, && (4.11)
\end{aligned}
$$

and the magnetic field is similarly given by,

$$
\begin{aligned}
B_z &= \frac{\beta_m}{\omega} \frac{u_m}{\beta_m a} J_n(u_m) \sqrt{\frac{a}{r}} \cos(n\theta) \sin[\omega t - \beta_m z - \beta_m \mu (r-a)] e^{-\alpha_m z} && (4.12) \\
B_r &= -\frac{\beta_m}{\omega} E_\theta && (4.13) \\
B_\theta &= \epsilon_w \frac{\beta_m}{\omega} E_r && (4.14)
\end{aligned}
$$

For linearly polarised radially symmetric modes at zeroth order, we require $n = 1$. We note that the propagation constant's two terms for the EH_{1m} modes are given by [28; 97],

$$
\begin{aligned}
\beta_m &= \frac{2\pi}{\lambda} \left[1 - \frac{1}{2} \left(\frac{u_m \lambda}{2\pi a} \right)^2 \right] && (4.15) \\
\alpha_m &= \left(\frac{u_m}{2\pi} \right)^2 \frac{\lambda^2}{a^3} \left(\frac{n_w^2 + 1}{2\sqrt{n_w^2 - 1}} \right). && (4.16)
\end{aligned}
$$

Figure 4.2 shows the electric field components E_r and E_θ for the EH_{11} fundamental mode for $a = 25$um. It is evident that for $r \leq a$, the field profile is very much dominated by the Bessel term. For $r > a$, the wave emerges and is slowly damped by the $\sqrt{r/a}$ term, which forms the energy loss from the lossy waveguide.

To get back to familiar Cartesian coordinates, we can perform a coordinate transform,

$$E_x = E_r \sin(\theta) + E_\theta \cos(\theta) \tag{4.17}$$

$$E_y = E_r \cos(\theta) - E_\theta \sin(\theta) \tag{4.18}$$

To zeroth order, we can approximate the x and y dependent electric field terms as,

$$E_x(r, \theta) \approx J_{n-1}(u_m \frac{r}{a}) \cos[(n-1)\theta] \tag{4.19}$$

$$E_y(r, \theta) \approx J_{n-1}(u_m \frac{r}{a}) \sin[(n-1)\theta]. \tag{4.20}$$

For the family of modes where $n = 1$, it is clear that the modes are linearly polarised in the x direction as $E_y = 0$. Hence, we can write the only component, e.g., the x-component, of the linearly polarised EH_{1m} mode as,

$$E_{1m}(r, z, t) = J_0\left(u_m \frac{r}{a}\right) e^{-i(\omega t - \beta_m z)} e^{-\alpha_m z} \tag{4.21}$$

Finally, for completeness, we normalise the modes,

$$E_{1m}(r) \rightarrow \frac{1}{\sqrt{\int_0^a E_{1m} E_{1m}^* 2\pi r dr}} E_{1m}(r) = \frac{J_0\left(u_m \frac{r}{a}\right)}{a\sqrt{\pi} J_1(u_m)} \tag{4.22}$$

where * denotes the usual complex conjugate, and we assume that the electric field can be neglected for $r > a$.

4.3 Mode Coupling

It can be shown that the normalized Bessel modes E_{1m} are orthonormal and complete in r for symmetric modes. Hence, any linearly polarised radially symmetric input beam profile can be expressed a linear combination of modes,

$$E_{in}(r) = \sum_{m=1}^{\infty} C_m E_{1m}(r) \tag{4.23}$$

where C_m is the complex coupling coefficient for the mth EH_{1m} mode, which is given by,

$$C_m = \int_0^a 2\pi r dr E_{1m}(r) \cdot E_{in}(r). \tag{4.24}$$

If the total power of input beam can be expressed as,

$$P = \int_0^a 2\pi r dr E_{in} \cdot E_{in}^*, \tag{4.25}$$

then the fractional coupling of the mth mode is given by $C_m C_m^*/P$.

4.3.1 Gaussian coupling

For a linearly polarised Gaussian beam $E_{in}(r) = E_0 e^{-r^2/w_0^2}$ of waist size w_0 at focus coupled into the waveguide, the coupling coefficient is given as,

$$C_m = E_0 \int_0^a 2\pi r dr E_{1m} e^{-r^2/w_0^2}. \tag{4.26}$$

To couple into the fundamental EH_{11} mode, it has been found that there is an optimal beam width to waveguide radius ratio of $w_0 = 0.6435a$ which gives $C_1 C_1^*/P = 0.98$, or 98% of incident power is coupled into the first order mode [28]. Figure 4.3 shows the coupling power of the first four modes as a function of beam width to radius ratio.

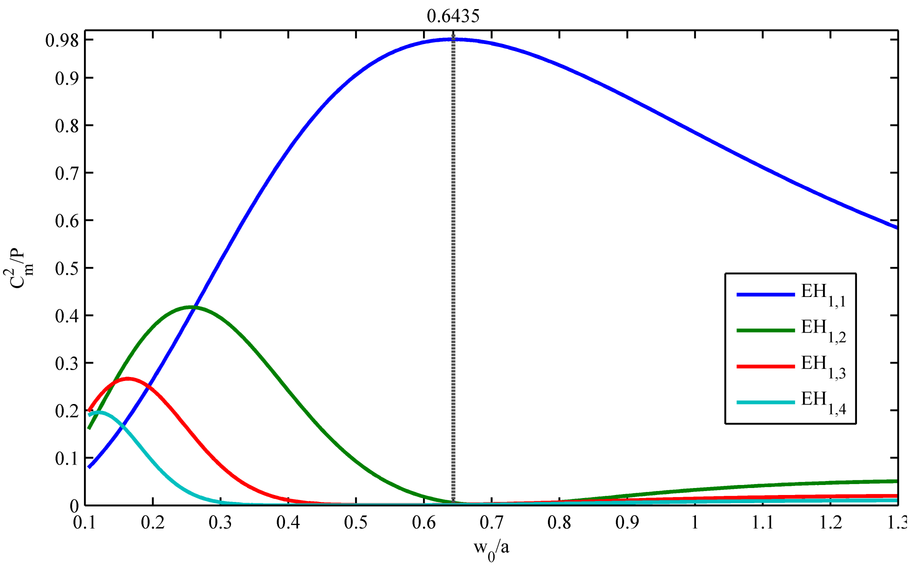

Figure 4.3: Proportion of the incident power coupled into the first four modes, as a function of w_0/a, the ratio of the incident spot radius to the capillary inner bore radius. Waveguide attenuation increases for higher-order modes, so the transmission of a capillary is maximised when the lowest-order mode is preferentially excited. Maximum coupling into the lowest order mode occurs when $w_0/a = 0.6435$, figure and caption from [97]

4.3.2 Spatial filtering

It is clear that for a Gaussian beam even optimal coupling excites approximately 2% of higher order modes. Moreover, in a realistic experimental situation, perfect coupling is even more difficult. As we will see in Chapter 10, spatial shaping of beams using a spatial light modulator is one way of achieving better coupling. However, even in the absence of ideal coupling, the waveguide itself acts as a spatial filter that amplifies the relative power of the lower order modes. In fact the current group now use a longer 100mm waveguide for QPM HHG experiments in order to achieve better mode quality [84].

Noting Equation (4.16), we notice that as m increases, u_m must increase as well. Given that the α_m term has a u_m^2 relation, a higher order mode implies a higher damping coefficient. Table 4.1 gives the $1/e^2$ attenuation lengths for the first four modes. Hence, after a some propagating distance, the higher order modes are damped away.

4.4 Linear Mode Beating

For a combination of linearly polarised modes (in the same direction and polarisation state), the electric field can be written as,

$$
\begin{aligned}
E(r,z,t) &= \sum_m C_m E_{1m}(r) e^{-i(\omega t - \beta_m z)} e^{-\alpha_m z} && (4.27)\\
&= e^{-i\omega t} \sum_m C_m \frac{J_0\left(u_m \frac{r}{a}\right)}{a\sqrt{\pi} J_1(u_m)} e^{+i\beta_m z} e^{-\alpha_m z}. && (4.28)
\end{aligned}
$$

We note here that each sum component is made up of four parts: C_m is the complex coupling coefficient, the Bessel terms represent the spatial profile of the mode, the complex exponent $e^{i\beta_m z}$ represent the mode propagation along the z axis and the real exponent $e^{-\alpha_m z}$ represents the mode dampening term. Finally, the frequency term $e^{-i\omega t}$ can be factored outside the sum given that it is the same for all modes.

4.4.1 Intensity beating

Intensity of the propagating modes can be written as,

$$
I(z,r) = \frac{\epsilon_0 c}{2} E E^*. \tag{4.29}
$$

After some algebra, the interference period of the intensity, or beat length between two modes m and m' is given by,

$$
2L_{b,m-m'} = \frac{2\pi}{|\Delta\beta|} = \frac{2\pi}{|\beta_m - \beta_{m'}|} \tag{4.30}
$$

As we shall also see in Chapter 5, this beat length is also the polarization beat length under a birefringent system if m and m' have perpendicular polarisations. Note also that the factor of two in $2L_{b,m-m'}$ is meant to harmonize the definition of beat length as

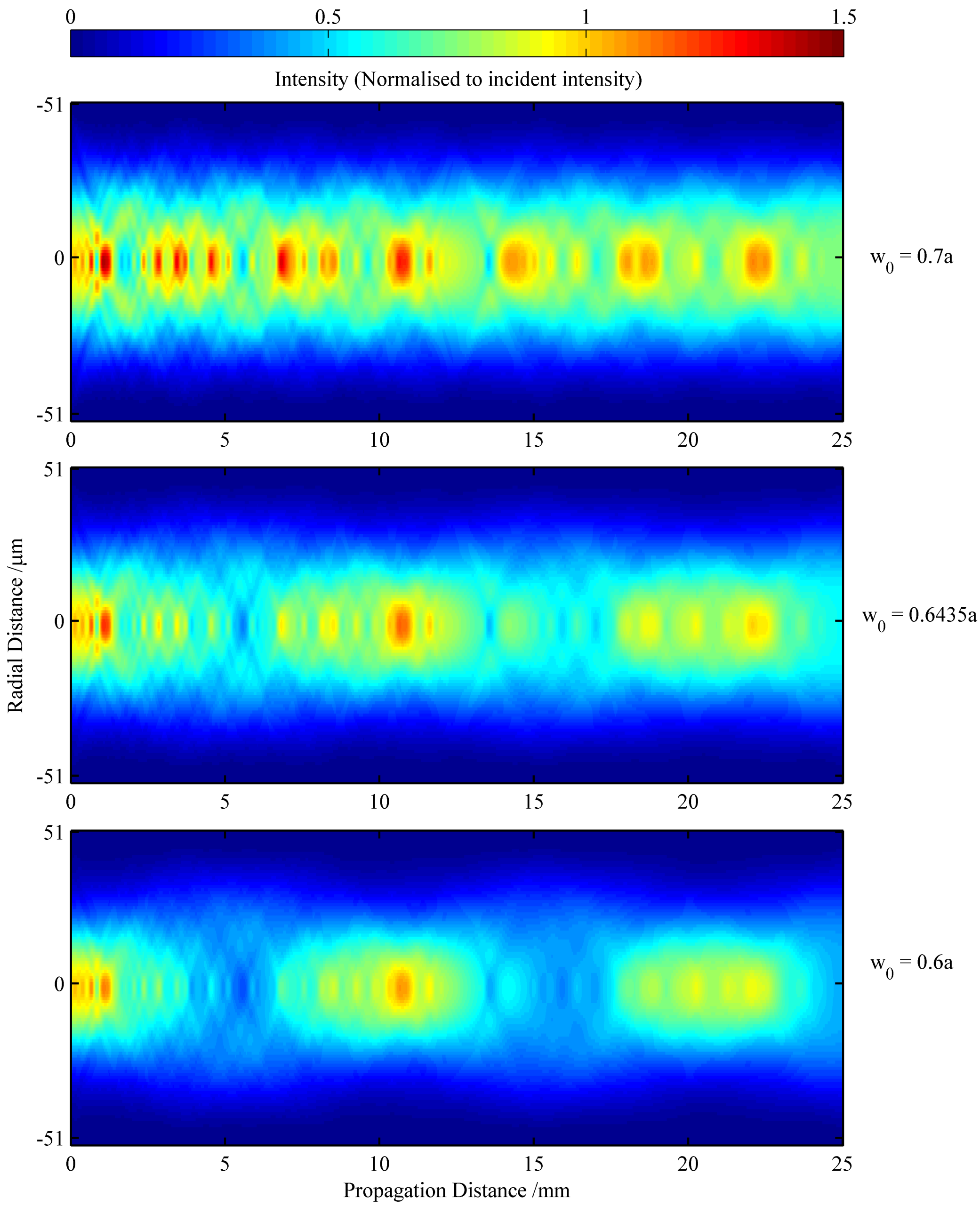

Figure 4.4: Calculated intensity, normalised to the incident intensity, as a function of radial position and propagation distance for three different coupling conditions, for a capillary with $a = 51$um. Figure and caption from [97]

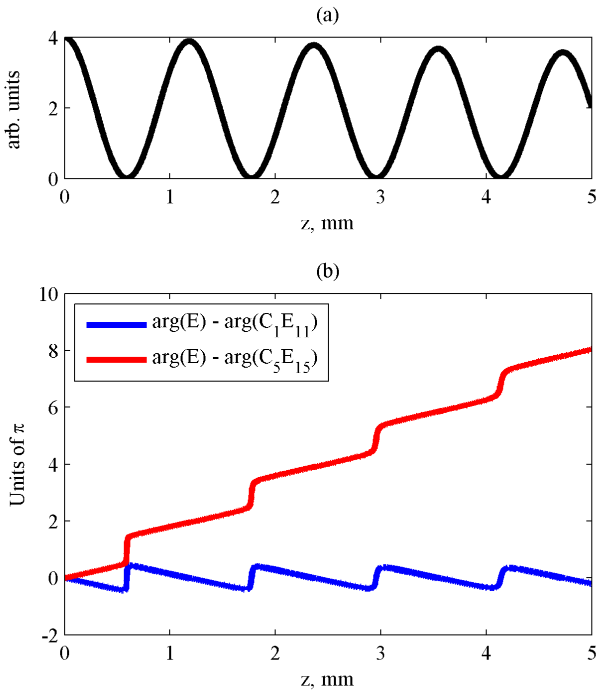

Figure 4.5: Figure (a) shows the intensity of the combined modes (assuming dampening), $I(z)$ as a function of propagation distance z. Figure (b) shows the phase differential between the first order mode and combined modes (blue line) and between the fifth order mode and the combined modes (red). Both figures assume a 800nm laser pulse in an $a = 51$um radius waveguide with wall index of refraction of $n_w = 1.45$

discussed in the forthcoming chapters.

Figure 4.4 shows the intensity modulation for a continuous beam of radiation with $\lambda = 800$nm with three different Gaussian mode coupling ratios ($w_0/a = 0.7, 0.6435, 0.6$) with a hollow-core waveguide radius of $a = 51$um and index of refraction of $n_w = 1.45$. It is clear that for $w_0/a = 0.6$, the two main modes coupled are the $m = 1$ and $m = 2$ modes as seen in Figure 4.3, which has a beat length of $2L_{b,1-2} = 10.4$mm with these parameters. It is clear from the figures that the areas of peak brightness are spaced roughly apart by 10.4mm [97].

4.4.2 Phase modulation

It is evident that mode beating will also cause the phase of the guided radiation to become modulated. It is clear that for, say, two modes coupled into the waveguide, $m = 1$ and $m = 5$, $\arg(E) \neq \arg(C_1 E_{11}) \neq \arg(C_5 E_{15})$. Figure 4.5 shows the phase differentials $\arg(E) - \arg(C_1 E_{11})$ and $\arg(E) - \arg(C_5 E_{15})$. We see that the phase modulation has the same period as the intensity modulation given by the mode beat length $2L_{b,1-5}$. An algebraic analysis of this will be conducted in Chapter 7.

Given the phase sensitivity for phase and quasi-phase matching in HHG, the phase modulation from mode beating may play an important part of the generation process. In Chapter 7, we will explore the impact of this on quasi-phase matching and in Chapter 8 we will see how this can potentially impact random phase matching.

4.4.3 Mode beating in pulsed lasers

Table 4.1: Modal properties for a $\lambda = 800$nm, 50 fs laser pulse with a waveguide core radius of $a = 51$um and $n_w = 1.45$, table from [97]

Mode	$1/e^2$ intensity attenuation length	Group velocity	Distance for 50fs separation from EH_{11}
EH_{11}	96cm	0.99998c	N/A
EH_{12}	18cm	0.99990c	19.5cm
EH_{13}	7.4cm	0.99977c	7.0cm
EH_{14}	4.0cm	0.99957c	3.6cm
EH_{15}	2.5cm	0.99931c	2.2cm

In Section 4.2, we calculated the phase velocity or mode propagation constant β_m for different modes. So far, all the analysis above assumes a continuous-wave (CW) laser. In reality, in order to generate harmonics, ultrafast, pulsed lasers must be used, which are around the tens of femtosconds pulse width. The group velocity is also dependent on mode number and is given by,

$$v_{g,m} = \left(\frac{\partial \beta_m}{\partial \omega}\right)^{-1} = c\left[1 + \frac{1}{2}\left(\frac{u_m \lambda}{2\pi a}\right)^2\right]^{-1}. \tag{4.31}$$

Table 4.1 gives calculated group velocities for its given parameters. Note that for higher order modes, the group velocities decrease. This suggests that for a pulsed laser, as the modes propagate down the waveguide, lower and higher order modes will slip as a result of group velocity dispersion. Table 4.1 also calculated the distance it would take for a 50fs laser pulse of the specified mode number to separate from the first order mode.

To calculate the electric field of the mode moving along the first order mode, we need to assume a pulse width τ and shape. Assuming a Gaussian temporal profile, the field propagating along $m = 1$ can be written as,

$$E_{m=1}(z, r, t) = \sum_m C_m E_{1m}(r) e^{-i(\omega t - \beta_m z)} e^{-\alpha_m z} e^{-2\ln 2 \frac{(t - z/v_{g,m})^2}{\tau^2}} \tag{4.32}$$

where the last exponential term $e^{-2\ln 2 \frac{(t - z/v_{g,m})^2}{\tau^2}}$ describes the mode slippage. We note that the equation above is a simplification. In reality, the laser pulse contains a spectrum of optical frequencies, and that to calculate propagating field, we need to integrate over the frequencies. However, in the equation above, we have neglected chromatic dispersion and any dependency on wavelength.

Figure 4.6 shows the mode beating intensity as a function of propagation distance for a CW and for 50fs, 25fs, and 10fs pulses. Note that the mode beating effect is damped faster for shorter pulses because the lower order modes no longer overlap with the higher order modes. As we discuss in future chapters, this is one area of limitation for QPM schemes based on mode beating.

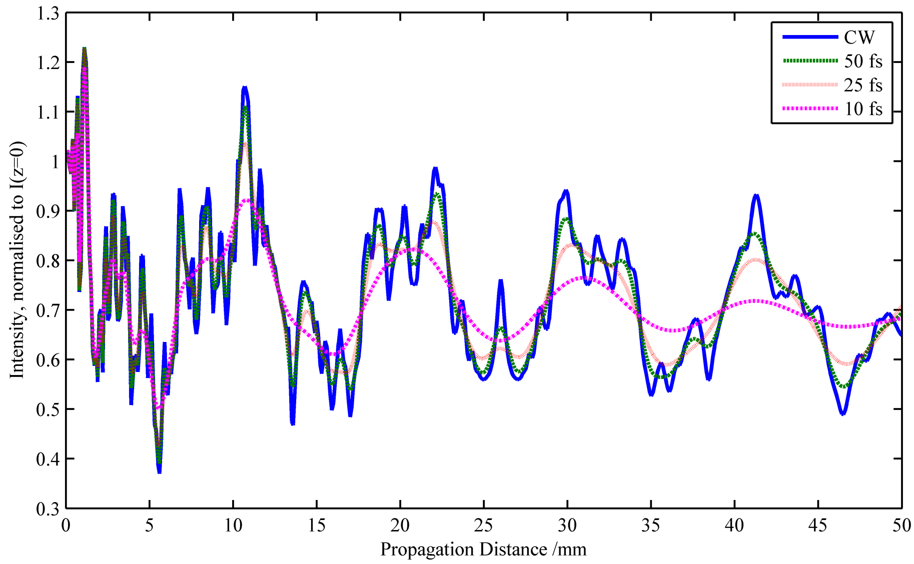

Figure 4.6: Longitudinal intensity variation in a capillary with $w_0 = 0.6345a$, due to beating between the ten lowest order modes, for the case of three different pulse durations as well as the CW case, figure and caption from [97]

4.5 Conclusion

In this chapter, we presented the modes for radially symmetric hollow-core waveguides based on [28]. We then outlined the theory behind mode coupling and mode beating. The basis for this chapter will provide the mathematical framework for discussions in the next few chapters around polarisation-beating, optical-rotation, and multi-mode QPM, whose schemes are all based on mode interference.

Chapter 5

Polarisation Beating Quasi-Phase Matching

5.1 Introduction

In Chapter 3, we discussed the origins and potential solutions of the phase-mismatch problem noting that QPM is a potential solution, and in the previous chapter, we discussed how modes propagate through a hollow core waveguide. Now, we discuss a novel QPM technique – polarization-beating QPM (PBQPM) – which utilizes polarization beating in a birefringent waveguide to modulate the generation of harmonics [70; 73; 74]. The key advantage of PBQPM is its simplicity, since it avoids the need for additional laser pulses or longitudinally-structured gas targets. Instead, the only requirement is a birefringent waveguide with a suitable value of the birefringence. Induced birefringence from mode beating may also be exploited, which we will explore in Chapter 7.

5.2 Polarization Beating QPM

In Chapter 2, we discussed the single-atom efficiency of HHG dependence on the polarisation of the driving field [7; 8; 20; 110], which arises from the fact that the ionized electron must return to the parent ion in order to emit a harmonic photon.

In PBQPM a birefringent waveguide is used to generate beating of the polarization state of a driving linearly-polarized driving laser pulse, thereby modulating the harmonic generation process. QPM will occur if the period of polarization beating is suitably matched to the coherence length of the harmonics. In a birefringent waveguide, the incident radiation can be resolved into two components polarized along the birefringent axes. For linearly-polarized incident light these components are initially in phase, but the difference in their phase velocity will cause the two components to develop a phase difference which increases linearly with propagation distance. As a consequence, the resultant polarization state will evolve from linearly polarized at an angle Θ to (for example) the fast axis, through (say) right-handed elliptical polarization to linearly polarized at an angle $-\Theta$ to the fast axis, and thence through elliptical polarization back to linearly-polarized radiation parallel to the incident light.

The polarization beat length L_b is defined to be the distance for the two polarization components to develop a phase difference of π, and hence:

$$L_b \equiv \frac{\pi}{\Delta\beta} = \frac{\pi}{kB} = \frac{\lambda}{2B} \tag{5.1}$$

where $\Delta\beta$ is the difference in propagation constant for the two polarization components, λ is the vacuum wavelength, and $B = \frac{\lambda\Delta\beta}{2\pi}$ is the dimensionless birefringence parameter

Thus, by matching the beat length to an appropriate multiple of L_c, harmonic generation can be turned on and off along the length of the waveguide in a controlled way – enabling quasi-phase matching. As described in Chapter 2, since the harmonics are

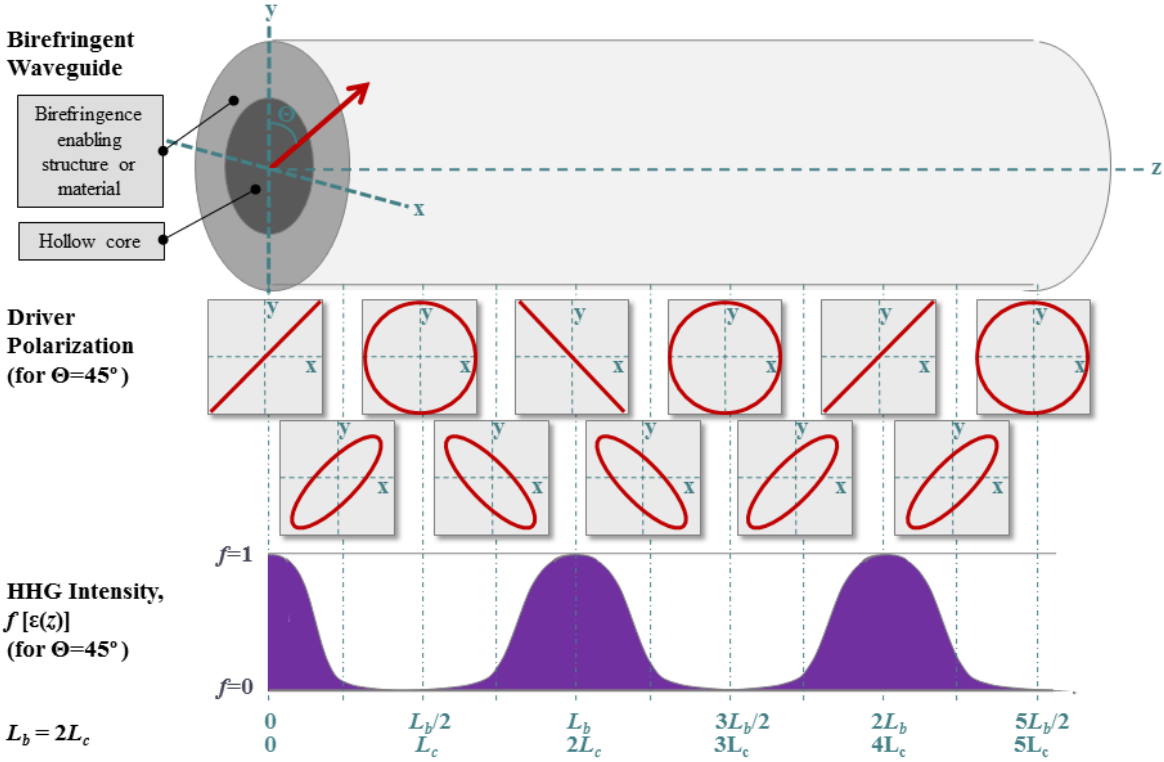

Figure 5.1: Cartoon schematic for PBQPM

generated most efficiently for linear polarization, the general condition for lowest-order for PBQPM is that the separation, L_b, of adjacent points of efficient harmonic generation is equal to an even number of coherence lengths, i.e. PBQPM requires, $L_b = nL_c$, where n is an even integer As is discussed in more detail below, since the coherence lengths for harmonics polarized parallel to the $\hat{x}$- and $\hat{y}$-axes are different, for a given L_b it is only possible to quasi-phase-match one of these components. As a consequence the output harmonics will be predominantly linearly polarised along the matched birefringent axis. Moreover, as discussed below, Θ and the harmonic order q determine the width of the generation zone in relation to L_b where Θ can be optimized. Figure 5.1 shows a cartoon schematic for PBQPM.

5.3 The envelope function for PBQPM

If we write the electric field of the qth harmonic as

$$E_q(z,t) = \xi(z,t)e^{i[k(q\omega)z - q\omega t]} \tag{5.2}$$

then, within the slowly-varying envelope approximation:

$$\frac{\partial \xi}{\partial z} = A\Gamma(z)e^{-i[k(q\omega) - qk(\omega)]z} \tag{5.3}$$

where ξ is the electric field envelope, $k(\omega) = \beta(\omega)$ is the propagation constant for radiation of frequency ω, A is a normalization constant and $\Gamma(z)$ is a relative source term.

As in Chapter 3, for each polarization the wave vector mismatch for a specific harmonic, q, can be written as:

$$\begin{aligned} \Delta k &= k(q\omega) - qk(\omega) && (5.4) \\ &= \Delta k_{plasma} + \Delta k_{neutral} + \Delta k_{waveguide} && (5.5) \end{aligned}$$

and the envelope function can be solved as:

$$\xi(z) = A\int_0^z dz' e^{-i\Delta k z'}\Gamma(z'). \tag{5.6}$$

5.3.1 Effect of polarization state on HHG

The relative number of harmonic photons generated in the qth harmonic by a driving beam of ellipticity ε may be written as:

$$f(\varepsilon) \approx \left(\frac{1-\varepsilon^2}{1+\varepsilon^2}\right)^{\alpha} \tag{5.7}$$

where ε is defined as the ratio between the minor axis to major axis.

Within the perturbative regime $\alpha = q - 1$, as verified by Budil et al [20] for harmonics $q = 11$ to 19, and by Dietrich et al for harmonics up to $q \approx 31$ [31]. Schulze et al found that for higher-order harmonics the sensitivity of harmonic generation to the ellipticity of the driving radiation is lower than predicted by Eqn (5.7) with $\alpha = q-1$ [104], although in this non-perturbative regime the efficiently of harmonic generation still decreases strongly with ε. Further measurements of the dependence of harmonic generation on ellipticity have been provided by Sola et al [110]. It is recognized that Eqn (5.7) is an approximation, but it will serve our purpose of demonstrating the operation of PBQPM.

The offset angle and ellipticity of the harmonics generated by elliptically-polarized radiation have been shown to depend on the ellipticity and intensity of the driving radiation, and on the harmonic order [7; 8; 77; 104; 112]. Propagation effects can also play an important role. Since the amplitude with which harmonics are generated decreases strongly with increasing ellipticity, we are most interested in the ellipticity of the harmonics generated for small ε. It has been shown that for higher-order harmonics, and/or high driving intensities, both the ellipticity and change in ellipse orientation of the harmonics generated by radiation with $\varepsilon \approx 0$ are close to zero [8]. We will therefore make the simplification that the generated harmonics are linearly polarized along the major axis of the driving radiation, and that the harmonics polarized along the fast and slow axes of the waveguide may be treated separately.

5.3.2 Birefringence & evolution of the ellipticity of polarization

In this section, the evolution of the driving field's ellipticity will be developed. We assume azimuthal symetry of the modes. Let $\hat{x}$ and $\hat{y}$ be the birefringent axes of the waveguide with the $\hat{x}$ axis being the slower axis such that $\beta_x < \beta_y$. The driving field can be decomposed into the $\hat{x}$ and $\hat{y}$ components:

$$\vec{\mathfrak{E}}(r,z,t) = \begin{pmatrix} \mathfrak{E}_x \\ \mathfrak{E}_y \end{pmatrix} = E(r) \begin{pmatrix} e^{i([(\beta_y - \Delta\beta)z - \omega t]} \sin\Theta \\ e^{i[(\beta_y)z - \omega t]} \cos\Theta \end{pmatrix} \tag{5.8}$$

where $E(r)$ describes the transverse electric field profile as a function of the distance r from the propagation axis.

At a given point z the electric field has an ellipticity given by:

$$\varepsilon(z) = \sqrt{\frac{\sin^2\Theta\cos^2(\phi_{min} - \Delta\beta z) + \cos^2\Theta\cos^2(\phi_{min})}{\sin^2\Theta\cos^2(\phi_{max} - \Delta\beta z) + \cos^2\Theta\cos^2(\phi_{max})}} \tag{5.9}$$

where

$$\tan^2\Theta = -\frac{\sin[2\phi]}{\sin[2(\phi + \Delta\beta z)]} \tag{5.10}$$

Here ϕ_{max} and ϕ_{min} are the values of $\phi = \omega t$ which give respectively the maximum and minimum magnitude of the electric field.

Although the ellipticity is periodic with period L_b, the electric field is periodic with period $2L_b$. The beating of the ellipticity as a function of propagation distance for various different angles of incidence is shown in Figure 5.2.

5.3.3 Wave-vector mismatch in a birefringent waveguide

In a birefringent waveguide the wave vector mis-match Δk is polarization-dependent. However, the only polarization-dependent term in Eqn (5.5)is $\Delta k_{waveguide}$, the wave vector mis-match arising from the waveguide dispersion. Hence we may write,

$$\begin{cases} \Delta k_{x,waveguide} = \beta_x(q\omega) - q\beta_x(\omega) \\ \Delta k_{y,waveguide} = \beta_y(q\omega) - q\beta_y(\omega) \end{cases} \tag{5.11}$$

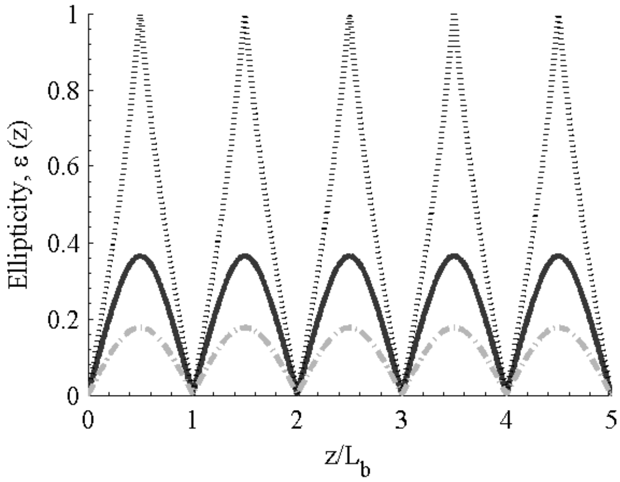

Figure 5.2: Ellipticity beating for different incidence angles Θ. From top to bottom: Dotted light gray line shows $\Theta = 45°$, Solid gray line shows $\Theta = 30°$ and $\Theta = 70°$; and dot-dashed gray line shows $\Theta = 20°$ and $\Theta = 80°$.

From this, we may then write,

$$\Delta k_x = \Delta k_y + \delta k_{xy},$$

where,

$$\delta k_{xy} = \Delta k_{y,waveguide} - \Delta k_{x,waveguide} \tag{5.12}$$

$$= q\Delta\beta(\omega) - \Delta\beta(q\omega) \tag{5.13}$$

$$\approx q\Delta\beta(\omega) \tag{5.14}$$

and the approximation follows if the birefringence is small at the frequency of harmonic q.

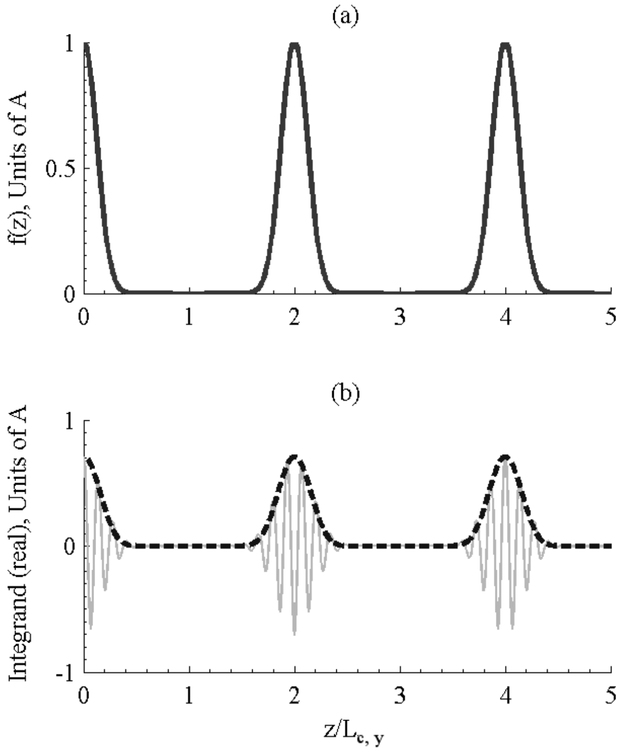

Figure 5.3: Top graph (a): Variation of the harmonic generation efficiency, $f(z) = f[\varepsilon(z)]$, as function z for $q = 27$ and $\Theta = 45°$. Bottom graph (b): Real part of the of the $\hat{x}$ component of the integrand (solid gray) and $\hat{y}$ component (dashed black line). Assuming $L_b = 2L_{c,y}$, $\Theta = 45°$ and $q = 27$

5.3.4 Constructing the PBQPM envelope function

From the discussion in Section 5.3.1 we may treat each polarization separately, and hence Eqn (5.6) becomes:

$$\begin{cases} \xi_x(z) = A \int_0^z dz' e^{-i\Delta k_x z'} \Gamma_x(z') \\ \xi_y(z) = A \int_0^z dz' e^{-i\Delta k_y z'} \Gamma_y(z') \end{cases} \tag{5.15}$$

where

$$\begin{cases} \Gamma_x(z') = \sqrt{f[\varepsilon(z')]} \sin\Theta \\ \Gamma_y(z') = \sqrt{f[\varepsilon(z')]} \cos\Theta \end{cases} \tag{5.16}$$

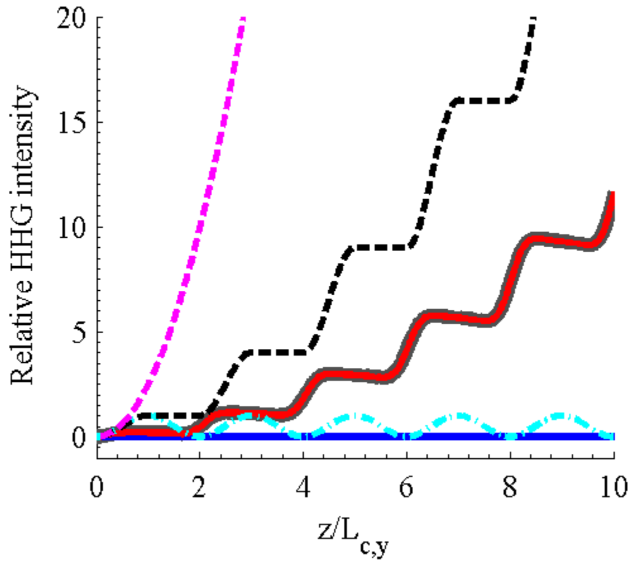

Figure 5.4: Relative HHG intensity for different phase matching conditions assuming that $L_b = 2L_{c,y}$, $q = 27$, $\Theta = 20°$ for PBQPM. Dashed magenta line shows perfect phase matching, dashed black line for perfect quasi-phase matching, dot-dashed cyan line for no phase matching. The solid blue line shows the relative amplitude squared for the $\hat{x}$ component whilst the dashed yellow line shows the relative amplitude squared for the $\hat{y}$ component. The thick gray line shows the total HHG intensity for PBQPM.

are the relative source terms. In terms of the faster polarization state (the $\hat{y}$ component),

$$\begin{cases} \xi_x(z) = A\sin\Theta \int_0^z dz' e^{-i(\Delta k_y + q\Delta\beta)z'} \sqrt{f[\varepsilon(z')]} \\ \xi_y(z) = A\cos\Theta \int_0^z dz' e^{-i\Delta k_y z'} \sqrt{f[\varepsilon(z')]} \end{cases} \tag{5.17}$$

Figure 5.3 shows an example of $f[\varepsilon(z)]$ and the real part of the envelope function intergrand, assuming $\alpha = q - 1$ and $L_b = 2L_{c,y}$. Notice that integrating across the $\hat{y}$ component would result in a monotonic increase of the HHG amplitude whereas for the $\hat{x}$ component, no net increase in harmonic amplitude would result owing to the rapid oscillations of the integrand. We conclude that the the polarization of the output harmonic will be almost perfectly linear, in this case with an electric field parallel to the y-axis since it is for that polarization that the polarization beating has been matched to the coherence length

Figure 5.4 compares PBQPM for these parameters against perfect phase matching and perfect QPM; we define the latter to correspond to square-wave modulation of the local harmonic generation with a period $2L_c$ and complete suppression of the out of phase zones.

5.4 Properties of PBQPM

5.4.1 Coherence length and beat length matching

For a waveguide with fixed birefringence B the condition for PBQPM can be realized by tuning the gas pressure and/or adjusting the driving laser intensity until the period of polarization beating and the coherence length are appropriately matched. The general condition for QPM is that the distance over which harmonics are generated and that over which generation is suppressed are both equal to an odd number of coherence lengths, i.e. to $(2l+1)L_c$ and $(2m+1)L_c$ respectively, where l and m are integers. Thus the QPM period is in general $2(l+m+1)L_c = nL_c$ and hence the general condition for PBQPM is $L_b = nL_c$, where n is even. Note that if the distances over which harmonics are generated and suppressed are equal, i.e. $l = m$, then PBQPM requires satisfaction of the more restrictive condition $L_b = 2(2l+1)L_c$. These considerations are illustrated by Figure 5.5 which shows the calculated growth of the harmonic intensity for the cases $n = 1, 2, 3$ and 4. It may be seen that monotonic growth of the harmonics does not occur when n is odd, as expected. Notice that PBQPM does occur for the case $n = 4$, which corresponds to the lengths of the suppressed and unsuppressed regions of harmonic generation being unequal; this is possible for PBQPM since the efficiency of harmonic generation is very sensitive to the ellipticity, so that it is possible for the harmonic generation regions to be shorter than those in which generation is suppressed.

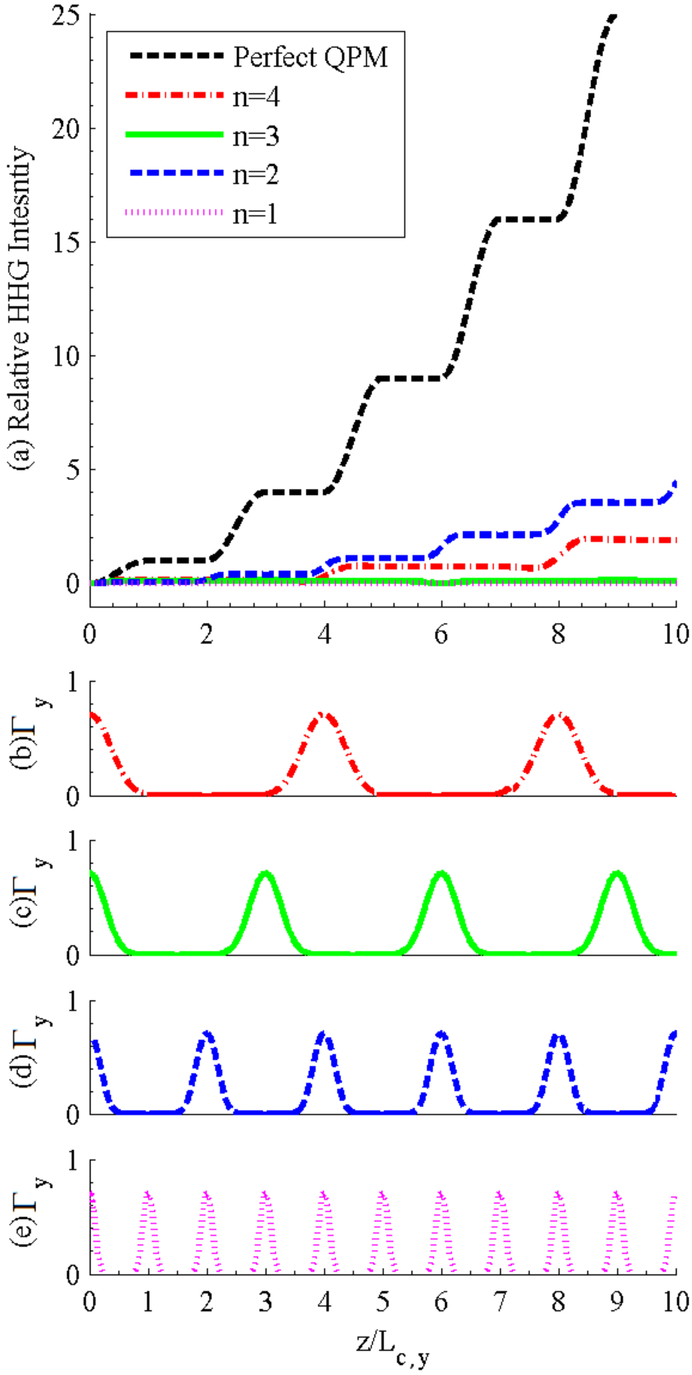

Figure 5.5: PBQPM for $\Theta = 34^o$, $q = 27$, and $L_b = nL_{c,y}$ with $n = 1, 2, 3, 4$. The top graph shows the relative harmonic intensity as a function of propagation distance z for perfect QPM (dashed black line), $L_b = 4L_{c,y}$ (dot-dashed red line), $L_b = 3L_{c,y}$ (solid green line), $L_b = 2L_{c,y}$ (dashed blue line), and $L_b = L_{c,y}$ (dotted magenta line). The bottom four graphs show the $p = y$ polarization source term Γ_y as a function of propagation distance z for (b)$L_b = 4L_{c,y}$,(c)$L_b = 3L_{c,y}$, (d)$L_b = 2L_{c,y}$, and (e)$L_b = L_{c,y}$

5.4.2 Output intensity and coupling angle Θ

It can be expected that the coupling angle Θ has an optimum: if Θ is small then the ε remains small for all z, and the harmonic generation is not sufficiently suppressed in the out of phase zones; if it is too large then harmonics are only generated for a small fraction of the in-phase zones. Figure 5.6 shows the relative harmonic intensity as a function of propagation distance for various coupling angles Θ. Figure 5.7a shows as a function of Θ, and for various harmonics q, the normalized harmonic signal after one beat length. Also shown is the optimum coupling angle as a function of harmonic order q.

The optimum coupling angle, $\hat{\Theta}$, will decrease with harmonic order since higher-order harmonics are more sensitive to the ellipticity of the driving radiation as discussed in Section 5.3.2 , and hence for these harmonics it is possible to couple more of the polarization of the incident radiation along the polarization of the harmonics to be generated by PBQPM. Figure 5.7b confirms this for the case of $L_b = 2L_{c,y}$.

5.5 Realisation of PBQPM

Having introduced the concept of PBQPM and explored its operation in theory, we now discuss how this quasi-phase-matching scheme might be realized in practice. Several types of birefringent waveguides have been developed to date: elliptical or rectangular waveguides [83]; waveguides made from birefringent materials [79]; waveguides with nonuniform refractive index [83]; photonic crystal fibers (PCFs) [2; 23; 132]; waveguides constructed with tunable piezoelectric material [119]; tunable stress-induced birefringent waveguides [83]. Many of these birefringent waveguides employ solid cores, and are therefore not suitable for PBQPM. However, we note that (non-birefringent) gas-filled PCFs have been used to generate high harmonics [48]. Moreover, commercially available hollow core birefringent PCFs have been demonstrated with birefringence parameters as large as

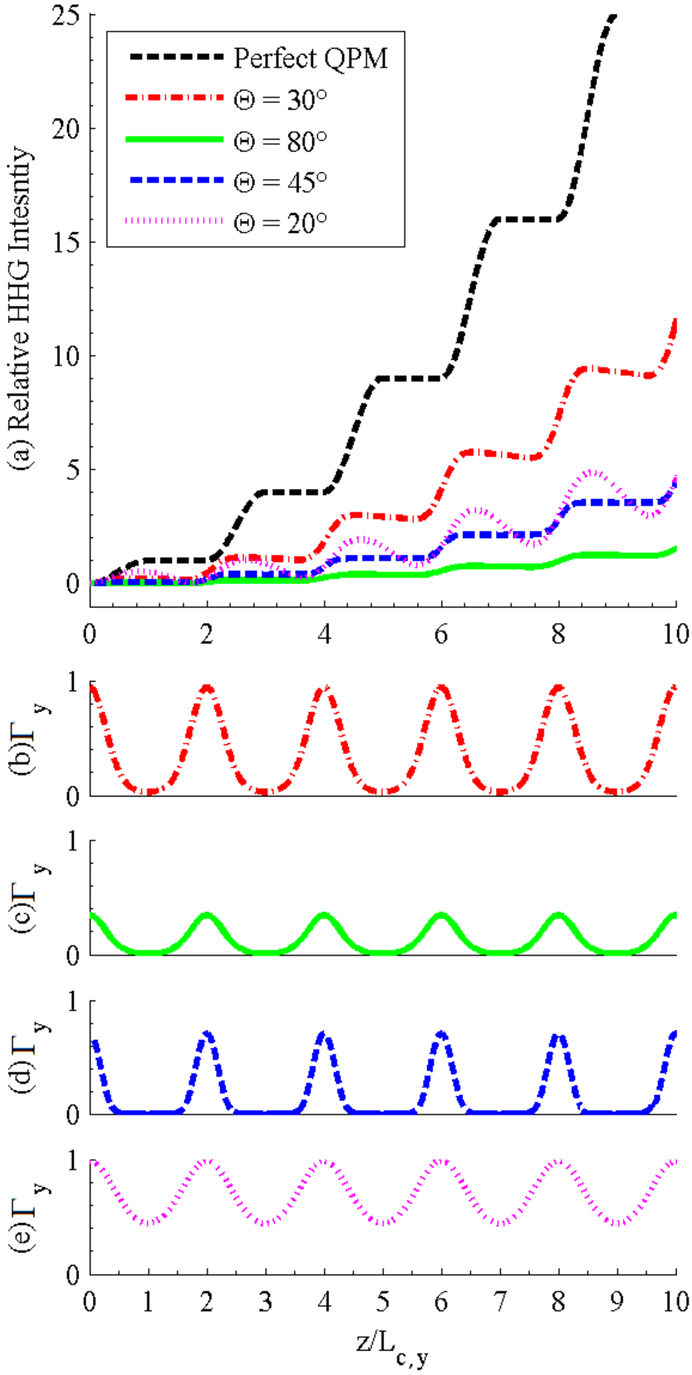

Figure 5.6: PBQPM for $q = 27$ and $L_b = 2L_{c,y}$ with $\Theta = 30^o, 80^o, 45^o, 20^o$. The top graph shows the relative harmonic intensity as a function of z for perfect QPM (dashed black line) and coupling angles of $\Theta = 30°$ (dot dashed red line), $\Theta = 80°$ (solid green line), $\Theta = 45°$ (dashed blue line), $\Theta = 20°$ (dotted magenta line). The bottom four groups show the $p = y$ polarization source term Γ_y as a function of z for (b)$\Theta = 30°$, (c)$\Theta = 80°$, (d)$\Theta = 45°$, and (e) $\Theta = 20°$.

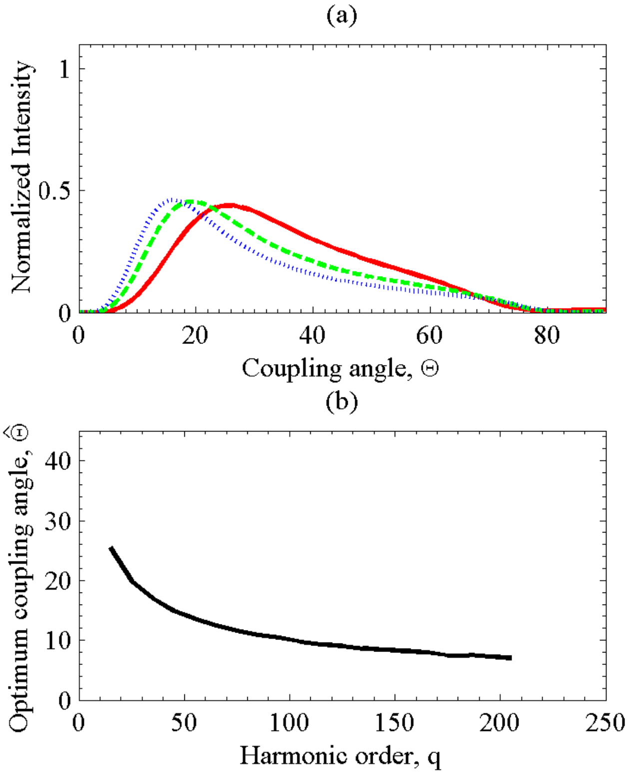

Figure 5.7: Top graph (a): Relative HHG intensity as a function of coupling angle Θ, normalized to perfect QPM after one beat length where $L_b = 2L_{c,y}$ for $q = 15$ (solid red line), $q = 27$ (dashed green line) , $q = 39$ (dotted blue line). Bottom graph (b): Optimal angle $\hat{\Theta}$ as a function of harmonic order q for $L_b = 2L_{c,y}$

$B > 10^{-4}$ [2; 96], corresponding to matching a coherence length of $\sim$ 1mm, and solid-core PCFs with $B > 10^{-3}$ have been demonstrated [17]. The birefringence of optical crystals can be as large as $B \approx 0.4$ [59]. Although the birefringence of hollow-core waveguides made from materials of this type would be only a fraction of that of the wall material, it seems likely that construction of hollow-core waveguides with sufficient birefringence to match coherence lengths in the range of a few hundred microns will be possible. The development and study of hollow-core birefringent waveguides of this type will form the basis of future work.

The principal advantage of PBQPM (as is optical rotation QPM as we shall see in the next chapter) is the simplicity of the experimental set up: a single laser pulse correctly coupled into a birefringent waveguide. Other QPM techniques are likely to be limited by several factors: for pulse-train QPM, the number of ultrafast pulses which can be generated; the precision with which corrugated waveguides or gas jet arrays can be manufactured; or, for multi-mode QPM, different damping rates for the two waveguide modes. PBQPM does not suffer from these difficulties. As for any HHG scheme limits will be set by absorption of the harmonics and variation of the ionization level – and hence of the coherence length – within the driving pulse; and as for other techniques employing a waveguide, damping of the driving radiation may, in principle, limit the length over which harmonics will be generated. A potential limitation unique to PBQPM is dispersion of the two polarization components: the slower polarization will lag the faster one until the two polarization states separate and polarization beating ceases. In principle this limitation could be overcome by reversing the birefringence after the two polarization components have slipped significantly; the limits imposed by all these mechanisms will be explored in future work. Moreover, in our analysis we assumed that phase and polarisation of the driving pulse to remain constant, which may not necessarily be the case under experimental conditions.

Finally we note that it is also possible to achieve PBQPM in non-birefringent waveguides by exciting different-order waveguide modes with nonparallel polarizations. In this arrangement the different phase velocities of the modes will lead to polarization beating in addition to the beating of the intensity which is utilized in multi-mode QPM [97; 135]. Indeed, driving PBQPM with different-order waveguide modes increases the available parameter space and could allow higher-order harmonics to be quasi-phase-matched and greater efficiencies to be achieved, and we will explore this concept, as mentioned, in Chapter 7.

5.6 Conclusion

In this chapter, we have proposed a new method for quasi-phase-matching HHG – polarization-beating QPM (PBQPM) – in which polarization beating in a birefringent waveguide is employed to modulate the efficiency with which harmonics are generated. Quasi-phase-matching may then be achieved by suitably matching the period of polarization beating with the coherence length.

We have developed a theoretical model of PBQPM and used this to demonstrate that PBQPM can indeed enhance the intensity with which harmonics can be generated. This model was also used to explore the optimum coupling angle for PBQPM and to show that this depends on the harmonic order q.

In the next chapter, we will discuss a natural extension of PBQPM, where instead of linear birefringence, we explore what happens to QPM under circular birefringence. In the chapter after that, we will discuss how mode beating and polarisation beating are related, and in Chapter 10, we will discuss how spatial light modulators (SLMs) can be utilized to achieve mode beating in a hollow-core non-birefringence waveguide.

Chapter 6

Optical Rotation Quasi-Phase Matching

6.1 Introduction

In the previous chapter, we proposed a new QPM technique: polarization beating QPM (PBQPM) [70; 73]. In this approach, a linear birefringent system modulates the polarization of the driving pulse, causing it to beat between linear and elliptical. Because harmonic generation is suppressed for elliptically polarized light, QPM can be achieved if the period of the polarization beating is suitably matched to the coherence length. In this chapter, we discuss a novel, more efficient, QPM scheme that enables the generation of circularly polarized high harmonics: Optical Rotation Quasi Phase Matching (ORQPM) [71; 72]. ORQPM utilizes a waveguide with circular birefringence (as opposed to linear birefringence), which causes the plane of polarization of linearly polarized light to rotate with propagation distance at a constant rate, with period $2L_r$. By matching $L_r = L_c$, the generated harmonics will grow monotonically. As we show in detail below, ORQPM allows harmonics beyond the true phase-match limit to be generated with comparable efficiencies to that obtained with true phase-matching. Fig. 6.1 shows a schematic diagram

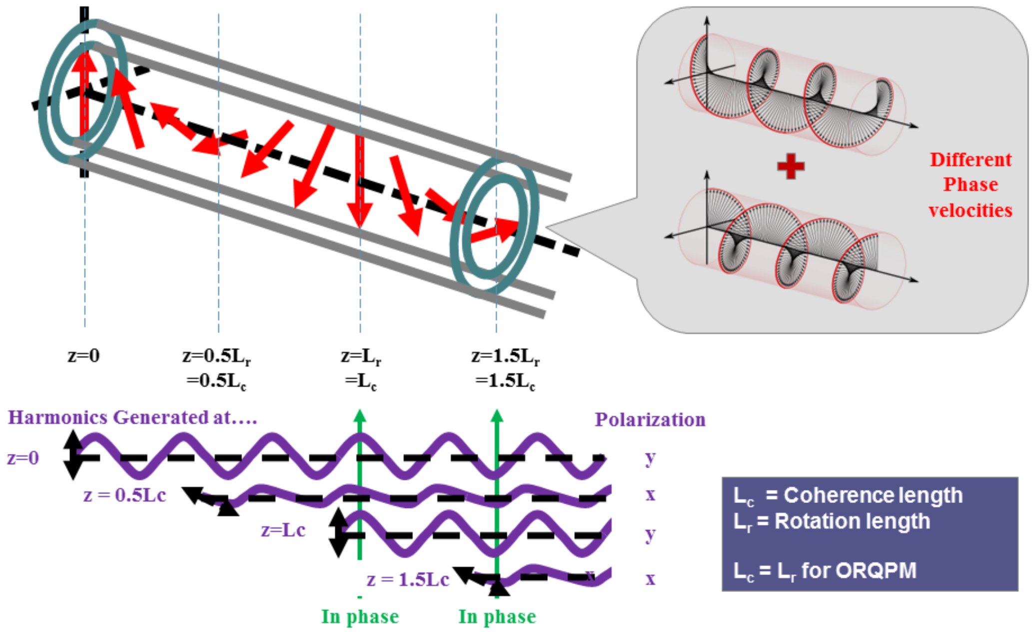

Figure 6.1: Cartoon schematic of ORQPM.

of ORQPM. We note that we will follow closely our discussion in our paper [72].

6.2 Circularly and elliptically polarised XUV and soft X-rays

ORQPM is the first QPM scheme to generate circularly polarized high harmonics; bright sources of circularly polarized soft x-radiation would find widespread application in studies of ultrafast spin dynamics [63] and nano-lithography [91]. We also note that a polarization gating technique in metallic macrostructures has been proposed to generate circuarly polarized high harmonics [55] and that phase matched circularly polarised harmonics have been achieved using counter-rotating circularly-polarized laser pulses[61]. Moreover, we note that that second harmonic generation quasi-phase matching has been previously achieved in an optically active solid media [21]. In this chapter we describe ORQPM in detail, demonstrate its operation by means of a simple model, and discuss three techniques by which it might be realized.

6.3 Theoretical Derivation

The driving electric field can be written as a linearly polarized wave with a plane of polarization that rotates with propagation along the z axes with period $L_r = \pi/\nu$, where ν is the optical rotation power:

$$\vec{E}_{\text{driver}}(z,t) = E_0 e^{i(\beta z - \omega t)} \begin{pmatrix} \cos(\nu z) \\ \sin(\nu z) \end{pmatrix}. \tag{6.1}$$

where $\beta = k(\omega)$ is the propagation constant and E_0 is the field amplitude. For the purpose of demonstrating ORQPM, we will assume that the damping of the driving radiation is negligible.

In the slowly-varying envelope approximation, the electric field of the qth harmonic can be written as:

$$\vec{E}_q(z,t) = \vec{\xi}(z,t) e^{i[k(q\omega)z - q\omega t]} \tag{6.2}$$

where $\vec{\xi}$ is the electric field envelope. The Rayleigh range of the harmonic beam will be approximately q times that of the driving beam; as such we will ignore the effect of the waveguide on the wave-vector $k(qw)$ of the harmonic beam. We note that in cases where $k(qw)$ is affected by the waveguide, ORQPM will still occur if there is a difference between the circular birefringence experienced by the driving and generated beams.

Under a continuous-wave approximation, the amplitude of the x- and y- components

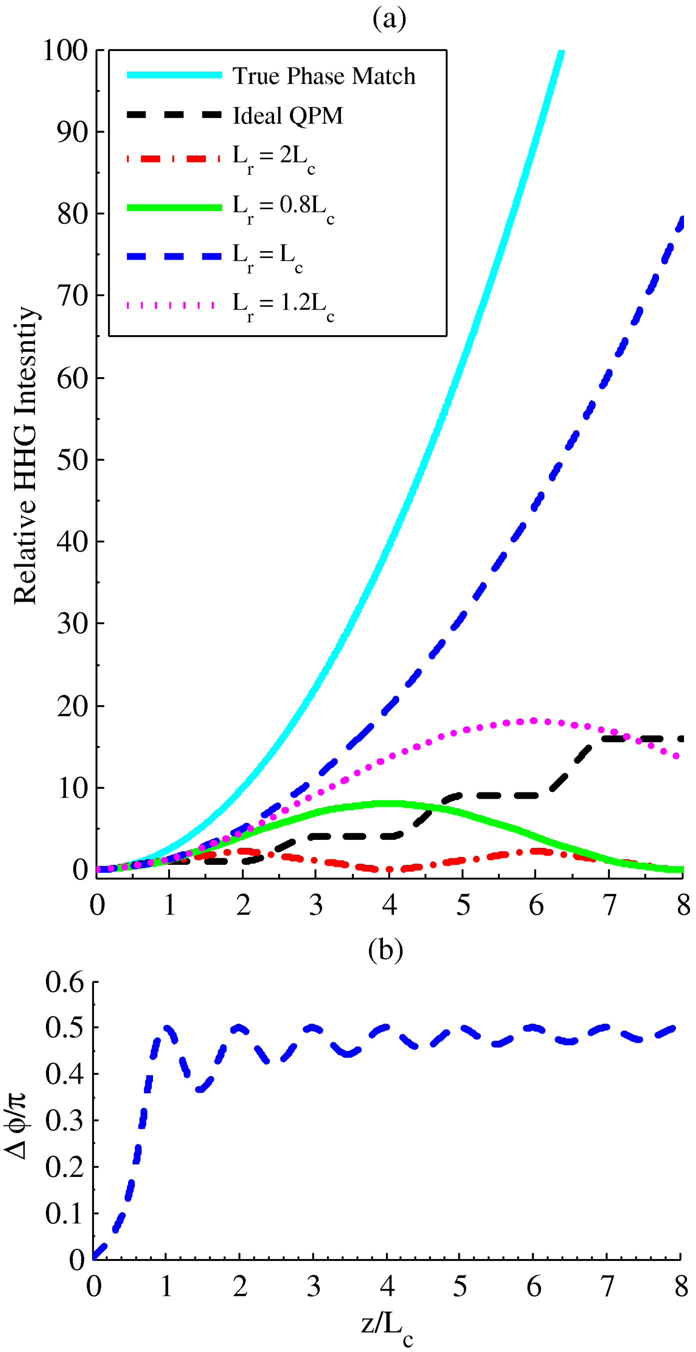

Figure 6.2: (a) Relative HHG intensity for true phase matching (solid cyan line), ideal QPM (dashed black line), and ORQPM for $L_r = 2L_c$ (dot-dashed red line), $0.8L_c$ (solid green line), L_c (dashed blue line), $1.2L_c$ (dotted pink line) normalized to the the output after a single coherence length with no phase matching. (b) Phase difference $\Delta\phi = \arg(\hat{\xi_x}) - \arg(\hat{\xi_y})$ between the x and y polarization components as a function of z for $L_r = L_c$.

of the harmonic envelope will grow according to,

$$\begin{cases} \frac{\partial \xi_x}{\partial z} = A\Gamma_x(z)e^{-i\Delta k z} \\ \frac{\partial \xi_y}{\partial z} = A\Gamma_y(z)e^{-i\Delta k z} \end{cases} \tag{6.3}$$

where A is a normalization constant, and Γ_x and Γ_y are the relative source terms. In this case the driving radiation has the same intensity at all points along the system, and is always linearly polarized. The locally generated harmonics will have a polarization parallel to that of the driving beam, and hence $\Gamma_x = \cos(\nu z)$ and $\Gamma_y = \sin(\nu z)$.

Assuming that A and Δk are constant, Eqn. (6.3) yields,

$$\begin{cases} \xi_x(z) = iA\frac{\Delta k - e^{i\Delta k z}[\Delta k \cos(\nu z) + i\nu \sin(\nu z)]}{\Delta k^2 - \nu^2} \\ \xi_y(z) = A\frac{-\nu + e^{i\Delta k z}[\nu \cos(\nu z) + i\Delta k \sin(\nu z)]}{\Delta k^2 - \nu^2} \end{cases} . \tag{6.4}$$

ORQPM corresponds to setting $\nu \to \Delta k$, whereupon,

$$\begin{cases} \hat{\xi}_x(z) = \lim_{\nu \to \Delta k} [\xi_x(z)] = A\frac{2\Delta k z - i + ie^{-2i\Delta k z}}{4\Delta k} \\ \\ \hat{\xi}_y(z) = \lim_{\nu \to \Delta k} [\xi_y(z)] = A\frac{-2i\Delta k z + 1 - e^{-2i\Delta k z}}{4\Delta k} \end{cases} . \tag{6.5}$$

From this the intensity, $\hat{I}(z) = \hat{\xi}_x \hat{\xi}_x^* + \hat{\xi}_y \hat{\xi}_y^*$ is found to be:

$$\hat{I}(z) = A^2 \left[\frac{1}{2} z^2 + \frac{1 - \cos(2\Delta k z)}{4(\Delta k)^2} \right] . \tag{6.6}$$

We see that the growth of the harmonic intensity comprises a quadratic term, which dominates at large z, plus a weak co-sinusoidal modulation. It is clear that in the limit of large z, ORQPM is half as efficient as would be true phase-matching — i.e. setting $\Delta k = 0$ — under otherwise identical conditions.

These analytical results are confirmed by the results of numerical integration of Eqn.

(6.3), as shown in Fig. 6.2. When properly matched, ORQPM causes the intensity of the harmonic to grow almost monotonically, and it may be seen that at large z that the intensity is half that which would be obtained with true phase-matching. Notice that with ORQPM the harmonic intensity grows $\pi^2/2 \approx 5$ times faster than ideal QPM, defined to be the square-wave modulation of the local harmonic generation with a period $2L_c$ and complete suppression of harmonic generation in the out of phase zones.

In Fig. 6.2(b) the phase difference between the two polarization states of the harmonic is illustrated; it is seen that after a few coherence lengths this phase difference is close to $\pi/2$, corresponding to circular polarization of the harmonic. This can also be seen in Eqn (6.5), where the dominating terms for the $x-$ and $y-$ components of the envelope function, $\frac{A}{2}z$ and $-\frac{iA}{2}z$ respectively, have the same amplitude but are $\pi/2$ out of phase, corresponding to circular polarization. For fixed t, the rotation with z of the plane of polarization of the harmonic radiation is in the same sense as that of the driving beam, i.e. right(left)-hand polarized harmonics are generated by right(left)-rotating driving radiation.

6.4 Experimental considerations

In order to achieve ORQPM in practise it would be necessary to guide a laser pulse over an extended region using a waveguide with circular birefringence that has a rotation length shorter than 1mm. Such a waveguide could be constructed in a number of ways. One possibility for achieving ORQPM is a waveguide constructed from a material with a high Verdet constant V, which would allow ORQPM to be achieved by tuning the applied magnetic flux density B until $\nu = VB = \Delta k$. We note that Verdet constants lie in the range 100 deg mm^{-1} T^{-1} to 10^5 deg mm^{-1} T^{-1} [62]. Solid-core waveguides exhibiting Faraday rotation have been developed,although the hollow-core systems which would be required for ORQPM have yet to be developed [133; 134].

Alternatively, the waveguide walls could be constructed from optically active materials, which have rotary powers in the range 10^2 to 10^4 deg mm^{-1} [57; 64]. Further, we note that polarization rotating photonic crystal fibres have been developed with $L_r < 1$mm [47] and that HHG has been acheived using PCFs [48].

Finally, we also note that ORQPM could be achieved in non-birefringent waveguides by exciting two circularly polarized waveguide modes with different mode velocities. The resultant superposition of these two modes will be linearly polarized with rotating polarization. Further exploration of circular birefringence waveguides will be conducted in Chapter 11.

As for any QPM scheme limits will be set by absorption of the harmonics and variation of the coherence length [85]. As for other QPM schemes based on polarization-control of the driving laser, the distance over which ORQPM can be achieved may be limited by relative slippage of the constituent polarizations similar to PBQPM discussed in the previous chapter. However, we note that in principle this limit can be avoided by reversing the rotation of the driving field when the two modes have slipped apart, although the polarization of the resultant harmonic field may no longer be perfectly circularly polarized. Finally, we point out that ORQPM may also be limited by chromatic despersion from either waveguide or Faraday effects.

6.5 Conclusion

In this chapter, we have proposed a novel QPM scheme for high harmonic generation that relies on rotation of the driving radiation using a circularly birefringent waveguide. By matching the rotation length to the coherence length, circularly polarized harmonics may be produced with an efficiency up to 50% of that obtained with true phase-matching and 5 times more efficient than conventional QPM. These findings were confirmed by numerical simulations. Three systems in which ORQPM might be achieved have been identified; exploration of these will form the basis of future work.

Chapter 7

Polarisation Beating Quasi-Phase Matching Using Mode Beating

7.1 Introduction

In Chapter 4 we outlined the idea of mode-beating where intensity and phase modulates if two or more modes are coupled into a waveguide. As discussed in Chapter 3, this can be employed for QPM – Multi-mode QPM (MMQPM), which relies on coupling in two or more waveguide modes [33; 97; 135]. If the two modes travel at different phase velocities, then the intensity will beat along the propagation length, thereby modulating harmonic generation resulting in QPM . In this chapter, we investigate the effect on HHG of the modulation in both the intensity *and* phase of the beating driving radiation. We show that under certain conditions, phase modulation due to mode beating enables harmonics to be generated with greater efficiency than ideal square-wave QPM modulation. Moreover we show that MMQPM is dominated by modulation of the phase, rather than the intensity, of the driving radiation — an effect which was not considered in the current group's earlier analysis [33; 97; 135].

In Chapter 5, we proposed a novel form of QPM based on modulation of the polarization state of the driving radiation within a hollow core waveguide [70; 71; 72; 73]. This chapter describes a generalization of MMQPM and PBQPM which combines these two schemes: multi-mode polarization beating quasi-phase matching (MMPBQPM), which utilizes beating between two waveguide modes to modulate the intensity, phase, and/or polarization of the guided radiation. These modulations can lead to QPM if the coherence length L_c of the harmonic generation is appropriately matched to the beat length, L_b, which is the distance it takes for the two modes to develop a phase difference of π. In addition to controlling the relative input polarizations of the two modes, the relative polarization angle between the two modes can also be controlled. This increased parameter space affords greater opportunities for QPM.

In addition we further analyze MMPBQPM using a Jacobi-Anger and Fourier decomposition which affords additional insight into the processes leading to QPM. Similar Fourier techniques used to analyze quasi-phase matching for HHG can be found in [14; 108].

The chapter is organized as follows: in Sec. 7.2, the equations for MMPBQPM are derived for two modes, Sec 7.3 presents the the Jacobi-Anger and Fourier analytical analysis, and Sec. 7.4 discusses numerical simulation results. Moreover, we note that this chapter is closely based on our paper in Ref [74].

7.2 Derivation of the Envelope Equation

7.2.1 Mode Propagation Equations

In this section, we develop the set of general mode propagation equations for two linearly polarized modes with azimuthal symmetry. If we assume that two modes are excited, then within the waveguide the electric field may written in cylindrical coordinates as,

$$\begin{aligned}\vec{\mathfrak{E}}(r,z) &= E_0\Big\{c_1\vec{E_1}(r)e^{i[(\beta_1+i\alpha_1)z-\omega t]} \\ &\quad + c_2\vec{E_2}(r)e^{i[(\beta_2+i\alpha_2)z-\omega t]}\Big\}\end{aligned} \tag{7.1}$$

where r is the radial coordinate from the propagation axes, $\vec{E_1}$ and $\vec{E_2}$ are the normalized transverse electric fields of the driving mode $m = 1$ and modifying mode $m = 2$ respectively, E_0 is the electric field amplitude constant, β_m and α_m are the propagation constant and damping rate of mode m, and ω is the angular frequency of the driving radiation.

Here, the polarizations of the modes $m = 1$ and $m = 2$ are respectively taken to be parallel to, and at an angle Ω, to the x-axis:

$$\vec{E_1}(r) = \begin{pmatrix} M_1(r) \\ 0 \end{pmatrix} \tag{7.2}$$

$$\vec{E_2}(r) = \begin{pmatrix} M_2(r)\cos(\Omega) \\ M_2(r)\sin(\Omega) \end{pmatrix} \tag{7.3}$$

where $M_m(r)$ is the normalized transverse electric field profile for the mth mode.

At time $t' = t + \Delta t$, where $\Delta t = -\beta_1/\omega z$, the electric field components are given by,

$$\begin{aligned}\Re\left[\begin{pmatrix} \mathfrak{E}_x \\ \mathfrak{E}_y \end{pmatrix}\right] &= E_0\begin{pmatrix} c_1M_1(r)\cos(\omega t') \\ 0 \end{pmatrix} \\ &\quad + E_0\begin{pmatrix} c_2M_2(r)\cos(\Omega)\cos(\omega t' + \Delta\beta z) \\ c_2M_2(r)\sin(\Omega)\cos(\omega t' + \Delta\beta z) \end{pmatrix}.\end{aligned} \tag{7.4}$$

where $\Delta\beta = \beta_1 - \beta_2$, and the beat length $L_b = \pi/(\Delta\beta)$.

From this, the values of t' corresponding to the maximum and minimum electric field amplitudes can be found, from which the ellipticity is given by,

$$\varepsilon(r,z) = \sqrt{\frac{\Re\{\mathfrak{E}[t'_{max}(r,z);r,z]\}^2}{\Re\{\mathfrak{E}[t'_{min}(r,z);r,z]\}^2}} \tag{7.5}$$

where $\Re[\mathfrak{E}]^2 = \Re[\mathfrak{E}_x]^2 + \Re[\mathfrak{E}_y]^2$, and the angle of the major axis is given by,

$$\Theta(r,z) = \tan^{-1}\left(\frac{\Re[\mathfrak{E}_y][t'_{max}(r,z);r,z]}{\Re[\mathfrak{E}_x][t'_{max}(r,z);r,z]}\right). \tag{7.6}$$

It is useful to note that the relative intensity of the driving wave at any given point is given as:

$$\begin{aligned} I(r,z) &= \mathfrak{E}_x(r,z)\mathfrak{E}_x^*(r,z) + \mathfrak{E}_y(r,z)\mathfrak{E}_y^*(r,z) && (7.7) \\ &\approx c_1^2M_1^2 + c_2^2M_2^2 \\ &\quad +2c_1M_1c_2M_2\cos(\Omega)\cos(\Delta\beta z) && (7.8) \end{aligned}$$

assuming that the damping terms are small. For the remaining of the chapter, we will focus on $r = 0$ and will define $M_1 = M_1(0)$, $M_2 = M_2(0)$ to simplify notation. Moreover, to simplify arguments, we will stipulate the following normalization condition: $c_1^2M_1^2 + c_2^2M_2^2 = 1$ where we have taken c_mM_m to be real, which can always be achieved by a suitable shift of the z or t coordinates.

7.2.2 Derivation of the growth equation

If we write the electric field of the qth harmonic as,

$$\vec{E} = \frac{1}{2}\vec{\xi}^{(q\omega)}e^{i[k(q\omega)z-q\omega t]} + \text{c.c} \tag{7.9}$$

then, within the slowly-varying envelope approximation, the equation for the growth of the amplitude of the qth harmonic becomes,

$$2ik(q\omega)e^{ik(q\omega)z}\frac{d\vec{\xi}^{(q\omega)}}{dz} = -\mu_0(q\omega)^2\vec{P}_{\mathrm{NL}}^{(q\omega)} \tag{7.10}$$

where $\vec{P}_{\mathrm{NL}}^{(q\omega)}$ is the component of the non-linear polarization oscillating with angular frequency $q\omega$. Now, $\vec{P}_{\mathrm{NL}}^{(q\omega)} = \vec{F}'(I,\epsilon)e^{iq\phi_p(z)}$, where $\vec{F}'(I,\epsilon)$ gives the dependence of the non-linear response on the intensity and ellipticity of the driving field, and $\phi_p(z)$ is the phase of the driving field of the pth polarization component. We may write $\phi_x(z) = k_1(\omega)z+\psi_x(z)$ and $\phi_y(z) = k_2(\omega)z+\psi_y(z)$, where $\psi_p(z)$ is the additional phase arising from interference of the waveguide modes and $k_m(\omega) = \beta_m(\omega)$ is the waveguide propagation constant for the driving pulse. Henceforth all equations will refer to the qth harmonic, and so in order to avoid clutter we will drop the (qw) superscripts. The growth equation for the amplitude of the harmonic for the x- and y- components may then be written in the form,

$$\frac{d\xi_x}{dz} = F_x(I,\varepsilon)e^{-i\Delta k_1 z}e^{i\psi_x(z)} = \mathfrak{P}_x\left|\vec{F}\right|e^{+i\Psi_x(z)} \tag{7.11}$$

$$\frac{d\xi_y}{dz} = F_y(I,\varepsilon)e^{-i\Delta k_2 z}e^{i\psi_y(z)} = \mathfrak{P}_y\left|\vec{F}\right|e^{+i\Psi_y(z)} \tag{7.12}$$

where Ψ_x and Ψ_y are the total phase for the x- and y- components respectively; $\vec{\mathfrak{P}}$ is a projection term that relates the nonlinear polarization to x- and y- components of the envelope function, as developed below; $\Delta k_m = k(q\omega) - qk_m(\omega)$; and $\vec{F}(I,\epsilon) = i\mu_0(q\omega)^2\vec{F}'(I,\varepsilon)/2k(q\omega)$. We note that, as discussed below, $\vec{F}(I,\varepsilon)$ is in general complex since the phase of the nonlinear polarization depends on the trajectory of the ionized electron, and therefore on both the intensity and ellipticity of the driving field. In the equation above, we have factored these phase terms into Ψ_x and Ψ_y.

Considering first the x-polarization, the driving field may be written as,

$$\begin{aligned} E_x(\vec{r}, z, t) &= \left[c_1 M_1 + c_2 M_2 \cos\Omega e^{-i\Delta\beta z}\right] e^{i(\beta_1 z - \omega t)} \\ &= u_x(z) e^{i(\beta_1 z - \omega t)} \end{aligned} \tag{7.13}$$

where $\Delta\beta = \beta_1 - \beta_2$. Hence we find,

$$\begin{aligned} \psi_x(z) &= \arg[u_x(z)] \\ &= \tan^{-1}\left[\frac{-c_2 M_2 \cos\Omega \sin(\Delta\beta z)}{c_1 M_1 + c_2 M_2 \cos\Omega \cos(\Delta\beta z)}\right] \\ &\approx -\frac{c_2 M_2}{c_1 M_1} \cos\Omega \sin(\Delta\beta z) \end{aligned} \tag{7.14}$$

where in the last step, the approximation is valid if $|c_1| \gg |c_2|$. Similar considerations show that $\psi_y = 0$ and $\phi_y(z) = \beta_2$.

The strength of the nonlinear polarization, $|\vec{F}(I, \epsilon)|$, depends on the intensity and polarization of the driving laser field. Evaluation of $|\vec{F}(I, \epsilon)|$ requires a model of the interaction of the driving field with the atom, as, for example, developed by Lewenstein et al. [68]. However, for our purposes it is sufficient to assume that the amplitude of the nonlinear polarization, $\left|\vec{F}\right|$ can be written in the form:

$$\left|\vec{F}[I(z), \varepsilon(z)]\right| = AG[I(z)]H[\varepsilon(z)] \tag{7.15}$$

where $A \propto \mu_0 (q\omega)^2 / 2k(q\omega)$ is a constant, $G[I(z)]$ is the intensity-dependent term ranging from $[0, 1]$, and $H[\varepsilon(z)]$ is the ellipticity-dependent term ranging from $[0, 1]$.

For the purposes of illustrating the operation of MMPBQPM it is sufficient to assume that the intensity-dependent term takes the form of a power law $G(I) \approx I^{\eta/2}$. We will assume $\eta \approx 6$, in accordance with earlier work [7; 8; 33]; but note that the the broad conclusions of the present chapter do not depend strongly on the value of η.

It is also well known that the single-atom efficiency of HHG depends sensitively on the polarization of the driving laser field [20] which arises from the fact that the ionized electron must return to the parent ion in order to emit a harmonic photon. Following the argument given in Chapter 5 and in [73], for a given driving intensity the number of harmonic photons generated as a function of ellipticity maybe approximated by:

$$h(\varepsilon) \approx \left(\frac{1+\varepsilon^2}{1-\varepsilon^2}\right)^{\mu} \tag{7.16}$$

where $H(\varepsilon) = \sqrt{h(\varepsilon)}$.

As per Chapter 5, it is predicted that $\mu = q - 1$ within the perturbative regime, as verified [20] by Budil et al. for harmonics $q = 11$ to 19, and by Dietrich et al. for harmonics up to $q \approx 31$ [31]. Schulze et al. found that for higher-order harmonics the sensitivity of harmonic generation to the ellipticity of the driving radiation is lower than predicted by Eqn (7.16) with $\mu = q - 1$ [104], although in this non-perturbative regime the efficiency of harmonic generation still decreases with ε. Further measurements of the dependence of harmonic generation on ε have been provided by Sola et al. [110]. It is recognized that Eqn (7.16) is an approximation, but it will serve our purpose of demonstrating the operation of MMPBQPM.

The offset angle and ellipticity of the harmonics generated by elliptically-polarized radiation have been shown to depend on the ellipticity and intensity of the driving radiation, and on the harmonic order [7; 8; 77; 104; 112]. Propagation effects can also play an important role. Since the amplitude with which harmonics are generated decreases strongly with increasing ellipticity, we are most interested in the ellipticity of the harmonics generated for small ε. It has been shown that for higher-order harmonics, and/or high driving intensities, both the ellipticity and change in ellipse orientation of the harmonics generated by radiation with $\varepsilon \approx 0$ are close to zero [8]. We will therefore make the simplification that the generated harmonics are linearly polarized along the major axis of the driving radiation and that we resolve separately the harmonics polarized along the fast and slow axes of the waveguide. Thus, the projection term may be written as:

$$\vec{\mathfrak{P}}(z) = \begin{pmatrix} \cos[\Theta(z)] \\ \sin[\Theta(z)] \end{pmatrix}, \tag{7.17}$$

and by following the arguments of [73], the coherence lengths for harmonics polarized parallel to the x- and y- axes are different, and hence for a given L_b it is only possible to quasi-phase-match one of these components. Thus, for the remainder of this chapter, we will focus on analyzing the harmonics polarized along the x-axis. Therefore, we can approximate $I_q = \xi_x \xi_x^* + \xi_y \xi_y^* \approx \xi_x \xi_x^*$.

Moreover, the phase of the nonlinear polarization depends on the intensity of the driving radiation [67; 107] and its ellipticity [8; 112]. We will ignore the effect of ellipticity on the phase of $\vec{F}(I, \epsilon)$ since, as shown below, harmonic generation is dominated by those regions in which the driving radiation is close to linear polarization. We may write the intensity-dependent phase as a Taylor expansion around I_0,

$$\begin{aligned} \Phi(I) &= \Phi(I_0) + \left.\tfrac{d\Phi}{dI}\right|_{I_0} (I - I_0) + \ldots & (7.18) \\ &\approx \Phi_0 + \nu q\, (I - I_0)\,. & (7.19) \end{aligned}$$

where $\nu = d\Phi/dI|_{I_0}$. For simulations in this chapter, we assume $\nu/q \approx 0.2\,\mathrm{rad}/10^{14}\mathrm{W\,cm^{-2}}$ based on previous calculations [107].

We may now gather the contributions to the total phase $\Psi_x(z)$:

$$\begin{aligned} \Psi_x(z) &= -\Phi(I_0) - \Delta k_1 z + q\psi_x(z) - q\nu\,(I - I_0) & (7.20) \\ &\approx \Psi_0 - \Delta k_1 z - q\frac{c_2 M_2}{c_1 M_1} \cos\Omega \sin(\Delta\beta z) & (7.21) \\ &\quad -2q\nu c_1 M_1 c_2 M_2 \cos\Omega \cos(\Delta\beta z) & (7.22) \end{aligned}$$

where $\Psi_0 = -\Phi(I_0) - 2q\nu c_1 M_1 c_2 M_2 \cos\Omega$, and the approximation holds if $|c_2| \ll |c_1|$. From Eqns. (7.12) and (7.22), we can rewrite the the differential equation for the x-component as:

$$\frac{d\xi_x}{dz} = \cos[\Theta(z)]\,|F[I(z),\varepsilon(z)]|\,e^{+i\Psi_x(z)} \tag{7.23}$$

$$= A'\Gamma(z)e^{-i\Psi'_x(z)} \tag{7.24}$$

where

$$A'(z) = Ae^{+i\Psi_0} \tag{7.25}$$

$$\Gamma(z) = \cos[\Theta(z)]\,|F[I(z),\varepsilon(z)]| \tag{7.26}$$

$$\Psi'_x(z) = -\Psi_x(z) + \Psi_0 \tag{7.27}$$

$$= \Delta k_1 z + \gamma\sin(\Delta\beta z) + \rho\cos(\Delta\beta z) \tag{7.28}$$

in which $\gamma = q\frac{c_2 M_2}{c_1 M_1}\cos\Omega$ is the mode interference phase term and $\rho = 2q\nu c_1 M_1 c_2 M_2 \cos\Omega$ is the intensity-dependent phase term.

7.3 Analysis of the Growth Equation

7.3.1 Phase Analysis using the Jacobi-Anger Expansion

The exponential term in Eqn (7.24) can be expanded into the products of two infinite sums using the Jacobi-Anger Expansion:

$$e^{-i\Psi'_x(z)} = e^{-i\Delta k_1 z}\left[\sum_{l=-\infty}^{+\infty} i^l J_l(-\rho)e^{+il\Delta\beta z}\right] \times \left[\sum_{j=-\infty}^{+\infty} J_j(-\gamma)e^{+ij\Delta\beta z}\right] \tag{7.29}$$

where J_l and J_j are Bessel functions of the first kind and $l, j \in \mathbb{Z}$. It is insightful to factor terms of constant $\sigma = l + j$ to give:

$$e^{-i\Psi'_x(z)} = e^{-i\Delta k_1 z} \sum_{\sigma=-\infty}^{\infty} U_\sigma e^{i\sigma\Delta\beta z} \tag{7.30}$$

where

$$U_\sigma = \sum_{l+j=\sigma} i^l J_l(-\rho) J_j(-\gamma). \tag{7.31}$$

We see that the modulation caused by intensity dependent phase and mode beating can be resolved into harmonics $\sigma\Delta\beta$ of the difference in spatial frequency $\Delta\beta$ of the two modes.

7.3.2 Source Amplitude Spatial Fourier Analysis

The analysis above suggests that it would be useful to write the source modulus Γ as a superposition of Fourier components with frequency $\kappa\Delta\beta$ (with $\kappa \in \mathbb{Z}$). For periodic modulation of the driving radiation, the source modulus can be written as a Fourier series:

$$\Gamma(z) = \sum_{\kappa=-\infty}^{\infty} V_\kappa e^{i\kappa\Delta\beta z} \tag{7.32}$$

and hence the growth differential equation can be written as:

$$\frac{1}{A'} \frac{d\xi_x}{dz} = e^{-i\Delta k_1 z} \sum_{\sigma,\kappa\in\mathbb{Z}} U_\sigma V_\kappa e^{i(\sigma+\kappa)\Delta\beta z}. \tag{7.33}$$

The terms that contribute to monotonic harmonic growth are those for which the phase is stationary, in other words, $\frac{\partial \Psi_x}{\partial z} = 0$. This implies that for QPM we require

$\Delta k_1 = (\sigma + \kappa)\Delta\beta$. We see that the harmonics of the modulation frequency allow QPM of larger wave vector mismatch Δk or, equivalently, of shorter coherence lengths $L_{c,1}$. The fundamental modulation spatial frequency $\Delta\beta$ has a period $2L_b = 2\pi/\Delta\beta$, and hence we may write the QPM condition as $L_b = (\sigma + \kappa)L_{c,1} = nL_{c,1}$, where $n = \sigma + \kappa$ is the order of the QPM process. Factoring all the terms contributing to monotonic harmonic growth, and ignoring the oscillating terms, the growth equation becomes:

$$\frac{1}{A'}\frac{d\xi_x}{dz} \approx \sum_{\sigma+\kappa=n} U_\sigma V_\kappa \tag{7.34}$$

for a fixed n, keeping in mind that each of the terms of the sum is complex and may have different signs. Eqn (7.34) can easily be solved, from which the harmonic intensity is found to be:

$$I_q \approx \frac{1}{2}A'Sz^2 \tag{7.35}$$

where $S = \sum_{\sigma+\kappa=n} U_\sigma V_\kappa$. It is useful to note that the σ and κ terms result from phase and intensity modulation of the driver respectively.

7.4 Simulation Results

7.4.1 Detailed simulations for $L_b = 2L_{c,1}$ and $L_b = L_{c,1}$

To test these ideas, we have conducted a series of simulations. Figure 7.1 presents the results of simulations for $L_b = 2L_{c,1}$ ($n = 2$) and three values of Ω and c_2M_2 for $q = 51$ while Figure7.2 presents the same parameters for $L_b = L_{c,1}$ ($n = 1$), $\Omega = 0^o$ and two different values of c_2M_2 for $q = 51$. These values are compared against ideal QPM, which is defined by the square wave modulation between zero and one of the harmonic generation with a period of $2nL_{c,1}$.

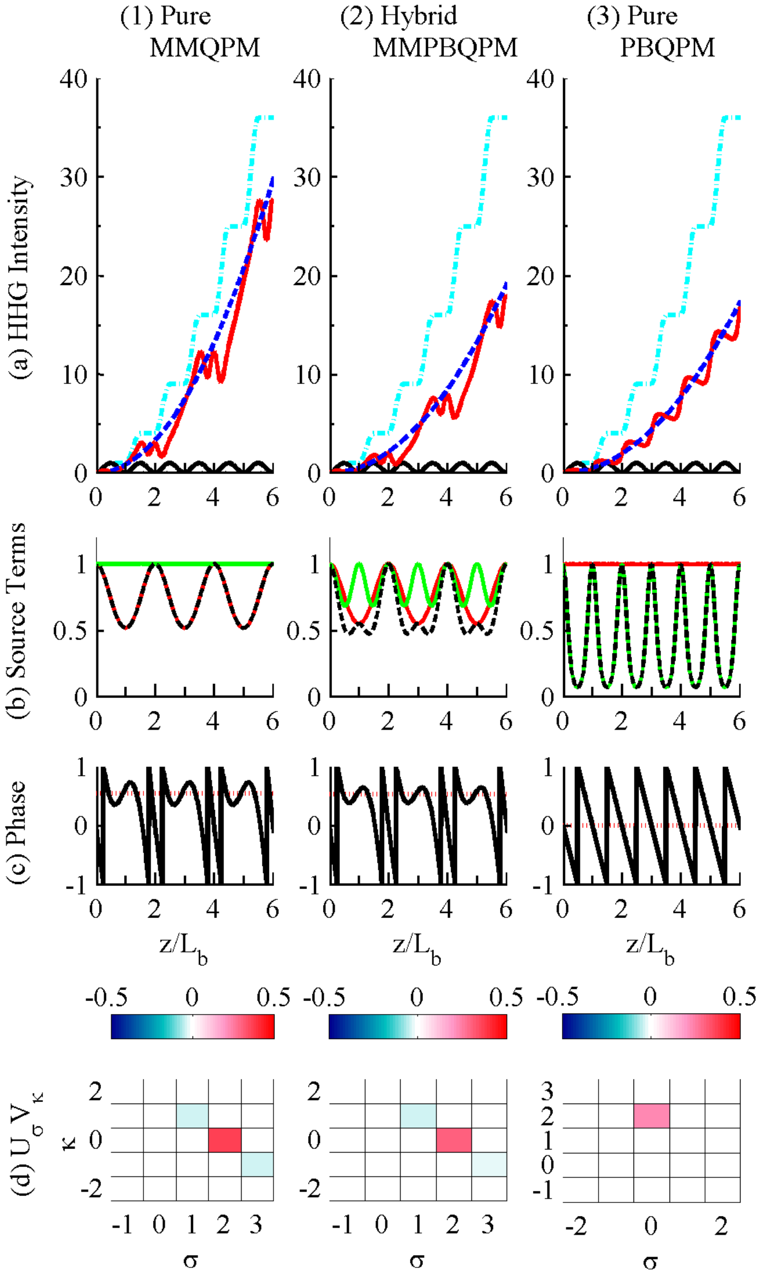

Figure 7.1: Simulation results for Columns - (1) "Pure MMQPM" ($c_2M_2 = 0.002$, $\Omega = 0^o$) (2) "Hybrid MMPBQPM" ($c_2M_2 = 0.01$, $\Omega = 60^o$), and (3) "Pure PBQPM" ($c_2M_2 = 0.05$, $\Omega = 90^o$); all for $L_b = 2L_c$ and $q = 51$. Row (a) shows the relative HHG intensity. Dot dashed cyan line shows ideal square wave QPM, solid red line shows the indicated form of MMPBQPM, solid black line shows the intensity for no phase matching, and the dashed blue line shows the harmonic intensity calculated from Eqn (7.35). Row (b) shows the modulus of the intensity-dependent source term $G[I(z)]$ (solid red line), ellipticity-dependent source term $H[\varepsilon(z)]$ (solid green line), and the combined source terms $|F| = GH$ (dashed black line). Row (c) shows $\Psi_x(z)$, the total phase of $d\xi_x/dz$ (solid black line) and Ψ_x for large z (dotted light red line). Row (d) shows the $U_\sigma V_\kappa$ distribution as a function of σ and κ for $n = \sigma + \kappa$ for $n = 2$

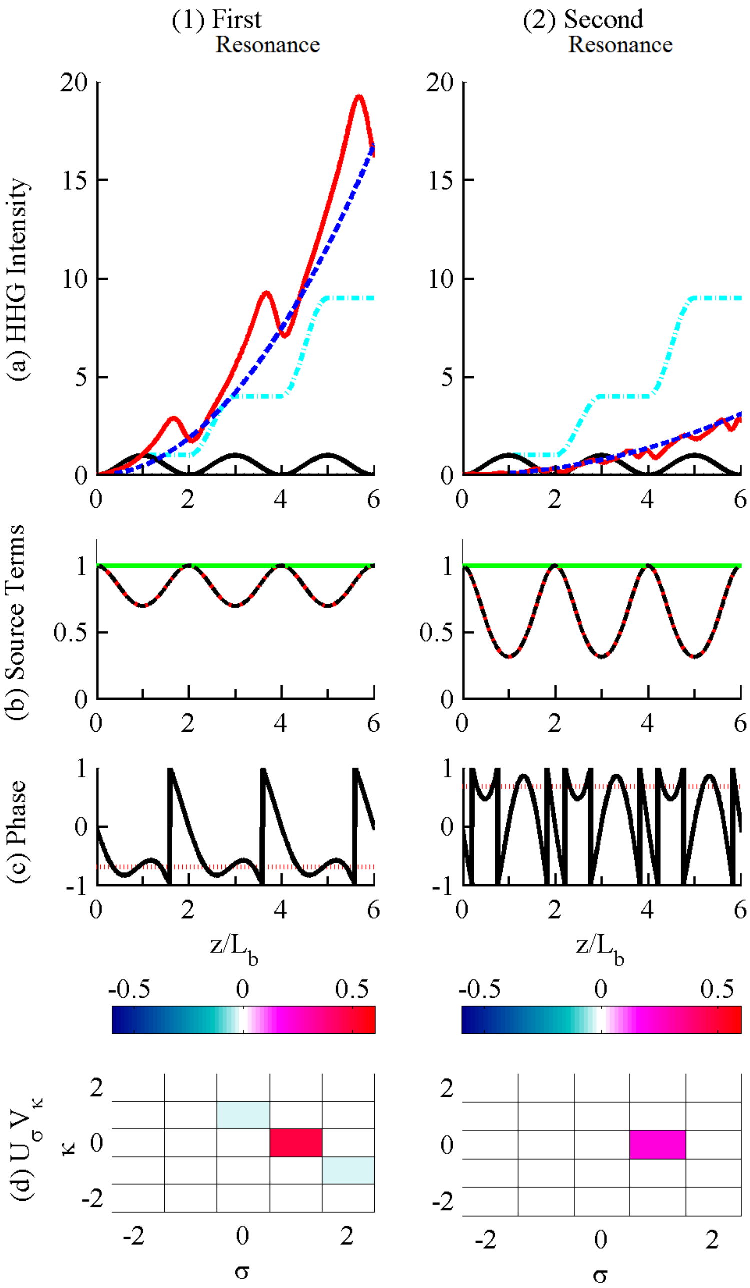

Figure 7.2: Simulation results for Columns - (1) the first resonance ($c_2M_2 = 0.0009$, $\Omega = 0^o$) and (2) the second resonance ($c_2M_2 = 0.0091$, $\Omega = 0^o$); all for $L_b = L_c$ and $q = 51$. Row (a) shows the relative HHG intensity. Dot dashed cyan line shows ideal square wave QPM, solid red line shows the indicated form of MMPBQPM, solid black line shows the intensity for no phase matching, and the dashed blue line shows the harmonic intensity calculated from Eqn (7.35). Row (b) shows the modulus of the intensity-dependent source term $G[I(z)]$ (solid red line), ellipticity-dependent source term $H[\varepsilon(z)]$ (solid green line), and the combined source terms $|F| = GH$ (dashed black line). Row (c) shows $\Psi_x(z)$, the total phase of $d\xi_x/dz$ (solid black line) and Ψ_x for large z (dotted light red line). Row (d) shows the $U_\sigma V_\kappa$ distribution as a function of σ and κ for $n = \sigma + \kappa$ for $n = 1$.

When $\Omega = 0^o$ MMPBQPM is equivalent to "pure MMQPM" since the driving radiation remains linearly polarized at all points within the waveguide; this is seen in Figure7.1-Col (1) where Figure7.1-(1)(b) indicates that modulation of the source term arises from mode-beating alone.

When $\Omega = 90^o$, MMPBQPM is equivalent to PBQPM since the mode beating causes the polarization of the driving radiation to beat in an analogous way to PBQPM driven by a linearly polarized beam propagating in a birefringent waveguide. This is seen in Figure 7.1-Col (3). More specifically, as seen in Figure 7.1- (3)(b), the modulation of the source term is seen to arise from solely polarization beating. It should be noted that for $\Omega = 90^o$ the simulations presented here agree with earlier calculations of PBQPM [73]. For intermediate values of Ω (such as in Col (2) where $\Omega = 60^o$), modulation of both the intensity and polarization of the driving radiation play a role in QPM.

Figure 7.1 also compares the growth of the calculated harmonic intensity with the approximation of Eqn. (7.35). It can be seen that the approximation agrees closely with the exact calculation, indicating clearly the dominant role played by the terms for which $\sigma + \kappa = n = 2$ as seen in Figure 7.1 - Row (a).

Moreover, Figure7.1 - Row (d) maps the values of $U_\sigma V_\kappa$, modulus phase (the terms in the sum in Eqn (7.34)), as a function of σ and κ where $\sigma + \kappa = n$ for a fixed $n = 2$. Hence, only where $\sigma + \kappa = 2$ is $U_\sigma V_\kappa$ is nonzero. For the case of Pure MMQPM, Col (1), and Hybrid MMPBQPM, Col (2), the dominant contributing term is $(\sigma, \kappa) = (2, 0)$ indicating that QPM arises predominantly from phase modulation of the driver, not intensity modulation. This can also be seen in Figure 7.1-1c and Figure 7.1-2c where the regions of harmonic growth occur for points where the phase Ψ_x is within $\pi/2$ of the phase of ξ_x for large z. In contrast, for the case of Pure PBQPM, Figure 7.1 - Col(3), the dominant term is $(\sigma, \kappa) = (0, 2)$. This suggests, as expected, that for Pure PBQPM, phase modulation does not contribute to QPM but only the modulation of the amplitude of the source term caused by caused by polarization beating.

Figure 7.2 presents the same parameters in Figure 7.1 for $n = 1$ (or $L_b = L_{c,1}$), for two different values of c_2M_2 and $\Omega = 0^0$. We see that for both columns, the only terms which contribute are those for which $\sigma + \kappa = 1$, as expected. For Col (1), optimal MMQPM enables harmonics to be generated with intensities greater than for ideal square wave QPM. As indicated in Figure 7.2-(1)(c), the region of harmonic growth coincides with Ψ_x being within $\pm\pi/2$ of the phase of ξ_x for large z . Moreover, the largest contributing term of $U_\sigma V_\kappa$ in Figure 7.2-(1)(d) is $(\sigma, \kappa) = (1, 0)$; this suggests that QPM is caused primarily by phase modulation, and not by amplitude modulation as reported earlier for MMQPM [33; 97; 135]. Moreover, the phase modulation explains why higher growth than ideal square-wave QPM occurs. Figure 7.2 - Col (2) shows the output at a different mode mix where $c_2M_2 = 0.0091$ and $c_1M_1 = 0.9909$. As discussed below, the mode mixtures for which results are shown in Fig 7.2 correspond to two of the peaks in a plot of the output of harmonic $q = 51$ as a function of c_1M_1 and c_2M_2.

7.4.2 Parameter Space Scans

This section presents a series of parameter space scans for optimizing the harmonic generation by MMPBQPM. In an HHG experiment, pressure, coupling angle Ω, and the mode mix ratio of c_1 to c_2 are parameters that can be adjusted. Pressure tuning equates to tuning the coherence length, or tuning the ratio $L_b/L_{c,1}$ assuming that L_b is fixed for a specific pair of driving and modifying modes.

Figure 7.3a shows, for the MMQPM case ($\Omega = 0^o$), the variation of the harmonic output as a function of $L_b/L_{c,1}$ and mode mix c_2M_2. Note that here the magnitude of the harmonic amplitude, not intensity, is plotted in order to show more clearly the variation of the harmonic output. As expected, MMQPM is optimized for integer n. Moreover, the peaks shift to increasing c_2M_2 with increasing n. When $n = 1$, the QPM

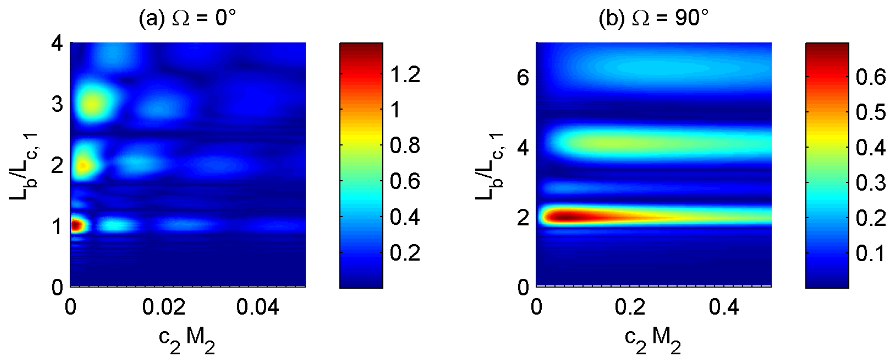

Figure 7.3: Relative HHG amplitude $|\xi_x(z)|$ for $q = 51$ at large z ($z = 10L_{c,1}$) as a function of $L_b/L_{c,1}$ and $m = 2$ mode coupling strength $c_2^2M_2^2$ where $c_1^2M_1^2 = 1 - c_2^2M_2^2$, normalized to ideal square wave QPM for: (a) $\Omega = 0^o$, and (b) $\Omega = 90^o$.

condition becomes $\sigma + \kappa = l + j + \kappa = 1$. The three lowest-order solutions satisfying this condition are $\{l, j, \kappa\} = \{1, 0, 0\}, \{0, 1, 0\}$, and $\{0, 0, 1\}$. We therefore expect peaks in the HHG intensity to occur for values of c_2M_2 corresponding to peaks in $|J_1(-\rho)J_0(-\gamma)|$, $|J_0(-\rho)J_1(-\gamma)|$, or $|J_0(-\rho)J_0(-\gamma)|$. The maxima along the line $L_b/L_{c,1}$ shown in Fig 7.3a arise from the variations of c_2M_2 which optimize the functions of $|J_l(-\rho)J_j(-\gamma)|$.

When $n = 2$, $\sigma + \kappa = l + j + \kappa = 2$, and the three lowest order terms are $\{1, 1, 0\}$, $\{0, 1, 1\}$, or $\{1, 0, 1\}$. Thus the values of optimal for c_2M_2 will be around the extrema of $|J_1(-\rho)J_1(-\gamma)|$, $|J_0(-\rho)J_1(-\gamma)|$, $|J_1(-\rho)J_0(-\gamma)|$. Because the positions of the local extremas of the Bessel function increase with increasing $|l|$ or $|j|$, optimal ρ and γ and thus optimal c_2M_2 will increase as well. Therefore, increasing n will result in larger values of $|l|$ and $|j|$ contributing to the harmonic growth corresponding to the Bessel function peaks shifted to higher values of $(-\rho)$ and $(-\gamma)$ and hence higher values of c_2M_2.

Similarly, Figure 7.3b shows the PBQPM case where $\Omega = 90^0$. As discussed in [73], PBQPM will occur when $L_b = nL_{c,1}$ and n is even – as is evident in Figure 7.3b. Since $\Omega = 90^o$, $\rho = \gamma = 0$, and since $J_l(0)J_j(0) = 0$ unless $l = j = 0$, monotonic harmonic growth can only occur for $\sigma = l + k = 0$. Hence optimal PBQPM occurs when the Fourier coefficient V_k is large for even κ. Furthermore, PBQPM does not contribute to any phase modulation because $\sigma = 0$ as seen from Eqn (7.30). The optimal value of c_2M_2 increases

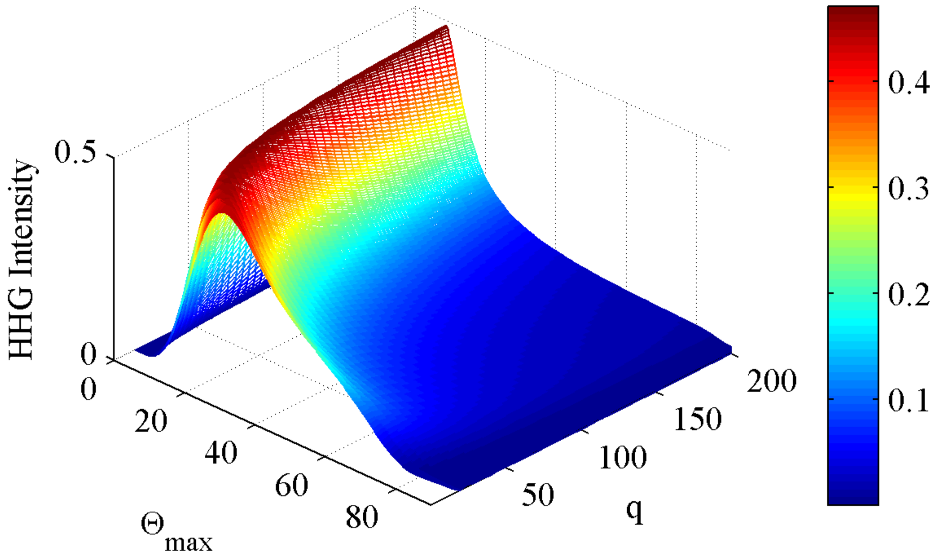

Figure 7.4: Relative HHG intensity at $z = L_b$ for $L_b = 2L_{c,1}$ as a function of $\Theta_{max} = \tan^{-1}\left(\frac{c_2 M_2}{c_1 M_1}\right)$ and q, normalized to ideal QPM.

with the order n of QPM since increasing this parameter shifts the Fourier spectrum of the driving intensity modulations to higher orders. The optimal value of $c_2 M_2$ is explored more clearly in Figure 7.4, which shows the normalized harmonic intensity for $\Omega = 90^o$ as a function of the harmonic order q and the maximum angle $\Theta_{max} = \tan^{-1}\left(\frac{c_2 M_2}{c_1 M_1}\right)$ the major axis of the elliptical driving radiation makes with the x-axis. If Θ_{max} is too close to 0^o, then the ellipticity modulation is not enough to suppress the destructive zones. If Θ_{max} is too close to 90^o, then the harmonic generation suppression zone is too large to create efficient harmonics.

Figure 7.5 plots, for the cases $L_b = L_{c,1}$ and $L_b = 2L_{c,1}$, the calculated relative amplitude at $z = 2L_b$ of the $q = 51$ harmonic as a function of Ω and the relative intensity of the $m = 2$ mode. In the case of Figure 7.5a, $L_b = L_{c,1}$, the relative amplitude achieved with "pure MMQPM" (i.e. $\Omega = 0$) is greater than that of ideal square wave QPM as explained above. For $\Omega = 0^o$, the intensity oscillates with increasing $c_2 M_2$, with the size of the resonant peaks decreasing with increasing $c_2 M_2$. These resonance peaks are

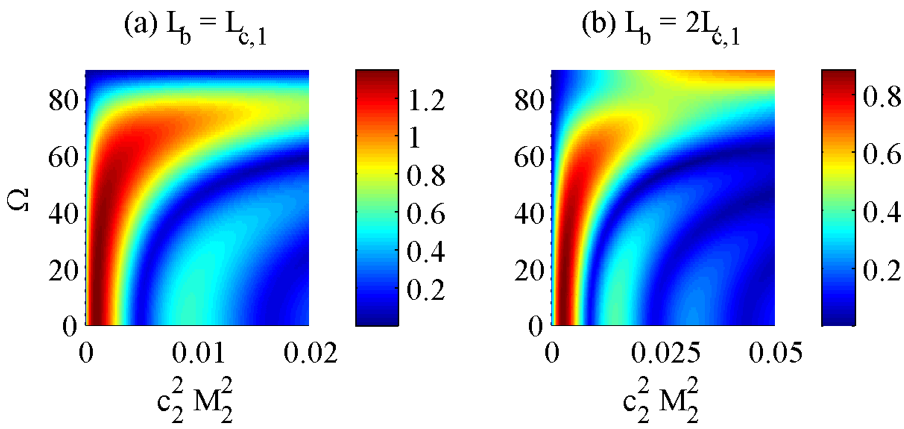

Figure 7.5: Relative HHG amplitude for $q = 51$ after $2L_b$ as a function of coupling angle Ω and $m = 2$ mode coupling strength $c_2^2 M_2^2$ where $c_1^2 M_1^2 = 1 - c_2^2 M_2^2$, normalized to ideal QPM for: (a) $L_b = L_{c,1}$, and (b) $L_b = 2L_{c,1}$.

caused by peaks of the products $J_l(-\rho)J_j(-\gamma)$ with ρ and γ being a linear function of c_2M_2 (for small c_2M_2) as explained above. For the case of pure PBQPM, i.e. $\Omega = 90^o$ and $L_b = L_{c,1}$, the harmonic intensity is seen to be very low and almost independent of the relative intensity of the two modes since the phase-matching condition for lowest-order PBQPM is not satisfied, and QPM is not achieved.

Lowest-order QPM occurs for $n = 2$, as shown in Fig 7.5b, a region of bright harmonic generation occurs for $\Omega = 90^o$ and $c_2M_2 \approx 0.04$. When $\Omega = 0^o$ the harmonic intensity oscillates in a similar manner to that observed in Figure 7.5a.

7.5 Conclusion

We have developed a generalized analysis of MMQPM and PBQPM together with a simplified Fourier analysis which gives additional insights into the dominant contributions of quasi phase-matching. In addition we have shown that PBQPM could be achieved without a birefringent waveguide by exciting a pair of waveguide modes with two orthogonal polarizations.

Our analysis of MMQPM showed, in contrast to the group's earlier analysis [33; 135], that QPM is dominated by the modulation of phase of the harmonic source term, not of its amplitude. This allows, under optimal conditions, MMQPM to generate harmonics with an intensity greater than possible with ideal, square-wave QPM.

We note that this analysis can be readily modified for the circular birefringence case, where two circular polarisation states, one left-handed, one right-handed, with different phase velocities can result in optical rotation. Moreover, this analysis can also be carried out for three or more modes, which may be more realistic under experimental conditions.

In the next chapter, we generalize our Fourier analysis idea to random phase matching. Finally, we note that MMPBQPM is just one way of achieving PBQPM. In the next Chapters 9 and 10, we discuss how might one achieve mode control using a spatial light modulator. In Chapter 11, we will discuss using birefringence waveguides as a method for achieving PBQPM or ORQPM.

Chapter 8

Random Phase Matching

8.1 Introduction

In the previous three chapters we described a novel QPM technique involving the control of modes and polarisation states. In this chapter, we will focus on a potential way of getting around the phase-mismatch problem called random phase matching. Some initial simulations of random quasi-phase matching of high harmonic generation have been performed by the Murnane Group; Bahabad et al. have shown that random QPM may result in a wider harmonic spectrum and that it may be a way of enhancing harmonic generation by a few orders of magnitude [13]. Random QPM, as defined by Bahabad et al. is random spacing of the on and off zones of harmonic generation. Figure 8.1 shows the simulated harmonic spectrum and theoretical enhancement versus square-wave QPM from Bahabad et al. Work prior has focused on random QPM for broad spectrum second harmonic generation [95] and for three wave mixing in bulk polycrystalline isotropic nonlinear materials [16]. Figure 8.2 shows the schematic for random QPM in Ref [16] where the author considers discrete grains in random phases contributing to output field strength growth on order $\sqrt{\mathcal{N}}$ where $\mathcal{N}$ here is the number of grains. In particular [16] provides a discrete model for random QPM, which we develop independently below for

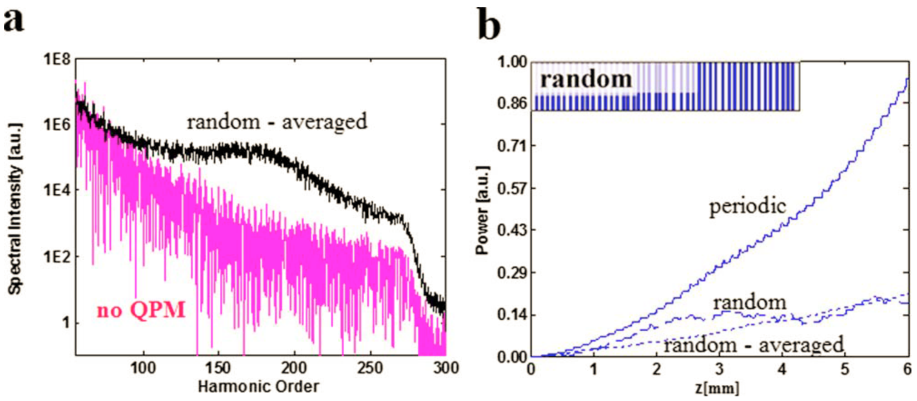

Figure 8.1: (a), Spectral intensity of the emitted harmonic emission with random QPM for enhancing the emission in a wide spectral window around the 183rd harmonic (black), compared with the emission with no QPM. The intensity with random QPM is averaged over an ensemble of 40 different random modulation patterns. (b), Power buildup of the 183rd harmonic as a function of propagation length for a periodic QPM (solid line), for a typical random pattern (dashed line), and for the average over the ensemble (dotted line). The inset shows a typical spatial modulation pattern, figure and caption from [13]

the analogous HHG situation.

In this Chapter, we consider an alternative form of random QPM, which we call random phase matching. Instead of considering random spacing of QPM zones, we consider, instead, random phase fluctuations in the driving or harmonic field, similar to phase diffusion that causes laser linewidth broadening [66; 121]. Given the noisy realistic conditions in many experiments, random phase matching may also be responsible for some harmonic enhancements and spectral broadening in those situations, for example in Ref [25; 46; 88]. QPM requires the different zones to add in phase, and the more zones the more difficult this becomes [84; 85]. Some of the the potential causes for random phase fluctuations might be due to pressure, ionisation, polarisation, or mode variations.

Although an analogous discrete model has been developed by [16], to date no work has been done to derive the analytical theory behind continuous random phase matching or phase fluctuations. Hence, Section 8.2 develops a continuous model based on phase diffusion and show how that can lead to enhancement of a broad spectrum of high harmonics.

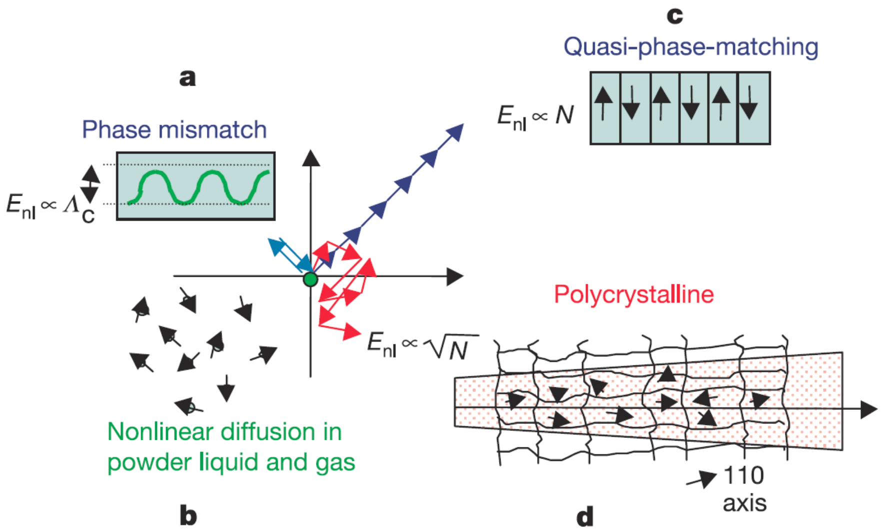

Figure 8.2: Three-wave mixing mechanisms in bulk, powder, periodically poled and polycrystalline materials. In bulk nonlinear optical materials, the relative phase of the three interacting fields grows continuously with the propagating distance, gaining a phase lag of π every coherence length L_c. The transfer of energy between the waves thus oscillates with a period of $2L_c$, leading to a small (if not null) conversion efficiency (a). In quasi-phase-matched materials, the orientation of the crystal is rotated every L_c, compensating the phase lag of π so that the energy transfer E nl adds up constructively with the propagating distance $E_{nl} \propto \mathcal{N}$, where $\mathcal{N}$ is the number of grains) (c). In a totally disordered material (powder, gas, liquid), each particle behaves independently, scattering the nonlinearly generated fields in an incoherent way (b). In polycrystalline materials, the relative phase diffuses in phase space, leading to a coherent growth of the nonlinear generated fields according to $E_{nl} \propto \sqrt{\mathcal{N}}$. Figure and caption adapted from[16].

We then independently develop a discrete model in Section 8.3 with similar arguments as the one in [16]. We then show in Section 8.4 the connection between the discrete and continuous models and show in Section 8.5 the connection between QPM and random phase matching.

8.2 Continuous phase-mismatch diffusion model

8.2.1 Set-up of the phase-mismatch diffusion equation

From the last chapter, we can write the harmonic growth equation for the qth harmonic in the familiar form,

$$2ik(q\omega_0)e^{k(q\omega)}\frac{d\xi}{dz} = \mu_0 q^2 \omega_0^2 \mathcal{P}_{\mathrm{NL}} \tag{8.1}$$

where $k(\omega)$ is the propagation constant of angular frequency ω, ω_0 is the driver frequency, ξ is the harmonic envelope function, μ_0 is the permitivity of free space, z is the propagation distance, and $\mathcal{P}_{\mathrm{NL}}$ is the nonlinear polarisation. As before, the nonlinear polarisation can be written as,

$$\mathcal{P}_{\mathrm{NL}} = \mathcal{P}_{\mathrm{NL},0}e^{iq\phi(z)} \tag{8.2}$$

where $\mathcal{P}_{\mathrm{NL},0}$ is the nonlinear polarisation amplitude modulus, $\phi(z)$ is the phase evolution of the driving pulse. We can write $\phi(z) = k(\omega_0)z + \psi_0(z) + \psi_{\mathrm{NL}}(z)$ where $\psi_0(z)$ is an additional phase term that could arise from any form of phase fluctuation of the driving pulse such as mode beating and $\psi_{\mathrm{NL}}(z)$ is phase fluctuations of the nonlinear response caused by effects such as intensity dependent phase or polarisation dependencies.

If we collect all the terms we can rewrite the Equation (8.1) as,

$$\frac{d\xi}{dz} = d_z\xi(z) = A_0 e^{i\Psi(z)} \tag{8.3}$$

where A_0 incorporates contains all the constant terms and the total phase evolution $\Psi(z)$ can be written as,

$$\Psi(z) = -\Delta k'(z)z + q(\psi_0 + \psi_{\mathrm{NL}}) \tag{8.4}$$

where

$$\Delta k'(z)z = \Delta kz + q\psi_{\Delta k}(z) \tag{8.5}$$

is the phase-mismatch plus an additional phase term describing possible fluctuations in ionisation, pressure, or other parameters. We can then collect all the fluctuation terms as,

$$\psi(z) = \psi_0(z) + \psi_{\mathrm{NL}}(z) - \psi_{\Delta k}. \tag{8.6}$$

If $\psi(z) = 0$, $\Psi(z) = \Delta kz$, then we have no harmonic growth, which is the no-phase matched condition described in Chapter 3. However, for fluctuations around a dominate phase-mismatch Δk, we can rewrite the phase-mismatch term as,

$$\Psi(z) = \Delta kz + q\psi(z) \tag{8.7}$$

where Ψ is the total phase difference evolution between the harmonic and the driving pulse as before and ψ is the total phase fluctuation. If we treat ψ as a continuous random walk we can define the phase-diffusion constant as,

$$D = \frac{d\langle q^2\psi^2\rangle}{dz} = q^2 D_0 \tag{8.8}$$

where $D_0 = \frac{d\langle\psi^2\rangle}{dz}$, $\langle\psi^2\rangle$ is the expected value of ψ^2 and, under a random walk, grows linearly with propagation distance z. We note that for a given physical system, we can expect D_0 to remain constant across harmonic orders, but D itself is dependent on harmonic order. Another interesting point is that given the q^2 relationship in Equation (8.8), even very slight phase fluctuations in D_0 may become noticeable at higher harmonic orders. This may become an important effect, especially in extremely high orders of harmonics, such as in the case with mid-IR drivers [92]. In Figure 8.3, we performed a Monte Carlo simulation, with 1,000 iterations, of harmonic growth assuming no absorption where $D = 2\Delta k$ (which turns out to be the optimal diffusion coefficient as we will prove below). We note that for all Monte Carlo simulations discussed, we sliced each coherence length into 100 segments where $dz \to \delta z = L_c/100$. For continuous random phase matching, the ψ term had a 50%-50% chance of increasing or decreasing by phase step size $\sqrt{D\delta z}/\delta z$ in order to fulfill Equation (8.8).

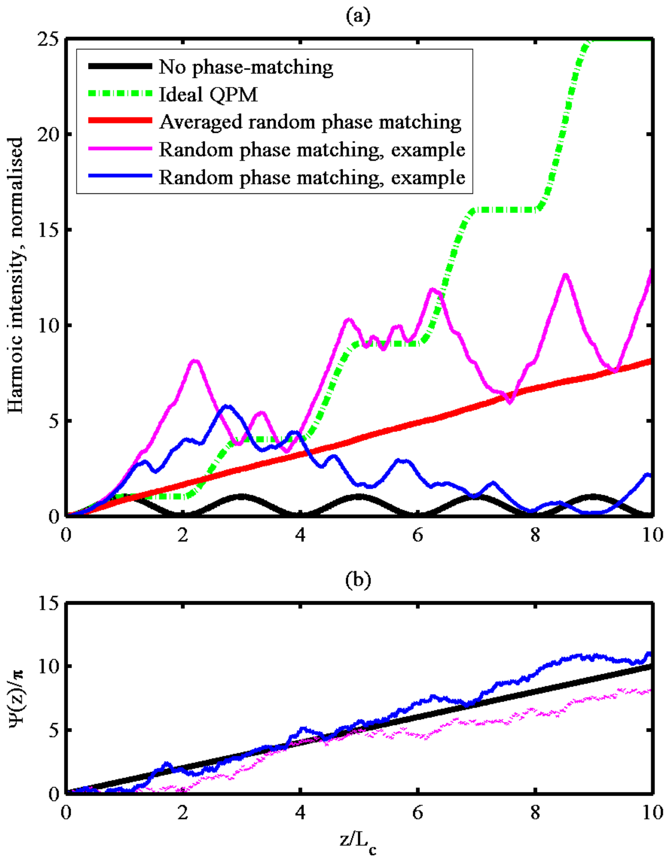

Figure 8.3: Plot (a) shows the harmonic intensity as a function of propagation distance comparing no-phase matching, ideal square-wave QPM, Monte-Carlo averaged random phase matching, and two random phase matching examples. Plot (b) shows the phase-difference $\Psi(z)$ as a function of propagation distance comparing no-phase matching and the two respective random phase matching examples.

8.2.2 Derivation of harmonic growth rates

Although we can explore the parameter space with Monte-Carlo simulations, it is more insightful to derive an analytical theory around expected harmonic growth under random phase matching. In order to do this, we need to use a similar approach to that discussed in Chapter 7 or our paper in Ref [74]. In particular, we need to calculate the Fourier transform of the growth equation $\frac{d\xi}{dz}$, where the zeroth order spatial frequency will give us the harmonic growth rate because the non-zero spatial frequency components will be integrated away for large z.

However, given that $e^{i\Psi}$ is a random variable, we shall seek to find the expected value of the modulus squared of the Fourier transform, $\langle\mathfrak{F}(d_z\xi)\mathfrak{F}(d_z\xi)^*\rangle = A_0^2\langle\mathfrak{F}(e^{i\Psi})\mathfrak{F}(e^{i\Psi})^*\rangle$, instead, where $\mathfrak{F}$ is the Fourier transform as defined by the following convention,

$$\mathfrak{F}(f) \quad = F(\nu) = \tfrac{1}{\sqrt{2\pi}}\int_{-\infty}^{\infty} f(z)e^{-i\nu z}dz \tag{8.9}$$

$$\mathfrak{F}^{-1}(F) \quad = f(z) = \tfrac{1}{\sqrt{2\pi}}\int_{-\infty}^{\infty} F(\nu)e^{+i\nu z}dz. \tag{8.10}$$

To calculate this, we exploit a previously solved problem of phase diffusion of laser line-widths [66; 121]. According to the Wiener-Khinchin theorem, the spectral density of a function (in this case the spatial-spectral density) can be computed by taking the Fourier transform of its autocorrelation. In our case,

$$\langle d_z\xi(z)d_z\xi(0)^*\rangle \quad = \quad \langle A_0e^{i\Psi(z')} \mid A_0e^{i\Psi(0)}\rangle \tag{8.11}$$

$$= \quad A_0^2\langle e^{i\psi} \mid e^{i\psi(0)}\rangle e^{-i\Delta kz} \tag{8.12}$$

It follows from [66] that,

$$\langle e^{i\psi} \mid e^{i\psi(0)}\rangle \quad = \quad e^{-\frac{1}{2}\langle\psi^2(z)\rangle} \tag{8.13}$$

$$= \quad e^{-\frac{D|z|}{2}} \tag{8.14}$$

where we have substituted $D|z| = \langle\psi^2(z)\rangle$. Plugging Equation (8.14) into Equation (8.12), we get,

$$\langle d_z\xi(z)d_z\xi(0)^*\rangle = A_0^2 e^{-\frac{D|z|}{2}} e^{-i\Delta kz} \tag{8.15}$$

which has a very familiar Fourier transform, which is the Lorentzian or Cauchy distribution [66]. Hence, it follows from Refs [66; 121] that the expected value of modulus squared of the Fourier Transform of a phase diffusion function, $e^{i\Psi}$ with diffusion coefficient D and central frequency Δk can be written as Cauchy distribution as,

$$F(\nu) = A_0^2\langle\mathfrak{F}(e^{i\Psi})\mathfrak{F}(e^{i\Psi})^*\rangle = A_0^2 \frac{2\left(\frac{D}{2}\right)}{\left(\frac{D}{2}\right)^2 + (\nu - \Delta k)^2} \tag{8.16}$$

where D, the diffusion coefficient, is also the FWHM of the Cauchy distribution. Note that this is the expected value modulus squared Fourier transform signal of a phase diffusion shifted by Δk (if $\Delta k = 0$, then the center of the Cauchy distribution would have been at $\nu = 0$). From Chapter 7 or Ref [74], we showed that for there to be harmonic growth, we must have a stationary phase $\frac{d\Psi}{dz} = 0$. This means that we must pick out the zero spatial frequency $\nu = 0$ component of $F(\nu)$. Hence, our expected value of the intensity growth rate, G is,

$$\begin{aligned} G &= \frac{d\langle\xi\xi^*\rangle}{dz} = \frac{d\langle I\rangle}{dz} && (8.17)\\ &= F(0) && (8.18)\\ &= A_0^2 \frac{D}{\left(\frac{D}{2}\right)^2 + (\Delta k)^2} && (8.19) \end{aligned}$$

Next, we can write the expected harmonic intensity by integrating Equation (8.19) along

z as,

$$\langle I_c \rangle = Gz \tag{8.20}$$

$$= \left[A_0^2 \frac{D}{\left(\frac{D}{2}\right)^2 + (\Delta k)^2} \right] z \tag{8.21}$$

which, in general, is a function of propagation distance z and diffusion coefficient D. For constant central Δk and phase-diffusion constant, the intensity of the harmonic grows linearly with respect to propagation distance. We have also labelled the expected intensity in the equation above as I_c for this continuous model.

For ease of comparison across different coherence lengths or harmonic orders, Equation (8.21) can be normalised against the harmonic intensity output of a single coherence length with no phase-matching, which from Chapter 3, is $I_0 = \frac{4A_0^2}{\Delta k^2}$. Figure 8.4 shows both the expected harmonic intensity for three different values of diffusion coefficients and their normalised respective expected value squared of the Fourier transform signal, $F(\nu)$. The value of F equals exactly with the linear rate of growth of the harmonics as expected. We note that for $D = 0.1\Delta k$, the Monte Carlo simulations show a slowly damped oscillation with period of $2L_c$ and a slight offset because the phase diffusion rate is much less than Δk. The peaks of the Cauchy distributions for all values of the diffusion coefficient are located at $\nu = \Delta k = \pi/L_c = \pi$ as expected, where ν is normalised to L_c.

For a given coherence length, there is an optimal phase-diffusion constant, which can be calculated by finding the zero of the first derivative of $G(D)$ with respect to D,

$$\frac{\partial G}{\partial D} = -4A_0^2 \frac{[D^2 - 4(\Delta k)^2]}{[4(\Delta k)^2 + D^2]^2} = 0 \tag{8.22}$$

We find the optimal phase-diffusion constant to be,

$$D' = 2\Delta k \tag{8.23}$$

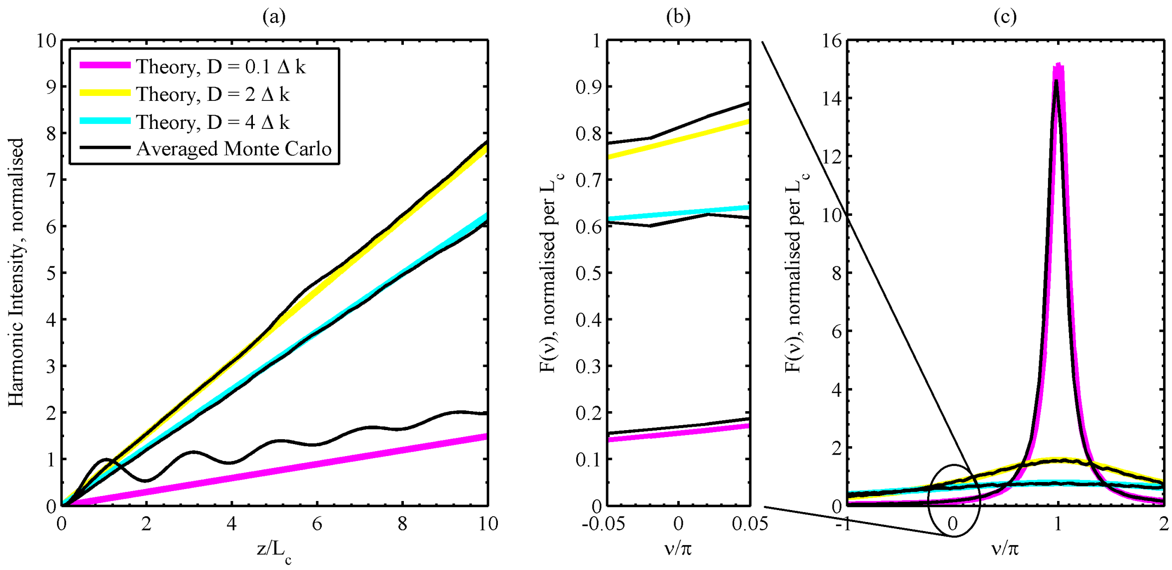

Figure 8.4: Plot(a) shows the expected harmonic intensity under random phase matching (phase diffusion) as a function of propagation distance across ten coherence lengths for three different values of diffusion coefficients $D = 0.1\Delta k$, $2\Delta k$, $4\Delta k$ with $D = 2\Delta k$ being the optimal coefficient. The thick colored lines show the theoretical linear growth whilst the black lines show the averaged Monte Carlo simulations. Plot (c) plots the expected value modulus squared of the Fourier transform of $\frac{d\xi}{dz}$, $F(\nu)$, normalised against the output of one coherence length with no phase-matching, I_0. As before, the thick colored lines represent the calculated theoretical Cauchy distributions for $D = 0.1\Delta k$, $2\Delta k$, $4\Delta k$ (magenta, yellow and cyan respectively). The black lines are the respective averaged Monte Carlo results, which shows excellent agreement with the analytic theory. Plot (b) is a magnification of Plot (c) around $\nu = 0$, where the value of $G = F(0)$ equals exactly with the harmonic intensity growth, as expected. For each diffusion coefficient, the Monte Carlo simulation were conducted over 2,000 iterations.

where we took the positive root. Hence, the maximum relative growth per coherence length normalised to I_0 is,

$$G_{\text{norm.}} L_c = \frac{I(D = 2\Delta k, z = L_c)}{I_0} = \frac{\pi}{4} \approx 0.7854 \tag{8.24}$$

Figure 8.5 plots $G(D)$ normalized to the maximum intensity achieved in a no phase-matching scenario, I_0. Both the analytic curve of $G(D)$ and the averaged Monte Carlo simulations (across 2,000 iterations per value of D) are plotted, showing excellent agreement between the simulations and the theory. As calculated, the optimal value of the

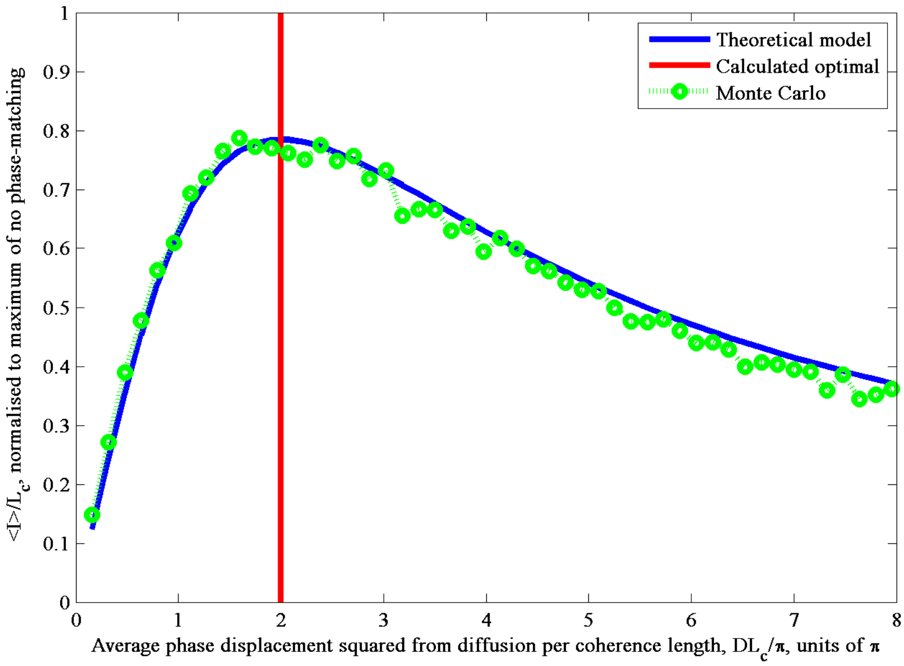

Figure 8.5: Intensity growth per coherence length GL_c as a function of diffusion coefficient D. The plot compares both the analytic theoretical model along with the averaged Monte Carlo simulations.

diffusion coefficient sits at $D' = 2\Delta k$ with the relative normalised linear harmonic growth rate of $\pi/4 \approx 0.7854$ as seen in Figure 8.5.

8.2.3 Broad high harmonic spectrum

The relatively broad profile in Figure 8.5 suggests that random phase matching may lead to the amplification of a broad spectrum of harmonics. To test this idea, we conducted a simulation under realistic parameters for harmonics generated in a $a = 51\,\mu\text{m}$ radius 10mm long hollow-core waveguide with wall index of refraction of $n = 1.5$, with harmonics generated at ionisation fraction of $\eta = 0.3$ and average pressure of 30mbars. Absorption was ignored to focus on the impact of random phase matching on harmonic amplification. Figure 8.6 shows the results of this simulation comparing random phase matching to ideal square wave QPM. Both schemes were optimized to the $q = 51$ harmonic.

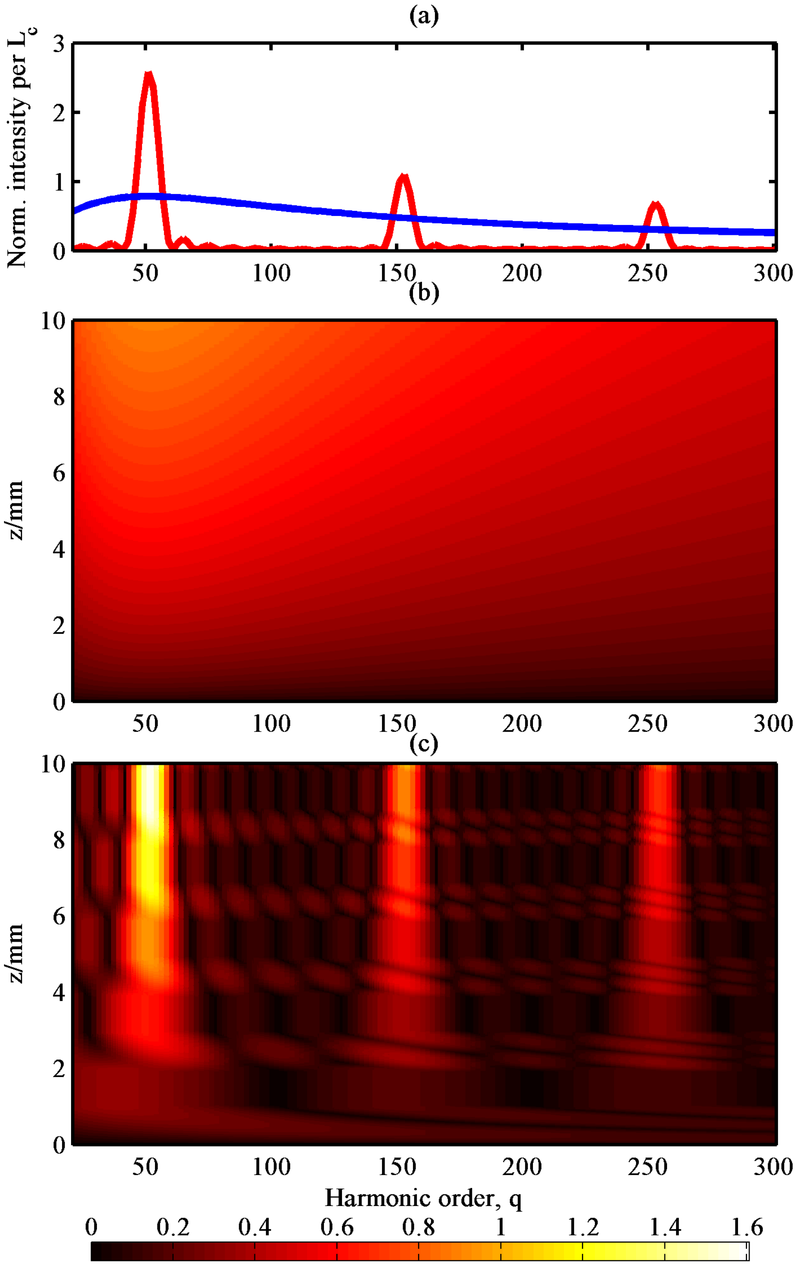

Figure 8.6: Plot (a) shows the harmonic intensity generated per coherence length, normalised to the output after a single coherence length with no-phase matching I_0, as a function of q. The red line shows the growth for ideal square wave QPM optimized for $q = 51$; note that QPM is quadratic growth per zone. The blue line shows the growth for random phase matching, with the diffusion coefficient optimized for $q = 51$; note that random phase matching gives linear growth. Plot(b) and (c) shows the amplitude modulus (square root of intensity), normalised as above, as a function of both propagation distance and harmonic order for random phase matching (Plot b) and ideal square wave QPM (Plot c) respectively. It is evident that random phase matching affords a much broader spectrum even though it is not as efficient as QPM.

Figure 8.6a shows the harmonic growth per coherence length (normalised to the output after a single coherence length with no-phase matching, I_0). Although random phase matching is less efficient than ideal square-wave QPM, it affords a significantly broader spectrum. It is also evident from this graph that the second and third order QPMs are visible in the peaks centered around $q = 151$ and $q = 251$. Moreover, it is important to note that random phase matching provides a linear growth, hence the average growth per coherence length is independent of the total length of the waveguide. For QPM however, the growth is quadratic of order $\mathcal{N}^2$ where $\mathcal{N}$ is the number of quasi-phase matched zones. Hence, the average amplification for 20mm, for example, would be twice as large.

8.3 Discrete model

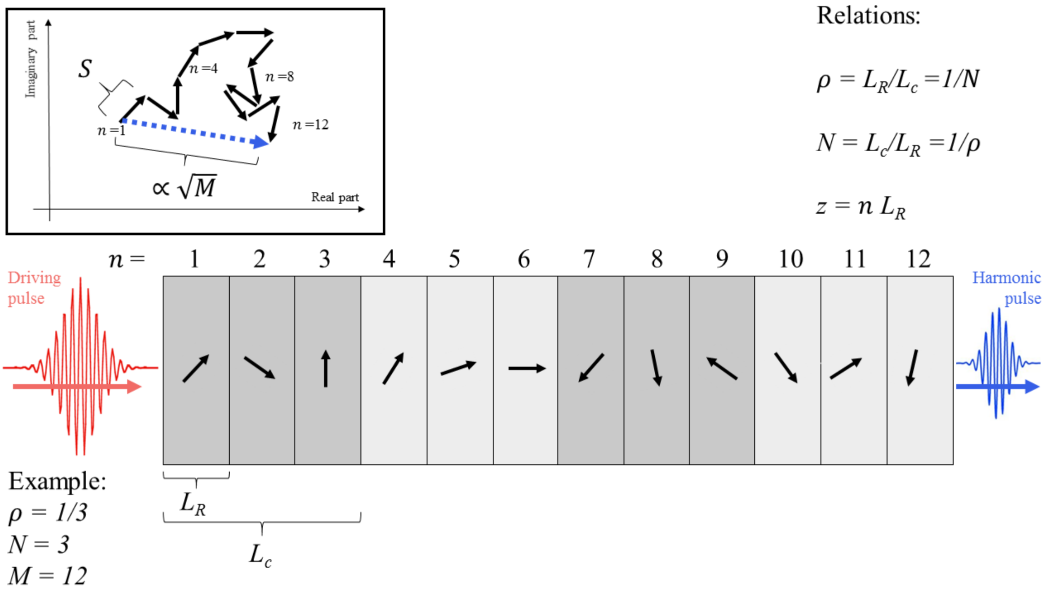

Figure 8.7: Schematic for discrete random phase matching for high harmonic generation.

In the last section, we assumed a continuous diffusion (or Brownian motion) of the phase Ψ with a central frequency Δk, which led to linear harmonic intensity growth. Another way of thinking about this problem is to construct a discrete model instead.

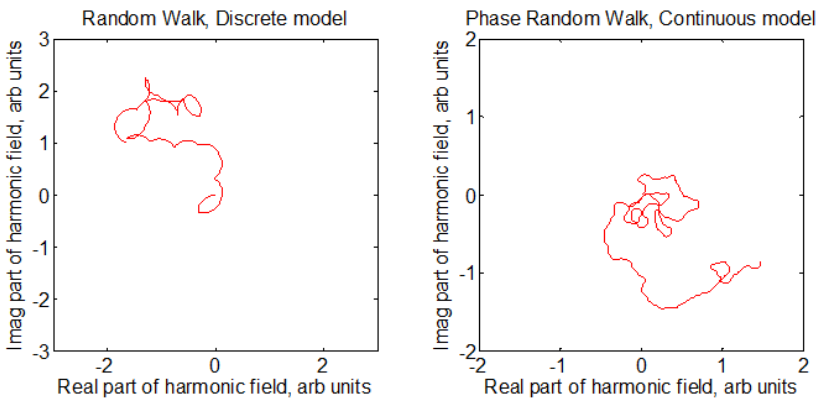

Figure 8.8: Left: Real and imaginary part of random walk path of ξ in two-dimensional a complex plane calculated using the discrete model starting at the origin. Right: Real and imaginary part of the path of ξ as its phase undergo a random walk using the continuous model.

Here, we can discretize the complex differential $d\xi \to \Delta\xi$. Instead of a continuous random walk of phase as before, we can model a discrete two dimensional random walk on the complex plane $(\Re[\xi], \Im[\xi])$, where $\Re[.]$ and $\Im[.]$ are the real and imaginary parts respectively. Figure 8.7 shows a schematic of the discrete model. In this model, L_R is the length scale for each random walk zone. We think can relate the coherence length L_c to L_R by defining the ratio between,

$$N = \frac{L_c}{L_R} \tag{8.25}$$

which can be thought of as the number of times the coherence length is spliced by random zones. N can roughly be thought of as the rate of the random walk, and for larger N, the more random zones there per unit length. We will relate N to the diffusion coefficient D below in Section 8.4.

We also define M to be the total number of random zones, and S to be the amplitude of each zone. We we can relate propagation distance z to the nth zone by $z = nL_R$, and at the end of the generation zone, $z = ML_R$.

Moreover, just for comparison and using the phasor diagrams described in Chapter

3, Figure 8.8 shows an example of random walks for both the discrete and continuous (phase-diffusion) case.

8.3.1 Derivation

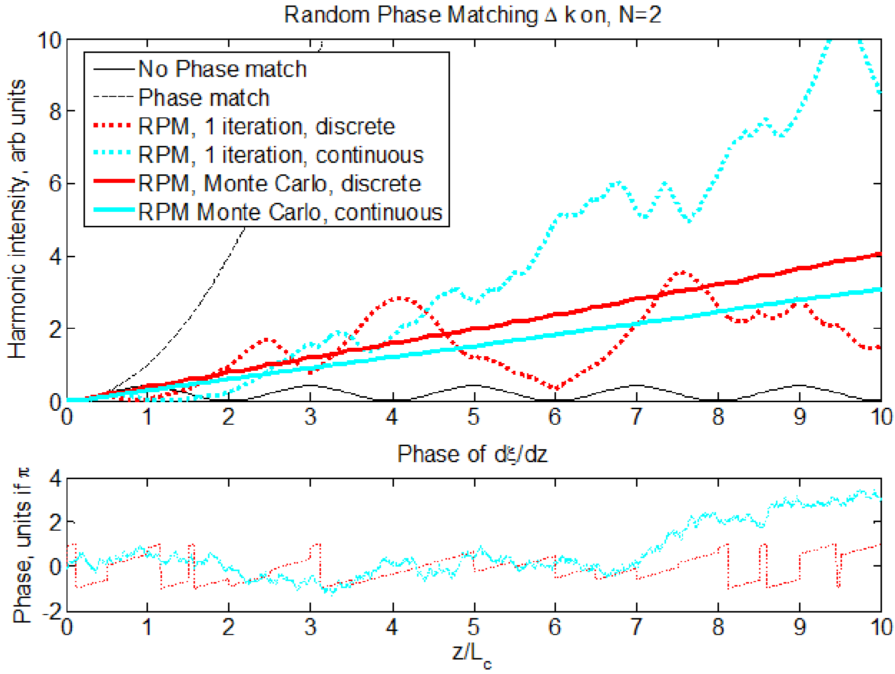

Figure 8.9: Top: Comparison of different harmonic generation schemes – no phase matching, ideal phase matching, random phase matching example using the discrete model, random phase matching using the continuous model, averaged discrete random phase matching over 100 samples, and averaged continuous random phase matching over 100 samples. Bottom: Comparison of the phase of $d\xi/dz$ for discrete and continuous models.

It is well known that the mean distance squared of any random walk in two dimensional space is given by [41],

$$\langle |R|^2 \rangle = MS^2 \tag{8.26}$$

where in our case, the expected intensity is given by $\langle I \rangle = \langle |R|^2 \rangle$. We will use this relation below to calculate the expected intensity.

In the discrete model, we can write down the growth equation as,

$$\frac{d\xi}{dz} = A_0 e^{i[-\Delta k z + h(z)]} \tag{8.27}$$

where we replaced $q\psi(z) = h(z)$ and,

$$h(z) = \begin{cases} h_1 & 0 \leq z < L_R \\ h_2 & L_R \leq z < 2L_R \\ h_3 & 2L_R \leq z < 3L_R \\ h_n ... & (n-1)L_R \leq z < nL_R \end{cases} \tag{8.28}$$

is the random phase variable ranging from $h_n \in [0, 2\pi)$, a random number with equal probability between 0 and 2π. This is the equivalent of saying that after length L_R, the complex phase vector $\Delta\xi$ takes on new, random direction in two-dimensional complex plane, undergoing a random walk. Figure 8.8 shows the random walks for both the discrete model and continuous model. Figure 8.9 shows harmonic growth and phase-differential modulation profiles for both the discrete and the continuous model.

Equation (8.27) is the correct growth equation but is difficult to compute the expected value of the intensity in closed analytical form. To do this, we first break apart the integral resulting from Equation (8.27) into each of the steps,

$$\xi(z) = \sum_{n=1}^{M} \left[A_0 e^{ih_n} \int_{(n-1)L_R}^{nL_R} dz' e^{-i\Delta k z'} \right] \tag{8.29}$$

where $M = zN/L_c$ as before. This is still unwieldy, but we may assume that the phase of each step is independent from the previous step because of the random phase h_n. Hence, we can absorb any extra phase in the integral above into h_n,

$$\xi(z) = \left[A_0 \int_0^{L_R} dz' e^{-i\Delta k z'}\right] \sum_{n=1}^{M} \left[e^{ih_n}\right] \tag{8.30}$$

and we factored out the terms not dependent on n. We can now write down the harmonic amplitude of each step as,

$$S = \left| A_0 \int_0^{L_R} dz' e^{-i\Delta k z'} \right| = \left| \frac{2A}{\Delta k} \sin\left(\frac{\pi}{2N}\right) \right|. \tag{8.31}$$

Note that for $N = 1$, we have $S = I_0$ as expected from Section 8.2.2. Applying Equation (8.26), the expected value intensity becomes,

$$\begin{aligned} \langle I_d \rangle &= \left[\frac{4A_0^2}{\Delta k^2} \sin^2\left(\frac{\pi}{2N}\right)\right] \frac{N}{L_c} z & (8.32) \\ &= \left[\frac{4A_0^2 L_c N}{\pi^2} \sin^2\left(\frac{\pi}{2N}\right)\right] z. & (8.33) \end{aligned}$$

where, as in the continuous model, the intensity grows linearly with propagation distance. We have also labelled the expected intensity in the equation above as I_d for discrete model for ease of comparison later.

8.3.2 Asymptotic behavior, $N \to \infty$, and further simulations

It is useful to understand the asymptotic behavior of the discrete model by taking the limit $N \to \infty$ of Equation (8.33),

$$\begin{aligned} \langle I_{N\to\infty} \rangle = \lim_{N\to\infty} \langle I_d \rangle &= \frac{4A_0^2}{\Delta k^2} \left[\frac{\pi}{2N}\right]^2 \frac{N}{L_c} z & (8.34) \\ &= \frac{A_0^2 L_c}{N} z & (8.35) \end{aligned}$$

where $\sin^2\left(\frac{\pi}{2N}\right) \approx \left(\frac{\pi}{2N}\right)^2$ for large N. As expected, the impact of Δk drops out because the phase is varying on a much faster length scale than L_c.

To test our analytic expressions, we compared Equation (8.33) with Monte Carlo simulations under the same parameters. Figure 8.10 shows the result of the simulations for both cases, which gives good agreement between theory and simulation. The Monte Carlo simulations were conducted with 3000 iterations per value of N. Moreover, we see the convergence of the two scenarios for larger N.

8.4 Connection between continuous and discrete models

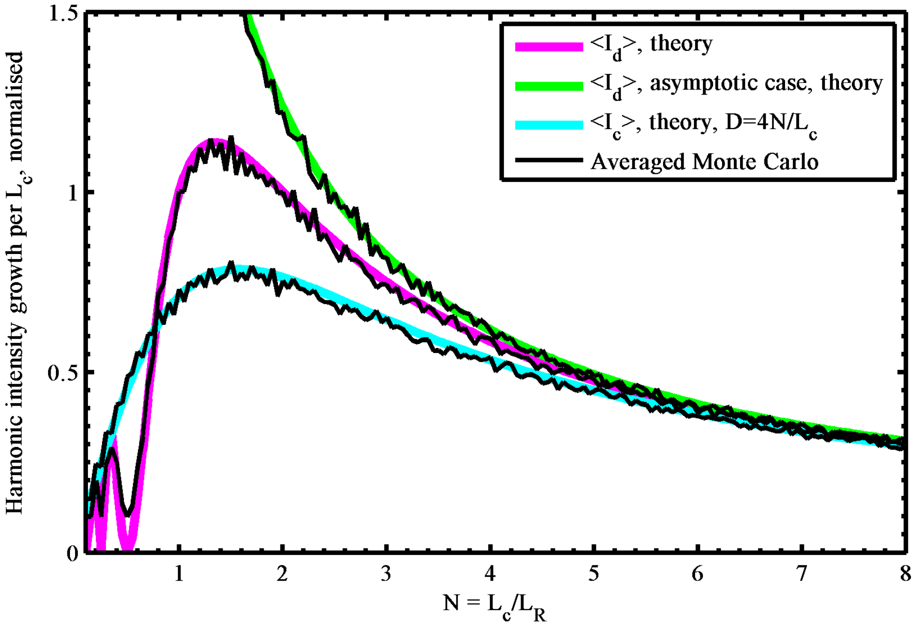

Figure 8.10: Harmonic intensity growth per L_c normalized to I_0 as a function of N for Equation (8.33) (discrete model, magenta line), Equation (8.35) (discrete asymptotic model where $N \to \infty$, green line), and Equation (8.21) (continuous model with $D = 4N/L_c$, cyan line) comparing Monte Carlo simulations after 2000 iterations (black lines hugging the theoretical curves) Analytic expressions and Monte Carlo simulations show good agreement as expected.

The asymptotic behavior analysis above enables us to connect the discrete and continuous models. For large N, the corresponding situation in the continuous case is when $D^2 \gg \Delta k^2$. In this situation, we can rewrite Equation (8.21) as,

$$\lim_{D\to\infty} \langle I_c \rangle = A_0^2 \frac{1}{4D} z \tag{8.36}$$

which is the situation where the phase-diffusion dominates. If we set the asymptotic equations to equal each other; in other words, setting Equation (8.21) to equal Equation (8.35), we have

$$A_0^2 \frac{1}{4D} z = \frac{A_0^2 L_c}{N} z. \tag{8.37}$$

We can then relate the diffusion coefficient D with the number of steps per coherence length N,

$$D = \frac{4N}{L_c} = \frac{4}{L_R}. \tag{8.38}$$

Interestingly, this means that the average phase displacement squared per length L_R needs to equal 4 radians in order to be equivalent to a random walk in the two dimensional complex plane with step length L_R.

Figure 8.10 also shows the continuous model versus the discrete one, where it is clear that the asymptotic behavior matches for larger N. Moreover, the optimal diffusion coefficient (in terms of N) is close to the optimal N for the discrete model. This suggests that the much simpler discrete model is a useful way of describing some of the processes in random phase matching.

8.5 Connection between random phase matching and QPM

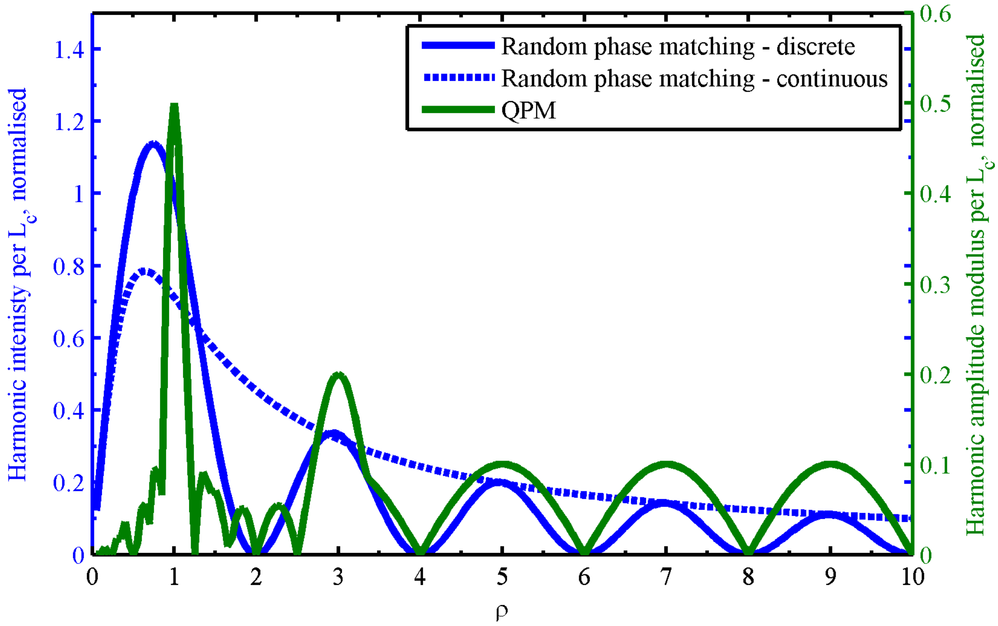

Figure 8.11: Comparison of harmonic generation efficiency between random phase matching and QPM as a function of ρ. Left (blue): harmonic generation intensity (normalised against I_0) per coherence length L_c for random phase matching using the discrete model (solid blue line, $\rho = L_R/L_c$) and continuous model (dashed line, $\rho = 4/(DL_c)$). Right (green): harmonic generation *amplitude modulus* (normalised against $\sqrt{I_0}$) for QPM (solid green line, $\rho = \Lambda/(2L_c)$).

In order to more rigorously compare QPM with random phase matching, it is useful to define a unit-less scaling term ρ that describes the length scale the modulation of the system. In the case of QPM,

$$\rho_{\text{QPM}} = \frac{\Lambda/2}{L_c} \tag{8.39}$$

where Λ is the QPM period of an square wave source amplitude modulation as defined in the previous Chapter. We have ideal square wave QPM of lowest order when $\Lambda = 2L_c$, or $\rho = 1$. In the case of discrete random phase matching, we have the length of each random zone scaled by coherence length,

$$\rho_{\text{RPM,d}} = \frac{L_R}{L_c} = \frac{1}{N}. \tag{8.40}$$

Finally for continuous random phase matching, we can use the connection between the discrete and continuous models discussed above in Equation (8.38),

$$\rho_{\text{RPM,c}} = \frac{4/D}{L_c}. \tag{8.41}$$

Figure 8.11 compares the harmonic efficiency of these three schemes. Note that because the intensity in random phase matching grows linearly with z, the scale shows intensity per coherence length for random phase matching. However, because *amplitude* in QPM grows linearly with z (intensity quadratically with z), the scale shows amplitude modulus per coherence length for QPM. It is interesting to note that as ρ increases, the peaks of the discrete random phase matching model hugs the curve for the continuous model. More interestingly, however, is that the higher order QPMs peaks are aligned to the peaks for discrete random phase matching. This means that a QPM half period $\Lambda/2$ corresponds to the length of a random zone L_R.

8.6 Conclusion

In this Chapter, we explored random phase matching and derived analytical expressions for the expected values of intensity. We learned that although random phase matching may not be able to provide the high level of enhancements that QPM or phase matching may provide, it may be a useful tool to generate extremely broad spectrum harmonics beyond the phase matched cut-off limit. Specifically, the intensity of random phase matching scales as roughly one (~ 0.8) coherence length worth of intensity, I_0, per coherence length of propagation distance.

We note that the effect of random phase fluctuations could potentially explain the amplification of a broader than expected harmonic spectrum in hollow-core optical waveguides [25; 46; 85; 88; 92; 125]. Moreover, random phase matching may be a further reason why HHG in a cluster jet is more efficient than traditional gas cell techniques [40; 86; 124] in addition to relative decreased harmonic absorption [86] or phase matching in cluster jets [116].

An explicit practical experiment to demonstrate this would need to be developed, but it is beyond the scope of this thesis. However, from our paragraph above, potential paths towards towards controlled random phase matching could be the utilization of random modes or controlled cluster jets.

Chapter 9

Mode Decomposition Analysis

9.1 Introduction

This thesis focuses on the high harmonic generation process inside a hollow-core waveguide. As such, it is important to be able to measure and analyse the modes excited inside the waveguide. In Chapter 4, we described the modes of a hollow-core waveguide, and this chapter focuses on methods to decompose them based on single shot CCD intensity measurements. Applications in modal decomposition beyond HHG include modal multiplexing in optical communications [6; 9; 87] and supercontinuum generation [93].

Previous methods of mode and phase retrieval have been realized in various forms including a single intensity measurement in the Fourier plane [80; 109]. Deducing the mode superposition from measurement of the transverse intensity profile in two planes, and the application of the Gerchberg-Saxton algorithm has become quite standard in decomposing the modes[45]. More recently a method developed by Shapira et al. at MIT using four measurements (two polarizations for both far field and near field) has shown to be very effective in decomposing eigenmodes [106].

However, most of the methods focus on decomposition use either multiple methods or iterative approaches which increases computation time. In this chapter, we present four novel methods, to our knowledge, for waveguide modal decomposition with a single shot CCD measurement. The internal MATLAB least squares fitting routing is used as a reference. These methods were tested against experimental data using a HeNe laser and a series of hollow-core 51 µm diameter waveguides of different lengths to demonstrate the effectiveness of mode and phase retrieval of the first two fundamental waveguide modes. These methods are analyzed and compared for accuracy, precision, noise tolerance, and speed using synthetic data.

9.2 Overview of eigenmode decomposition with a single intensity measurement

9.2.1 Linear Independent Expansion

As described in Chapter 4, the amplitude profile of the propagating electric field, $E(\vec{r})$ can be written as a set of modes:

$$E(\vec{r}) = c_1 j_1(\vec{r}) + c_2 j_2(\vec{r}) + ...c_M j_M(\vec{r}) = \sum_{m=1}^{M} c_i j_m(\vec{r}) \tag{9.1}$$

where $c_i \in \mathbb{C}$ provides both the amplitude and phase information of each eigenmode $\{j_m\}$, each j_m is assumed to be real, and M is the number of modes assumed to be in the system. In general, M is assumed to be a countable infinite number of modes, but in reality, we have to make a guess as to how many modes we wish to retrieve.

In an intensity measurement, the measured signal is proportional to EE^*, where the phase information is apparently lost. However, they can be retrieved under certain conditions. The term EE^* can be expanded into $N \equiv M + \frac{M^2-M}{2}$ linearly independent functions:

$$EE^* = (c_1 j_1 + c_2 j_2 + ...c_M j_M)(c_1^* j_1 + c_2^* j_2 + ...c_M j_M) \tag{9.2}$$

$$= [c_1 c_1^* j_1^2 + ...c_M c_M^* j_M^2] + [(c_1 c_2^* + c_2 c_1^*) j_1 j_2 + ... \tag{9.3}$$

$$+(c_M c_{M-1}^* + c_M^* c_{M-1}) j_M j_{M-1}]. \tag{9.4}$$

Note that the first set of terms in the sum has M terms defining the amplitude of the modes, and the second set of terms in the sum has $\frac{M^2-M}{2}$ cross terms relating to the relative phase differences between the modes.

After rearranging, it is convenient to think of $\{j_1 j_1, j_1 j_2, ...j_M j_M\}$ as a set of (generally not orthogonal) basis vectors, and thus we redefine them as:

$$\{v_1, v_2, ...v_n...v_N\} \equiv \{j_1 j_1, j_1 j_2, ...j_M j_M\} \tag{9.5}$$

and the subspace of the Hilbert space $\mathbb{H}$ spanned by these vectors as:

$$S \equiv span\{v_n\} \tag{9.6}$$

From this, it is convenient to rewrite $w(\vec{r}) \equiv E(\vec{r})E^*(\vec{r})$ as:

$$w(\vec{r}) = \Omega_{(1,1)} v_1(\vec{r}) + \Omega_{(1,2)} v_2(\vec{r}) + ...\Omega_{(M,M)} v_N(\vec{r}) \tag{9.7}$$

$$= \Omega_1 v_1(\vec{r}) + \Omega_2 v_2(\vec{r}) + ...\Omega_n v_n(\vec{r}) + ...\Omega_N v_N(\vec{r}) \tag{9.8}$$

where $\Omega_n \in \mathbb{R}$ is the modulus squared and cross-term coefficients, keeping in mind that $w \in S$.

It is a well known fact that if a set of linearly independent basis vectors span a subspace, then any vector in that subspace has a *unique* set of coefficients for its basis vectors that define said vector. Therefore, by this argument, if the $\{v_n\}$ are all linearly independent, we are able to mathematically determine both the amplitude and relative phase of all the known modes. All the methods described below rely on this expansion and on the uniqueness property, and they all attempt to resolve the Ω coefficients.

However, all physical measurements contain noise, and at this point, we introduce a 'realistic measurement' $\tilde{w}$, defined as:

$$\tilde{w}(\vec{r}) = w(\vec{r}) + \epsilon(\vec{r}) \tag{9.9}$$

where $\epsilon(\vec{r}) \notin S$ is the noise added to the pure $w(\vec{r}) \in S$ intensity squared function.

9.2.2 Solving for c_m and System Constraints

There are two major types of constraints in solving for the c_m coefficients from Ω_n. The first constraint assumes that the modes describe the complete system; we will call this *Constraint A*. The second constraint stipulates that the phase angles between the modes must add correctly; this will be called *Constraint B*.

Constraint A stipulates that:

$$\sum_{m=1}^{M} c_m c_m^* = \sum_{m=1}^{M} \Omega_{(m,m)} = 1 \tag{9.10}$$

Constraint B stipulates that for a set of phase angle differences between three modes, $\phi_{(i,j)}$, $\phi_{(i,k)}$, $\phi_{(j,k)}$,

$$\phi_{(i,k)} = \phi_{(i,j)} + \phi_{(j,k)} \tag{9.11}$$

assuming $\phi_i < \phi_j < \phi_k$. Using the coefficients of Ω_n and stipulating $\phi_1 = 0$, this constraint is manifested as:

$$\begin{aligned}\Omega_{(i,j)} &= 2Re[C_i]Re[C_j] \pm 2Im[C_i]Im[C_j] && (9.12)\\ &= \frac{\Omega_{(i,i)}\Omega_{(j,j)}}{\Omega_{(1,1)}} \pm \sqrt{\Omega_{(i,i)} - \frac{\Omega_{(i,i)}}{2\Omega_{(1,1)}}}\sqrt{\Omega_{(j,j)} - \frac{\Omega_{(j,j)}}{2\Omega_{(1,1)}}} && (9.13)\end{aligned}$$

9.3 Least Squares Fit Method

The most direct and obvious way of determining the Ω coefficients is a least squares fit method(LSF). A variation of least squares fit in determining modal decomposition has been achieved in [109].

In MATLAB, for a system of N Ω coefficients and L points of discretization, a simple one line of code can be written to achieve this for a one dimensional system:

$$\text{Omega} = \text{VMatrix}/\text{wPrime} \quad \textit{\%MATLAB for least squares fit} \tag{9.14}$$

where Omega is a $1 \times N$ array of the Ω coefficients, VMatrix is an $L \times N$ rectangular matrix of the discretized $\{v_n\}$ vectors and wPrime is the $1 \times L$ descretized measurement data $\tilde{w}$. For a two dimensional data set, which is the case for most CCD measurements, it is straightforward to map the two dimensions onto one line. For example, an $L_x \times L_y$ pixel system can be mapped into an an $L = L_x L_y$ length array.

The advantage of this method is the ease of implementation, as it requires only one line of code for the actual calculation in MATLAB. However, as we shall see in the forthcoming sections, LSF is not as fast as some of the more novel methods developed in this chapter and is unable to cope with any noise if the system has more than two modes.

9.4 Error Reduction & Modal Decomposition by Hilbert Space Projection Method

This method constructs a Hilbert subspace from the given modes and projects the measurement data onto the subspace. Error can be drastically reduced by projecting the data onto the subspace and the modal coefficients can be retrieved via a coordinate transformation. HSP is effective for high frequency noise filtering. For decomposing two modes, it is also more accurate and faster than a least squares fit, but like least squares, the method is sensitive to error for more than two modes.

9.4.1 Error Reduction & Subspace Projection

At the end of Section 9.2.1 we defined $\tilde{w} = w + \epsilon$ where ϵ is the noise added to the pure set of eigenmodes. We recall that $w \in S$ and $\epsilon \notin S$ by definition.

Now it is possible to construct a set of orthogonal basis vectors $\{u_n\}$ that only span the subspace S such that $span\{u_n\} = span\{v_n\} = S$ using an orthogonalization algorithm such as Gram-Schmidt [118] or Householder [53]. Note that we have used a modified Gram-Schmidt, as the original algorithm in general is not numerically stable [118].

We now define the standard Projection Operator as:

$$\mathrm{proj}_u(v) = \frac{\langle v \mid u \rangle}{\langle u \mid u \rangle} u \tag{9.15}$$

where $\langle v \mid u \rangle = \int_{\mathbf{V}} (vu^*) dV$ is the inner product over the Hilbert space with domain $\mathbf{V}$ and, dV is the area element over the domain; in most cases $dV = dxdy$ or $dV = 2\pi r dr$.

Because we now have an orthogonal basis, we can project $\tilde{w}$ onto the subspace $\mathbf{S}$ and thus eliminating ϵ by performing the following operation,

$$w = \sum_{n=1}^{N} \text{proj}_{u_n}(\tilde{w}) \tag{9.16}$$

.

With $\tilde{w}$ 'cleaned up', we can now apply the newly constructed w in the various methods described in this discussion, the most obvious one being the coordinate transformation described immediately below.

9.4.2 Decomposing Eigenmodes by Subspace Projection

The 'cleaned up' intensity profile, w, was constructed using a linear combination of projections onto the $\mathbf{S}$ subspace spanned by orthogonal basis vectors $\{u_n\}$. Thus, it is possible to write w as:

$$w = \sum_{n=1}^{N} \text{proj}_{u_n}(\tilde{w}) = \sum_{n=1}^{N} b_n u_n \tag{9.17}$$

where b_n is the projected coefficient,

$$b_n = \frac{\langle w' \mid u_n \rangle}{\langle u_n \mid u_n \rangle} \tag{9.18}$$

.

Now that we are able to write w as a sum of M linearly independent vectors, it is straightforward to convert all the $\{b_n u_n\}$ into $\{\Omega_n v_n\}$ by way of a basis transformation.

9.5 Linear Form Matrix Inversion Method (LFMI)

This method applies a set of linear forms (such as a definite integral) onto the measurement data and also onto a set of functions determined by the given modes to form matrix equation. This matrix equation is solved to retrieve the modal coefficients. For decomposing two modes, it is a factor of three faster than least squares, but it is sensitive to error beyond two modes. This method has potential applications in an electronic analogue form for modal multiplexing. Below we discuss this method as applied for two modes. A generalization for M modes is given in the Appendix.

9.5.1 LFMI for Two Modes

First consider a two-mode example where:

$$\begin{aligned} w &= c_1 c_1^* j_1^2 + (c_1 c_2^* + c_2 c_1^*) j_1 j_2 + c_2 c_2^* j_2^2 && (9.19) \\ &= \Omega_1 v_1 + \Omega_2 v_2 + \Omega_3 v_3 && (9.20) \end{aligned}$$

Now we define three arbitrary linearly independent real functions f_1, f_2, f_3 and perform the following set of integrals, defining A_n as follows:

$$A_1 = \int_{\mathbf{V}} w f_1 dV \quad (9.21)$$

$$A_2 = \int_{\mathbf{V}} w f_2 dV \quad (9.22)$$

$$A_3 = \int_{\mathbf{V}} w f_3 dV \quad (9.23)$$

These integrals can then be expanded:

$$A_1 = \Omega_1 \int_{\mathbf{V}} v_1 f_1 dV + \Omega_2 \int_{\mathbf{V}} v_2 f_1 dV + \Omega_3 \int_{\mathbf{V}} v_3 f_1 dV \quad (9.24)$$

$$A_2 = \Omega_1 \int_{\mathbf{V}} v_1 f_2 dV + \Omega_2 \int_{\mathbf{V}} v_2 f_2 dV + \Omega_3 \int_{\mathbf{V}} v_3 f_2 dV \quad (9.25)$$

$$A_3 = \Omega_1 \int_{\mathbf{V}} v_1 f_3 dV + \Omega_2 \int_{\mathbf{V}} v_2 f_3 dV + \Omega_3 \int_{\mathbf{V}} v_3 f_3 dV \quad (9.26)$$

These three equations can then be simplified into one linear matrix equation, in Einstein matrix notation,

$$A_n = T_n^l \Omega_q \tag{9.27}$$

where $n = 1, 2, 3$, $l = 1, 2, 3$, and

$$T_n^l = \langle v_l \mid f_n \rangle = \int_{\mathbf{V}} v_l f_n dV \tag{9.28}$$

Equation 9.27 can then be solved to determine the Ω coefficients.

It is important to note that the matrix, T, and its inverse T^{-1} needs only to be computed once as they are not dependent on the measurement data but only on the preset modes that one wishes to analyze. As we shall see Section 9.9.2, this fact enables the LFMI method to be three times faster than standard least squared decomposition methods.

9.6 Eigenmodes Decomposition by Difference Operators

This algorithm isolates each coefficient by iteratively applying a difference operator (such as a derivative) and inverse functions determined by the given modes. This is unfortunately more sensitive to error than the other methods.

9.6.1 Two Mode, One Dimensional, Differentiation Example

As before, we will provide a simple two mode, one dimensional example. We know that we can expand w by

$$w(x) = \Omega_1 v_1(x) + \Omega_2 v_2(x) + \Omega_3 v_3(x) \tag{9.29}$$

Now say that we want to retrieve Ω_3. We then perform the following set of operations, first by dividing both sides by v_1:

$$\begin{aligned}\frac{w}{v_1} &= \Omega_1\frac{v_1}{v_1} + \Omega_2\frac{v_2}{v_1} + \Omega_3\frac{v_2}{v_1} &\quad (9.30)\\ &= \Omega_1 + \Omega_2\frac{v_2}{v_1} + \Omega_3\frac{v_2}{v_1} &\quad (9.31)\end{aligned}$$

where Ω_1 is now a stand-alone constant. One important thing to keep in mind is that we know the left side of the equation from measurements but don't know the right side of the equation, which is what we are trying to solve.

Now we differentiate to eliminate Ω_1:

$$\frac{d}{dx}\left(\frac{w}{v_1}\right) = \frac{d}{dx}\left(\Omega_1\right) + \Omega_2\frac{d}{dx}\left(\frac{v_2}{v_1}\right) + \Omega_3\frac{d}{dx}\left(\frac{v_2}{v_1}\right) \quad (9.32)$$

$$\Rightarrow \left(\frac{w}{v_1}\right)' = 0 + \left(\Omega_2\frac{v_2}{v_1}\right)' + \left(\Omega_3\frac{v_2}{v_1}\right)' \quad (9.33)$$

Now we want to eliminate Ω_2 so we perform the similar operation first by dividing by $\left(\frac{v_2}{v_1}\right)'$ on both sides:

$$\left(\frac{w}{v_1}\right)' = 0 + \Omega_2\left(\frac{v_2}{v_1}\right)' + \Omega_3\left(\frac{v_2}{v_1}\right)' \quad (9.34)$$

$$\frac{\left(\frac{w}{v_1}\right)'}{\left(\frac{v_2}{v_1}\right)'} = \Omega_2\frac{\left(\frac{v_2}{v_1}\right)'}{\left(\frac{v_2}{v_1}\right)'} + \Omega_3\frac{\left(\frac{v_2}{v_1}\right)'}{\left(\frac{v_2}{v_1}\right)'} \quad (9.35)$$

Differentiating...

$$\left(\frac{\left(\frac{w}{v_1}\right)'}{\left(\frac{v_2}{v_1}\right)'}\right)' = \Omega_3\left(\frac{\left(\frac{v_2}{v_1}\right)'}{\left(\frac{v_2}{v_1}\right)'}\right)' \quad (9.36)$$

$$\Omega_3 = \frac{\left(\frac{(w/v_1)'}{(v_2/v_1)'}\right)'}{\left(\frac{(v_2/v_1)'}{(v_2/v_1)'}\right)'} \quad (9.37)$$

We can now repeat this process to obtain Ω_1 and Ω_2, which are also both calculated from measured data.

One issue that may arise is that all of the v_j vectors have zero value for some x, resulting in a singularities in the denominator. This can be solved by simply avoiding those zeros by setting piece-wise domains for x. We note that the generalization of this is in the Appendix.

9.7 Eigenmodes Decomposition by Integral Convergence

This algorithm applies the triangle inequality over a Hilbert Space in an iterative fashion to converge on the modal coefficients. Although it is two order of magnitudes slower than least squares, ICM is precise even with higher level of noise for several modes and beyond.

9.7.1 Basic Principle & Two-Mode Example

The basic principle of this decomposition method lies in the triangle inequality. In this particular form, for unit length vectors, where $\langle V_i \mid V_i \rangle = 1$, $\langle V_i \mid V_j \rangle < 1$ if $i \neq j$. By iterating through the coefficients, this convergence method is able to "integrate out" the non-target components leaving only the target coefficient of order unity.

As before, it is simple to give an example of two modes where

$$w = \Omega_1 v_1 + \Omega_2 v_2 + \Omega_3 v_3 \tag{9.38}$$

The current set of basis vectors, v_n, is not of unit length. Therefore, we first normalize

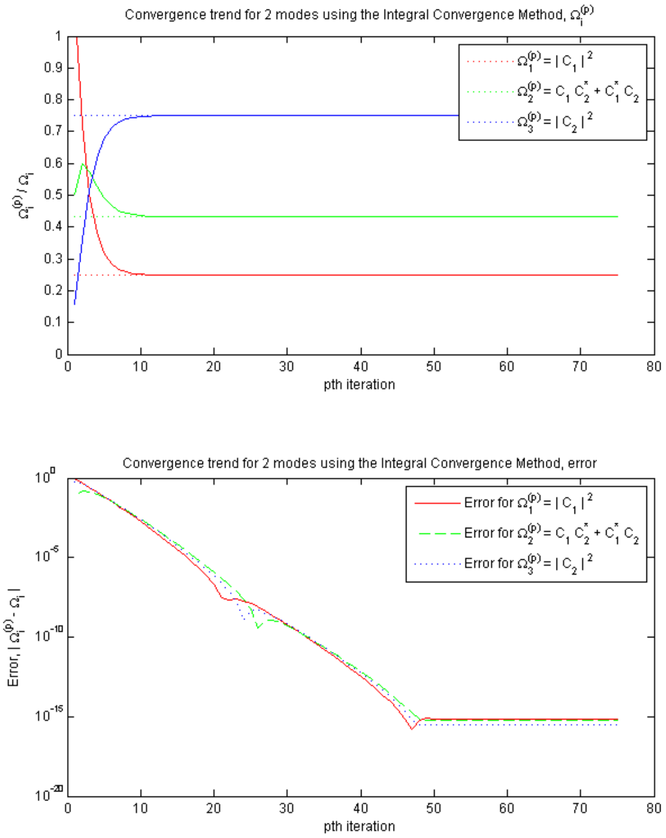

Figure 9.1: The algorithm converging to the pre-set solution. Top graph shows the calculated solution at each iteration; bottom graph shows the error for each variable

all basis vectors:

$$V_n = \frac{1}{\sqrt{\int_{\mathbf{V}} dV v_n v_n^*}} v_i \tag{9.39}$$

$$\xi_n = \Omega_n \sqrt{\int_{\mathbf{V}} dV v_n v_n^*} \tag{9.40}$$

such that

$$w = \xi_1 V_1 + \xi_2 V_2 + \xi_3 V_3 \tag{9.41}$$

To simplify notation, we define a symbol, δ_{nj} for $n \neq j$ for the set of inner products:

$$\delta_{ij} = \langle V_n \mid V_j \rangle \tag{9.42}$$

where $\delta_{nj} < 1$ due to the triangle inequality. More loosely, for any $n \neq j$, $\delta \sim \delta_{nj}$. We will sometimes use δ without the subscripts to talk about all inner products between two different V vectors to simplify the notation.

We will explicitly walk through the first iteration to show how the convergence algorithm works. We calculate the first iteration of ξ_n, defined as $\xi_n^{(1)}$.

First we calculate for $n = 1$

$$\begin{aligned}
\xi_1^{(1)} &= \langle V_1 \mid w \rangle = \xi_1 \langle V_1 \mid V_1 \rangle + \xi_2 \langle V_1 \mid V_2 \rangle + \xi_3 \langle V_1 \mid V_3 \rangle && (9.43) \\
&= \xi_1 + \xi_2 \delta_{12} + \xi_3 \delta_{13} && (9.44)
\end{aligned}$$

Then we calculate for $n = 2$

$$\begin{aligned}
\xi_2^{(1)} &= \langle V_2 \mid w - \xi_1^{(1)} V_1 \rangle && (9.45) \\
&= \xi_1 \delta_{12} + \xi_2 + \xi_3 \delta_{23} - (\xi_1 + \xi_2 \delta_{12} + \xi_3 \delta_{13}) \delta_{12} && (9.46) \\
&= \xi_2 + \xi_3 \delta_{23} - (\xi_2 \delta_{12} + \xi_3 \delta_{13}) \delta_{12} && (9.47)
\end{aligned}$$

Now that we have $\xi_1^{(1)}$ and $\xi_2^{(1)}$, we will isolate ξ_3 as much as we can in this iteration,

$$\begin{aligned}
\xi_3^{(1)} &= \langle V_3 \mid w - \xi_1^{(1)} V_1 - \xi_2^{(1)} V_2 \rangle && (9.48) \\
&= (\xi_1 \delta_{13} + \xi_2 \delta_{23} + \xi_3) - (\xi_1 + \xi_2 \delta_{12} + \xi_3 \delta_{13}) \delta_{13} \\
&\quad - [\xi_2 + \xi_3 \delta_{23} - (\xi_2 \delta_{12} + \xi_3 \delta_{13}) \delta_{12}] \delta_{23} && (9.49) \\
&= \xi_3 - (\xi_2 \delta_{12} + \xi_3 \delta_{13}) \delta_{13} - [\xi_3 \delta_{23} - (\xi_2 \delta_{12} + \xi_3 \delta_{13}) \delta_{12}] \delta_{23} && (9.50)
\end{aligned}$$

Taking a pause, we notice that $\xi_3 - \xi_3^{(1)}$ is of error order $\sim \delta^2$, and given that $\delta < 1$, $\delta^2 < \delta$, but yet the term ξ_3 is still preserved.

Now to calculate $\xi_1^{(2)}$, we attempt to isolate the ξ_1 term:

$$\xi_1^{(2)} = \langle V_1 \mid w - \xi_2^{(1)} V_1 - \xi_3^{(1)} V_2 \rangle \tag{9.51}$$

which will be of lowest order $\sim \delta^2$.

For $\xi_2^{(2)}$ and $\xi_3^{(2)}$,

$$\xi_2^{(2)} = \langle V_2 \mid w - \xi_1^{(2)} V_1 - \xi_3^{(1)} V_3 \rangle \tag{9.52}$$

$$\xi_3^{(2)} = \langle V_2 \mid w - \xi_1^{(2)} V_1 - \xi_2^{(2)} V_2 \rangle \tag{9.53}$$

Noting that $\xi_2^{(2)}$ is of error order δ^2 and $\xi_3^{(2)}$ is of error order δ^3.

We keep on iterating this K times for $\xi_i^{(K)}$ until $\delta^K \to 0$, which each successive step getting converging to the solution where,

$$\Omega_n^{(K)} = \frac{\xi_n^{(K)}}{\sqrt{\int_{\mathbf{V}} dV v_n v_n^*}}. \tag{9.54}$$

Figure 9.1 shows the example of convergence across 75 iterations. In this example an artificial intensity profile was created with the amplitudes being $\mid c_1 \mid^2 = .75$, $\mid c_2 \mid^2 = .25$, and phase difference information being $c_1 c_2^* + c_1^* c_2 = .43$. The calculated solution of each iteration was recorded. It appears that for 2 modes, convergence to roughly machine double precision (1.11×10^{-16}) in about 50 steps.

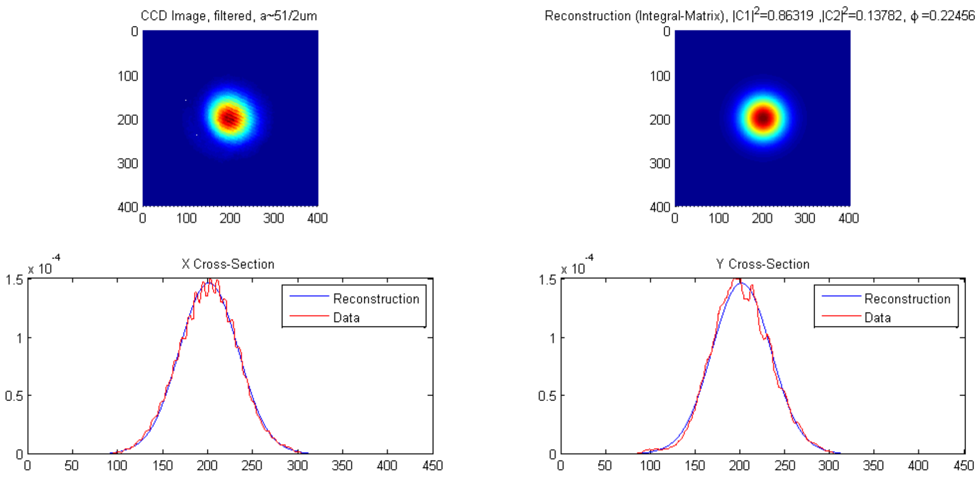

Figure 9.2: Raw modal analysis output for a 26.1mm waveguide, phase difference in units of π (as per the output text in the top of the upper-right plot), all axis lengths in pixels (20 pixels per micron using a 20X objective lens), using the LFMI method. The x-cross cross-section is taken horizontally from the centre; similarly, the y-cross section is taken vertically from the center.

9.8 Two Mode Decomposition experiment with a HeNe laser

The demonstration experiments were conducted with a HeNe laser (633nm) coupling into a hollow-core waveguide of radius a =25.5 µm. The focal waist size is $w \sim 0.30a$ to $0.37a$ enabling simultaneous coupling of the first two fundamental modes. The output mode at the exit plane of the waveguide was recoded using a 20X objective lens and a CCD camera (PointGrey Flea2 model), and the mode amplitude and phase information was extracted using the five different techniques explained above.

From Chapter 4, we have derived the fundamental radially symmetric waveguide modes for a hollow-core waveguide as,

$$\mathrm{EH}_{1M}(r) = J_0(u_M r/a) \tag{9.55}$$

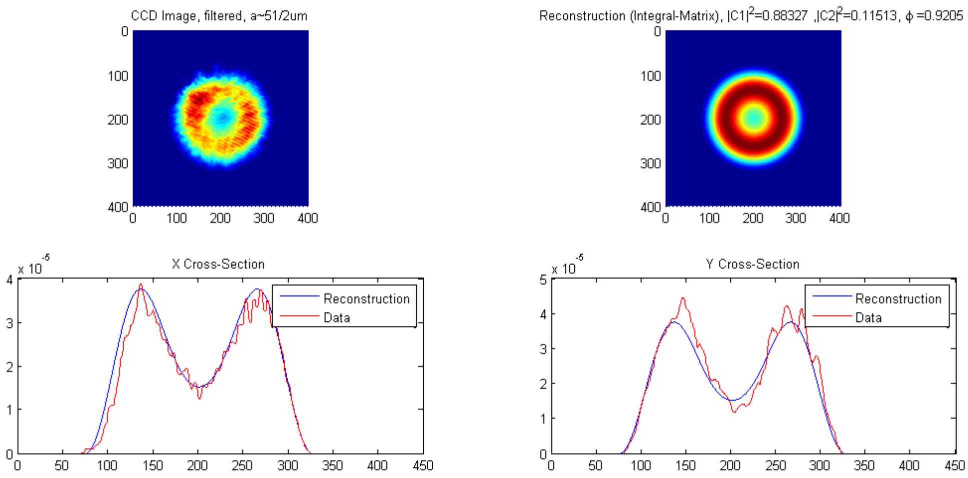

Figure 9.3: Raw modal analysis output for a 30.5mm waveguide, phase difference in units of π (as per the output text in the top of the upper-right plot), all axis lengths in pixels (20 pixels per micron using a 20X objective lens), using the LFMI method. The x-cross cross-section is taken horizontally from the centre; similarly, the y-cross section is taken vertically from the center.

where J_0 is the zeroth order Bessel function of the first kind and u_M is the Mth root of the equation $J_0(u_M) = 0$.

The coupling coefficients at a point z in the waveguide can be calculated as,

$$c_m(z) = \int_{\mathbf{V}} \widetilde{\mathrm{EH}}_{1M} E_{\mathrm{in}}(z)^* dV = \int_0^a \widetilde{\mathrm{EH}}_{1m} E_0 e^{-r^2/w_0^2} 2\pi r dr \tag{9.56}$$

where $E_0 e^{-r^2/w_0^2}$ and $\tilde{E}_{1m}$ represent the normalized input beam and mode amplitudes respectively. The relative phase difference between two coupled modes is,

$$\Delta\phi(z) = \mid (\beta_2 - \beta_1) z \; mod \; \pi \mid \tag{9.57}$$

In analyzing the data from this experiment, only the first two modes, EH_{11} and EH_{12}, were included. This simplifies the analysis, but more importantly, the first two modes dominate the coupling coefficients at this waist size; at the input plane of the waveguide

EH_{13} only accounts for 2% − 8% of total coupling power for $w = .37a$ and $w = .30a$ respectively. Moreover, at waveguide radius $a = 25.5\mu m$, the EH_{13} mode attenuates to under 1% in less than 10mm.

The exit modes of ten waveguides of different lengths were measured. Figures 9.2 and 9.3 show the raw analysis output for two of the ten waveguides. The top left graph show the measured intensity profile from the CCD and top right shows the reconstructed intensity profile using the linear form matrix inversion (LFMI) method of two dimensions as an example as described in Section 9.5. The bottom two graphs show an x and y cross section of intensity for both the actual measurement and the reconstructed intensity.

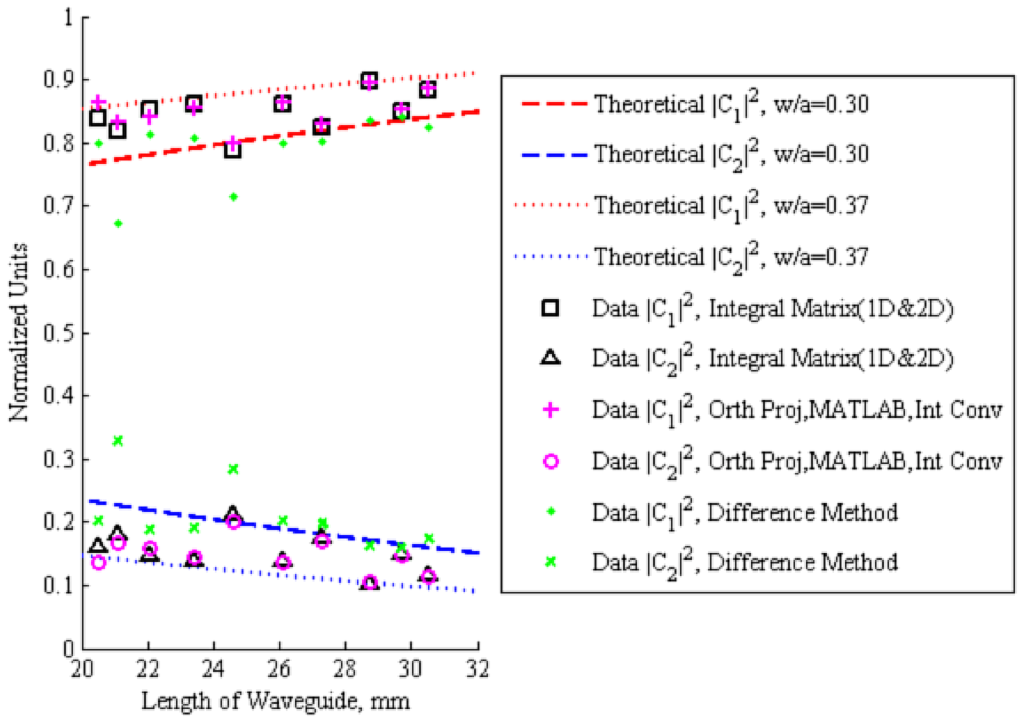

Figure 9.4: Relative energy of the first and second fundamental modes at exit plane as a function of the length of the waveguide. Data points retrieved across 10 waveguides, data and theoretical curve; error bars were not included to reduce clutter in the graph, but the two theoretical lines for $w_0/a = 0.30$ and $w_0/a = 0.37$ represent the uncertainty in the coupling entrance plane.

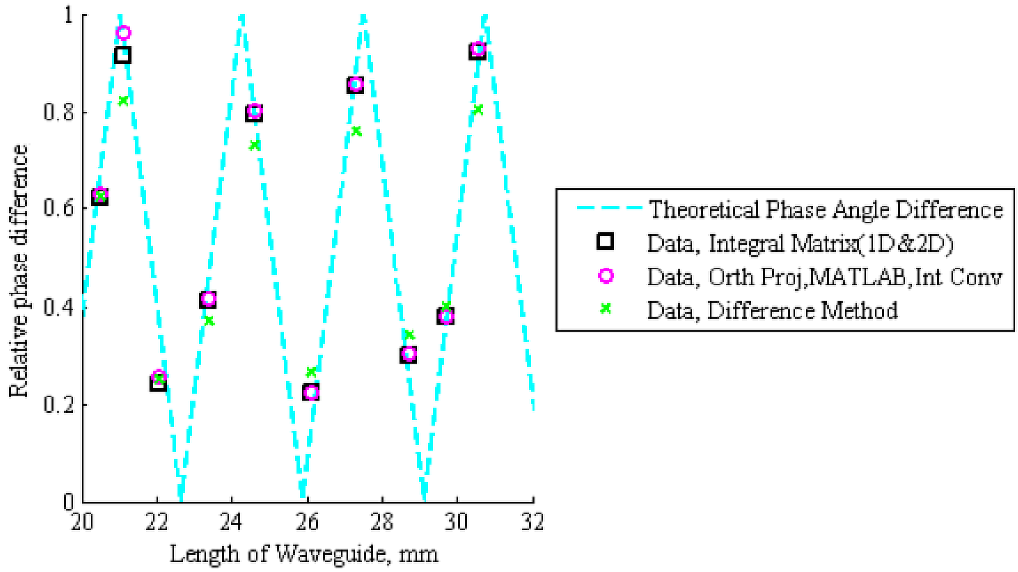

Figure 9.5: Relative phase difference (in units of π of the first two fundamental modes at exit plane as a function of waveguide length). Retrieved phase difference from the data are plotted against theoretical curves; error bars were not included to reduce clutter but each point has an uncertainty of $\pm \sim 0.1\pi$.

As discussed in Chapter 4, the attenuation of the EH_{12} mode will be faster than that of the EH_{11} mode across the waveguide length. This effect has been observed by measuring the mode mixture for waveguides of different length. Figure 9.4 plots $|c_1|^2$ and $|c_2|^2$, the mode coupling strengths for EH_{11} and EH_{12} respectively. The data points along with their theoretical curves for $w = .37a$ and $w = .30a$ are shown, and we have shown the analysis output of all five methods. The higher order modes have been ignored as per the argument above. It is evident that the data fits well within the theoretical curves. More importantly, these algorithms are also able to retrieve the relative phase difference between the two modes, and the phase modulation due to mode beating between the two modes have also been observed. Figure 9.5 shows the retreived relative phase difference and its beating between the two modes plotted against the theoretical plot. The data suggests that the algorithms are able to adequately retrieve phase information from just the intensity information taken from a CCD. In summary, accurate intensity and modal transmission measurements have been made and phase mode beating has been observed. The novel methods have been demonstrated to be accurate for two modes.

9.9 Comparison of mode decomposition methods

9.9.1 Comparison of accuracy and precision

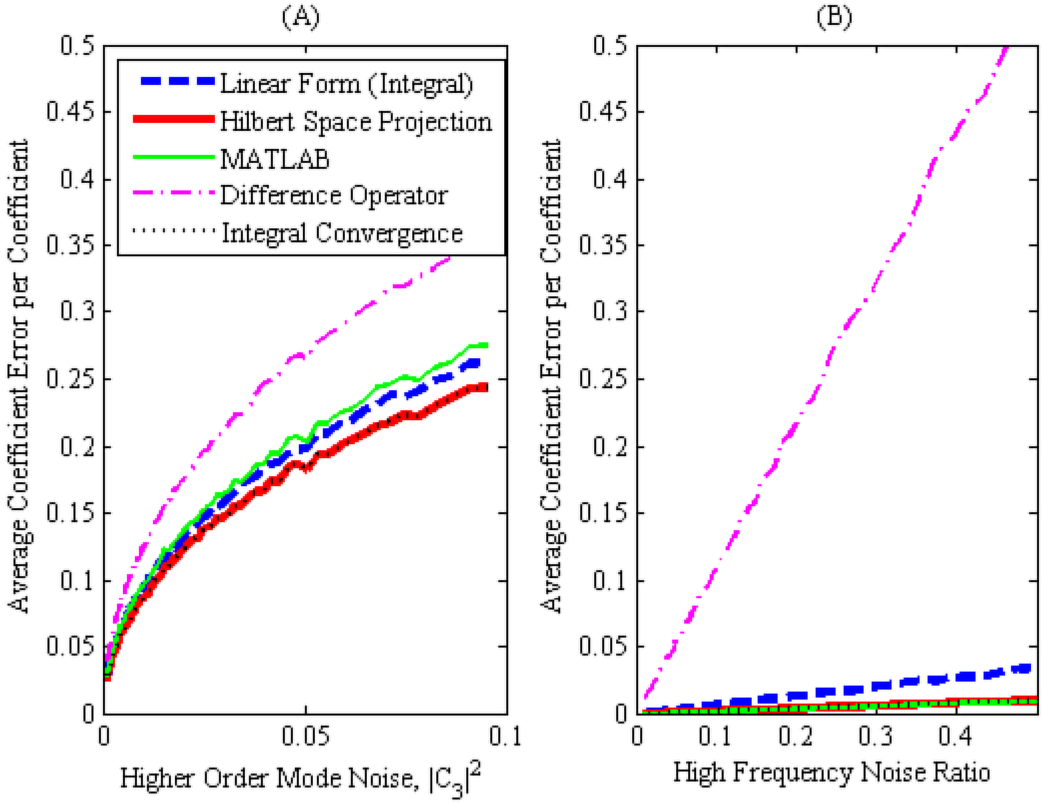

Figure 9.6: (a) Plot of the average coefficient error, $< \mathfrak{E} >$, by method for resolving two modes (EH_{11}, EH_{12}) as a function of the intensity $C_3C_3^*$ of an added higher order EH_{13}, $K = 10,000$ (b) Plot of the average coefficient error, $< \mathfrak{E} >$, by method for resolving two modes (EH_{11}, EH_{12}) as a function of random noise level R_{HFnoise}. $K = 10,000$

The sensitivity to random high frequency noise of modal decomposition accuracy has been analyzed for two modes and three modes. The sensitivity to the existence of a higher order mode was also explored; for example, the impact of the EH_{13} mode when

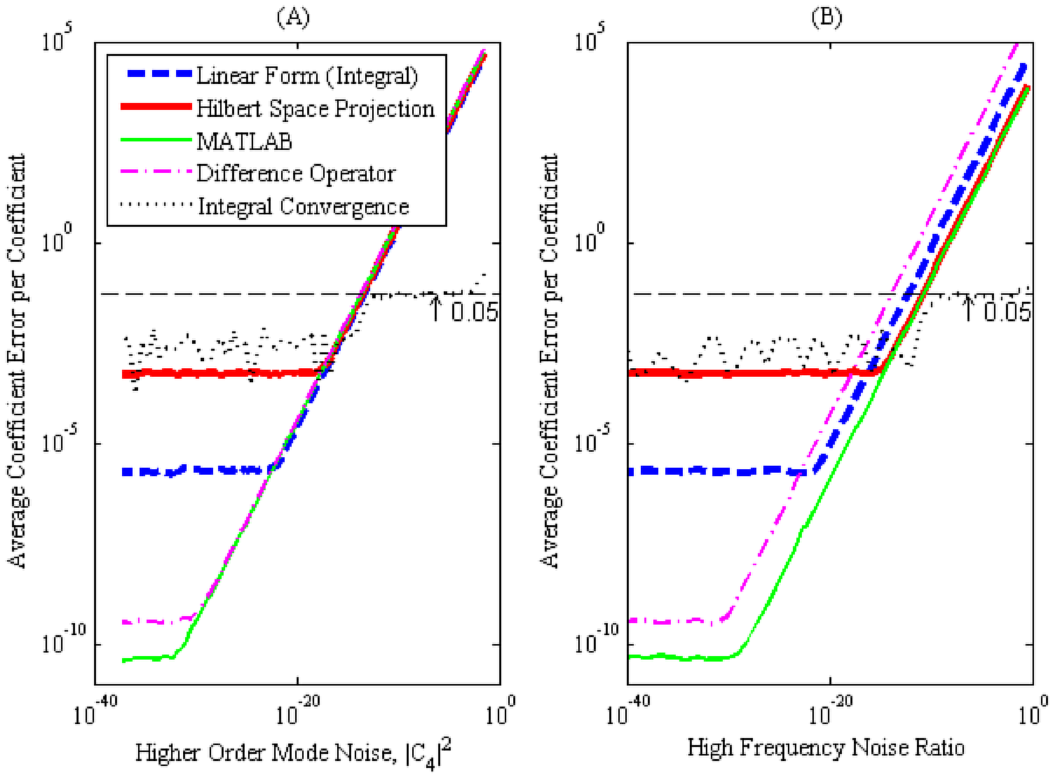

Figure 9.7: (a) Plot of the average coefficient error, $< \mathfrak{E} >$, by method for resolving three modes (EH_{11}, EH_{12}, EH_{13}) as a function of the intensity $C_4C_4^*$ of an added higher order EH_{14} mode on a log scale. $K = 10,000$ (b) Plot of the average coefficient error, $< \mathfrak{E} >$, by method for resolving three modes (EH_{11}, EH_{12}, EH_{13}) as a function of random noise level R_{HFnoise}. $K = 10,000$

we are only analyzing the first two modes. Each of the methods have been tested against 10,000 different random modal configurations. The simulations were conducted in one dimension of $L = 2000$ pixels with $dV = 2\pi r dr$. The difference operator was selected to be the derivative with $L/10$ points for DOM.

As before, the noise added function is defined as $\tilde{w} = w + \epsilon$ as before with w being the 'pure' function and ϵ being the noise. Here the calculated coefficients of $\tilde{w}$ are defined as $\tilde{\Omega}$ and the correct answer is defined as Ω. The average error per coefficient, $< \mathfrak{E} >$ across

$K = 10,000$ iterations is defined as:

$$< \mathfrak{E} >= \frac{1}{K}\sum_{i=1}^{K}\left(\frac{1}{N}\sum_{n=1}^{N} \mid \tilde{\Omega}_{i,n} - \Omega_{i,n} \mid\right) \tag{9.58}$$

Two types of noises have been evaluated. The first type was to test the sensitivity these methods have to the existence of a higher order mode, in this case, the next order mode. A higher order mode is added into the overall field function and the field function is then renormalized. For Figures 9.6a and 9.7a, $< \mathfrak{E} >$ is plotted against $C_3C_3^*$ and $C_4C_4^*$ respectively.

The second type of noise is the high frequency noise added on a pixel scale, which are shown in 9.6b and 9.7b. For each pixel, a random value is added to w to simulate random noise that might occur in a measurement. The noise ratio is then defined as:

$$R_{\text{HFnoise}} = \frac{\int_{\mathbf{V}} |\varepsilon|^2 dV}{\int_{\mathbf{V}} |w|^2 dV} \tag{9.59}$$

Figure 9.6 suggests that for decomposing two modes HSP and ICM provide the most accurate results whilst DOM is the least accurate with respect to both type of noises as expected. However, DOM's accuracy could potentially be improved by selecting a more suitable difference operator.

Figure 9.7 illustrates that the ICM with constraint optimization (see Appendix) provides a significantly more accurate method than any other methods for analyzing three modes. The lower accuracy for the other methods for three modes is because the determinant of the basis transformation matrix and of T respectively is close to singular due to the spatial frequency required to resolve more than three modes with these two methods.

9.9.2 Computation time

The time it takes for each of the methods to calculate the coefficients for the data collected of the ten waveguides with the EH_{11} and EH_{12} modes were analyzed. Each algorithm ran 100 times for each data set resulting in 1000 timing measurements for each method; we ran the calculations on a standard T61 Lenovo Laptop (Intel Core i5 CPU at 2.53 GHz and 4 GB RAM)

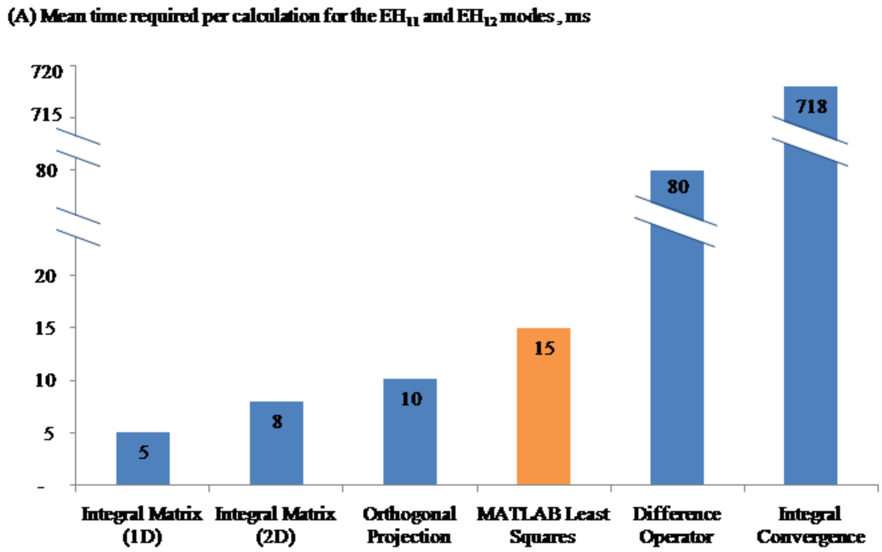

(B) Basic Statistics on speed of calculation for different methods, ms

	Integral Matrix (1D)	Integral Matrix (2D)	Orthogonal Projection	MATLAB Least Squares	Difference Operator	Integral Convergence
Min	4.6	7.3	9.2	13.3	65.1	667
Mean	5.1	8.0	10.2	15.0	79.6	718
Max	10.5	13.2	17.0	23.9	158	1020
Stddev	0.46	0.62	0.80	1.40	8.82	31.2

Figure 9.8: (a) Time of of calculation for each method in milliseconds for the HeNe data collected in resolving the EH_{11} and EH_{12} modes, $n = 1000$. (b) Basic statistics on speed of calculation for of the data from chart (a), in milliseconds.

Figure 9.8 compares the speed of calculation across each of the methods. The one-dimensional Integral Matrix (LFM) calculation is three times faster than the internal MATLAB least squares routine whilst the Integral-Convergence method is roughly two orders of magnitudes slower. However, as we have seen in Section 9.9.1, the Integral-Convergence method seems to be the only method able to cope with high noise beyond two modes. On the other hand, LFM may be useful for real-time mode decomposition of two modes due to the fact that it is significantly faster than all other methods.

9.10 Conclusion

In this chapter, four novel modal phase and amplitude retrieval methods are proposed. A demonstration experiment using a HeNe laser and a hollow core waveguide was conducted, where a two-modal decomposition showed good fit with theoretical predictions. The methods were compared against the internal MATLAB least squares fit routine for both precision and accuracy as well as computational time. In the next chapter, we will use these methods to analyse modes excited by a spatial light modulator.

Chapter 10

Beam Control with a Spatial Light Modulator

In the previous chapter, we discussed identifying and analysing modes. This chapter, we will focus on controlling the beam profile and exciting higher order modes with a spatial light modulator (SLM).

Not only are spatial shaping of beams important for exciting specific modes for high harmonic generation, it is also important for other applications including lithography [123], micro-machining [102], and chemical imaging [36]. In fact, in [36], our method described in this Chapter has been employed to conduct dynamic imaging of surfaces. In applications of this type it is often required to control the amplitude and phase of radiation in the back focal plane of an optical system.

Present methods to achieve this include using two spatial light modulators (SLMs), one for phase control and the other for amplitude control [126]; controlling the input polarization state [126]; mapping two conjugate planes onto a single SLM [58]; or iterative algorithms such as the Gerchberg-Saxton algorithm [42; 45; 102].

Several techniques for achieving amplitude control with a single phase-only SLM have been developed. In essence these achieve amplitude control by introducing a pattern of high spatial frequency phase jumps to the SLM in order to diffract a portion of the incident radiation to large angles, thereby effectively introducing a partial loss. Control of the loss which is introduced has been achieved by modulating the width of square wave phase jumps [30], introducing phasor manipulation for adjacent SLM pixels [54], and applying saw-tooth [122] or top-hat [12; 82] phase modulations of varying amplitude. In the latter, for example, an analytic solution can be found where the height of the square phase jumps is proportional to $2\arccos(|T|)$, where $|T|$ is the required amplitude transmission of the mask [12].

For a single phase only SLM the three examples described above give a recipe for a *particular* shape of phase mask [12; 82; 122]. However, to our knowledge, no *general* analytic solution has been proposed for the pattern which should be applied to a phase-only SLM to generate a prescribed complex amplitude in the far field. This chapter proposes such a solution and provides a general framework for generating a suitable phase-only mask. By introducing two domains at the focal plane, a domain of interest and a domain that can be ignored, we can identify slow- and fast-varying components of the near-field beam which correspond to these two domains. This allows us to calculate analytically the phase mask required for *any* type of fast modulation. Our method therefore provides a mathematical framework for unifying the various methods for calculating single-SLM phase masks. In this chapter we describe this method in detail and demonstrate its application in proof-of-principle experiments; the arguments follow that from our paper [69].

10.1 Theoretical derivation

We first start with the familiar integrals relating the amplitude $u(x, y)$ of radiation of wavelength λ in the near-field to that, $U(X, Y)$, in the back focal plane of an optical

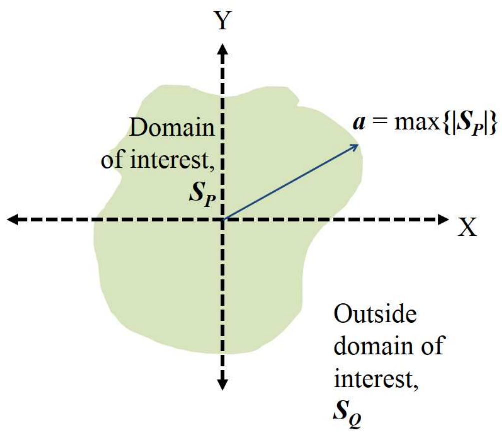

Figure 10.1: Illustrative domains for the focal plane where S_P is the domain of interest and S_Q is outside this. The value a is defined as the the maximum distance from the origin of the boundary between S_P and S_Q.

system of focal length f:

$$\begin{cases} U(X,Y) &= \frac{e^{ik\sqrt{X^2+Y^2+f^2}}}{\lambda f} \int_{-\infty}^{\infty}\int_{-\infty}^{\infty} dxdy \\ & \times u(x,y)e^{-i\frac{k}{f}(xX+yY)} \\ \\ u(x,y) &= \int_{-\infty}^{\infty}\int_{-\infty}^{\infty} dXdY \\ & \times \frac{U(X,Y)}{e^{ik\sqrt{X^2+Y^2+f^2}}} e^{+i\frac{k}{f}(xX+yY)} \end{cases} \tag{10.1}$$

where $k = 2\pi/\lambda$ is the angular wave number. The incident amplitude u can be written as $u = |u_0|e^{i\psi_0}T$, where $|u_0|$ and ψ_0 are the amplitude and phase of the incident beam respectively, and T is the complex amplitude transmission function of the SLM.

In the focal plane we define a domain of interest, S_P, in which we wish to control the amplitude and phase of the radiation, and a domain S_Q which lies outside S_P. We also define a as the maximum distance from the origin to the boundary of S_P.

From these definitions, illustrated in Fig. 10.1, we can write,

$$\begin{aligned}
u(x,y) \quad &= \int\int_{S_P} dXdY \frac{U_P(X,Y)}{e^{ik\sqrt{X^2+Y^2+f^2}}} e^{+i\frac{k}{f}(xX+yY)} \\
&+ \int\int_{S_Q} dXdY \frac{U_Q(X,Y)}{e^{ik\sqrt{X^2+Y^2+f^2}}} e^{+i\frac{k}{f}(xX+yY)} \qquad (10.2) \\
&= P(x,y) + Q(x,y) \qquad (10.3)
\end{aligned}$$

where U_P is the beam profile we wish to control — which we will call the 'target beam profile', U_Q is the beam profile outside the zone of interest, and P and Q are the two integrals across the S_P and S_Q domains respectively. Since U_P is known, the amplitude P is also known. Further, since P is related to the complex amplitude in the domain of interest S_P, which is close to the axis, the spatial frequencies contained with P will be low. In contrast, the high spatial frequencies in Q is related to radiation diffracted to regions away from the axis, and will therefore be associated with the S_Q domain.

An exact solution of Eqn (10.1) would require T to have a spatially-varying amplitude and phase. However, for a phase-only SLM we have the restriction $|T| = 1$. Since P is defined by the target beam profile we need to find a Q that fulfills the phase-only constraint. Writing $Q(x,y) = Q_0(x,y)e^{i\phi(x,y)}$, the constraint $|T| = 1$ becomes

$$Q_0^2 + (Pe^{-i\phi} + P^*e^{+i\phi})Q_0 + (PP^* - u_0^2) = 0, \qquad (10.4)$$

from which Q_0 can be found for each point (x,y). The phase mask $T = ue^{-i\psi_0}/|u_0|$ is given by solving the quadratic equation:

$$\begin{aligned}
|u_0|e^{i\psi_0}T \qquad &= P + e^{+i\phi}\left\{-\Re[Pe^{-i\phi}]... \right. \\
&\left. \pm\sqrt{\Re[Pe^{-i\phi}]^2 - (|P|^2 - |u_0|^2)}\right\} \qquad (10.5)
\end{aligned}$$

where $\Re$ denotes the real part.

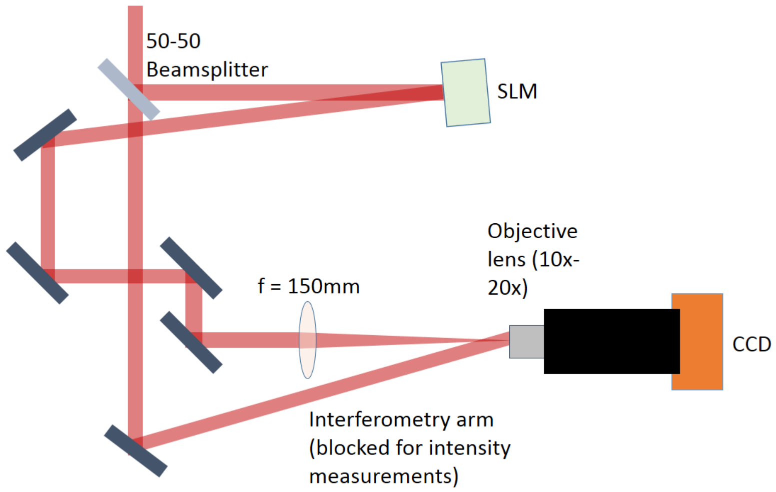

Figure 10.2: General schematic for demonstration experiment. Note that the interferometry arm is blocked for intensity measurements.

Note that a solution for the phase mask has been found without specifying the form of the fast phase modulation ϕ, in contrast to earlier work which from the outset assumed a square wave [12] or sawtooth [122] modulation. The general framework established above allows different types of phase modulation to be employed and offers a route for optimizing the aspects of the mask performance, such as its efficiency. For example, if we set $\phi = \text{sgn}[\cos(bx)]\pi/2 + \arg(P)$ and discretize each half period, the solution for T is identical to the square-wave modulation described in [12] with period of b.

10.2 Demonstration experiments

In our experiments discussed below, we use a simple phase modulation on Q, where we consider a phase modulation of the form $\phi(x, y) = b_x x + b_y y$ where $b_x \gg ak/f$ and $b_y \gg ak/f$.

Fig 10.2 shows schematically the arrangement employed in our experiments. We employed a HeNe laser operating at 633nm with a phase-only SLM (Hamamatsu X10468-02) with 800×600 pixels that is 16 by 12mm wide and with a bit depth of 256 and an

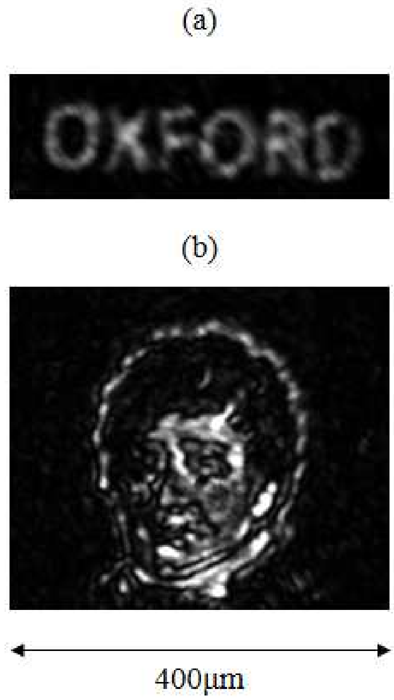

Figure 10.3: Measured far-field intensity profiles for generation of (a) text; (b) a portrait of Joseph Fourier

aperture ratio of 95%. A Gaussian beam with a spot size of 6.4mm was reflected from the SLM at near normal incidence and was focused by a lens of focal length $f = 150$mm. The analysis above assumes that the lens captures all light diffracted by the SLM. In practice light diffracted at large angles may miss the lens and so not form part of the image, although this is unimportant if the light would have been focused outside the domain of interest. The transverse intensity profile in the back focal plane of the lens was recorded by using a 10x or 20x microscope objective to image this plane onto a 1600 x 1200 pixel CCD array (Point Grey Flea 2: FL2-20S4M-C, 12 bits). A beam splitter was used to create a plane reference beam which could be interfered with radiation in the back focal plane of the lens; this allowed the phase of the focused beam to be determined from the interference pattern produced. Phase retrieval from the interferometry data was performed using the method outlined by Takeda et al [113]. The reference beam was

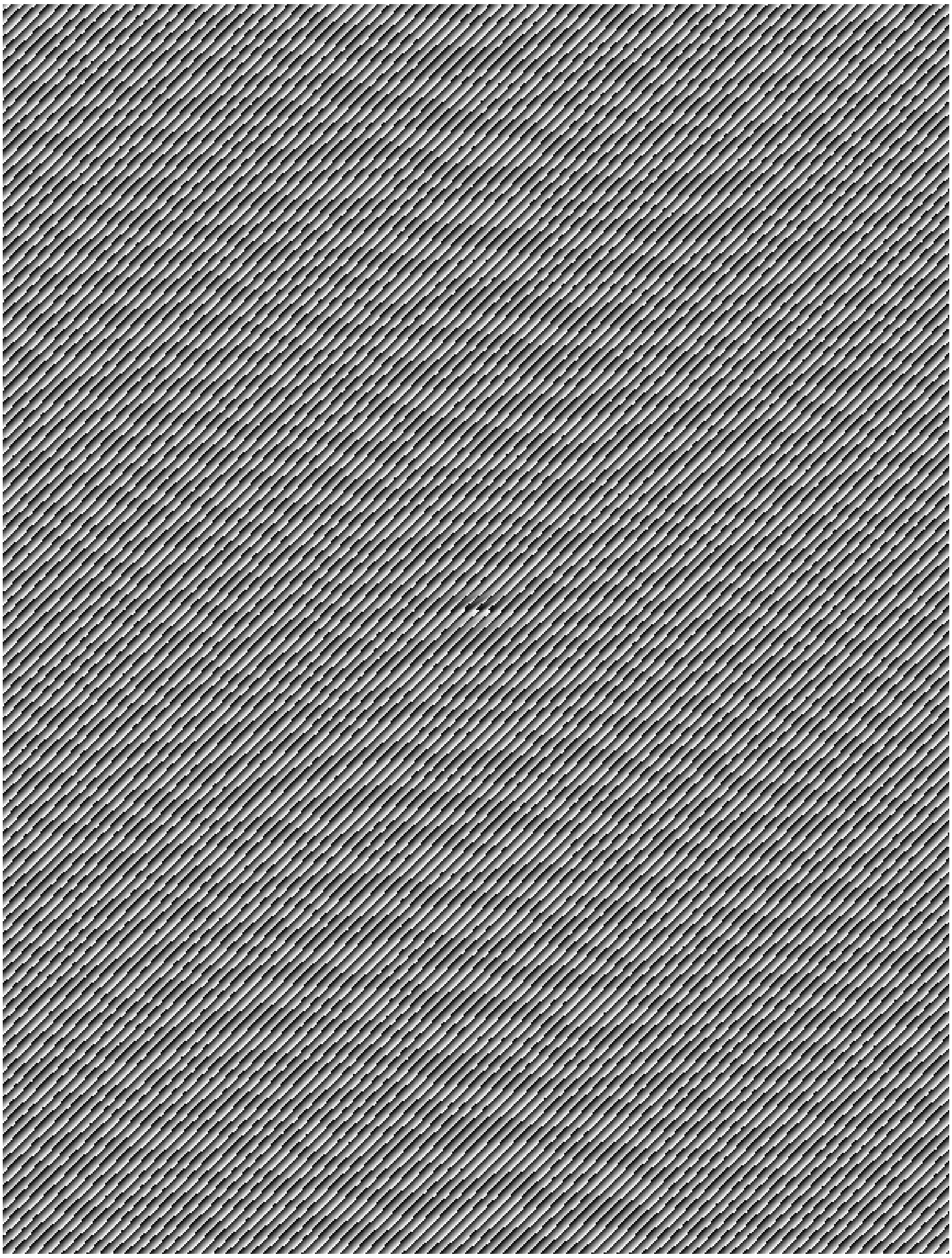

Figure 10.4: Phase mask applied for the portrait of Joseph Fourier from Figure 10.3b; phase displayed on a grayscale where black is 2π radians and white is 0 radians.

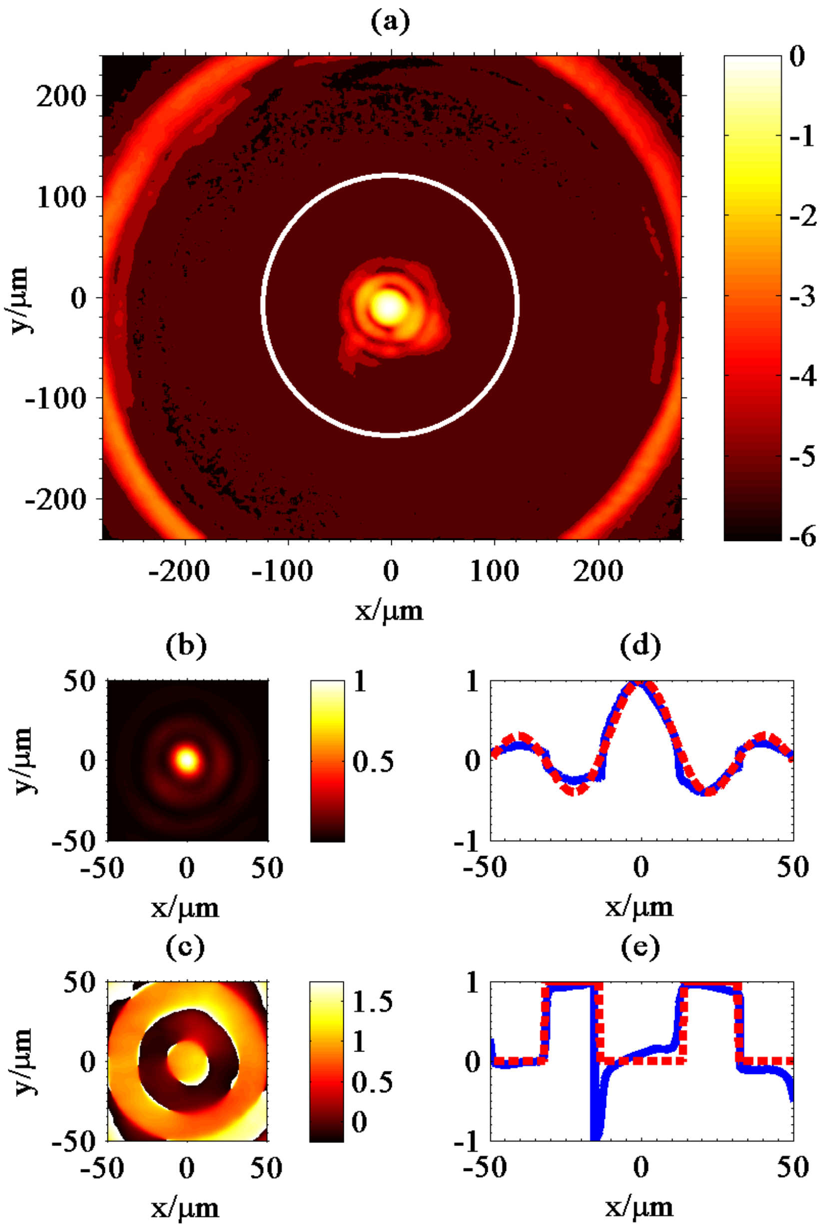

Figure 10.5: Generation of the EH_{13} mode by a phase-only SLM. (a) shows the intensity profile, on an arbitrary logarithmic scale, inside and outside the domain of interest, the boundary between these domains being indicated by the white circle. (b) and (c) show respectively the measured profiles in the axial region of the transverse profiles of the intensity in arbitrary units and phase in units of π. (d) and (e) compare lineouts of the measured (blue, solid) and target (red, dashed) real part of the field amplitude in arbitrary units (d) and phase in units of π (e).

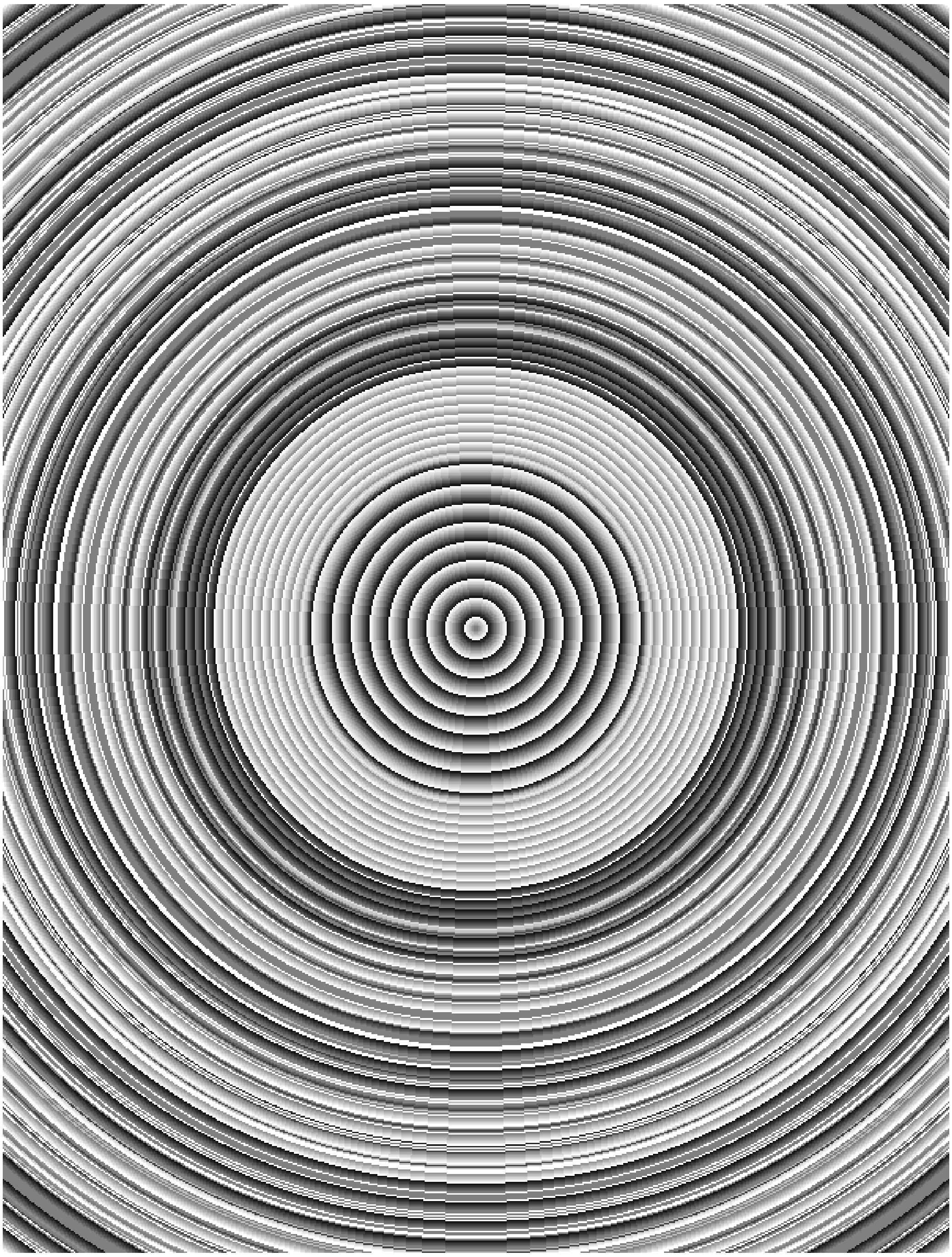

Figure 10.6: Phase mask applied for the EH_{13} mode as shown in Figure 10.5; phase displayed on a grayscale where black is 2π radians and white is 0 radians.

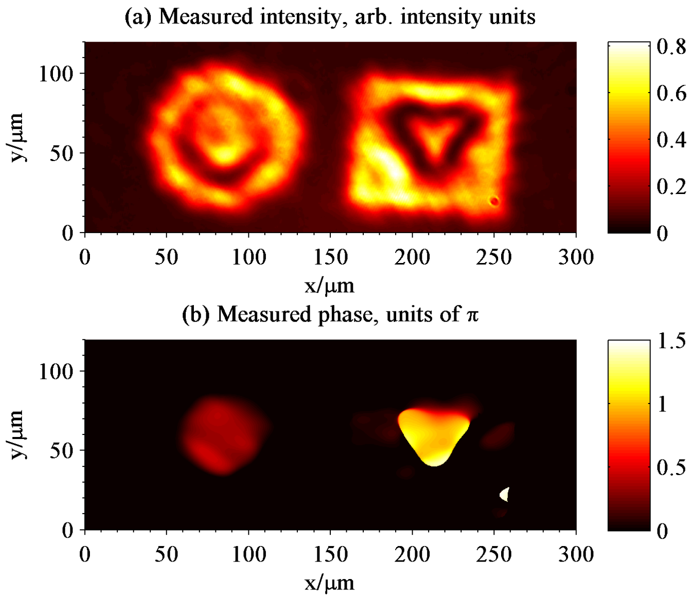

Figure 10.7: Demonstration of simultaneous control of amplitude and phase by generating: (left) a circle of uniform intensity, within which is a circular region with a phase of $\pi/2$ relative to the surrounding annulus; (right) a square, within which is a triangular region with a phase shifted by π relative to the surrounding region. The measured transverse intensity and phase profiles are shown in (a) and (b) respectively. We also note that the phase in (b) was set to zero if the intensity was below 10% of maximum.

blocked for measurements of the transverse intensity profile. We note that light diffracted outside the domain of interest could be removed from the back focal plane by inserting a spatial filter; however, this was not necessary for these experiments.

Fig 10.3 shows two examples of the control of the far-field intensity (but not phase) to produce text and an image; for these examples the period of oscillation was set to $2\pi/b_x = 2\pi/b_y = 7$pixels. Figure 10.4 shows the phase mask applied to the SLM to generate the image in Figure 10.3b.

Fig 10.5 demonstrates the generation of a waveguide mode, the EH_{13} hybrid mode [28] of a hollow capillary waveguide using a radially-symmetric phase modulation of the form $\phi(r) = b_r r$ with $2\pi/b_r = 16$ pixels. In Fig 10.5a the outermost ring results from light diffracted out of the domain of interest from regions in the near field with a low required transmission. It can be seen that within S_P the amplitude and phase profiles are

Figure 10.8: Raw phase measurement data with the interferometry arm unblocked.

in excellent agreement with the target profile. Figure 10.6 shows the phase mask applied to the SLM to generate the EH_{13} mode.

As a final example, Fig 10.7 shows simultaneous control of the transverse amplitude and phase profiles in the far field. Note that the dark areas in the intensity profiles of Fig 10.7a result from the step change in phase at these points, and hence a region in which the amplitude passes through zero. As a reference, Figure 10.8 provides the raw CCD measurement of the phase with the interferometry arm unblocked.

10.3 Limits and optimization

The maximum size of the domain of interest can be determined as follows. For an ideal SLM providing both phase and amplitude control, the maximum linear size of the region in the image plane in which the complex amplitude could be controlled is $f\lambda/h$ where h is the spacing of the SLM pixels. However, for a phase-only SLM it is necessary to devote more than a single pixel to control the complex amplitude in the domain of interest, which increases the effective size of the pixels. For example, for a linear ramp with $b = \pi/(Nh)$ the effective pixel size is Nh and hence the size of the region over which phase and amplitude can be controlled is $f\lambda/(Nh)$, i.e. $1/N$th of that possible with an SLM providing both phase and amplitude control. For a phase-only SLM at least two pixels are required to provide phase and amplitude control [54], and hence the maximum

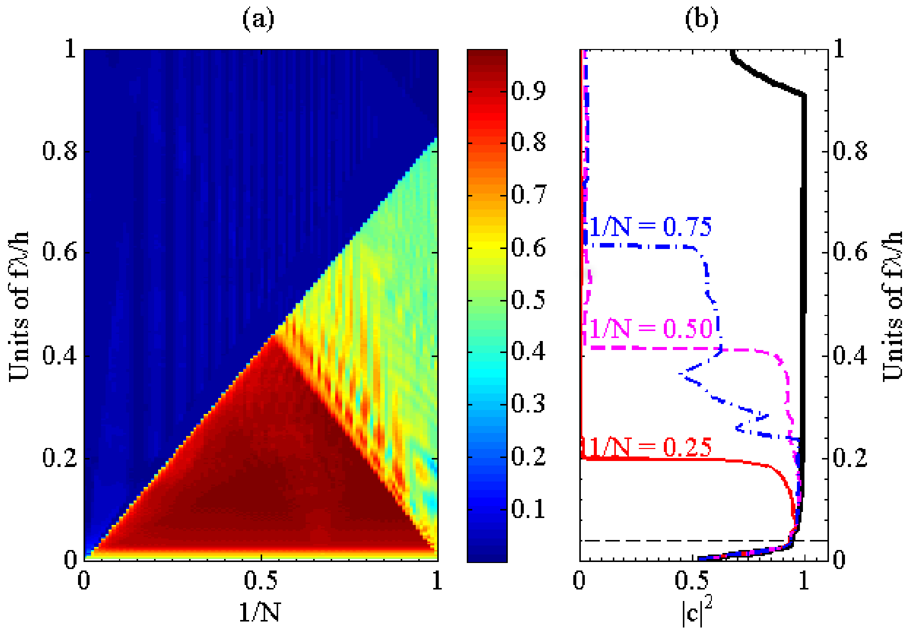

Figure 10.9: Plot (a) shows the agreement ratio $|c|^2$ as a function of size of area of interest in units of $f\lambda/h$ and normalised slope of the linear ramp bh/π in units of $1/N$. Plot (b) shows the lineouts for cases where $1/N = 0.25, 0.5, 0.75$ respectively; the solid black line shows the agreement ratio for a theoretical ideal SLM with both amplitude and phase modulation. The parameter space scan was conducted using a one-dimensional system where the test function was a top-hat with the size of the area of interest in question.

size of the domain of interest is $f\lambda/(2h)$.

Figure 10.9 shows a parameter space scan of the slope of the linear ramp and size of the area of interest. The agreement ratio $|c|^2$ is calculated as the normalised inner product between an ideal top-hat versus the generated beam profile at the focal plane. As expected, as the phase slope increases from 0 to $0.5/N$, the available size of the domain of interest increases as well, with a maximum dominan of interest at $f\lambda/(2h)$ as expected from the argument above.

10.4 Mode beating experiments with an SLM

In the previous sections, we have shown that we have complete control over phase and amplitude on the beam profile using an SLM. More specifically, in Section 10.2, we have

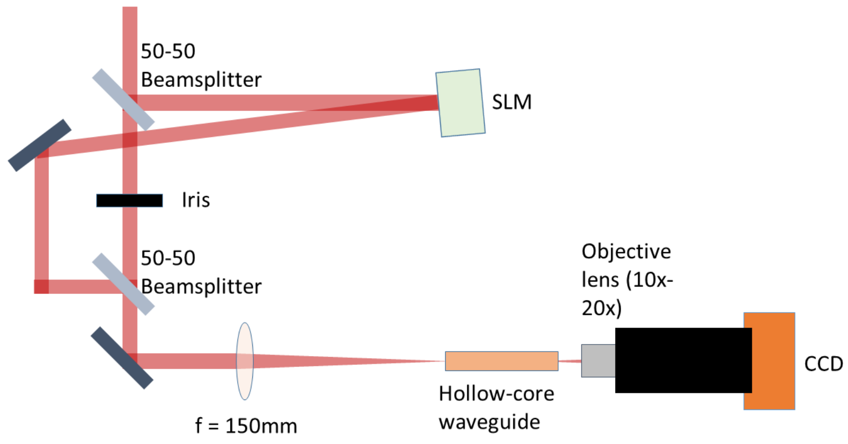

Figure 10.10: General schematic for mode excitation experiment.

shown that it is possible to generate the EH_{13} mode to very high accuracy. In this section, we will couple in two modes to simulate one of the HHG experiments described in the previous chapters. Figure 10.10 shows a schematic for an experiment that attempts to excite two modes. The HeNe beam is split into two, one beam is adjusted by an iris optimized to excite the fundamental EH_{11} mode; the other beam is modified by the SLM to generate the beam profile of the EH_{12} mode at the focal plane. The two beams are then combined by another beam splitter and focused into an a = 51um radius hollow core waveguide. The waveguide is 4cm long, and an imaging system is set up with an objective lens at the exit of the waveguide.

At the exit plane, the phase difference between the first and second order modes is dependent on the phase difference between the two input beams. For this, small vibrations from un-stabilized experimental set-up and/or air currents caused the phase difference between the two input modes to fluctuate on a time-scale of a few seconds. As a consequence, mode beating was observed in the output plane.

Figure 10.11 shows three separate CCD measurement and mode retrieval results. We set the mode intensities to be roughly equal at the exit of the waveguide. We then

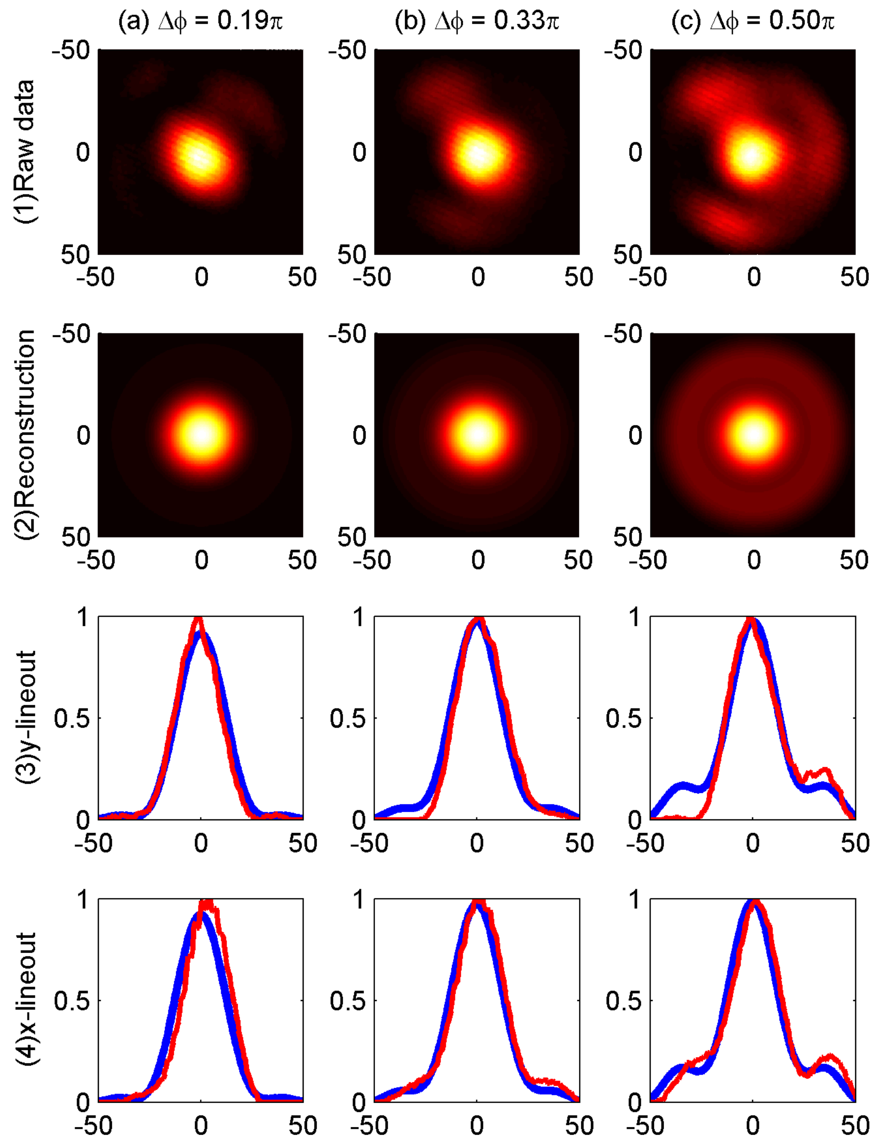

Figure 10.11: Three sets of CCD measurements and mode analysis outputs. Column (a) shows the set of measurements and outputs retrieved phase difference of $\Delta\phi = 0.19\pi$ with retrieved mode coupling strengths of $|c_1|^2 = 0.5$, $|c_2|^2 = 0.5$; Column (b) for $\Delta\phi = 0.33\pi$ with $|c_1|^2 = 0.54$ and $|c_2|^2 = 0.46$; Column (c) for $\Delta\phi = 0.5\pi$ with $|c_1|^2 = 0.5$ and $|c_2|^2 = 0.5$. Row (1) shows the raw measured intensity data. Row (2) shows the reconstruction based on retrieved mode information using the Linear Form/Integral Algorithm described in the previous chapter, Row(3) shows the y-axis lineout and Row (4) shows the x-axis lineout. For Rows (3) and (4), the blue line represents the theoretical reconstruction whilst the red line shows the actual data. For Rows (1) and (2) the vertical axis is the x/µm axis whilst the horizontal axis is y/µm axis; for Rows (3) and (4), the horizontal axis is in units of µm whilst the vertical axis is intensity in arbitrary units.

used the Linear Form/Integral mode (LMFI) retrieval process detailed in the previous chapter. The effect of mode-beating is seen in the retrieved difference in phase of the input modes, whereas the relative energies of the two modes remained reasonable constant. The reconstructed beam profiles are in good agreement with the measured data, showing that the exit modes are well described by the expected super-position of the selected input modes.

10.5 Conclusion

In conclusion, we have presented a method for simultaneous control of the far-field transverse amplitude and phase profiles of a beam using a phase-only SLM. The framework we have described is general in the sense that the method can be used with any functional form of the applied phase $\phi(x, y)$. This flexibility will allow optimization of measurements of the mask performance, such as its efficiency or accuracy.

Moreover, we have used this method to couple the first two modes in a hollow-core waveguide, providing a basis for future experiments in multi-mode or polarisation-controlled QPM for high harmonic generation.

In this chapter we assumed that the area of interest S_P corresponded to low spatial frequencies in the near-field. In principle, it is possible using the same techniques to control areas in the back-focal plane corresponding to high spatial frequencies in the near field instead by setting ϕ to be slowly varying.

Chapter 11

Hollow-Core Birefringent Waveguides

11.1 Introduction

In Chapters 5 and 6, we briefly discussed advances in linear and circular birefringent waveguides in the context of potentially achieving PBQPM and ORQPM respectively. In this chapter, we will discuss this topic in more detail. We will also discuss some original work by the Author around hollow-core rectangular waveguides and show some very initial evidence of optical rotation and birefringence.

In exploring the literature of birefringent waveguides, authors often neglect the difference between phase and group birefringence [44]. Up until this point, when we discussed birefringence, B, we referred to *phase birefringence*, the difference in the mode propagation between the two polarization states,

$$B = B_{\text{phase}} = \frac{\lambda|\beta_X - \beta_Y|}{2\pi}. \tag{11.1}$$

where β_X and β_Y are the mode propagation constants as defined in Chapter 4.

However, it is also important to discuss group birefringence; as mentioned in Chapters 5 and 6, the group dispersion between the slower and the faster polarisation states may cause the two modes to separate, and thus end polarization beating in a driving pulse after a some propagation length. The group birefringence can be written as [44],

$$B_{\text{group}} = \frac{\partial \beta_X}{\partial k} - \frac{\partial \beta_Y}{\partial k} = \frac{\partial(\beta_X - \beta_Y)}{\partial k} = B(\lambda) - \lambda \frac{\partial B}{\partial \lambda}. \tag{11.2}$$

In many cases, the difference between group and phase birefringence is only around $10 - 15\%$; hence, waveguides with high group birefringence often also have high phase birefringence [3; 24]. For the purposes of PBQPM (or ORQPM) however, it is important to have high phase birefringence but low group birefringence. We note however, that PBQPM or ORQPM can be 're-phased' by reversing the birefringence after a certain propagation length.

11.2 Photonic crystal fibres (PCFs)

Photonic crystal fibres (PCFs) are a new class of optical waveguide fibres that are based on periodic structures that confine and modify the properties of light that propagate through them. Given that they can be fabricated with a wide variety of optical properties, a significant amount of effort has been expended by the scientific community to better understand and commercialize them. In this section, we will discuss hollow-core linear birefringent but not hollow-core circular birefringent PCFs. This is because some progress has been made around linear birefringence in hollow-core PCFs so far, but the focus is still around solid-core for circular birefringence.

Another potential issue with PCFs for HHG is that the harmonic generation process requires extremely high laser intensities. Given the delicate nature of PCFs, driving HHG within such structures requires considerable care – but this has been achieved in Ref [48]

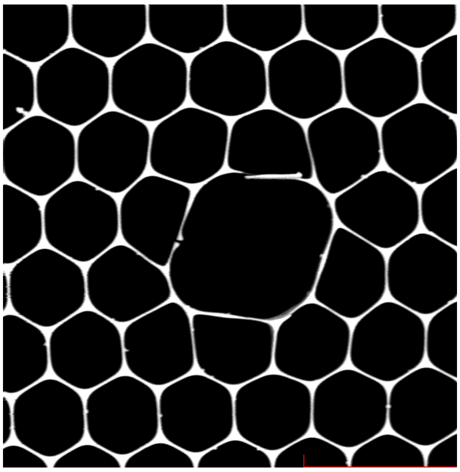

Figure 11.1: Cross section of the hollow-core PBGF profile. The dark regions are air, while the white regions are glass. Caption and figure from [24].

with driver pulses of 30-fs at 10 µJ using special kagome-like fibers that guide nearly all the light in the core, preventing damage to the walls [27; 34; 48].

11.2.1 Linear birefringent PCFs

To date, significant progress has been made in maximizing the birefringence (both group and phase) for PCFs in the mid-IR range (1-2 microns wavelengths) due to potential applications in optical communications, devices and fibre sensors[2; 3; 24; 96]; in fact commercially available birefringent PCFs in this optical range have been realized by NKT Photonics [2].

These birefringent PCFs are often constructed with asymmetry between the x- and y- axes. Figure 11.1 shows a scanning electron micrograph of one of the first highly birefringent hollow-core PCFs at 1550nm from Chen et al. [24], while Figure 11.2 provides specifications for the PCF. Figure 11.3 compares the simulations of these birefringent PCFs from Alam et al. with the data from Chen et al. [3; 24]. The simulations also provided a view of the electric field distributions in these PCFs, which is shown in Figure 11.4.

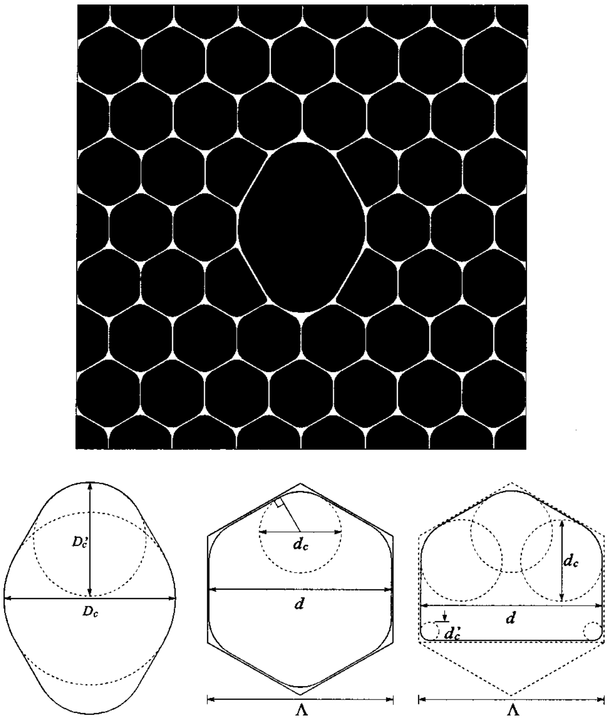

Figure 11.2: Top, cross section of the realistic Hi-Bi PBGF [24]; bottom, design of the core and the air holes. Here $\Lambda = 4.0$ mm, $d/\Lambda = 0.98$, $d_c/\Lambda = 0.54$, $D_c = 7.85$ mm, $D_c' = 5.28$ mm, and $d_c'/\Lambda = 0.1$. Air-filling fraction $f \approx 0.928$. Caption and figure from [3].

In the PCF configuration discussed above, group birefringence was optimized to be as high as possible. However, for PBQPM, more generation zones can be achieved for lower group birefringence. Alam et al. also provided an alternative design which allowed for zero group birefringence [3]. Figure 11.5 shows the schematic for the PCF whilst Figure 11.6 shows the calculated phase and group birefringence. However, the wavelength that gives zero group birefringence is around the minimal for phase birefringence; further work for PBQPM with PCFs must be explored enabling the optimization of phase as opposed to group birefringence.

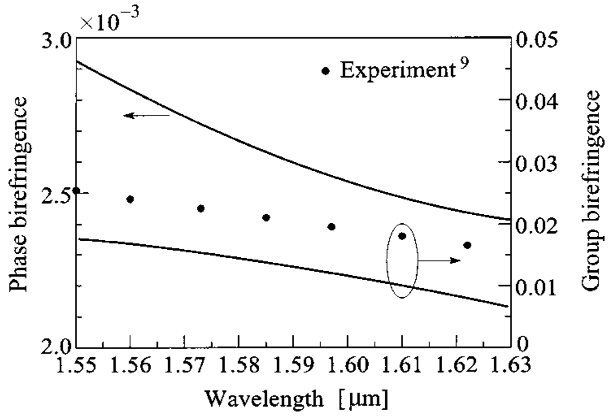

Figure 11.3: Phase and group birefringence as a function of wavelength; Lines are simulated output whilst the dots are experimental data from [24]. Figure from [3].

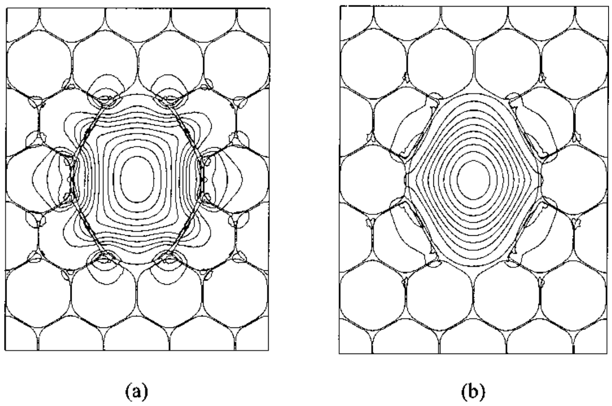

Figure 11.4: Electric field distributions of (a) the x-polarized mode and (b) the y-polarized mode at a wavelength of 1.6 um. Figure and caption from [3].

11.2.2 Circular birefringent PCFs

To date work on circularly birefringent PCFs has concentrated exclusively on solid-core PCFs [130; 131]. These circularly birefringent PCFs are based on the idea that a twisted linear birefringent waveguide may exhibit optical activity, which has been well understood in simpler fibres for decades [128; 129].

A team in Russell's group at the Max Planck Institute for the Science of Light managed to show circular birefringence in twisted PCFs; they define circular birefringence as [131],

$$B_c = n_{RC} - n_{LC} \tag{11.3}$$

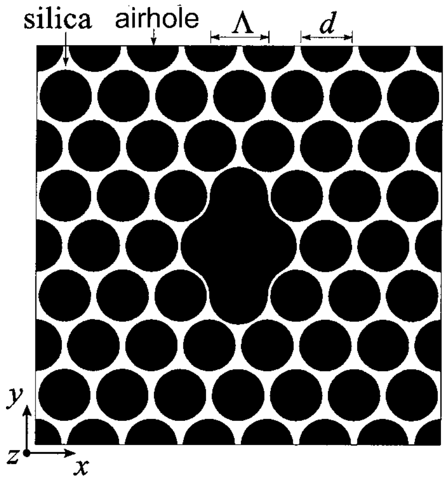

Figure 11.5: Cross section of the Hi-Bi PBGF. Figure and caption from [3].

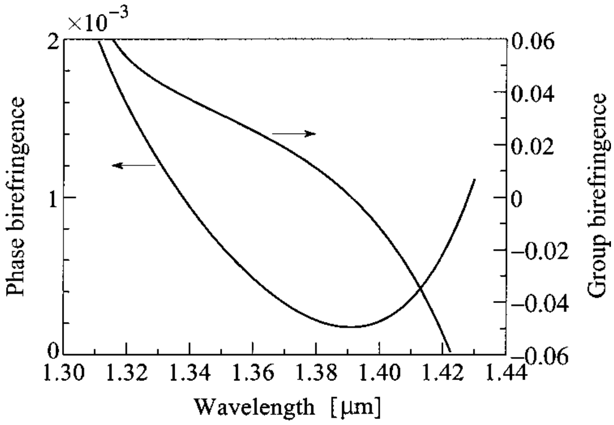

Figure 11.6: Phase birefringence and group birefringence of the PBGF8 of Fig. 11.5, when $d/\Lambda = 0.9$ and $\Lambda = 2.0$ mm. Figure and caption from [3].

where n_{RC} and n_{LC} are the effective refractive indices for the RC and LC polarised modes respectively. In the language of Chapter 6, we can rewrite B_c as a function of rotation length L_r as,

$$B_c = \frac{\lambda}{L_r} \tag{11.4}$$

where L_r is the length it takes for the linear polarisation state to rotate by π.

Figure 11.7 shows a schematic of the twisted PCF over one period from Wong et al [130]. The circular birefringence, B_c, was measured and calculated by the team and was

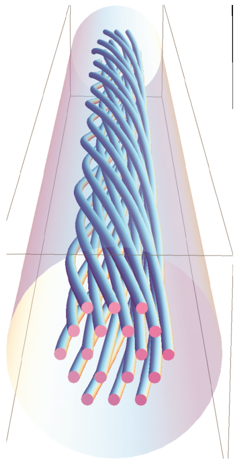

Figure 11.7: Perspective view of one period $L(= 2\pi/\alpha$, where α is the twist rate) of a helical PCF with a negative twist (i.e., anticlockwise looking in the direction of propagation, $+z$). The blue tubes represent the hollow channels passing through the glass, and the solid glass core is formed by a missing channel at the center. For clarity, the twist rate is greatly exaggerated in this sketch (L/Λ is of order 100 in the experiments, where Λ is interhole spacing). Figure and caption from [130]

shown to increase linearly with the twist rate [131]. The team also developed an analytical perturbation theory to explain this phenomenon, which can be explored in more detail in Xi et al [131].

If circularly birefringent waveguides are shown to work for solid core PCFs, then presumably similar techniques could be employed for hollow-core waveguides in order to achieve ORQPM.

11.3 Elliptical hollow-core waveguides

Birefringent hollow-core waveguides have potential applications in terahertz communications and other terahertz applications, which is an area of development for various research groups [19; 80; 81; 94; 115]. To reduce losses of terahertz radiation in waveguides, some groups developed the dielectric-coated metallic hollow fibre (DMHF) [19; 80; 81]. Since the systems are scale invariant [115], in theory, we could adapt these waveguides for the optical regime required for HHG.

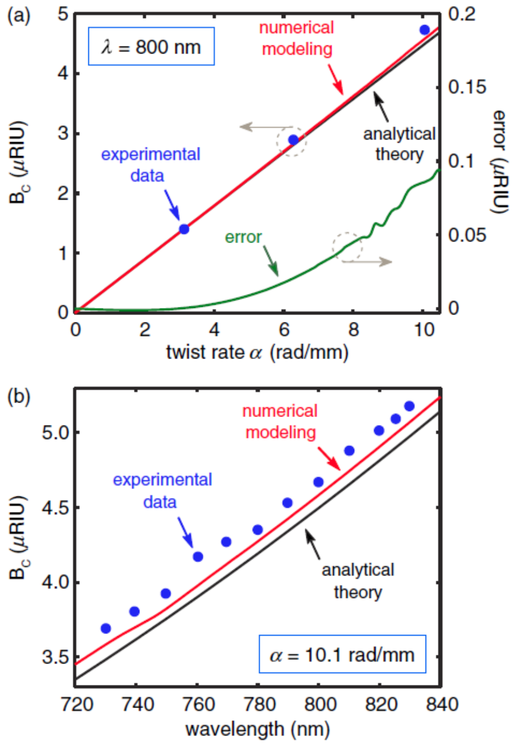

Figure 11.8: (a) Circular birefringence as a function of twist rate at a wavelength of $\lambda_0 = 800$ nm. The error is the difference between the numerically modeled (by solving the full Maxwell equations with a finite element method) and the values of B_C calculated using perturbation theory; (b) B_C as a function of wavelength for a twist rate of 10.1 rad/mm. Figure and caption from [131]

Tang et al. numerically calculated elliptical birefringent DMHF in the terahertz regime and showed some interesting results [115]. Figure 11.9 shows the overall schematic for an elliptical birefringent DMHF whilst Figure 11.10 shows the mode composition for the x- and y- polarized fundamental modes. In an DMHF, the radiation is guided inside a hollow-core. The core is bounded by a dielectric layer, which in turn is coated by a metallic layer. Since, as we saw in Chapter 4, hollow-core waveguides are inherently leaky [28], the metallic layer is used to prevent leakage.

Figure 11.11 shows the birefringence and attenuation of an elliptical DMHF for the terahertz regime as a function of ellipticity. In Figure 11.11a, as expected, the birefringence and attenuation is a function of ellipticity. Birefringence increases as the ellipticity

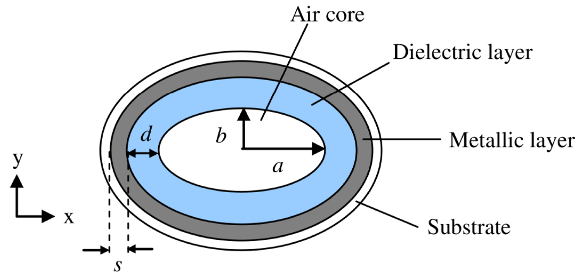

Figure 11.9: Schematic cross section of an elliptical waveguide. Figure and caption from [115]

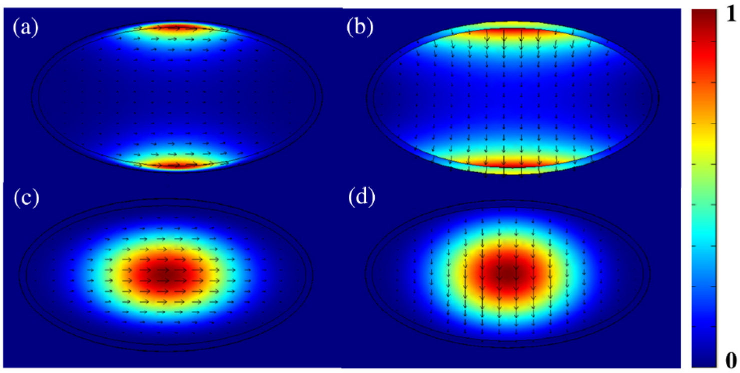

Figure 11.10: Normalized z-component power flow and electric field vector distribution for (a) the cladding HE_{11X} mode at 1.88 THz, (b) the cladding HE_{11Y} mode at 0.69 THz, (c) the core HE_{11X} mode at 2 THz, and (d) the core HE_{11Y} mode at 2 THz. The power flow is presented by the colors and the electric field is presented by the arrows. Figure and caption from [115]

increases but evens out around an ellipticity of ~ 3. Tang et al. suggests that when constructing a birefringent DMHF, it is not necessary for the waveguide to have an ellipticity above ~ 3. Attenuation decreases as a function of ellipticity because the analysis held the minor radius constant, which means that as ellipticity increases, the overall waveguide size increased as well (since the major radius needs to increase to increase ellipticity). As we saw in Chapter 4, the larger the waveguide, the smaller the attenuation, hence we see a monotonically decreasing attenuation as a function of ellipticity for a fixed minor radius.

Figure 11.12 shows the birefringence and attenuation as a function of the normalised

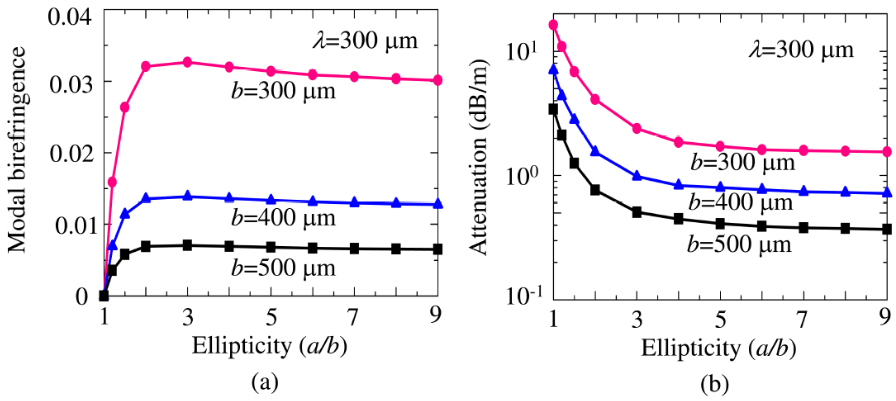

Figure 11.11: (a) Modal birefringence and (b) attenuation for the HE_{11X} mode as a function of a/b (major to minor radius ratio). Figure and caption from [115]

.

core size (or normalised geometric mean) $\sqrt{ab}/\lambda$. Note that the normalised core size is scale invariant. The smaller the core size, the higher the birefringence, but also the higher the attenuation. Below in Section 11.4.4.2, we will compare the elliptical DMHFs with similar rectangular waveguides.

11.4 Solutions for rectangular waveguides

In this section, we compute the mode properties of modes in hollow core rectangular waveguides with either one dielectric layer or a dielectric layer coated by a metal. The argument follows similar methods as discussed for solid-core waveguides in Okamoto's *Fundamentals of Optical Waveguides* [83], which was originally proposed by Marcatili [78]. We first start with a one dimensional slab waveguide and use the solutions to derive a two-dimensional rectangular waveguide.

11.4.1 Slab Waveguide

The rectangular waveguide can be decomposed into two perpendicular slab waveguides. Hence, we will first solve the slab waveguide with the following index of refraction profile:

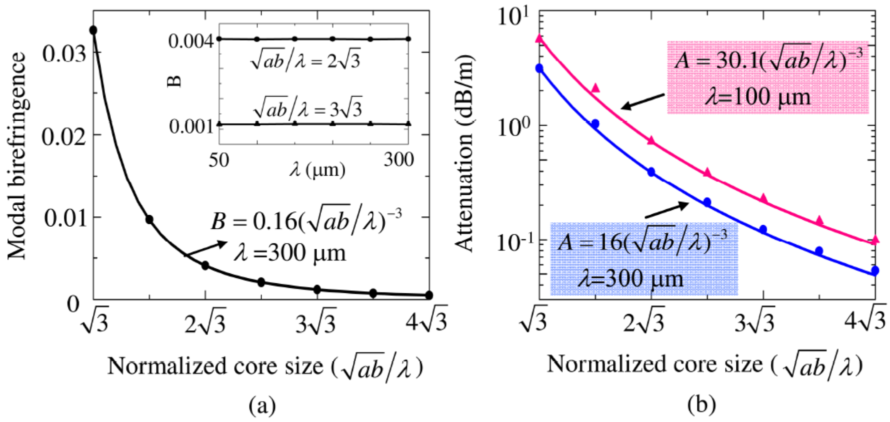

Figure 11.12: (a) Modal birefringence and (b) attenuation for the HE_{11X} mode as a function of the normalized core size ($\sqrt{ab}/\lambda$). The dotted data are the numerical results and the expressions for the curves are given in the figure. The inset in Plot (a) is the modal birefringence as a function of the wavelength. $a/b = 3$ (major to minor radius ratio). Figure and caption from [115].

$$n(x) = \begin{cases} n_0 & , |x| \leq a \\ n_1 & , a < |x| \leq l \\ n_2 & , |x| > l \end{cases} \tag{11.5}$$

where $n_0 = 1$ is air, $n_1 = 1.5$ is the dielectric layer (here we assume Borosilicate glass), and n_2 is the second layer which can either be more dielectric ($n_2 = 1.5$), air ($n_2 = 1$), or a silver layer ($n_2 = .142 + 5.2891i$).

11.4.1.1 Solution for the TE_y-polarization

Let us first consider the polarization where E_y is dominant. We define the eigenvalues for the wave equation in each region as:

$$\begin{cases} k_y^2 = k_0^2 n_0^2 - K^2 & , |x| \leq a \\ \sigma^2 = K^2 - k_0^2 n_1^2 & , a < |x| \leq l \\ \gamma^2 = K^2 - k_0^2 n_2^2 & , |x| > l \end{cases} \tag{11.6}$$

where $k_0 = 2\pi/\lambda$ is the free-space wave number and K is the complex propagation constant for the mode.

The electric field must be continuous at the boundaries of the slab layers. Because we are looking only at the even solutions (as we want to maximize the central peak intensity for HHG), let us consider only the $x > 0$ half. With that assumption, the even solution can be guessed as:

$$E_y(x) = \begin{cases} \cos(k_y x)(C_+ + C_-) & , x \le a \\ \cos(k_y a)(C_+ e^{+\sigma(x-a)} + C_- e^{-\sigma(x-a)}) & , a < x \le l \\ \cos(k_y a)(C_+ e^{+\sigma(d)} + C_- e^{-\sigma(d)})e^{-\gamma(x-l)} & , x > l \end{cases} \tag{11.7}$$

where $a + d = l$ and C_- and C_+ are constants subject to boundary conditions. The magnetic field $H_z \sim \frac{\partial E_y}{\partial x}$ must be continuous at the boundary. Hence we can just look at $\frac{\partial E_y}{\partial x}$:

$$\frac{\partial E_y}{\partial x} = \begin{cases} -k_y \sin(k_y x)(C_+ + C_-) & , |x| \le a \\ \sigma \cos(k_y a)(C_+ e^{+\sigma(x-a)} - C_- e^{-\sigma(x-a)}) & , a < |x| \le l \\ -\gamma \cos(k_y a)(C_+ e^{+\sigma(d)} + C_- e^{-\sigma(d)})e^{-\gamma(x-l)} & , |x| > l \end{cases} \tag{11.8}$$

where

$$\begin{cases} -\sigma \frac{C_+ - C_-}{C_+ + C_-} = k_y \tan(k_y a) & \text{,continuous at } x = a \\ \\ -\frac{\gamma}{\sigma} = \frac{C_+ e^{\sigma d} - C_- e^{-\sigma d}}{C_+ e^{\sigma d} + C_- e^{-\sigma d}} & \text{,continuous at } x = l \end{cases} \tag{11.9}$$

Now, since C_- and C_+ are related to the boundary conditions, we choose $C_- + C_+ = A$. A is arbitrary since it is just the amplitude of the mode and can be factored out. Now, we can solve for C_- in Eqn. (11.9) as a function of A:

$$C_- = A\frac{\sigma + k_y \tan(k_y a)}{2\sigma} \tag{11.10}$$

Plugging this into the second part of Eqn (11.9), we get the dispersion relation:

$$0 = \frac{\gamma}{\sigma} + \frac{(A - C_-)e^{\sigma d} - C_- e^{-\sigma d}}{(A - C_-)e^{\sigma d} + C_- e^{-\sigma d}} \tag{11.11}$$

where we solve for k_y. Note that k_y will in general be complex if $n_1 > n_0$.

11.4.2 Solution for the TM_x-polarization

Please refer to the Appendix .5.

11.4.3 Dispersion relation for a rectangular waveguide

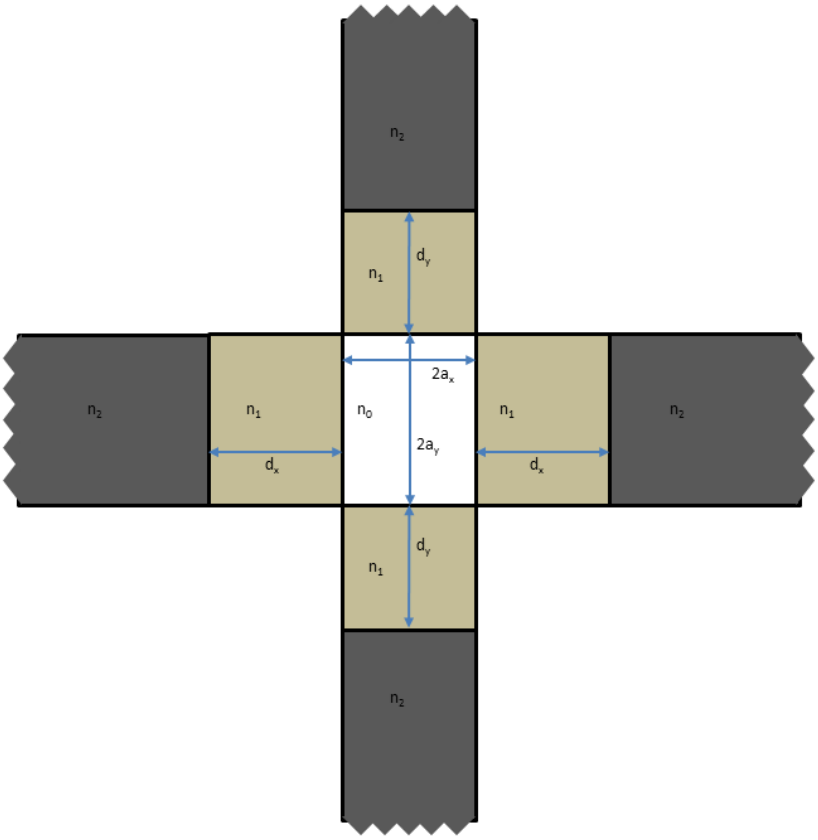

Figure 11.13: Schematic for the rectangular waveguide

The schematic for a rectangular waveguide can is shown in Fig 11.13. To solve for the rectangular waveguide, the equations for the TE_x and the TM_y polarization states must be written down. We will hence call the x-polarization state the combination of the TE_x and TM_x states where the E_x is the dominate electric field polarization and the y-polarization state the combination of TE_y and TM_y respectively.

11.4.3.1 The x-polarization state

We define the eigenvalues similar as above except that the propagation constant $K_{(X)}$ is now a function of both k_x and k_y:

$$\begin{cases} k_x^2 + k_y^2 = k_0^2 n_0^2 - K_{(X)}^2 & , |x| \leq a_x, |y| \leq a_y \\ \sigma_x^2 = k_0^2(n_0^2 - n_1^2) - k_x^2 & , a_x < |x| \leq l_x \\ \gamma_x^2 = k_0^2(n_0^2 - n_2^2) - k_x^2 & , |x| > l_x \\ \sigma_y^2 = k_0^2(n_0^2 - n_1^2) - k_y^2 & , a_y < |y| \leq l_y \\ \gamma_y^2 = k_0^2(n_0^2 - n_2^2) - k_y^2 & , |y| > l_y \end{cases} \tag{11.12}$$

and two sets of equations need to be solved for k_x and k_y respectively where for k_x:

$$\begin{cases} -\sigma \frac{C_+ - C_-}{C_+ + C_-} = k_x \tan(k_x a_x) \frac{n_1^2}{n_0^2} & \text{,continuous at } x = a_x \\ \\ -\frac{\gamma n_1^2}{\sigma n_2^2} = \frac{C_+ e^{\sigma d} - C_- e^{-\sigma d}}{C_+ e^{\sigma d} + C_- e^{-\sigma d}} & \text{,continuous at } x = l_x \end{cases} \tag{11.13}$$

Similarly, for k_y:

$$\begin{cases} -\sigma \frac{C_+ - C_-}{C_+ + C_-} = k_y \tan(k_y a_y) & \text{,continuous at } y = a_y \\ \\ -\frac{\gamma}{\sigma} = \frac{C_+ e^{\sigma d} - C_- e^{-\sigma d}}{C_+ e^{\sigma d} + C_- e^{-\sigma d}} & \text{,continuous at } y = l_y \end{cases} \tag{11.14}$$

After solving these two set of equations, the propagation $K_{(X)}$ can be solved by

$$K_{(X)} = \pm\sqrt{k_0^2 n_0^2 - k_{x,(X)}^2 - k_{y,(X)}^2} \tag{11.15}$$

noting that we have added the $_{(X)}$ subscripts to k_x and k_y to emphasize that they are constants for the x-polarization state.

11.4.3.2 The y-polarization state

Please refer to the Appendix .6.

11.4.3.3 Birefringence and mode damping

After solving for the two polarisation states, the birefringence can be calculated as the difference in the phase velocity between the two modes,

$$\begin{aligned} B &= |\beta_X - \beta_Y| && (11.16) \\ &= |\Re(K_{(X)}) - \Re(K_{(Y)})|. && (11.17) \end{aligned}$$

where $\beta_X = \Re(K_{(X)})$ and $\beta_Y = \Re(K_{(Y)})$ are the mode propagation constants and $\Re()$ is the real component.

The mode damping can be calculated by taking the imaginary parts of the complex mode constant,

$$\begin{cases} \alpha_X = \Im(K_{(X)}) \\ \alpha_Y = \Im(K_{(Y)}) \end{cases} \tag{11.18}$$

where $\Im()$ is the imaginary component.

11.4.4 Numerical calculations of birefrigent rectangular waveguides

11.4.4.1 Simple glass rectangular waveguide

It is evident that if $a_x \neq a_y$, $\beta_X \neq \beta_Y$, then we have birefringence. In Section 11.3, we noted that the optimal ratio between the long and short radii of an elliptical waveguide is around $\sim$ 3. To test our calculations for a rectangular waveguide, we will set $a_x = 5$um and $a_y = 15$um for a $\lambda = 800$nm laser. The waveguide itself has a simple borosilicate glass wall with $n_1 = n_2 = 1.5$, which we assume to be 1mm wide in each dimension.

Figure 11.14 shows the X- and Y- polarized lowest order modes for the rectangular waveguide described. Inside the hollow-core, the lowest order modes contain the cos() terms as expected. In the glass walls, the small oscillations caused by the leaky waveguide have similar characteristics as the hollow core circular waveguides described in Chapter 4 and by Cros et al [28].

In this arrangement, the beat length is on the order of $\sim$ 100mm, which is 2-3 orders of magnitudes too high for PBQPM. Moreover, the $1/\alpha$ attenuation lengths are on the order of a few millimeters ($\sim$ 1.5mm for the X-polarized mode and $\sim$ 3.2mm for the Y-polarized mode). In other words, modes polarized parallel to the shorter axis has a higher attenuation rate, as we will also see evidence of below in Section 11.5. As we have discussed, the smaller the normalised core size, the stronger the damping coefficient is. In fact, for a 5um radius hollow-core circular waveguide based on Cros et al. at $\lambda = 800$nm [28], the $1/\alpha$ attentional length is around 1.5mm, which corresponds well to our calculations for the rectangular waveguide. Clearly this waveguide setup will not work for PBQPM given the low birefringence and extremely high damping rates of modes.

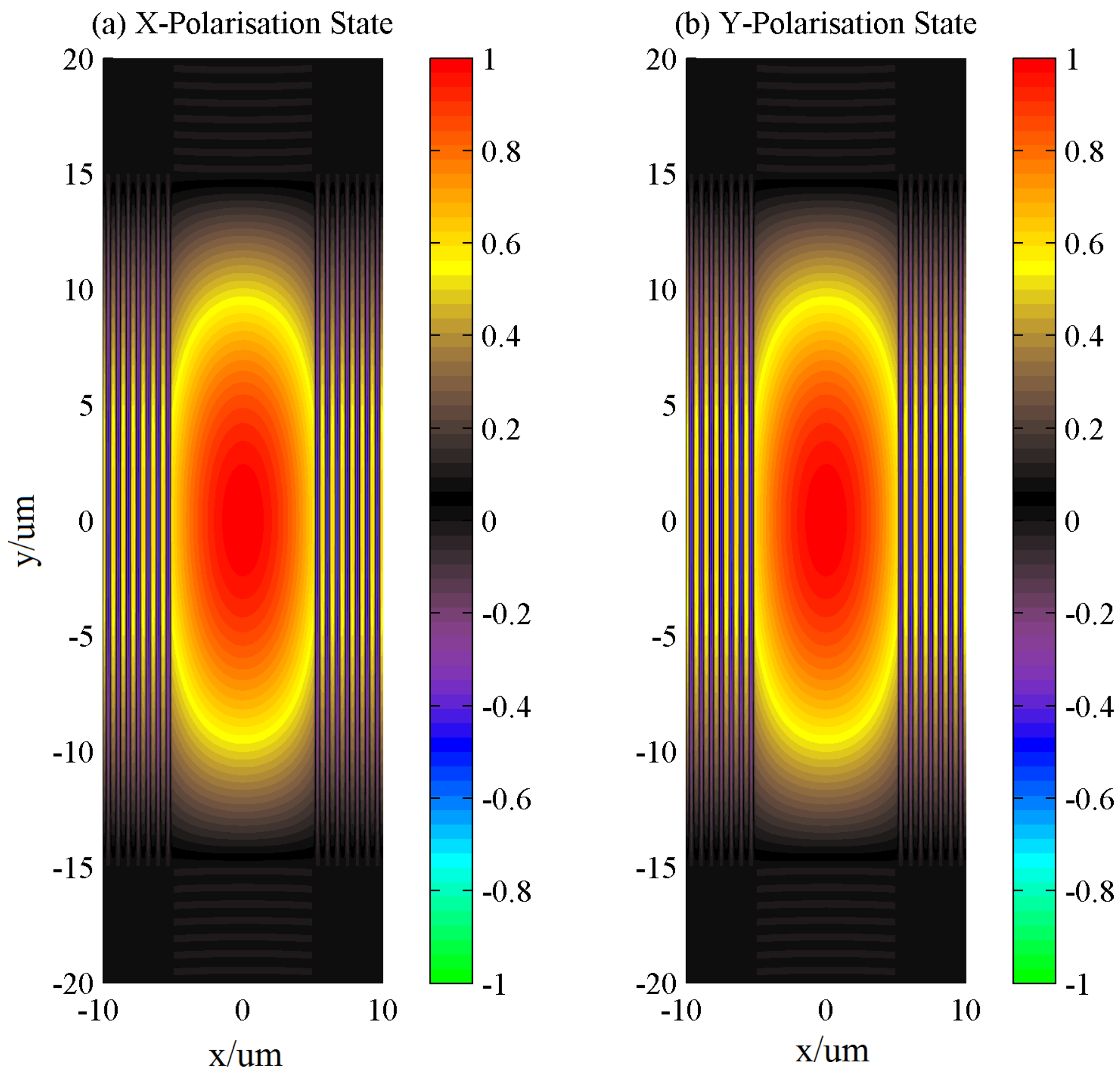

Figure 11.14: Electric field (real part) of the mode for the X- (Plot a) and Y- (Plot b) polarized lowest order modes with arbitrary electric field units; this waveguide had no silver coating

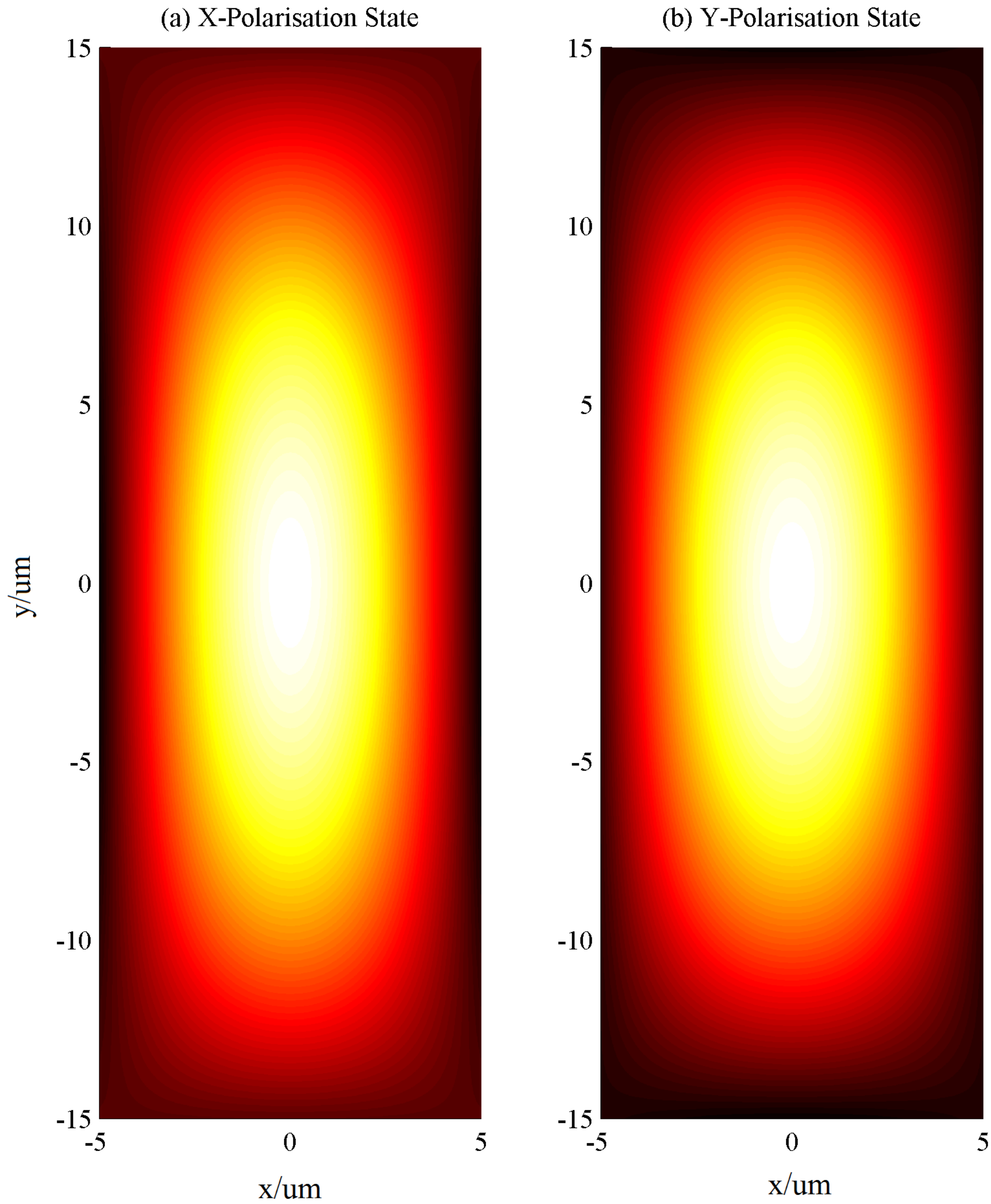

Figure 11.15: Electric field (real part) of the mode for the X- (Plot a) and Y- (Plot b) polarized lowest order modes with arbitrary electric field units; this waveguide had a silver coating

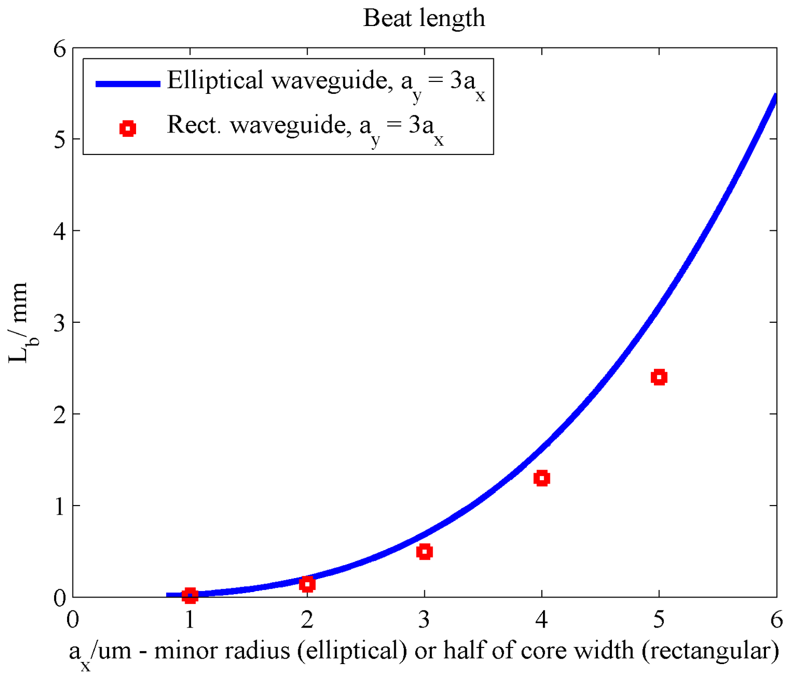

Figure 11.16: Modal birefringent beat length L_b for elliptical waveguides as described by Tang et al. from Equation 11.21 (solid blue line) and for rectangular waveguides (red squares) as a function of minor radius and core half-width a_x respectively.

11.4.4.2 Rectangular waveguides with silver coating

In Section 11.3, we discussed how silver coating can both increase birefringence as well as reduce leakage. In order to check our calculations, we tried to construct a rectangular waveguide with similar parameters to the Tang et al. [115] scaled down from the terahertz regime to 800nm, where as above, a_x = 5um, a_y = 15um. We assumed a wall width $d_x = d_y = 0.11$um, which corresponded to the optimal thickness given by [115],

$$d_x = d_y = \frac{\lambda}{2\pi\sqrt{n_1^2 - 1}} \arctan\left[\frac{n_1}{(n_1^2 - 1)^{1/4}}\right]. \tag{11.19}$$

Admittedly, a dielectric wall of 0.11um is somewhat unrealistic, but we wanted to check that our rectangular waveguide provided a similar answer to that from [115]. The dielectric layer had an index of refraction of $n_1 = 1.5$, and the silver layer had a complex index of refraction of $n_2 = .142 + 5.2891i$. Figure 11.15 shows the electric field of the X- and

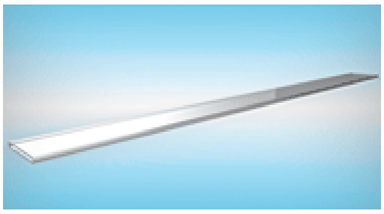

Figure 11.17: Cartoon of the type of (untwisted) capillary used in the demostration experiment, from CM Scientific.

Y- polarised modes.

Tang et al. gives the equation for mode birefringence for an elliptical waveguide where the minor to major axis ratio is 3 as [115],

$$B = 0.16\left(\sqrt{\frac{a_x a_y}{\lambda}}\right)^{1/3} \tag{11.20}$$

hence the beat length becomes,

$$L_b = \frac{\lambda}{2B} = \frac{\lambda}{2 \times 0.16(\sqrt{a_x a_y}/\lambda)^{1/3}} \tag{11.21}$$

where in this particular case a_x and a_y are the major and minor radii respectively. It is clear that the birefringence is scale invariant if $\sqrt{a_x a_y}/\lambda$ is constant [115]; hence we can compare the birefringence of our rectangular waveguide with the elliptical waveguide. Figure 11.16 compares the beat length from Equation 11.21 to the rectangular waveguide calculated in this chapter. As expected, for a major to minor ratio of 3, the two schemes shows good agreement. This provides an excellent sense check for the calculations for the rectangular waveguide.

Figure 11.18: Photograph of the actual twisted capillary used in the measurements.

11.5 Tentative evidence of birefringence and optical rotation

In this section, we show, to our knowledge, the first evidence of optical rotation with a hollow core waveguide at 633 nm. This was achieved using a hollow core rectangular borosilicate capillary (with $n = 1.5$) with a rectangular profile of 20x200μm with a length of 5 cm. The capillary was glued on the two ends and twisted by 15^o. Figure 11.17 shows a cartoon of the capillary used from CM Scientific whilst Figure 11.18 shows a photograph of the actual waveguide used in the measurements. Twisted waveguides have been predicted to achieve optical rotation in [128; 129].

The waveguide was placed in an experimental setup outlined in Fig 11.19. A circularly polarized collimated HeNe 633nm beam passes through a rotatable polarizer at an angle Θ_1 to the vertical axis. The front of the waveguide was oriented so that its long side was at $\Psi_1 = -75^o$ to the vertical axis; the exit was oriented so that its long side made an angle $\Psi_2 = -60^o$ to the vertical. To clarify the presentation, we will shift all angular coordinates such that the angle of the major axis at the front of the axis is $\Psi_1 \rightarrow \Psi_1 - (-75^o)$ such that $\Psi_1 \rightarrow 0$; as a result, $\Psi_2 \rightarrow 15^o$.

The exit of the waveguide was then imaged using an objective lens, and the output

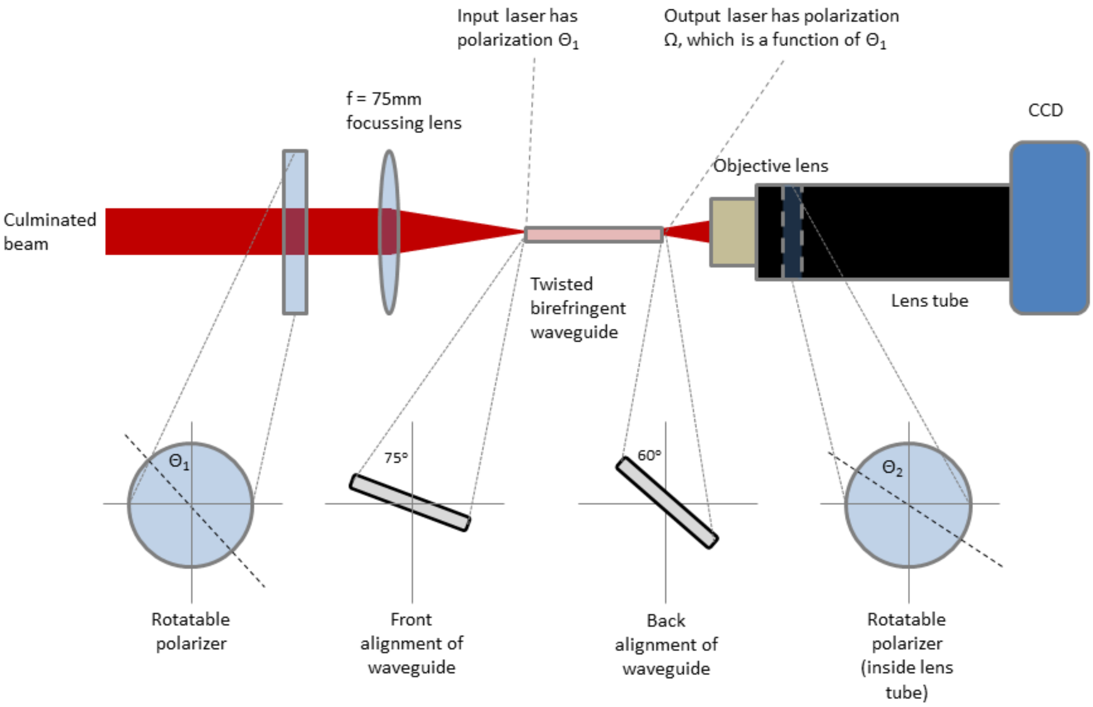

Figure 11.19: Outline of experimental setup

beam is then linearly polarized by second rotating polarizer with an angle of Θ_2. Note that the HeNe had been turned on for over ten hours in order to stabilize it any intensity drift from HeNe oscillations.

By taking a series of measurements of different Θ_1 and Θ_2, the output polarization state can be compared with the input polarization state. Figure 11.20a shows the analysis of polarization states of the output polarization Ω for varying input polarization Θ_1. The output polarization angle for the most part hugs Ψ_2, which suggests that the polarization state of the guided light follows the polarization mode parallel to the longer axis of the waveguide, which is evidence for optical rotation. When $\Theta_1 \approx \Psi_1 + \pi/2$, the polarization state is not rotated with respect to the waveguide.

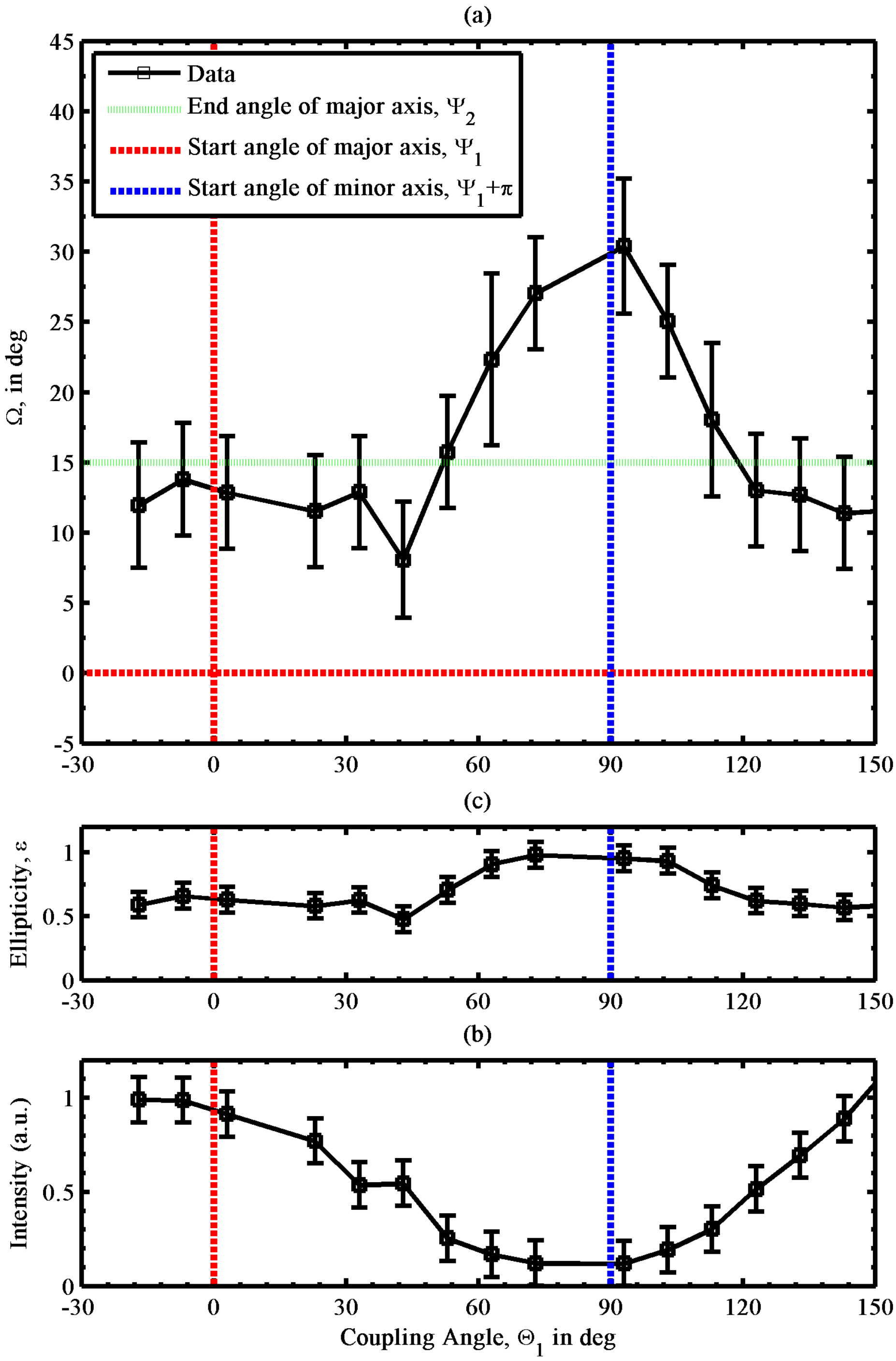

Figure 11.20: Plot (a) shows the exit polarization angle of the laser Ω as a function of input polarization state Θ_1. Note that the polarisation state shifted from the entrance major axis angle Ψ_1 to the exit major axis angle Ψ_2 after propagating through the waveguide for coupling angles Θ_1 around Ψ_1. Plot(b) shows the ellipticity of the output mode as a function of coupling angle Θ_1. Plot (c) shows the normalised (to arbitrary units) intensity of the output light as a function of input polarisation state.

Ellipticity, shown in Figure 11.20b, was estimated for measurements by analysing outputs from measurements from multiple angles Θ_2. The estimated ellipticity of the output polarization is closer to linear when the input polarization Θ_1 is closer to angle at the fibre start Ψ_1 with an ellipticity estimated to be $\varepsilon \sim .5$. However, the ellipticity for coupling angles perpendicular to Ψ_1 such as $\Psi_1 + \pi/2$, the ellipticity increases to $\varepsilon > .9$. This is most likely because the modes initially excited at the entrance to the waveguide are are dominated by polarization states that are parallel to the longer axis, which is then rotated along the length of the waveguide following the longer axis.

Our numerical analysis above in Section 11.4.4.1 also suggested that the polarization modes parallel to the longer axis in an rectangular or elliptical waveguide exhibit significantly smaller attenuation rates; previous analysis of solid-core waveguides also provides a similar situation [83]. Moreover, Figure 11.20c also shows the output intensity has a minimum when the coupling polarisation angle is parallel to the shorter axis $\Psi_1 + \pi/2$.

In this setup, the rotation length, L_r, defined by the length it takes for the polarization to rotate by π, is in the order of centimeters. For ORQPM to be achievable, L_r must be in the order of a few millimeters or less [72]. However, this is a first demonstration of a technique that could achieve optical rotation in similar wavelength ranges. Moreover, as discussed above, much of the work done on twisted PCFs are around solid-core waveguides; this may be one of the first attempts at twisted hollow-core waveguides. We finally note that the analysis above assumed that the ellipticity of the exit field was elliptical, which may not necessarily be the case in general.

11.6 Conclusion

In this chapter, we provided a brief literature review of hollow-core linear birefringent waveguides and solid-core circular birefringent waveguides (that could potentially be adapted for hollow-core). We also derived from scratch analytic solutions for slab and rectangular waveguides with and without silver coating and showed that the analogous silver-coated rectangular waveguides provided similar birefringent scaling as the elliptical DMHFs in previous work in Ref [115]. We then showed some initial evidence of optical rotation in a hollow-core twisted birefringent rectangular waveguide. Future work would comprise of developing the right kind of waveguide that could withstand high intensities required for HHG with high birefringence required for PBQPM or ORQPM. Tables 11.1 and 11.2 summarize some of the recent work on linear and circular birefringent waveguides respectively.

Table 11.1: Summary of linear birefringent waveguide schemes. In the Reference column, E denotes experimental realisation, C denotes commercial, and T denotes theoretical.

Waveguide type	Norm. core size, µm	λ, µm	Beat length, mm	Birefringence, B	Ref
Hollow-core PCF	4.5	1.55	0.06	2.5×10^{-2}	[24]E
Hollow-core PCF	4.5	1.63	0.10	1.7×10^{-2}	[24]E
Hollow-core PCF	6.0	1.55	3.88	2.0×10^{-4}	[2]C
DMHF	~ 500	375	5.93	3.2×10^{-2}	[115]T
DMHF	~ 500	75	119	3.2×10^{-4}	[115]T
DMHF	~ 5	0.8	~ 0.5	$\sim \times 10^{-3}$	Sec 11.4.4.2T

Table 11.2: Summary of circular birefringent waveguide schemes. They have all been realised experimentally.

Waveguide type	Norm. core size, µm	λ, µm	Beat length, mm	Birefringence, B	Ref
Twisted solid-PCF	~ 2	1.0	190	5.3×10^{-6}	[10]
Twisted solid-PCF	~ 2	0.8	571	1.4×10^{-6}	[131]
Twisted solid-PCF	~ 2	0.8	276	2.9×10^{-6}	[131]
Twisted solid-PCF	~ 2	0.8	169	4.7×10^{-6}	[131]
Twisted hollow-rect. cap.	63	0.63	480	1.3×10^{-6}	Sec 11.5

We believe that kagome-type birefringent PCFs may be a way forward for PBQPM. Similarly, twisted PCFs used for PBQPM may also be attempted for ORQPM. On the other hand, simple elliptical or rectangular waveguides coated in metal may also be a relatively simple or inexpensive solution to demonstrate polarisation-controlled QPM.

Chapter 12

Conclusion

We discussed a novel class of quasi-phase matching scheme for high-harmonic generation, called polarisation-controlled. We provided simulations for both PBQPM, ORQPM, and a hybrid MMPBQPM. A theoretical framework for QPM and random phase matching were also explored. Polarisation-controlled QPM requires that the driving laser pulse is guided in a waveguide which is linearly- or circularly-birefringent. We therefore discussed some waveguide types which could be adapted for PC-QPM. We extend our theory on MMPBQPM to describing random phase matching as well. Given that polarisation-controlled QPM requires precise control of waveguide modes, this thesis also discussed mode analysis and experimental evidence of laser beam control using a novel analytic method employing a spatial light modulator. Finally, approaches to birefringent waveguides were discussed.

12.1 Summary of work

QPM is achieved in which polarisation beating occurs within a hollow-core birefringent waveguide, which was explored in Chapter 5. The evolution of the polarisation of a laser propagating in a birefringent waveguide is calculated and was shown to periodically modulate the HHG process. The optimum conditions for achieving QPM using this scheme was explored and the growth of the harmonic intensity as a function of experimental parameters were investigated.

Because PBQPM is based on linear birefringence, it was then a natural next step to consider the implications of circular birefringence for QPM, which led to the concept of optical rotation QPM as described in Chapter 6. In ORQPM, propagation of the driving radiation in a system exhibiting circular birefringence causes its plane of polarisation to rotate; by appropriately matching the period of rotation to the coherence length, it is possible to avoid destructive interference of the generated radiation. It is shown that ORQPM is approximately five times more efficient than conventional ideal-square wave QPM and half as efficient as true phase matching.

Polarization-beating QPM requires the phase velocity of two orthogonally-polarised modes. This is straightforwardly manifested in a birefringent waveguide, but it can also be achieved by beating two different, orthogonally polarised modes. This variant, MMP-BQPM, was described in Chapter 7. Hence the generalization of quasi-phase-matching using polarization beating and of multimode quasi-phase-matching (MMQPM) for the generation of high-order harmonics was explored, and a method for achieving polarization beating is proposed. If two (and in principle more) modes of a waveguide are excited, modulation of the intensity, phase, and/or polarization of the guided radiation will be achieved. By appropriately matching the period of this modulation to the coherence length, quasi-phase-matching of high-order-harmonic radiation generated by the guided wave can occur. We showed that it is possible to achieve efficiencies with multimode quasi-phase-matching greater than the ideal square wave modulation. In this chapter we also presented a Fourier treatment of QPM and use this to show that phase modulation, rather than amplitude modulation, plays the dominant role in the case of MMQPM. The experimental parameters and optimal conditions for this scheme were explored.

Next in Chapter 8, we extended our analysis to random phase matching and showed that the intensity of the harmonics under random phase matching increases linearly with propagation distance as opposed to the quadratic dependence found for true phase-matching and for QPM, and that random phase-matching led to generation of of bright harmonics over a large bandwidth. This behavior was confirmed by an analytical model. Furthermore we showed that it could potentially provide very broad spectrum high harmonics.

Since the crux of polarisation-controlled or multi-mode QPM rests on mode control, we developed several techniques for analyzing mode composition of a waveguide using a single shot CCD. Some of these techniques were shown to be significantly faster than standard in-built least-squares regression techniques. This work is described in Chapter 9.

In order to excite with high fidelity the modes in a hollow-core waveguide it is desirable to use a spatial light modulator (SLM) to control the amplitude and phase of the incident laser pulse. In Chaper 10, we developed a novel analytical solution for the phase introduced by a phase-only spatial light modulator to generate a given far-field amplitude and phase profile within some domain of interest. The solution was demonstrated experimentally and shown to enable excellent control of the far-field amplitude and phase. We also showed good coupling of higher order modes with this technique.

Finally, we explored potential approaches to birefringent waveguides in the literature. The modes of a metal-coated hollow rectangular dielectric waveguide were solved analytically, and it was shown that this type of waveguide could potentially lead to a low-loss highly linearly birefringent hollow-core waveguide for wavelengths appropriate for high harmonic generation. We also provided some initial experimental evidence for optical rotation in a twisted hollow-core linearly birefringent waveguide.

12.2 Future prospects

12.2.1 Polarisation-controlled QPM

The work in this thesis provides the initial theoretical groundwork for future work on polarization-controlled QPM. Polarisation controlled QPM using birefringent waveguides can theoretically provide a very clean way of achieving QPM without the use of complex optical setups. However, further development in current hollow-core waveguide technologies would be required to fabricate appropriate waveguides. Given the requirement for high phase birefringence and low group birefringence, PCFs may be the most promising waveguide technology for this purpose since their mode properties can be adjusted over a wide range and with high precision. Achieving suitably appropriate waveguides should be a priority for future work in this area. We emphasize that the prospect of achieving bright circularly polarized coherent soft X-rays is a major motivation for the exploration of polarisation-controlled QPM.

12.2.2 Random phase matching

Given that random phase matching most likely occurs in many experiments already, future work may entail attempting to control the random phase by either modal control using an spatial light modulator or via gas pressure modulation. Even though the growth for random phase matching is linear, as opposed to quadratic, the prospect of a very broad spectrum high harmonics is a very exciting one, especially for the generation of ultra-short harmonic pulses.

12.3 Financial support

The Author is grateful for the support from the UK Engineering and Physical Sciences Research Council (grant number EP/G067694/1) and by Merton College's James Buckee Scholarship.

12.4 Final remarks

The novel QPM techniques proposed and explored in this thesis open up new opportunities for generating bright efficient coherent X-rays in compact birefringent waveguide setups; the the possibility of circularly polarized sources coherent X-rays are also extremely exciting. Moreover, novel techniques in mode analysis and spatial shaping of laser beams could find widespread applications. Finally, it is hoped that this thesis provided a more thorough and fresh theoretical treatment of ideas that progress our understanding of high harmonic generation and optical systems.

Appendix - Mode Analysis Generalisations

.1 Generalization for LFMI

The example given in Chapter 9 is a limited case for two modes and for integrating a set of arbitrary functions $\{f_n\}$. In general, the matrix T and the vector A can be constructed from any N set of nontrivial linear forms $\mathfrak{L}_n : \mathbb{H} \to \mathbb{R}$ acting on w and v_n such that $\det(T) \neq 0$.

Consider a system with M modes and N coefficient terms to solve:

$$w = \Omega_1 v_1 + ...\Omega_N v_N \tag{1}$$

As before, we define a set of A_n:

$$\begin{aligned} A_1 &= \Omega_1 \mathfrak{L}_1(v_1) + ...\Omega_N \mathfrak{L}_1(v_N) && (2) \\ &\vdots \\ A_n &= \Omega_1 \mathfrak{L}_n(v_1) + ...\Omega_N \mathfrak{L}_n(v_N) && (3) \\ &\vdots && (4) \\ A_N &= \Omega_1 \mathfrak{L}_N(v_1) + ...\Omega_N \mathfrak{L}_N(v_N) && (5) \end{aligned}$$

This can be written as a matrix equation to be solved as before:

$$A_n = T_n^l \Omega_q \tag{6}$$

where $n = 1, 2, 3, ..N$, $l = 1, 2, 3, ...N$ and

$$T_n^q = \mathfrak{L}_n(v_l) \tag{7}$$

It is important to emphasize that the matrix T and its inverse needs only be calculated once, once the modes and linear forms are chosen, which speeds up the calculation process dramatically. Finally, it should be noted that the choice of linear forms will impact the error tolerance of the method.

.2 The General Difference Operator

From the example above, the key thing we learned is that from the w expansion, we can individually solve for each of the coefficients independently as long as we divide and differentiate each step to eliminate the coefficients we are not solving for.

The derivative is actually a special case and one doesn't necessarily need to differentiate to eliminate the other coefficients. In fact, the operator only needs the following criteria:

$$\mathfrak{D}(f) = \begin{cases} 0 & \text{if } f = constant; \\ Nonzero & \text{if } f \neq constant \end{cases} \tag{8}$$

Thus, $\mathfrak{D}(f)$ can be any form of operator that has some difference component, and can be expressed in the following form:

$$\mathfrak{D}(f(\vec{r})) = [f(\vec{r_k}) - f(\vec{r})]g(\vec{r}) \tag{9}$$

where $\vec{r_k} \neq \vec{r}$ is some value on the domain and $g(\vec{r})$ is a nonzero function. In the case of the one-dimensional derivative, $r_k = r + h$ and $g = 1/h$, where $h \to 0$.

In fact, often times the derivative is not the best choice for $\mathfrak{D}$ because a small error between two points may blow up very quickly given the number of derivatives and divisions this algorithm need, but there are essentially an infinite amount of choices for $\mathfrak{D}$.

.3 Difference Operator Method: Generalizing to Decomposing M Eigenmodes

In the general case of $M \geq 2$, the same method can be applied as above by dividing a term that associated with the target coefficient and then applying the D operator on both sides. The algorithm can be described as follows assuming that we are trying to solve for the Nth coefficient where $w = \Omega_1 v_1 + \Omega_2 v_2 ... + \Omega_N v_N$(keeping in mind that the order of v_j is arbitrary):

1. Divide both sides by the first nonzero term (excluding the coefficient).
2. Apply the D operator on both sides to eliminate the first term's coefficient
3. Repeat M-1 times until there is only one term left. Then solve for Ω_N with step (i).

All the coefficients individually can be calculated by rotating through the v_Ns. Each coefficient requires M steps, and to calculate all coefficients require M^2 steps.

One advantage of this is that because each coefficient can be calculated independently of each other, the overall result does not depend on each other. Moreover, depending on what the purpose of the coefficient retrieval is, one may not necessarily need to calculate all the terms (for example if one is only interested in amplitude).

.4 Integral Convergence Method: Generalizing to Decomposing M Eigenmodes

It is fairly straightforward to generalize the algorithm above for $M > 2$. In general, for the nth coefficient and pth step (with a total of K steps),

$$\xi_n^{(p)} = \langle V_n \mid w - \sum_{j \neq n} \xi_j^{(i)} V_j \rangle \tag{10}$$

where

$$i = \begin{cases} p & \text{if } n < j; \\ p-1 & \text{if } n > j \end{cases} \tag{11}$$

As before, there will be N number of terms and thus each pth step will have N integrals. Assuming that there are K iterations required to converge to acceptable tolerances, the algorithm will perform a total of NK number of integrations. From here we can rescale ξ coefficients back:

$$\Gamma_n = \frac{\xi_n}{\sqrt{\int_{\mathbf{V}} dV v_i v_i^*}} \tag{12}$$

One important point is that in general for $M > 2$, $\Gamma_n \neq \Omega_n$ as the algorithm would suggest. This is because as M increases, N increases quadratically, and that the compounding action on λ does not disappear as fast as the sum of all the λ terms due to the increased size of N.

However, despite this systematic error, there is still a way to retrieve the set of coefficients Ω_n. It is found that the systematic error generated by the algorithm behaves in a very linear and exact way. Specifically, Ω_n can be written as:

$$\Omega_n = \Gamma_n + \Lambda_n^s \mu_s \tag{13}$$

where Λ_n^s is an $S \times N$ matrix and μ_s has S terms such that

$$S = \begin{pmatrix} M-1 \\ 2 \end{pmatrix} \tag{14}$$

or $S = 2$ *choose* $(M-1)$. Here, Λ_n^s is an artefact of the algorithm that is dependent on the subspace S, but stays constant with respect to different measurements; it can be calculated by performing a multilinear regression on a large set of synthetic (non-noise added) data with a given set of modes where $r^2 = 1$ always. Here, μ_s can be directly solved by applying the angle constraints described in Section 9.2.2 and Ω_n is retrieved.

Appendix - Rectangular Birefringent Waveguide Solutions

.5 Slab waveguide: Solution for the TM_x-polarization

Let us then consider the polarization where E_x is dominant. This is equivalent to saying that H_y is dominant. We define the eigenvalues similar to that in Chapter11:

$$\begin{cases} k_x^2 = k_0^2 n_0^2 - K^2 & , |x| \leq a \\ \sigma^2 = K^2 - k_0^2 n_1^2 & , a < |x| \leq l \\ \gamma^2 = K^2 - k_0^2 n_2^2 & , |x| > l \end{cases} \tag{15}$$

The magnetic field H_y must be continuous at the boundaries of the slab layers, and the even solutions can be guessed as:

$$H_y(x) = \begin{cases} \cos(k_x x)(C_+ + C_-) & , x \leq a \\ \cos(k_x a)(C_+ e^{+\sigma(x-a)} + C_- e^{-\sigma(x-a)}) & , a < x \leq l \\ \cos(k_x a)(C_+ e^{+\sigma(d)} + C_- e^{-\sigma(d)}) e^{-\gamma(x-l)} & , x > l \end{cases} \tag{16}$$

where $a + d = l$. The electric field $E_z \sim \frac{1}{n^2}\frac{\partial H_y}{\partial x}$ must be continuous at the boundary. Hence we can just look at $\frac{\partial H_y}{\partial x}$:

$$\frac{1}{n^2}\frac{\partial H_y}{\partial x} = \begin{cases} -\frac{1}{n_0^2}k_x \sin(k_x x)(C_+ + C_-) & , |x| \leq a \\ \frac{1}{n_1^2}\sigma\cos(k_x a)(C_+ e^{+\sigma(x-a)} - C_- e^{-\sigma(x-a)}) & , a < |x| \leq l \\ -\frac{1}{n_2^2}\gamma\cos(k_x a)(C_+ e^{+\sigma(d)} + C_- e^{-\sigma(d)})e^{-\gamma(x-l)} & , |x| > l \end{cases} \tag{17}$$

where

$$\begin{cases} -\sigma\frac{C_+ - C_-}{C_+ + C_-} = k_x \tan(k_x a)\frac{n_1^2}{n_0^2} & \text{,continuous at } x = a \\ \\ -\frac{\gamma n_1^2}{\sigma n_2^2} = \frac{C_+ e^{\sigma d} - C_- e^{-\sigma d}}{C_+ e^{\sigma d} + C_- e^{-\sigma d}} & \text{,continuous at } x = l \end{cases} \tag{18}$$

Similar to above, we choose $C_- + C_+ = A$. Now, we can solve for C_- in Eqn. (18) as a function of A:

$$C_- = A\frac{\sigma + k_x \tan(k_x a)}{2\sigma} \tag{19}$$

Plugging this into the second part of Eqn (18), we get the dispersion relation:

$$0 = \frac{\gamma n_1^2}{\sigma n_2^2} + \frac{(A - C_-)e^{\sigma d} - C_- e^{-\sigma d}}{(A - C_-)e^{\sigma d} + C_- e^{-\sigma d}} \tag{20}$$

where we solve for k_x.

.6 Recantular waveguide: the y-polarization state

The y-polarization state can be solved in a similar way, where,

$$\begin{cases} k_x^2 + k_y^2 = k_0^2 n_0^2 - K_{(Y)}^2 & , |x| \leq a_x, |y| \leq a_y \\ \sigma_x^2 = k_0^2(n_0^2 - n_1^2) - k_x^2 & , a_x < |x| \leq l_x \\ \gamma_x^2 = k_0^2(n_0^2 - n_2^2) - k_x^2 & , |x| > l_x \\ \sigma_y^2 = k_0^2(n_0^2 - n_1^2) - k_y^2 & , a_y < |y| \leq l_y \\ \gamma_y^2 = k_0^2(n_0^2 - n_2^2) - k_y^2 & , |y| > l_y \end{cases} \tag{21}$$

and k_x is expressed by:

$$\begin{cases} -\sigma \frac{C_+ - C_-}{C_+ + C_-} = k_x \tan(k_x a_x) & \text{,continuous at } x = a_x \\ \\ -\frac{\gamma}{\sigma} = \frac{C_+ e^{\sigma d} - C_- e^{-\sigma d}}{C_+ e^{\sigma d} + C_- e^{-\sigma d}} & \text{,continuous at } x = l_x \end{cases} \tag{22}$$

and k_y by

$$\begin{cases} -\sigma \frac{C_+ - C_-}{C_+ + C_-} = k_y \tan(k_y a_y) \frac{n_1^2}{n_0^2} & \text{,continuous at } y = a_y \\ \\ -\frac{\gamma n_1^2}{\sigma n_2^2} = \frac{C_+ e^{\sigma d} - C_- e^{-\sigma d}}{C_+ e^{\sigma d} + C_- e^{-\sigma d}} & \text{,continuous at } y = l_y \end{cases} \tag{23}$$

After solving these two set of equations, the propagation $K_{(Y)}$ can be solved by

$$K_{(Y)} = \pm \sqrt{k_0^2 n_0^2 - k_{x,(Y)}^2 - k_{y,(Y)}^2} \tag{24}$$

where as above, we have added the $_{(Y)}$ subscript to indicate the y-polarisation state.

References

[1] Technical report, European XFEL Facts and Figures. 5

[2] Product Specification HC-1550-PM-01, NKT Photonics, 2011. 75, 77, 169, 191

[3] M.S. Alam, K. Saitoh, and M. Koshiba. High group birefringence in air-core photonic bandgap fibers. **30(8)**:824, 2004. 168, 169, 170, 171, 172

[4] D. Alessi and et al. Efficient excitation of gain-saturated sub-9-nm-wavelength tabletop soft-x-ray lasers and lasing down to 7.36 nm. *Phys. Rev. X*, **1**:021023, 2011. 6

[5] M. V. Ammosov, N. B. Delone, and V. P. Krainov. Tunnel ionization of complex atoms and of atomic ions in an alternating electromagnetic field. *JETP*, **23**:924, 1986. 13

[6] A. Amphawan. Review of optical multiple-input-multiple-output techniques in multimode fiber. *Optical Engineering*, **50(10)**:102001, 2011. 129

[7] P. Antoine and et al. Polarization of high-order harmonics. *Phys. Rev. A*, **55(2)**:1314, 1997. 65, 68, 93, 94

[8] Philippe Antoine and et al. Theory of high-order harmonic generation by an elliptically polarized laser field. *Phys. Rev. A*, **53(3)**, 1996. 65, 68, 93, 94, 95

[9] C. Argon and et al. Exploiting diversity in multimode fiber communications links via multisegment detectors and equalization. *IEEE Comm. Lett.*, **7(8)**, 2003. 129

[10] A. Argyros and et al. Circular and elliptical birefringence in spun microstructured optical fibres. *Opt. Express*, **17(18)**:15983, 2009. 191

[11] J. Arthur. *Linac coherent light source (lcls) design study report*, 1999. 3

[12] V. Bagnoud and J. D. Zuege. Independent phase and amplitude control of a laser beam by use of a single-phase-only spatial light modulator. *Opt. Lett.*, **29(3)**:295, 2004. 153, 156

[13] A. Bahabad and et al. Quasi-periodic and random quasi-phase matching of high harmonic generation. *Opt. Lett.*, **33(17)**:1936, 2008. 107, 108

[14] A. Bahabad and et al. Quasi-phase-matching of momentum and energy in nonlinear optical processes. *Nature Physics*, **4**:570, 2010. 89

[15] A. D. Bandrauk and et al. Quantum simulation of high-order harmonic spectra of the hydrogen atom. *Physical Review A*, **79**:023403, 2009. 18

[16] M. Baudrier-Raybaut and et al. Random quasi-phase-matching in bulk polycrystalline isotropic nonlinear materials. *Nature*, **432**:374, 2004. 107, 108, 109

[17] F. Beltran-Mejia and et al. Ultrahigh-birefringent squeezed lattice photonic crystal ber with rotated elliptical air holes. *Opt. Lett.*, **35(4)**:544, 2010. 77

[18] C Bostedt and et al. Ultra-fast and ultra-intense x-ray sciences: first results from the linac coherent light source free-electron laser. *J. Phys. B: At. Mol. Opt. Phys.*, **46**:164003, 2013. 5

[19] B. Bowden and et al. Silver/polystyrene-coated hollow glass waveguides for the transmission of terahertz radiation. *Opt. Lett.*, **32(20)**:2945, 2007. 173

[20] K. S. Budil, P.Salieres, M. D. Perry, and Anne L'huillier. Influence of ellipticity on harmonic generation. *Phys. Rev. A*, **48(5)**:R3437–R3440, 1993. 22, 65, 68, 94

[21] B. Busson and et al. Quasi-phase-matching in chiral materials. *Phys. Rev. Lett.*, **84(1)**:0031–9007, 2000. 82

[22] A. Cavalieri and et al. Attosecond spectroscopy in condensed matter. *Nature*, **449**:1029–1032, 2007. 8

[23] Yuan-Fong Chau, Han-Hsuan Yeh, and Din Ping Tsai. Analysis of high birefringence of four types of photonic crystal fiber by combining circular and elliptical air holes in fiber cladding. *Advances in Nonlinear Optics*, **2008**:239037, 2008. 75

[24] X. Chen and et al. Highly birefringent hollow-core photonic bandgap fiber. *Opt. Express*, **12(16)**:3888, 2004. 168, 169, 170, 171, 191

[25] Ivan Christov, Henry Kapteyn, and Margaret Murnane. Quasi-phase matching of high harmonics and attosecond pulses in modulated waveguides. *Opt. Express*, **7(11)**, 2000. 43, 108, 128

[26] P. B. Corkum. Plasma perspective on strong field multiphoton ionization. *Phys. Rev. Lett.*, **71(13)**, 1993. 11

[27] F. Couny and et al. Generation and photonic guidance of multi-octave optical-frequency combs. *Science*, **318(16)**:1118, 2007. 169

[28] B. Cros, C. Courtois, G. Matthieussent, A. Di Bernardo, N. Andreev D. Batan and, and S. Kuznetsov. Eigenmodes for capillary tubes with dielectric walls and ultraintense laser pulse guiding. *Phys. Rev. E.*, **65(2)**, 2002. 36, 51, 52, 53, 54, 56, 63, 161, 174, 182

[29] H. Daido. Review of soft x-ray laser researches and developments. *Reports on Progress in Physics*, **65**:1513, 2002. 6

[30] J. A. Davis, K. O. Valadez, and D. M. Cottrell. Encoding amplitude and phase information onto a binary phase-only spatial light modulator. *Applied Optics*, **42(11)**:6934, 2003. 153

[31] P. Dietrich and et al. High-harmonic generation and correlated two-electron multiphoton ionization with elliptically polarized light. *Phys. Rev. A*, **50(5)**:3585, 1994. 68, 94

[32] B. Dromey and et al. Generation of a train of ultrashort pulses from a compact birefringent crystal array. *Applied Optics*, **46**:5142–5146, 2007. 45

[33] B. Dromney and et al. Quasi-phasematching of harmonic generation via multimode beating in waveguides. *Opt. Express*, **15(13)**:7894, 2007. 88, 93, 102, 105

[34] C. Dumitrache and et al. High power spark delivery system using hollow core kagome lattice fibers. *Materials*, **7**:5700, 2014. 169

[35] C. G. Durfee and et al. Phase matching of high-order harmonics in hollow waveguides. *Phys. Rev. Lett.*, **83(11)**:2187–2190, 1999. 34, 35, 36, 37, 38

[36] C.T. Ertsgaard and et al. Dynamic placement of plasmonic hotspots for super-resolution surface enhanced raman scattering. *ACS Nano*, **30-Sept**:DOI:10.1021/nn504776b, 2014. 152

[37] C. Kan et al. Spectral and temporal structure in high harmonic emission from ionizing atomic gases. *Phys Rev. A*, **52(6)**:R4336, 1995. 20

[38] L. Yu et al. High-gain harmonic-generation free-electron laser. *Science*, **289**:5481, 2000. 5

[39] Gy Farkas and Cs Toth. Proposal for attosecond light pulse generation using laser induced multiple-harmonic conversion processes in rare gases. *Physics Letters A*, **168(5-6)**:447, 1992. 8

[40] T. Fennel and et al. Laser-driven nonlinear cluster dynamics. *Review of Modern Physics*, **82**:1793, 2010. 128

[41] Richard Feynman and et al. *The Feynman Lectures in Physics.* Caltech University Press, Pasadena, 1963. 121

[42] M. Galvan-Sosa, J. Portilla, J. Hernandez-Rueda, J. Siegel, L. Moreno, A. Ruiz de la Cruz, and J. Solis. Optimization of ultra-fast interactions using laser pulse temporal shaping controlled by a deterministic algorithm. *Applied Physics A*, page 1007, 2013. 152

[43] R. A. Ganeev, M. Suzuki, and H. Kuroda. Quasi-phase-matching of high-order harmonics in multiple plasma jets. *Phys. Rev. A*, **89**:033821, 2014. 42

[44] T. Geisler and S. Herstroml. Measured phase and group birefringence in elliptical core fibers with systematically varied ellipticities. *Opt. Express*, **19(26)**:B283, 2011. 167, 168

[45] R. W. Gerchberg and W. O. Saxton. A practical algorithm for the determination of the phase from image and diffraction plane pictures. *Optik*, **35**:237, 1972. 129, 152

[46] E. A. Gibson and et al. Coherent soft x-ray generation in the water window with quasi-phase matching. *Science*, **302(5642)**, 2003. 43, 44, 108, 128

[47] M. F. O. Hameed and S. S. A. Obayya. Polarization rotator based on soft glass photonic crystal fiber with liquid crystal core. *Journal of Lightwave Technology*, **29**:2725, 2011. 86

[48] O. H. Heckl and et al. High harmonic generation in a gas-filled hollow-core photonic crystal fiber. *Appl. Phys. B*, **97**:369, 2009. 75, 86, 168, 169

[49] C. Hernandez-Garcia, J. A. Prrez-Hernandez, T. Popmintchev, M. M. Murnane, H. C. Kapteyn, A. Jaron-Becker, A. Becker, and L. Plajal. Zeptosecond high harmonic kev x-ray waveforms driven by midinfrared laser pulses. *Phys. Rev. Lett.*, **111**:033002, 2013. 8

[50] Simon Hooker and Colin Webb. *Laser Physics*. Oxford University Press, Oxford, 2010. 1

[51] S.M. Hooker and C.E.Webb. Progress in vacuum ultraviolet lasers. *Prog. Quantum Electron*, **18**:227, 1994. 6

[52] Y. Hou and et al. Terahertz single-polarization single-mode hollow-core fiber based on index-matching coupling. *IEEE Photon. Technol. Lett.*, **24(8)**:637, 2012. 51

[53] A. S. Householder. Unitary triangularization of a nonsymmetric matrix. *Journal of the ACM*, **5(4)**:339, 1958. 134

[54] C. K. Hsueh and A. A. Sawchuk. Computer-generated double-phase holograms. *Applied Optics*, **17(24)**:3874, 1978. 153, 162

[55] A. Husakou and et al. Polarization gating and circularly-polarized high harmonic generation using plasmonic enhancement in metal nanostructures. *Opt. Express*, **19(25)**:25346, 2011. 81

[56] J Ducuing J. A. Armstrong, N. Bloembergen and P. S. Pershan. Interactions between light waves in a nonlinear dielectric. *Physical Review Online Archive (Prola)*, **127(6)**, 1962. 39

[57] J. Jerphagnon and D. S. Chemla. Optical activity of crystals. *J. Chem. Phys.*, **65**:1522, 1976. 86

[58] A. Jesacher, C. Maurer, A. Schwaighofer, S. Bernet, and M. Ritsch-Marte. Near-perfect hologram reconstruction with a spatial light modulator. *Optics Express*, **16**:2597, 2008. 152

[59] M. J. Katz and et al. Highly birefringent materials designed using coordination polymer synthetic methodology. *Angewandte Chemie International Ed.*, **46(46)**:8804, 2007. 77

[60] R. Keenan and et al. High-repetition-rate grazing-incidence pumped x-ray laser operating at 18.9 nm. *Phys. Rev. Lett.*, **94**:103901, 2005. 6

[61] O. Kfir and et al. Generation of bright phase-matched circularlypolarized extreme ultraviolet high harmonics. *Nature Photonics*, **12**:DOI: 10.1038/NPHOTON.2014.293, 2014.

[62] G. Koeckelberghs and et al. Regioregularity in poly(3-alkoxythiophene)s: Effects on the faraday rotation and polymerization mechanism. *Macromolecular Rapid Communications*, **27**:1920–1925, 2006. 85

[63] B. Koopmans. Spin dynamics: The ultimate view. *Nature Materials*, **6**:715, 2007. 81

[64] H. Koshima, M. Nagano, and T. Asahi. Optical activity induced by helical arrangements of tryptamine and 4-chlorobenzoic acid in their cocrystal. *J. Am. Chem. Soc.*, **127**:2455–2463, 2005. 86

[65] M. Landreman, K. O'Keeffe, T. Robinson, M. Zepf, B. Dromney, and S.M. Hooker. Comparison of parallel and perpendicular polarized counterpropagating light for supressing high harmonic generation. *Journal of the Optical Society of America B*, **24**:2421, 2007. 45

[66] M. Lax. Classical noise. v. noise in self-sustained oscillators. *Phys Rev.*, **160(2)**:290, 1967. 108, 113, 114

[67] M. Lewenstein, P Sailieres, and A L'Huillier. Phase of the atomic polarization in high-order harmonic generation. *Phys Rev. A*, **52**:4747, 1995. 95

[68] M. Lewenstein, P. Yu, A. Lcharhuillier, and P. B. Corkum. Theory of high harmonic generation by low-frequency laser fields. *Physical Review A*, **49(3)**:2117–2132, 1994. 15, 16, 93

[69] L. Z. Liu, K. O'Keeffe, D.T.Lloyd, and S. M. Hooker. General analytic solution for far-field phase and amplitude control, with a phase-only spatial light modulator. *Opt. Lett.*, **39(7)**:2137, 2014. 153

[70] L. Z. Liu, K. O'Keeffe, and S. M. Hooker. High harmonic optical generator [polarisation beating]. Isis Innovation, U.K. Patent Application No. GB1117355.6, 07 October 2011. 48, 64, 80, 89

[71] L. Z. Liu, K. O'Keeffe, and S. M. Hooker. High harmonic optical generator [optical rotation]. Isis Innovation, U.K. Patent Application No. GB1208753.2, 18 May 2012. 48, 80, 89

[72] L. Z. Liu, K. O'Keeffe, and S. M. Hooker. Optical rotation quasi-phase-matching for circularly polarized high harmonic generation. *Opt. Lett.*, **37(12)**:2415, 2012. 9, 48, 80, 81, 89, 190

[73] L. Z. Liu, K. O'Keeffe, and S. M. Hooker. Quasi-phase-matching of high harmonic generation using polarization beating in optical waveguides. *Phys Rev. A*, **85**:053823, 2012. 9, 48, 64, 80, 89, 94, 95, 101, 103

[74] L. Z. Liu, K. O'Keeffe, and S. M. Hooker. Quasi-phase-matching of high-order-harmonic generation using multimode polarization beating. *Phys Rev. A*, **87**:023810, 2013. 9, 48, 64, 89, 113, 114

[75] L. Z. Liu, K. O'Keeffe, D. T. Lloyd, and S. M. Hooker. General analytic solution for far-field phase and amplitude control, with a phase-only spatial light modulator. *Opt. Lett.*, **39(7)**:2137, 2014. 9

[76] A. L. Lytle, X. Zhang, P. Arpin, O. Cohen, M. M. Murnane, and H. C. Kapteyn. Quasi-phase matching of high-order harmonic generation at high photon energies using counterpropagating pulses. *Optics Letters*, **33(2)**:174–176, 2008. 45

[77] N. L. Manakov and Z. Ovsyannikov. *Sov. Phys. JETP*, **52**. 68, 94

[78] E.A. Marcatili. Dielectric rectangular waveguides and directional coupler for integrated optics. *Bell Syst. Tech. J.*, **48**, 1969. 176

[79] D. Marcuse and Ivan Kaminow. Modes of a symetric slab optical waveguide in birefringent media, part ii: Slab with coplanar optical axis. *IEEE Journal of Quantum Electroncs*, **15(2)**, 1979. 75

[80] Y. Matsuura and et al. *Electron Lett.*, **30**:1688, 1994. 129, 173

[81] O. Mitrofanov and et al. Dielectric-lined cylindrical metallic thz waveguides: mode structure and dispersion. *Opt. Express*, **18(3)**:1898, 2009. 173

[82] Sandile Ngcobo, Igor Litvin, and Liesl Burger andAndrew Forbes. A digital laser for on-demand laser modes. *Nature Comms.*, **4**:2289, 2013. 153

[83] Katsunari Okamoto. *Fundamentals of optical waveguides, Second Edition*. Academic Press, 2006. 51, 75, 176, 190

[84] K. O'Keeffe, D.T. Lloyd, and S.M.Hooker. Quasi-phase-matched high-order harmonic generation using tunable pulse trains. *Opt. Express*, **22(7)**:7722, 2014. 46, 57, 108

[85] K. OKeeffe, T. Robinson, and S. M. Hooker. Quasi-phase-matching high harmonic generation using trains of pulses produced using an array of birefringent plates. *Opt. Express*, **20(6)**:6236, 2012. 45, 86, 108, 128

[86] C. H. Pai. Tomography of high harmonic generation in a cluster jet. *Optics Letters*, **31(7)**:984, 2006. 128

[87] K. M. Patel and S. E. Ralph. Enhanced multimode fiber link performance using a spatially resolved receiver. *IEEE Photon. Tech. Lett.*, **14(3)**, 2002. 129

[88] A. Paul, R. A. Bartels, R. Tobey, H. Green, S. Weiman, I. P. Christov, M. M. Murnane, H. C. Kapteyn, and S. Backus. Quasi-phase-matched generation of coherent extreme ultraviolet light. *Nature*, **421(6918)**:51, 2003. 43, 108, 128

[89] P. M. Paul, E. S. Toma, P. Breger, G. Mullot, F. Auge, Ph Balcou, H. G. Muller, and P. Agostini. Observation of a train of attosecond pulses from high harmonic generation. *Science*, **292(5522)**:1689. 8

[90] Justin Peatross, Sergei Voronov, and I. Prokopovich. Selective zoning of high harmonic emission using counter-propagating light. *Opt. Express*, **1(5)**:114–125, 1997. 45

[91] S.J.H Petra and et al. Atom lithography with two-dimensional optical masks. *Applied Phys. B*, **79(3)**:279, 2004. 81

[92] T. Popmintchev and et al. Bright coherent ultrahigh harmonics in the kev x-ray regime from mid-infrared femtosecond lasers. *Science*, **8**:1287–1291, 2012. 2, 11, 38, 39, 112, 128

[93] J. H. V. Price and et al. *Appl. Phys. B.*, **B77**:291, 2003. 129

[94] G.B. Ren and et al. Polarization maintaining air-core bandgap fibers for terahertz wave guiding. *IEEE J. Quantum Electron*, **45(5)**:506, 2009. 173

[95] R. Rischer and et al. Broadband femtosecond frequency doubling in random media. *Applied Physics Letters*, **89**:2006, 2006. 107

[96] P. J Roberts and et al. Design of low-loss and highly birefringent hollow-core photonic crystal fiber. *Opt. Express*, **14(16)**:7329, 2006. 77, 169

[97] T. Robinson. *Quasi-Phase-Matching of High-Harmonic Generation*. D.Phil thesis, University of Oxford, 2007. 3, 12, 14, 15, 16, 18, 19, 38, 54, 57, 59, 60, 61, 63, 78, 88, 102

[98] T. Robinson and et al. Generation and control of ultrafast pulse trains for quasi-phase-matching high-harmonic generation. *J. Opt. Soc. Am. B*, **27(4)**:763, 2010. 45

[99] J.J. Rocca and et al. Demonstration of a discharge pumped table-top soft-x-ray laser. *Phys. Rev. Lett.*, **73(16)**:2192, 1994. 6

[100] A. R. Rundquist and et al. Phase-matched generation of coherent soft x-rays. *Science*, **280(5368)**:1412–1415, 1998. 34, 35, 36, 37

[101] R. L. Sandberg and et al. Lensless diffractive imaging using tabletop, coherent, high harmonic soft x-ray beams. *Phys. Rev. Lett.*, **99**:098103, 2007. 8

[102] Nicolas Sannerand, Nicolas Huot, and Eric Audouard. Programmable focal spot shaping of amplified femtosecond laser pulses. *Opt. Lett.*, **30(12)**:1479, 2005. 152

[103] M. Schultze and et al. Delay in photoemission. *Science*, **328**:1658–1662, 2010. 8

[104] D. Schulze and et al. Polarization of the 61st harmonic from 1053-nm laser radiation in neon. *Phys. Rev. A*, **57(4)**:3003, 1998. 68, 94

[105] J. Seres, V. S. Yakovlev, E. Seres, Ch Streli, P. Wobrauschek, Ch Spielmann, and F. Krausz. Coherent superposition of laser-driven soft-x-ray harmonics from successive sources. *Nature Physics*, **3(12)**:878–883, 2007. 42, 43

[106] O. Shapira and et al. Complete modal decomposition for optical waveguides. *Phys. Rev. Lett.*, **94**:143902, 2005. 129

[107] H. J. Shin and et al. Nonadiabatic blueshift of high-order harmonics from ar and ne atoms in an intense femtosecond laser field. *Phys Rev. A*, **63**:1050, 2001. 20, 21, 22, 23, 95

[108] P. L. Shkolnikov and et al. Optical quasi-phase-matching for high-order harmonic generation in gases and plasma. *Phys. Rev. A*, **50(6)**:R4461, 1994. 42, 89

[109] M. Skorobogatiy and et al. *Opt. Express*, **11**:2838, 2003. 129, 133

[110] I. J. Sola and et al. Controlling attosecond electron dynamics by phase-stabilized polarization gating. *Nature Physics*, **2**:320, 2006. 23, 24, 65, 68, 94

[111] V.V. Strelkov. Theory of high-order harmonic generation and attosecond pulse emission by a low-frequency elliptically polarized laser field. *Phys. Rev. A*, **74**:013405, 2006. 23, 24, 25

[112] V.V. Strelkov and et al. Origin for ellipticity of high-order harmonics generated in atomic gases and the sublaser-cycle evolution of harmonic polarization. *Phys. Rev. Lett.*, **107**:043902, 2011. 23, 24, 25, 26, 68, 94, 95

[113] Mitsuo Takeda, Hideki Ina, and Seiji Kobayashi. Fourier-transform method of fringe-pattern analysis for computer-based topography and interferometry. *JOSA*, **72(1)**:156, 1982. 157

[114] X. Tang and et al. Elliptical hollow fiber with inner silver coating for linearly polarized terahertz transmission. *IEEE Photon. Technol. Lett.*, **25(4)**:331, 2013. 51

[115] X.L. Tang and et al. Design and optimisation of low-loss high-birefringence hollow fiber at terahertz frequency. *Opt. Express*, **19(25)**:24967, 2011. 173, 174, 175, 176, 177, 185, 186, 191

[116] J. Tisch. Phase-matched high-order harmonic generation in an ionized medium using a buffer gas of exploding atomic clusters. *Physical Review A*, **62**:041802R, 2000. 128

[117] R. I. Tobey and et al. Ultrafast extreme ultraviolet holography: dynamic monitoring of surface deformation. *Optics Letters*, **32(3)**:286–288, 2007. 8

[118] L.N. Trefethen and B. David. *Numerical Linear Algebra*. SIAM, Philadelpha, PA, 1997. 134

[119] K. K. Tsia and et al. Electrical tuning of birefringence in silicon waveguides. *Applied Physics Letters*, **92**:061109, 2008. 75

[120] M. Uiberacker and et al. Attosecond real-time observation of electron tunnelling in atoms. *Nature*, **446**:627–632, 2007. 8

[121] M. P. van Exter, W. A. Hamel, and J. P. Woerdman. Nonuniform phase diffusion in a laser. *Phys Rev. A*, **43(11)**):6241, 1991. 108, 113, 114

[122] J. A. Vaughan and K.A. Nelson. Diffraction-based femtosecond pulse shaping with a two-dimensional spatial light modulator. *Opt. Lett.*, **30(3)**:323, 2009. 153, 156

[123] Georg von Freymann. Three-dimensional laser lithography: Finer features faster. *presented on CLEO-Europe 2013, Munich Germany, 12-16 May 2013*, 2013. 152

[124] C. Vozzi and et al. Cluster effects in high-order harmonics generated by ultrashort light pulses. *Applied Physics Letters*, **86**:111121, 2005. 128

[125] D. Walter and et al. Adaptive spatial control of fiber modes and their excitation for high-harmonic generation. *Opt. Express*, **14(6)**:3433, 2006. 128

[126] M. M. Wefers and K.A. Nelson. Independent phase and amplitude control, one for phase, one for amplitude. *Opt. Lett.*, **20**:1047, 1995. 152

[127] A. Willner and et al. Coherent control of high harmonic generation via dual-gas multijet arrays. *Phys. Rev. Lett.*, **107**:175002, 2011. 42

[128] H. G. Winful and A. Hu. Intensity discrimination with twisted birefringent optical fibers. *Opt. Lett.*, **11(10)**:668, 1986. 171, 187

[129] T. B. Woliski. Stress effects in twisted highly birefringent fibers. *SPIE*, **2070**:392, 1994. 171, 187

[130] G.K.L. Wong and et al. Excitation of orbital angular momentum resonances in helically twisted photonic crystal fiber. *Science*, **337**:446, 2012. 171, 172, 173

[131] X.M. Xi and et al. Optical activity in twisted solid-core photonic crystal fibers. *Phys. Rev. Lett.*, **110(14)**:143903, 2013. 171, 173, 174, 191

[132] Kuang-Yu Yang, Yuan-Fong Chau, Yao-Wei Huang, Hsiao-Yu Yeh, and Din Ping Tsai. Design of high birefringence and low confinement loss photonic crystal fibers with five rings hexagonal and octagonal symmetry air-holes in fiber cladding. *Journal of Applied Physics*, **109**:093103, 2011. 75

[133] H. Yu and et al. Magneto-optical effect in cobalt nanoparticle doped polymer optical material. Syndey, 2008. Opto-Electronics and Communications Conference, 2008 and the 2008 Australian Conference on Optical Fibre Technology. 85

[134] T. R. Zaman, X. Guo, and R. J. Ram. Faraday rotation in an indium phosphide waveguide. *Applied Physics Letters*, **90**:023514, 2007. 85

[135] M. Zepf, B. Dromey, M. Landreman, P. Foster, and S. M. Hooker. Bright quasi-phase-matched soft-x-ray harmonic radiation from argon ions. *Phys. Rev. Lett.*, **99**:143901, 2007. 46, 47, 78, 88, 102, 105

[136] Xiaoshi Zhang and et al. Quasi-phase-matching and quantum-path control of high-harmonic generation using counterpropagating light. *Nature Physics*, **3(4)**:270–275, 2007. 45